

When droplets deform, break up and propel microswimmers

THÈSE N° 8821 (2018)

PRÉSENTÉE LE 31 AOÛT 2018

À LA FACULTÉ DES SCIENCES ET TECHNIQUES DE L'INGÉNIEUR
LABORATOIRE DE MÉCANIQUE DES FLUIDES ET INSTABILITÉS
PROGRAMME DOCTORAL EN MÉCANIQUE

ÉCOLE POLYTECHNIQUE FÉDÉRALE DE LAUSANNE

POUR L'OBTENTION DU GRADE DE DOCTEUR ÈS SCIENCES

PAR

Giacomo GALLINO

acceptée sur proposition du jury:

Prof. J.-F. Molinari, président du jury
Prof. F. Gallaire, directeur de thèse
Prof. J. Magnaudet, rapporteur
Prof. S. Michelin, rapporteur
Prof. T. Schneider, rapporteur



ÉCOLE POLYTECHNIQUE
FÉDÉRALE DE LAUSANNE

Suisse
2018

To my parents
Domenico & Patrizia
and my brother
Giovanni

Acknowledgements

I am happy about many things that occurred along the way during these years at EPFL. However, what makes everything truly special is the people that I have met during this journey and that I would like to briefly acknowledge here.

First of all, I want to thank François for giving me the possibility to become part of LFMI. I have become passionate about fluid mechanics when I first came as Master student in the lab and I have been lucky enough to be able to continue this adventure as PhD. I really admire the infinite energy that you put into science and that you transmit to all of us in the lab. I have always appreciated the scientific freedom that I had on my project and I thank you for your guidance that has led to exciting results. I would like to acknowledge Jacques Magnaudet, Sebastien Michelin and Tobias M. Schneider for spending time reading in detail the thesis and for the interesting discussions that we have had during the thesis defense. In particular, I thank Tobias for the insightful discussion on the dynamical system approach to fluid mechanics, Sebastien for teaching me about asymptotics and Jacques for the sharp questions during the thesis defense. Also, I would like to thank Jean-François Molinari for presiding over the jury. I would like to thank Eric Lauga for hosting me six months in his lab in Cambridge where I could learn about the hydrodynamics of swimming microorganisms. It has been great to spend time in Cambridge, with its unique atmosphere blending scientific research and ancient colleges. I want to thank Jérôme Hoepffner for showing me the beauty of bifurcation theory, Filippo De Mari to which I owe my first look on nonlinear differential equations and Alessandro Bottaro for introducing me to fluid mechanics and for the interesting discussions and suggestions that he gave me over the years.

This adventure would not have been the same without amazing colleagues with which I have shared working time as well as fun time. I want to thank Gioele, we started and we are now finishing the PhD together and we have witnessed the transition between first and second

Acknowledgements

generation of LFMist! Francesco with whom I have shared funny moments and panoramic jogging by the Lac Lemman, Vlado who showed me that life looks different if you take it with joy and enthusiasms, Mathias N. and Laura that supervised me during my first times at LFMI, Eunok and Isha for the fun time in the best office room! Petra for her help in the administration and her kindness in ignoring my frequent grammatical errors in french and then Edouard, Andrea, Cristobal, Marc-Antoine, Yoan, PT, Lorenzo, Gaetan, Mathias B., Ludo, Simon, Hervé, Nicolas, Marta, Pier-Giuseppe and Shahab. I would also like to thank the colleagues of the neighboring lab ECPS for the lunch breaks we spent together and especially Simon for the hikes that we did, Florian for the nice swimming pool-based parties at his place and Mirko for organizing the amazing conference in Bari. A special mention goes to Lilai and to his unconventional pick on life and research from whom I have learnt a lot during these years. I would also like to thank the friends from Lausanne: Fernando for the nice after-work cycling in the Lavaux, Cristina C., Cristina R., Laura, Nathan, Clara, Cristopher, Sophie, Joel, Andrea, David, Vasilis, Nico, Masca, Roberta, Pisano, Cara, Andrea, Martina, Biasu, Giulio, Roberta, Valerio, Vale, Mathias and all the friends from football. Also, I thank the friends from Cambridge: Deba for the many Indian dinners, Gabriele, Justas and Maciej.

My deepest thanks go to my family, my parents Domenico & Patrizia and my brother Giovanni. Thank you for the love and support that you always gave me and that defines the person that I am today. Thank you because, even if we don't meet very often, every time I come back it seems like I had never left. I thank my mother for our endless discussions about life, feelings and happiness. I thank my father for reminding me that curiosity is sometimes more important than knowledge. I thank my brother, who I regard as another myself, for being always on my side. Finally, thank you Erica, meeting you has been the most beautiful thing in this journey.

Lausanne, 13 July 2018

Giacomo Gallino

Abstract

This thesis investigates the motion and breakup of droplets in low-Reynolds-number flows, focusing on two aspects. In the first part, we study the breakup of droplets in subcritical flow conditions, when there exists a linearly stable solution for the droplet shape, but a finite amplitude perturbation might trigger instabilities. Thus, there exists a finite basin of attraction of the stable solution, whose boundary separates droplets that break from those recovering the stable shape. Our effort is mostly devoted to the exploration of the state space in which the basin boundary is defined. To this end, we proceed by adapting theories initially developed to study laminar-turbulent transition, namely nonmodal analysis and edge tracking. We study the influence of non-normal effects in the breakup of a rising droplet, showing that the optimal shapes found with nonmodal analysis are more efficient in triggering breakup than initially ellipsoidal droplets. Afterwards, we investigate the relevance of edge state in the breakup of droplets in uniaxial extensional flows, finding that edge states select the path toward breakup. The exploration of the bifurcation diagram reveals a similar situation for biaxial extensional flows, where droplets are squeezed along the axis instead of being extended. In the second part we develop a joint chemical-hydrodynamics model to study the motion of bubble-propelled conical microswimmers. We conclude that the chemistry and the hydrodynamics partially decouple. In fact, chemistry dictates the time scale at which the microswimmer moves while the hydrodynamics governs the attained displacement. We furthermore find the geometrical and chemical parameters that optimize the swimming velocity. The effects of bubble deformability are then included. In this case, the swimming velocity is optimal for small cone opening angles. Furthermore, we find that the swimming efficiency, measured in displacement attained per fuel consumption, decreases when the bubble is more deformable. Finally, we study the motion of a sphere inflating close to a wall, which is relevant to the study of conical microswimmers and allows us to revisit the classical settling sphere problem. We find that depending on the boundary conditions imposed on the sphere, whether it is a rigid shell or a perfect free-shear bubble, the sphere-wall gap will close or open in time.

Key words: low Reynolds number flows, droplet breakup, nonlinear instabilities, catalytic microswimmers, self-propulsion, boundary integral method.

Riassunto

Questa tesi investiga la rottura di gocce in flussi a basso numero di Reynolds e si concentra su due aspetti. Nella prima parte, studiamo la rottura di gocce in flussi subcritici, quando esiste una soluzione linearmente stabile per la forma della goccia, ma una perturbazione di ampiezza finita può innescare delle instabilità. Di conseguenza, esiste un bacino di attrazione di taglia finita della soluzione stabile, i cui confini separano gocce che si rompono da quelle che ritornano alla forma stabile. I nostri sforzi sono dedicati soprattutto all'esplorazione dello spazio di stato in cui il confine del bacino di attrazione è definito. A questo fine, procediamo adattando teorie inizialmente sviluppate per studiare la transizione laminare-turbolenta, in particolare l'analisi non modale e la tecnica dell'*edge-tracking*. L'influenza di effetti non normali è studiata nel caso della rottura di una goccia che trasla in un fluido altrimenti in quiete, dove dimostriamo che le forme ottimali trovate con l'analisi non modale sono più efficienti nell'innescare instabilità rispetto a gocce inizialmente ellissoidali. Successivamente, investighiamo la rilevanza degli *edge state* nella rottura di una goccia in un flusso estensionale, dove troviamo che gli *edge state* selezionano il percorso che porta alla rottura della goccia. L'esplorazione del diagramma di biforcazione rivela che una situazione simile si verifica in un flusso estensionale biassiale, dove le gocce sono compresse nella direzione assiale invece che elongate. Nella seconda parte sviluppiamo un modello che considera gli effetti chimici e idrodinamici nella propulsione di microuotatori conici. Concludiamo osservando che la chimica e l'idrodinamica sono, in questo caso, disaccoppiate. Infatti, la chimica detta il tempo di movimento caratteristico mentre l'idrodinamica governa lo spostamento ottenuto. Inoltre, troviamo il valore ottimale dei parametri che dettano la massima velocità del microuotatore. Quindi, includiamo gli effetti della deformazione della bolla. In questo caso, la velocità è massima per piccoli angoli di apertura del corpo conico. Inoltre, troviamo che l'efficienza del microuotatore, misurata in spostamento ottenuto per carburante consumato, diminuisce quando la bolla diventa più deformabile. Infine, studiamo il movimento di una bolla sferica che si gonfia vicino ad un muro, fenomeno rilevante sia per lo studio dei microuotatori conici sia perché ci permette di rivisitare il classico caso di una sfera che si deposita. Troviamo che, se imponiamo condizioni al contorno di *no-slip* o *free-shear* sulla superficie della bolla, la distanza tra essa e il muro diminuisce o aumenta nel tempo.

Parole chiave: flussi a basso numero di Reynolds, rottura di gocce, instabilità nonlineari, microuotatori catalitici, auto-propulsione, metodo degli elementi di frontiera.

Contents

Acknowledgements	v
Abstract (English/Italian)	vii
1 Introduction	1
1.1 Droplet breakup in low-Reynolds-number flows	1
1.1.1 Learning from transition to turbulence: non-normal effects and edge states	5
1.1.2 In this thesis: Droplet breakup in a simple domains	7
1.2 Swimming at low Reynolds number	8
1.2.1 Conical microswimmers: state of the art	9
1.2.2 In this thesis: Conical microswimmers	10
1.3 Outline and personal contribution	11
2 Numerical method	13
2.1 The boundary integral equation for Stokes flows	13
2.1.1 The boundary integral equation for the fluid velocity	13
2.1.2 The boundary integral equation for the pressure	16
2.1.3 Droplet in unbounded domain	16
2.1.4 BIE for the flow generated by a moving rigid particle	18
2.1.5 Axisymmetric Stokes flow	18
2.2 The axisymmetric Boundary Integral Method	22
2.2.1 Boundary Element Method implementation	22
2.2.2 Deformable droplets and bubbles	25
2.2.3 Rigid particles in flows	26
2.2.4 Remeshing algorithms	28
2.2.5 Volume correction	30
2.2.6 Deflation technique for inviscid droplets	30
2.2.7 Spectral Boundary Integral Method	31
2.2.8 Remeshing in the Spectral BIM	34
2.3 Newton method and linear stability analysis	35
2.3.1 A well posed Newton method for deformable droplets	36
2.3.2 BEM based Newton method with singular preconditioning	37
2.3.3 Spectral BIM based Newton method	40
2.3.4 The novelty: Newton method for overturning droplet geometries	40

Contents

2.3.5	Linear stability analysis	43
2.4	Appendix	45
2.4.1	Appendix I: Study of the leading order singularity of Stokes kernels . . .	45
2.4.2	Appendix II: Computational efficiency of BIM	49
I	Droplet breakup in simple domains	51
3	The stability of a rising droplet: an inertialess non-modal growth mechanism	53
3.1	Introduction	53
3.2	Governing equations and linearisation	55
3.3	Non-modal analysis: Theory	56
3.4	Non-modal analysis: results	58
3.4.1	Transient growth and numerical range	58
3.4.2	Linear growth and shape evolutions	59
3.5	Nonlinear analysis	60
3.5.1	Nonlinear energy growth and shape evolution using DNS	60
3.5.2	Critical amplitude of the perturbation δ_c	61
3.6	Conclusion and discussions	62
4	Edge states control droplet breakup in subcritical extensional flows	65
4.1	Introduction	65
4.2	Numerical method	66
4.3	Results	68
4.3.1	Edge tracking	68
4.3.2	Bifurcation diagram	71
4.3.3	Numerical experiment: sudden change in flow conditions	72
4.3.4	Influence of the viscosity ratio	73
4.4	Conclusions	75
5	Further exploration of the parameter space of a droplet in an extensional flow	77
5.1	Introduction	77
5.2	Symmetry breaking bifurcation	78
5.3	The relaxation of a droplet in a quiescent flow	80
5.3.1	Relaxation of initially ellipsoidal droplets	80
5.3.2	Relaxation of initially non-ellipsoidal droplets	83
5.4	Biaxial extensional flow	83
5.5	Conclusions	86
II	Conical microswimmers	89
6	Physics of Bubble-Propelled Microrockets	91
6.1	Introduction	92

6.2	Model	93
6.2.1	Gas diffusion	94
6.2.2	Hydrodynamics	95
6.2.3	Numerical method and validation	96
6.3	Results	98
6.3.1	Dissolved gas distribution and bubble growth	98
6.3.2	Definition and dynamics of the bubble cycle	100
6.3.3	Influence of physico-chemical properties on the microrocket displacement	101
6.3.4	Microrocket displacement and average velocity for different opening angles	103
6.3.5	Optimal microrocket design	103
6.3.6	Perspectives: many bubbles interaction	105
6.4	Conclusions	107
7	The hydrodynamics of a microrocket propelled by a deformable bubble	109
7.1	Introduction	109
7.2	Model	110
7.2.1	Hydrodynamics	111
7.2.2	Numerical method	112
7.3	Velocity field and microrocket velocity over one bubble cycle	113
7.4	Influence of the opening angle	114
7.4.1	Direct numerical simulations	114
7.4.2	An empirical spring-like model for confined bubbles	117
7.5	Influence of the capillary number	119
7.6	Critical threshold for sustained bubble ejection	120
7.7	Conclusions	120
8	The motion of a bubble inflating next to a wall	123
8.1	Introduction	123
8.2	Description of the problem	124
8.3	Numerical results	125
8.4	Lubrication theory	126
8.5	Physical explanation: flow field within the gap	130
8.6	Conclusions	132
9	Conclusions and perspectives	133
	Bibliography	139
	Curriculum Vitae	151

1 Introduction

1.1 Droplet breakup in low-Reynolds-number flows

The study of droplet breakup at low Reynolds number dates back to the work of G.I. Taylor [1], Acrivos [2], Happel & Brenner [3] and further numerical and experimental studies [4, 5, 6, 7]. Droplet deformation results from two competing effects, the viscous forces stretching and shearing the droplet, and the surface tension forces reducing its deformation in order to minimize the droplet surface area, as in the case of a droplet elongated by an external flow shown in Figure 1.1a. When the ratio between viscous forces and surface tension forces is sufficiently large, the droplet may deform until breaking into smaller droplets, as in the case an initially ellipsoidal droplet rising due to gravitational forces or the relaxation of a very elongated droplet in a quiescent fluid (see Figure 1.1d-e respectively). A particular case of breakup is the so-called tip streaming, where a thin jet is produced from the pointed tip of a droplet, as shown in Figure 1.1b. As will be explained later more in detail, such a rich interfacial dynamics and diversity of droplet shapes results from the interface conditions, which are nonlinear and introduce a memory in the flow. Namely, droplets with different initial shapes undergo different time evolutions. For example, as shown if Figure 1.1c, two toroidal droplets of same volume might relax to a spherical shape or develop instabilities leading to breakup, depending on their initial shape.

Recently, there has been a renewed excitement in the field due to the promising applications of droplet-based microfluidics, emerging both in the context of industrial and academic research [15]. In fact, the low Reynolds number regime enables precise control of many complex phenomena like droplet formation, droplet coalescence and droplet transport. Even more importantly, droplet microfluidics has the advantage of manipulating small amounts of costly or dangerous substances. Some applications which benefit from droplet-based microfluidics are biology research, in controlling cells transport when executing cell analysis, or the chemical industry, in mixing small amount of reagents (see Figure 1.2b-c). However, generating a high number of monodispersed droplets, as in Figure 1.2a-b-c, requires a deep understanding of the fluid-mechanics involved. For example, in Figure 1.2d, a tip streaming

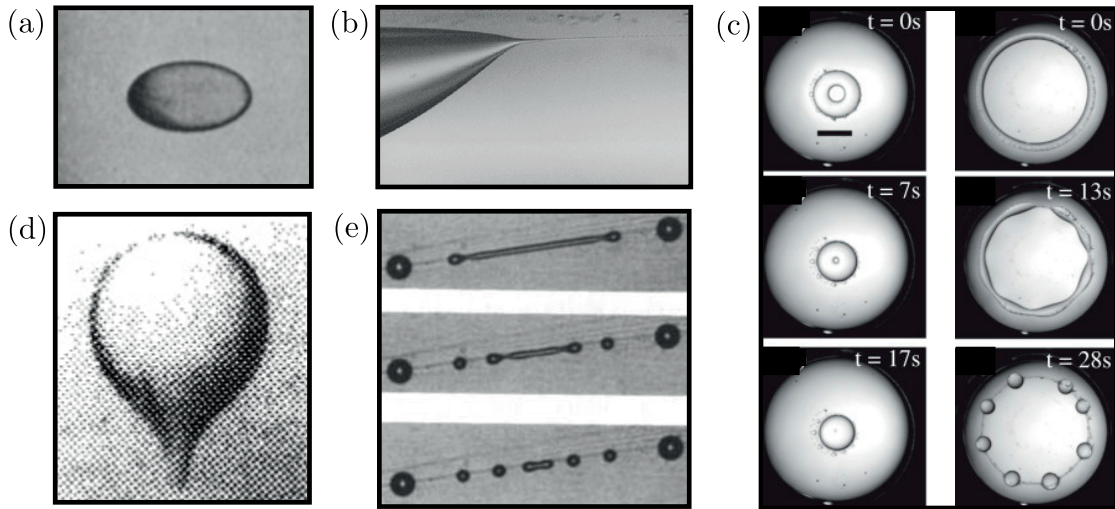


Figure 1.1 – Deformable droplet in low Reynolds number flows. (a) Droplet deforming in an extensional flow [1]. (b) Tip streaming, a small jet is produced at the droplet tip [8]. (c) Relaxing toroidal droplets (seen from above) recovering a spherical shape or breaking-up depending on the initial shape [9]. (d) The instability of a droplet rising in a gravitational field which develops an elongated tail, finally leading to breakup [10]. (e) An elongated thread break up while relaxing in an otherwise quiescent fluid [11].

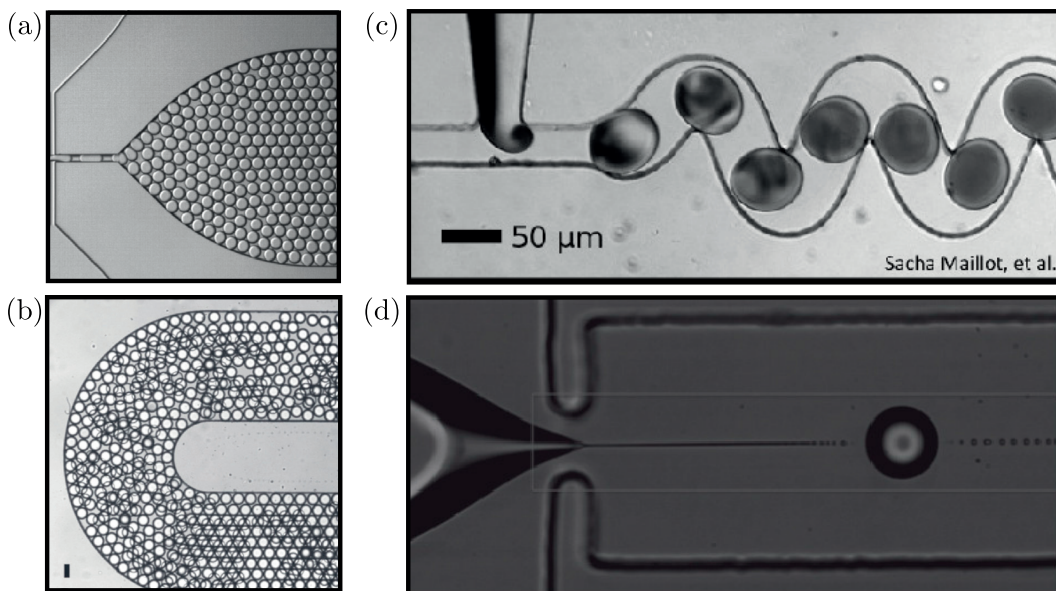


Figure 1.2 – Droplet based microfluidics. (a) Droplets are generated in a microfluidic device, from www.dolomite-microfluidics.com. (b) Cells encapsulated in droplets [12]. (c) Mixing in droplet [13]. (d) Tip streaming in microfluidics [14].

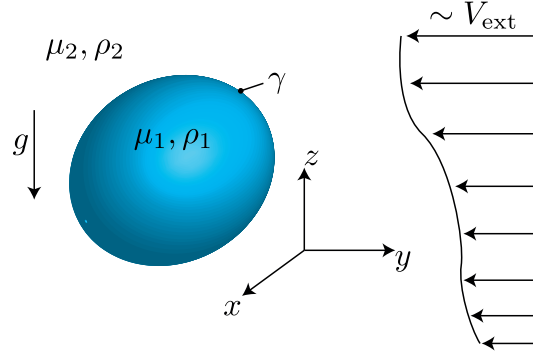


Figure 1.3 – Sketch of a droplet in a low Reynolds number flow.

jet occurs after droplet pinch-off and contaminates the suspending fluid with undesirable droplets.

In order to understand the fundamental physical ingredients influencing droplet breakup, we now introduce the equations governing the fluid motion. Referring to figure 1.3, we consider the general case of an unbounded droplet of fluid 1, volume $\frac{4}{3}\pi R^3$, viscosity μ_1 and density ρ_1 suspended into fluid 2 of viscosity μ_2 and density ρ_2 . The droplet is subjected to a gravitational field $-\mathbf{g}\mathbf{e}_z$ and a flow of characteristic velocity V_{ext} . The non-dimensional fluids velocity and pressure, modified by the hydrostatic term, (\mathbf{u}_1, p_1) and (\mathbf{u}_2, p_2) are found by solving the Stokes equations, a limiting case of the Navier-Stokes equations where inertia is neglected. This assumption is justified considering that, at microscale, the Reynolds number $\text{Re} = \rho_2 R V_{\text{ext}} / \mu_2$ comparing inertial to viscous effects is often very small, $\text{Re} < 10^{-2}$. Taking the reference scales

$$[L] = R, \quad [V] = \frac{\gamma}{\mu_2}, \quad [P] = \frac{\gamma}{R}, \quad (1.1)$$

where γ is the surface tension, the non-dimensional Stokes equations write

$$\begin{aligned} -\nabla p_1 + \lambda \nabla \mathbf{u}_1 &= \mathbf{0}, & \nabla \cdot \mathbf{u}_1 &= 0, \\ -\nabla p_2 + \nabla \mathbf{u}_2 &= \mathbf{0}, & \nabla \cdot \mathbf{u}_2 &= 0, \end{aligned} \quad (1.2)$$

where $\lambda = \mu_1 / \mu_2$ is the viscosity ratio between inner and outer fluid. The interface conditions, coupling fluid 1 and 2, read

$$(\boldsymbol{\sigma}_2 - \boldsymbol{\sigma}_1) \cdot \mathbf{n} = (\nabla_s \cdot \mathbf{n})\mathbf{n} + \text{Bo } z \mathbf{n}, \quad (1.3)$$

$$\mathbf{u}_1 = \mathbf{u}_2, \quad (1.4)$$

where $\boldsymbol{\sigma}$ is the stress tensor, \mathbf{n} is normal vector to the interface and $\nabla_s = (\mathbf{I} - \mathbf{nn})\nabla$ is the surface gradient operator. Equation (1.3) & (1.4) are the discontinuity of normal stresses due to surface tension and gravity and the continuity of velocity respectively. The Bond number $\text{Bo} = (\rho_2 - \rho_1)gR^2/\gamma$ compares gravity to surface tension effects. The far field boundary

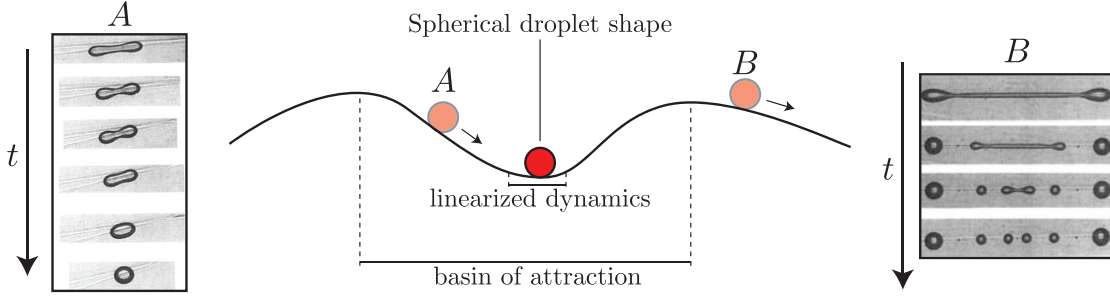


Figure 1.4 – Schematic representation of the basin of attraction of a droplet relaxing in an otherwise quiescent fluid. Depending whether the initial condition lies inside or outside the basin of attraction, the droplet relaxes toward the stable spherical shape (case A) or breaks into smaller droplets (case B). Pictures are taken from [11, 5].

condition imposes a far field flow

$$\mathbf{u}_2 \rightarrow Ca \mathbf{f}(\mathbf{x}), \quad p_2 \rightarrow 0 \quad \text{for } \mathbf{x} \rightarrow \infty \quad (1.5)$$

where $\mathbf{f}(\mathbf{x})$ is an arbitrary function. The capillary number $Ca = \mu_2 V_{\text{ext}} / \gamma$ compares the viscous effects due to the external flow of characteristic velocity V_{ext} to the surface tension effects. Finally, the time evolution of the droplet surface \mathbf{x}_s is dictated by its own velocity \mathbf{u}_s , through the impermeability condition

$$\frac{d\mathbf{x}_s}{dt} = [(\mathbf{u}_s - \mathbf{u}_{\text{drop}}) \cdot \mathbf{n}] \mathbf{n} + \mathbf{u}_{\text{drop}}, \quad (1.6)$$

where \mathbf{u}_{drop} is the velocity of the droplet center of mass. Namely, the first term on the right hand side is responsible for the droplet change in shape due to displacements normal to the interface while the second term accounts for the droplet translation. This equation of motion is a nonlinear because of the curvature in (1.3) and because of the advection of the material points of the surface given by $d\mathbf{x}_s/dt = \partial\mathbf{x}_s/\partial t + \mathbf{u}_s \cdot \nabla_s \mathbf{x}_s$. Therefore equation (1.6) is a nonlinear dynamical system for the time evolution of the droplet interface, similarly to the case of the Navier-Stokes equations, where the time evolution of the velocity field is a nonlinear function of the current velocity field [16]. Thus, interfacial flows exhibit a rich transient dynamics and might even show multiplicity of steady solutions because of the nonlinearity embedded in the interface conditions. Note that this is fundamentally different from the *path instabilities* of bubbles at finite Reynolds number [17, 18, 19], where the unstable evolution is given by the interplay between the fixed-shape bubble and the wake developing due to inertial effects.

Nonlinear dynamical systems are characterized by the fact that the temporal growth of perturbations depends on their initial amplitude [20, 21, 22]. For example, let's consider a spherical droplet in a quiescent fluid, the spherical shape is stable and small deformations of the droplet shape will exponentially decay in time [23, 24]. Referring to figure 1.4, this behavior can be analyzed with the linearized dynamics around the spherical solution. However, when the initial droplet elongation is large, the linearized dynamics is not able to capture the time

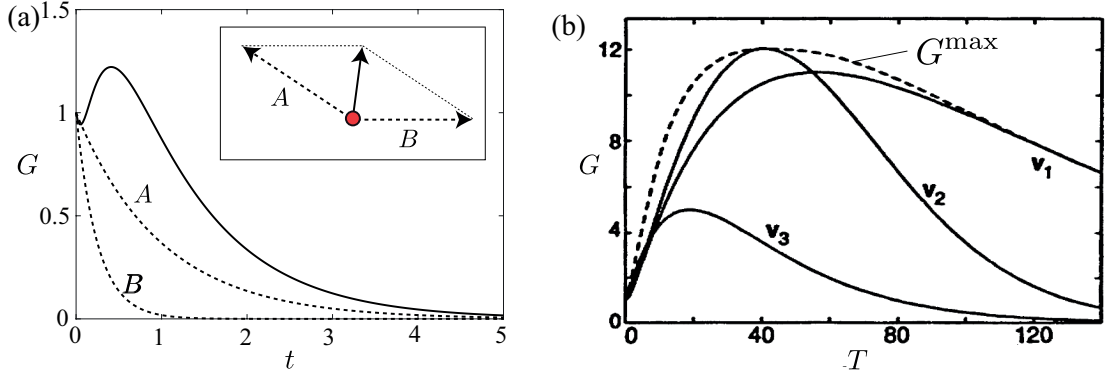


Figure 1.5 – (a) Energy gain G versus time in a simple model having two degrees of freedom. The two eigenvectors of the system A and B decay in time because are stable while their sum transiently increases at short time. The inset shows the eigenvectors which are non-normal. (b) Optimal gain G^{\max} at versus time horizon T for Couette flow at $\text{Re} = 350$, taken from [25]. Solid lines show the linear evolution of G for three optimal initial conditions (v_1, v_2, v_3) , maximizing the energy gain at different time horizons.

evolution. In fact, nonlinearities start to play a dominant role and, depending on the initial amplitude of the perturbation, the time evolution might lead to completely different results. For example, case A in Figure 1.4 shows a stable evolution while case B becomes unstable and lead to breakup with formation of smaller droplets. Finite amplitude perturbations therefore define a basin of attraction of the spherical solution, whose boundary separate droplets relaxing toward it from droplets breaking-up. Due to the high dimensionality of the state space of infinite droplet shapes in which the basin boundary is defined, it is an extremely challenging task to a-priori determine whether a droplet shape will undergo breakup or not. In the following paragraph, we will introduced theories which have provided insights for the understanding of nonlinear transition in single phase laminar flows. Our aim will be than to adapt such theories to investigate droplet breakup at low Reynolds number.

1.1.1 Learning from transition to turbulence: non-normal effects and edge states

Many laminar flows are linearly stable but undergo transition to turbulence due to finite amplitude perturbations, as for example pipe flow and Couette flow. In the past years, many efforts have been devoted to study laminar-turbulent transition and to better define the basin of attraction of the linearly stable solution. In this section, we introduce the results from these studies, that will lay the foundation for our work in droplet breakup in low-Reynolds-number flow.

The first approach that we describe is the so-called *nonmodal analysis*. In fact, one deficiency of classical linear stability analysis is that it monitors the temporal evolution of single modes, hence the name modal, without considering their interaction. It has been shown [25, 26] that, despite all modes being stable and thus decaying in time, their interaction might lead to a

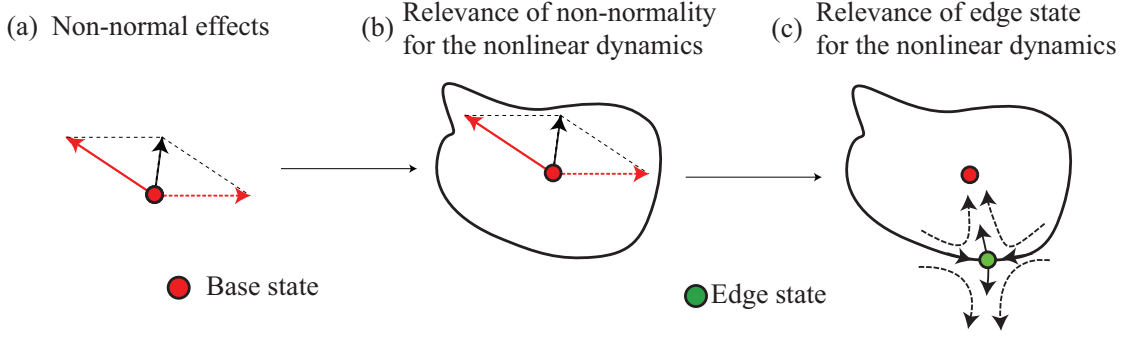


Figure 1.6 – (a) Non-normal eigenvector basis, leading to transient growth of energy at short time. (b) When nonmodal analysis is successful, it provides optimal shapes undergoing transition with small perturbation energy. (c) Edge states are unstable states whose stable manifold forms the basin boundary.

transient energy gain at short time (see Figure 1.5a). This linear amplification mechanism is possible only when the eigenvector basis is non-normal.

Non modal analysis has been frequently used to investigate whenever the transition to turbulence is affected from transient effects. Although once turbulence is established, it is sustained by the energy transport exerted by the nonlinear term of the Navier-Stokes equation, transient linear effects can indeed play an important role in the transition regime. This approach has given good results for many configurations [26], where a linear transient growth of energy has been found responsible for the escape of the laminar state, thus triggering nonlinearities sustaining the turbulent state. More precisely, the energy gain is defined as

$$G(t) = \frac{E(t)}{E(0)}, \tag{1.7}$$

where E is a scalar quantity which measures the growth of the instability, usually the perturbation kinetic energy. Furthermore, adjoint-based theory [26] provides the maximum gain that is possible to obtain at time horizon T

$$G^{\max}(T) = \max_{\mathbf{x}_0} \frac{E(T)}{E(0)}, \tag{1.8}$$

where \mathbf{x}_0 is the optimal initial condition whose linear evolution maximize G at time T . For example in Figure 1.5b we report the optimal gain for Couette flow. Almost surprisingly, linear nonmodal analysis is sometimes capable to give insights about the nonlinear transition, although there is no a priori guarantee of its effectiveness, since the transition is sometimes entirely dictated by nonlinear mechanisms. A sketch of this concept is shown in Figure 1.6, where we show schematically the results from nonmodal analysis and their possible link to the exploration of the basin of attraction. Indeed, linear nonmodal analysis can sometimes provide optimal initial conditions which succeed in triggering transition with small energy of the perturbation, somehow *pointing* into the direction where the distance between the basin

1.1. Droplet breakup in low-Reynolds-number flows

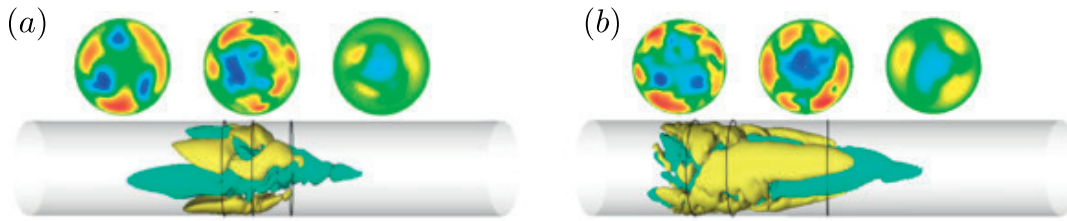


Figure 1.7 – Transition to turbulence in pipe flow at $Re = 1900$, the figures are taken from [27]. Cross-sectional instantaneous axial velocity u_z and $u_z \pm 0.07$ isosurfaces of (a) the edge state and (b) the turbulent state, respectively. The axial positions of the visualized cross-sections are indicated by rings. Red, green and blue indicate regions where the streamwise flow speed is higher than, similar to or lower than for the corresponding parabolic profile.

boundary and the stable state is minimal 1.6b.

As said previously, nonmodal analysis is not always successful in describing nonlinear transition. For this reason, other tools have been developed to study the evolution of finite amplitude perturbations in linearly stable flows. In particular, there has been in the past few years a development of numerical methods to track unstable states lying on the basin boundary, so called *edge states*. Edge states are unstable steady states embedded in the basin boundary, whose stable manifold form the basin boundary. Therefore, they are unstable in only one direction perpendicular to the basin boundary. Since they are stable but for one direction, they are mostly attracting during the transient evolution of dynamical system and often guide the transition to turbulence in shear flows [28] and pipe flows [27]. For example, an edge state in pipe flow is shown in Figure 1.7a. The resemblance of snapshots of the turbulent state shown in Figure 1.7b to the edge state suggests that the transition and turbulence structured are influenced by the nonlinear state.

1.1.2 In this thesis: Droplet breakup in a simple domains

The principal aim of this thesis is to have a better understanding of finite amplitude instabilities leading to droplet breakup. In this regime, where a stable droplet shape exists, very little is known about the basin boundary delimiting droplets that break up from those transiently returning to the steady state. Compared to the vast amount of previous studies concerning droplet breakup, our novelty consists in adapting theories developed to study transition to turbulence in subcritical laminar flows to the droplet phenomenon.

We proceed by considering canonical flows, for example a rising droplet or a droplet in an extensional flow. In both cases, there is a stable solution that undergoes breakup for a critical amplitude of the perturbation. In these simple flows, we develop the framework to perform nonmodal analysis (for the rising droplet), showing that linear energy amplification favors nonlinear instabilities. For the droplet in extensional flow, we compute the edge state and unravel, for the first time to our knowledge, a large part of the bifurcation diagram, finding

edge states that guide droplet breakup via an end-pinching mechanisms that has been indeed previously observed in experiments [5]. Furthermore, we find left-right non-symmetric steady shapes that, following our conjecture, might influence the tip streaming phenomenon.

Finally, we consider the case where a droplet is compressed in an axisymmetric manner, in a so-called bi-axial extensional flow. In this case, the bifurcation diagram is qualitatively similar to the one for the extensional flow. However, the bifurcation diagram suggests that for a certain subcritical capillary number, edge states might be toroidal droplets.

1.2 Swimming at low Reynolds number

Swimming at the microscale plays an important role in many biological processes, for instance marine microbes regulate the ocean ecosystem [29] and certain types of bacteria contribute to protect the human body from diseases [30]. From the engineering point of view, it is important and fascinating to design and manufacture synthetic micro/nano swimmers capable of achieving similar functions. Indeed, in the last decade, synthetic swimmers have been designed thanks to the new micro-fabrication techniques. Their ability to operate at small scale make them ideal to execute bio-medical operations inside the human body [31, 32], as well as to carry on complex tasks in microfluidics applications [33, 34, 35].

Nevertheless their small size poses great challenges regarding their manufacturing and the design of effective propulsion strategies, since the hydrodynamics of micro-swimmers is very different from the hydrodynamic of swimming at the macro scale.

The main feature of swimming at the microscale is that viscous effects prevail over inertial effects. To compare quantitatively the two effects we define the Reynolds number, a non-dimensional number given by the ratio between the inertial and viscous forces $Re = \rho UL/\mu$, where ρ and μ are the density and viscosity of the ambient fluid and L and U are the typical length and velocity scale of the swimmer. The order of magnitude of the Reynolds number for micro-swimmers is $Re < 10^{-1}$, while for humans swimming in water is $Re \approx 10^4$. The crucial consequence of neglecting inertia is that the equations for the fluid motion become linear and independent of time, these properties lead to *kinematic reversibility* [36]. This means that by reversing the direction of the micro-swimmer motion, the flow streamlines are not modified and only the direction of the flow changes, as stated in the scallop theorem [37]. Therefore a reciprocal movement would generate an equal forward and backward motion, resulting in an overall zero net translation. This imposes strong constraints on swimming at the microscale, since a non-reciprocal motion is needed in order to achieve a net displacement.

Biological swimmers have developed different strategies to perform non-reciprocal movements. *E. Coli* uses a relatively stiff helix rotated by a motor embedded in its body [38], sperm cells of many species adopt a flexible filament undergoing a wave-like motion due to molecular motors distributed along the length of the filament [39]. Other micro-swimmers propel themselves due to thousands of cilia distributed on their surface beating in a coordinated

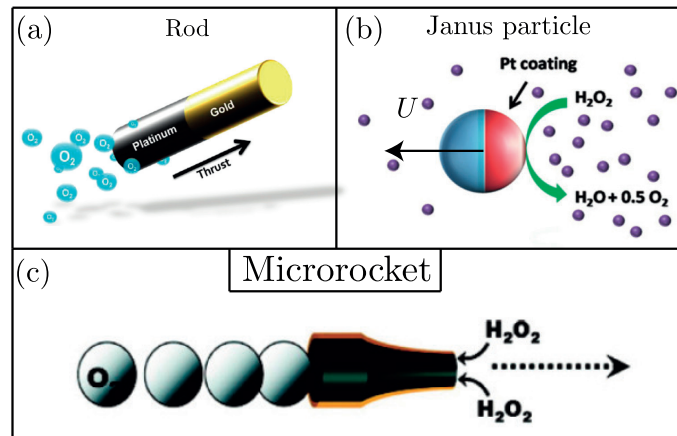


Figure 1.8 – Self-propelled catalytic micro-swimmers: (a) A rod [41] and (b) a Janus Particle moving because of a chemical asymmetry on their surface [42]. (c) A microrocket attains a displacement by ejecting bubbles from its larger opening [43].

manner, as in the case of *Paramecium* [40].

The non-reciprocal motion exploited by biological micro-swimmers is difficult to achieve in artificial devices, because it is extremely challenging to manufacture micron-sized moving parts. Therefore other *propulsion strategies for synthetic micro-swimmers* have been considered, since a net displacement is also obtained by a geometrical or chemical asymmetry. The main typologies of synthetic micro-swimmers employ these two features, catalytically converting chemical energy into propulsion energy. Rod-shaped micro-swimmers and Janus particles move by generating an asymmetry in chemical species concentration [44], see figure 1.8a-b. A third typology are microrockets, conical-shaped micro-swimmers propelled by bubbles moving toward their larger opening due to the asymmetric confinement imposed by their conical structure, sketched in figure 1.8(c).

1.2.1 Conical microswimmers: state of the art

Microrockets, or conical microswimmers, are emerging as one of the most promising micro-swimmers. Their high swimming velocity, up to 50 body length per second, positions them among the fastest microswimmers. Furthermore, their structure enables them to carry easily micro-objects, usually on the external cone surface. In Figure 1.9, we show the most common microfabrication procedures to build microrockets.

Microrockets have shown promising results for several engineering applications, for example drug delivery. Experimental studies have indeed demonstrated that microrockets can carry small micro-particles and cells and transport them through micro channels, see figure 1.10a-b. Usually, the loading of the cargo and the control of the direction of motion are executed by applying an external magnetic field [34]. A chemical treatment on the external part of the cone surface enables it to capture nanoparticles. In [47] this configuration has been used to carry

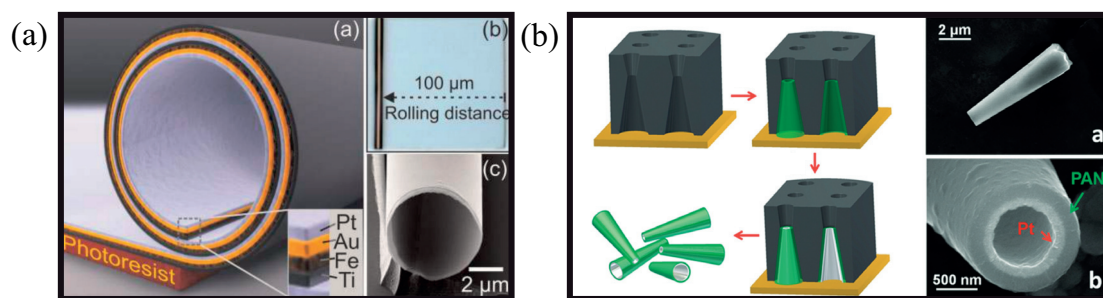


Figure 1.9 – Conical microswimmers fabrication techniques. (a) Self rolling of thin films[45]. (b) Template-assisted electrodeposition[46].

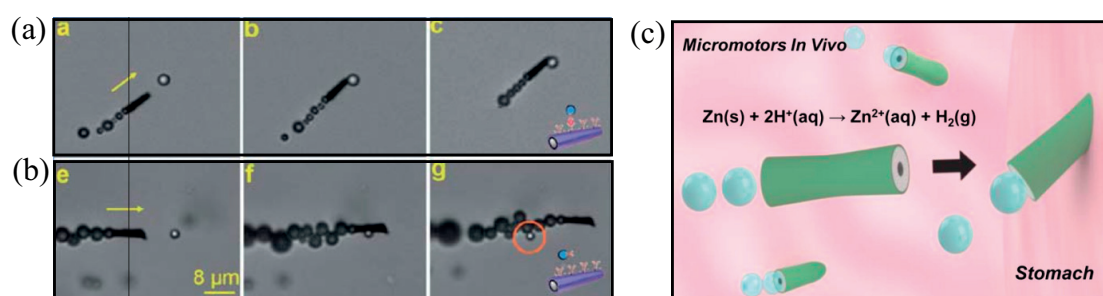


Figure 1.10 – Microrockets transporting a cargo: (a-b) Micro-objects transportation in microfluidics channels [34], selecting whether to pick-up the cargo or not (orange circle) depending on its chemical composition. (c) In vivo study of drug-delivery in the mouse stomach [47].

nano-particles for drug delivery purposes (see Figure 1.10c).

The propulsion of conical swimmers is obtained via a catalytic decomposition, transforming chemical energy into propulsion energy. These micro-swimmers are composed of a cone, internally coated with a catalysts. When immersed in fuel (usually hydrogen peroxide but other reaction are sometimes needed for bio-compatibility), the active part starts to catalytically decompose the hydrogen peroxide into water and molecular oxygen $2H_2O_2 \rightarrow 2H_2O + 2O_2$ [42] (see figure 1.8(c)). As a results of the catalytic decomposition, oxygen bubbles are generated and their growth inside the conical body propels the microswimmer.

1.2.2 In this thesis: Conical microswimmers

In this thesis we study the motion of a single conical microswimmer. In fact, despite the vast amount of experimental studies, their fundamental propulsion mechanisms remain quite unclear. Therefore, we proceed by solving numerically a joint chemical-hydrodynamic model for the hydrogen peroxide diffusion and fluid motion, assuming the the generated bubble are spherical. This allows us to identify the optimal geometrical and chemical parameters optimizing the swimming velocity. Furthermore, we conclude that the hydrodynamics and the chemistry decouple, the first setting the displacement attained by the microrocket while

the second the time scale of such displacement.

Afterwards, we relax the assumption on the sphericity of the bubble, considering a deformable one. This introduces a new time scale in the problem, given by the characteristic time relaxation of the interface. We find two different phases of the bubble growth with different characteristics, when the bubble is inside the cone and undergoes geometrical confinement and when it exists the cone, restoring its spherical shape.

Finally, we study the fundamental problem of a bubble inflating close to a wall. This simplified problem is the first step toward understanding the dynamics of the lubrication film in a bubble confined in conical microswimmers.

1.3 Outline and personal contribution

In **Chapter 2** we describe the numerical method utilized in all our work, which encompasses classical developments as well as some novelties that I have introduced. Novelties include the possibility of computing steady droplet shapes via a Newton method and to perform linear stability analysis of the droplet shape itself.

Part I: Droplet breakup in simple domains

In **Chapter 3** we study the influence of non-normality in the breakup of a rising droplet. We show that optimal shapes found with nonmodal analysis are more efficient than ellipsoids in triggering breakup. In this study, I have developed the DNS code and run the simulations while L. Zhu has carried out the linear analysis. Together with the co-authors, I have analyzed the results and written the manuscript.

In **Chapter 4** we study the relevance of edge states in the breakup of droplets in uni-axial extensional flows. We find that edge states select the path toward breakup and that this mechanism is robust for a wide variety of flow parameters. In this study, I have developed DNS code, the Newton method based continuation algorithm for computing the bifurcation diagram and to carry on linear stability analysis. I have analyzed the results with the co-authors and written the manuscript with input from the co-authors.

In **Chapter 5** we complement Chapter 4, carrying out the exploration of the bifurcation diagram of a droplet in an extensional flow. In particular, we focus on the particular case where the external flow is halted, comparing with ellipsoidal droplet relaxation, and when it compresses the droplet along the axis instead of elongating it. This study is technically based on the tools developed in Chapter 4.

Part II: Conical microswimmers

In **Chapter 6** we develop a joint chemical-hydrodynamics model to study the motion of bubble propelled conical microswimmers, neglecting bubble deformability. We find that in this system the chemistry, dictating the bubble growth rate, and the hydrodynamics partially decouple. Moreover, we find the geometrical and chemical parameters that optimize the swimming velocity. In this study, I have developed the numerical code to compute the gas diffusion and fluid motion around the microswimmer. Together with the co-authors, I have analyzed the results and written the manuscript.

In **Chapter 7** we introduce the interface deformation in the system studied in Chapter 6. In this case, the swimming velocity is optimal for cone opening angles $\theta \approx 1^\circ$ but it does not vary much as long as the this angle is kept small. Furthermore, we find that the swimming efficiency, measured in displacement attained per fuel consumptions, decreases when the bubble is more deformable. In this study, I have developed the DNS code and derived the empirical model described in section 2.4.2. Together with the co-authors, I have written the manuscript and analyzed the results.

In **Chapter 8** we study the motion of a sphere inflating close to a wall. This fundamental problem is relevant to the study of conical microswimmers, where a bubble grows in confined environment. We find that depending on the boundary conditions on the sphere, whether it is a rigid shell or a perfect free-shear bubble, the sphere-wall gap will close or open in time. In this study I have developed the DNS code and, together with S. Michelin, carried out the lubrication analysis. Together with my co-authors, I have analyzed the results and written the manuscript.

In **Chapter 9** we draw the conclusions of this thesis and we illustrate future perspectives.

2 Numerical method

2.1 The boundary integral equation for Stokes flows

It is well known that linear piecewise constant coefficients PDEs can be expressed as Boundary Integral Equations [48, 49]. In this section, we report the classical derivations that lead to the Boundary Integral Equation (BIE) for Stokes flows with a focus on the motion of particles and deformable droplets.

2.1.1 The boundary integral equation for the fluid velocity

This section follows the derivation in [49], section 2.3. We consider a domain of arbitrary shape and volume V , containing a fluid of viscosity μ (see Figure 2.1). The domain boundaries S are smooth, therefore the normal vector \mathbf{n} pointing inside the fluid domain is always well defined. Lorentz reciprocal theorem states [49] that two different solutions of the Stokes equations (7.2) $(\mathbf{u}, \boldsymbol{\sigma})$ and $(\mathbf{u}', \boldsymbol{\sigma}')$ satisfy the relation

$$\nabla \cdot [\mathbf{u}' \cdot \boldsymbol{\sigma} - \mathbf{u} \cdot \boldsymbol{\sigma}'] = 0. \quad (2.1)$$

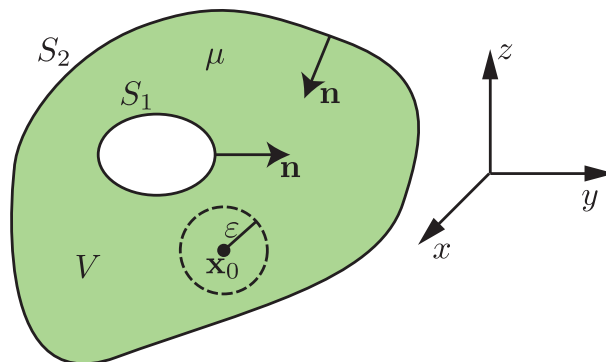


Figure 2.1 – Physical domain: a fluid volume V of viscosity μ is bounded by the domain boundary $S = S_1 + S_2$.

Chapter 2. Numerical method

Integrating (2.1) on the domain V and using divergence theorem we obtain the following equality

$$\int_V \nabla[\mathbf{u}' \cdot \boldsymbol{\sigma} - \mathbf{u} \cdot \boldsymbol{\sigma}'] dV = \int_S [\mathbf{u}' \cdot \boldsymbol{\sigma} - \mathbf{u} \cdot \boldsymbol{\sigma}'] \cdot \mathbf{n} dS = 0, \quad (2.2)$$

where $S = S_1 + S_2$ (we consider in Figure 2.1 two surfaces S_1 and S_2 just to show that the boundary integral equation works also for non-connected domains with 'holes'). Without loss of generality we can specify \mathbf{u}' and $\boldsymbol{\sigma}'$ as the Stokes solutions at $\mathbf{x} = (x, y, z)$ due to a forcing \mathbf{g} located at \mathbf{x}_0 , namely

$$\mathbf{u}'(\mathbf{x}) = \frac{1}{8\pi\mu} \mathbf{G}(\mathbf{x}, \mathbf{x}_0) \cdot \mathbf{g}(\mathbf{x}_0), \quad (2.3)$$

$$\boldsymbol{\sigma}'(\mathbf{x}) = \frac{1}{8\pi} \mathbf{T}(\mathbf{x}, \mathbf{x}_0) \cdot \mathbf{g}(\mathbf{x}_0), \quad (2.4)$$

where \mathbf{G} and \mathbf{T} are the Green's functions of Stokes equations (also referred as Stokeslet and Stresslet), which read

$$G_{ij} = \frac{\delta_{ij}}{d} + \frac{\hat{x}_i \hat{x}_j}{d^3}, \quad \text{for } i, j = x, y, z$$

$$T_{ijk} = -6 \frac{\hat{x}_i \hat{x}_j \hat{x}_k}{d^5}, \quad \text{for } i, j, k = x, y, z$$

where $\hat{\mathbf{x}} = \mathbf{x} - \mathbf{x}_0$ and $d = |\mathbf{x} - \mathbf{x}_0|$. Substituting equations (2.3) and (2.4) in (2.2), we find

$$\int_S [\mathbf{G} \cdot \boldsymbol{\sigma} - \mu \mathbf{u} \cdot \mathbf{T}] \cdot \mathbf{n} dS = 0. \quad (2.5)$$

In order to compute the fluid velocity at $\mathbf{x}_0 \in V$, we consider a sphere of radius ε and volume V_ε centered in \mathbf{x}_0 (see Figure 2.1). On the sphere surface S_ε , the Stokeslet and Stresslet write as

$$G_{ij} \approx \frac{\delta_{ij}}{\varepsilon} + \frac{\hat{x}_i \hat{x}_j}{\varepsilon^3}, \quad (2.6)$$

$$T_{ijk} \approx -6 \frac{\hat{x}_i \hat{x}_j \hat{x}_k}{\varepsilon^5}. \quad (2.7)$$

Therefore, equation (2.5) rewrites as

$$\int_S [G_{ij}(\mathbf{x}, \mathbf{x}_0) \sigma_{ik}(\mathbf{x}) - \mu u_i(\mathbf{x}) T_{ijk}(\mathbf{x}, \mathbf{x}_0)] n_k(\mathbf{x}) dS(\mathbf{x}) \quad (2.8)$$

$$= - \int_{S_\varepsilon} \left[\left(\delta_{ij} + \frac{\hat{x}_i \hat{x}_j}{\varepsilon^2} \right) \sigma_{ik}(\mathbf{x}) + 6\mu u_i(\mathbf{x}) \frac{\hat{x}_i \hat{x}_j \hat{x}_k}{\varepsilon^4} \right] \hat{x}_k d\Omega(\mathbf{x}), \quad (2.9)$$

where we have expressed $dS(\mathbf{x}) = \varepsilon^2 d\Omega(\mathbf{x})$ with $d\Omega$ being the solid angle, and $n_k = \hat{x}_k / \varepsilon$. Since \hat{x} scales like ε , as ε tend to zero, the stress term in the right hand side integral vanishes and the

2.1. The boundary integral equation for Stokes flows

velocity term converges to a finite value. Therefore, equation (2.9) becomes

$$\int_S [G_{ij}(\mathbf{x}, \mathbf{x}_0) \sigma_{ik}(\mathbf{x}) - \mu u_i(\mathbf{x}) T_{ijk}(\mathbf{x}, \mathbf{x}_0)] n_k(\mathbf{x}) dS(\mathbf{x}) \quad (2.10)$$

$$= -6\mu u_i(\mathbf{x}_0) \int_{S_\varepsilon} \frac{\hat{x}_i \hat{x}_j \hat{x}_k}{\varepsilon^6} \hat{x}_k dS(\mathbf{x}), \quad (2.11)$$

$$= -6\mu u_i(\mathbf{x}_0) \frac{1}{\varepsilon^4} \int_{S_\varepsilon} \hat{x}_i \hat{x}_j dS(\mathbf{x}), \quad (2.12)$$

Using the divergence theorem we develop the remaining part of the right hand side

$$\int_{S_\varepsilon} \hat{x}_i \hat{x}_j dS(\mathbf{x}) = \varepsilon \int_{S_\varepsilon} \hat{x}_i n_j dS(\mathbf{x}) = \varepsilon \int_{V_\varepsilon} \frac{\partial \hat{x}_i}{\partial x_j} dV(\mathbf{x}) = \delta_{ij} \frac{4}{3} \pi \varepsilon^4. \quad (2.13)$$

Therefore substituting in equation (2.10) we finally obtain

$$\int_S [-G_{ij}(\mathbf{x}, \mathbf{x}_0) \sigma_{ik}(\mathbf{x}) + \mu u_i(\mathbf{x}) T_{ijk}(\mathbf{x}, \mathbf{x}_0)] n_k(\mathbf{x}) dS(\mathbf{x}) = 8\pi \mu u_i(\mathbf{x}_0) \delta_{ij}, \quad (2.14)$$

$$= 8\pi \mu u_j(\mathbf{x}_0), \quad (2.15)$$

and, rearranging the terms and exploiting the symmetry property $G_{ij}(\mathbf{x}, \mathbf{x}_0) = G_{ji}(\mathbf{x}_0, \mathbf{x})$, we finally obtain the boundary integral equation for the velocity u_j in a point of the fluid domain \mathbf{x}_0

$$8\pi \mu u_j(\mathbf{x}_0) = - \underbrace{\int_S G_{ji}(\mathbf{x}_0, \mathbf{x}) \sigma_{ik}(\mathbf{x}) n_k(\mathbf{x}) dS(\mathbf{x})}_{\text{single layer potential}} + \underbrace{\mu \int_S u_i(\mathbf{x}) T_{ijk}(\mathbf{x}, \mathbf{x}_0) n_k(\mathbf{x}) dS(\mathbf{x})}_{\text{double layer potential}}. \quad (2.16)$$

The first integral on the right hand side is called as single-layer potential and the second integral is called as double-layer potential. The former represents a boundary distribution of point forces, while the latter represents a boundary distribution of point sources and point force dipoles [50].

As we will see in next sections, we are mostly interested in the velocities on the boundaries, for example to find a droplet or particle velocity. Therefore, it is crucial to write the boundary integral equation for a point \mathbf{x}_0 lying on S . Therefore we employ the integral identity

$$\lim_{x_0 \rightarrow S} \int_S T_{ijk}(\mathbf{x}, \mathbf{x}_0) n_k(\mathbf{x}) dS(\mathbf{x}) = \pm 4\pi \delta_{ij} u_i(\mathbf{x}) + \int_S^{PV} u_i(\mathbf{x}) T_{ijk}(\mathbf{x}, \mathbf{x}_0) n_k(\mathbf{x}) dS(\mathbf{x}), \quad (2.17)$$

where the sign depends on the orientation of the normal vector and PV indicates the Cauchy principal value integral. Substituting (2.17) in (2.16), we obtain the velocity on the boundary S as

$$4\pi \mu u_j(\mathbf{x}_0) = - \int_S G_{ji}(\mathbf{x}_0, \mathbf{x}) \sigma_{ik}(\mathbf{x}) n_k(\mathbf{x}) dS(\mathbf{x}) + \mu \int_S^{PV} u_i(\mathbf{x}) T_{ijk}(\mathbf{x}, \mathbf{x}_0) n_k(\mathbf{x}) dS(\mathbf{x}). \quad (2.18)$$

Other useful integral identities that will be used in the next section are

$$\int_S T_{ijk}(\mathbf{x}, \mathbf{x}_0) n_k(\mathbf{x}) dS(\mathbf{x}) = \begin{cases} 8\pi\delta_{ij} & \text{when } \mathbf{x}_0 \text{ is enclosed by } S \\ 4\pi\delta_{ij} & \text{when } \mathbf{x}_0 \text{ is on } S \\ 0 & \text{when } \mathbf{x}_0 \text{ is outside } S \end{cases} \quad (2.19)$$

when \mathbf{x}_0 lies on S the integral on the left hand side is a principal-value integral. Note that (2.17) and (2.19) have been derived considering that the normal vector \mathbf{n} is directed outward the volume enclosed by the surface, as in the case of S_1 . These results are readily usable considering the surface S_2 , simply by changing the sign of the normal vector. To conclude, equations (2.5), (2.16) & (2.18) are used to describe the flow on a point \mathbf{x}_0 respectively outside, inside or on the boundary of the domain.

2.1.2 The boundary integral equation for the pressure

As previously shown for the fluid velocity, we hereby show the boundary integral equation for the fluid pressure [49, 50]. Considering as before a point \mathbf{x}_0 in the fluid domain, the fluid pressure p is written as

$$8\pi\mu p(\mathbf{x}_0) = - \int_S P_i(\mathbf{x}_0, \mathbf{x}) \sigma_{ik}(\mathbf{x}) n_k(\mathbf{x}) dS(\mathbf{x}) + \mu \int_S u_i(\mathbf{x}) \Pi_{ik}(\mathbf{x}_0, \mathbf{x}) n_k(\mathbf{x}) dS(\mathbf{x}), \quad (2.20)$$

where

$$P_i(\mathbf{x}, \mathbf{x}_0) = 2 \frac{\hat{x}_i}{r^3} \quad (2.21)$$

$$\Pi_{ik}(\mathbf{x}_0, \mathbf{x}) = 4 \left(-\frac{\delta_{ik}}{r^3} + 3 \frac{\hat{x}_i \hat{x}_k}{r^5} \right) \quad (2.22)$$

are the pressure fields associated to the Stokeslet \mathbf{G} and Stresslet \mathbf{T} respectively. Note that \mathbf{P} and $\mathbf{\Pi}$ have higher order of the singularity compared to \mathbf{G} and \mathbf{T} . This feature might create numerical problems when evaluating the pressure field.

2.1.3 Droplet in unbounded domain

Let's consider a droplet of fluid 1 and viscosity μ_1 suspended in fluid 2 of viscosity μ_2 with undisturbed velocity \mathbf{u}^∞ . The fluid motion at a point \mathbf{x}_0 in the fluid 2 (see Figure 2.2) is expressed with equation (2.16) for the fluid domain 2, namely

$$\begin{aligned} 8\pi\mu_2 u_j(\mathbf{x}_0) = & 8\pi\mu_2 u_j^\infty - \int_S G_{ji}(\mathbf{x}_0, \mathbf{x}) \sigma_{ik}^{(2)}(\mathbf{x}) n_k(\mathbf{x}) dS(\mathbf{x}) \\ & + \mu_2 \int_S u_i^{(2)}(\mathbf{x}) T_{ijk}(\mathbf{x}, \mathbf{x}_0) n_k(\mathbf{x}) dS(\mathbf{x}). \end{aligned} \quad (2.23)$$

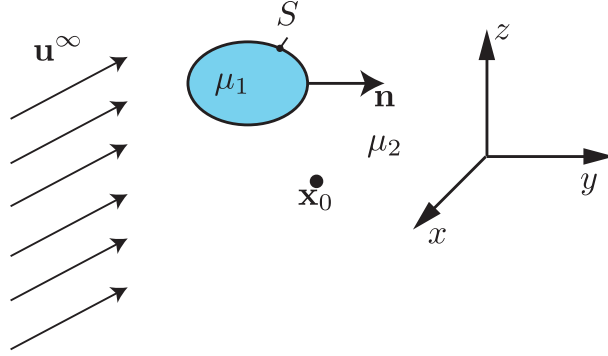


Figure 2.2 – Physical domain: drop of fluid 1 suspended in fluid 2.

where \mathbf{u}^∞ is a far-field velocity, that can be added as a background flow given the linearity of Stokes equations [49, 50]. However, since in this case there is also fluid 1, we can as well write (2.16) for domain 1 as

$$0 = \int_S G_{ji}(\mathbf{x}_0, \mathbf{x}) \sigma_{ik}^{(1)}(\mathbf{x}) n_k(\mathbf{x}) dS(\mathbf{x}) - \mu_1 \int_S u_i^{(1)}(\mathbf{x}) T_{ijk}(\mathbf{x}, \mathbf{x}_0) n_k(\mathbf{x}) dS(\mathbf{x}). \quad (2.24)$$

The signs change because the normal vector point outside the domain. Summing up equation (2.23) and (2.24) and assuming continuity of the velocity at the interface (1.4), we obtain the velocity in \mathbf{x}_0 due to the flow in the two control volumes

$$8\pi\mu_2 u_j(\mathbf{x}_0) = 8\pi\mu_2 u_j^\infty - \int_S G_{ji}(\mathbf{x}_0, \mathbf{x}) (\sigma_{ik}^{(2)}(\mathbf{x}) - \sigma_{ik}^{(1)}(\mathbf{x})) n_k(\mathbf{x}) dS(\mathbf{x}) + (\mu_2 - \mu_1) \int_S u_i(\mathbf{x}) T_{ijk}(\mathbf{x}, \mathbf{x}_0) n_k(\mathbf{x}) dS(\mathbf{x}), \quad (2.25)$$

Note that the fluid velocity is now expressed as a function of the traction difference across the interface, defined in (1.3). This proves to be very useful when the traction difference can be calculated from the droplet geometry, as for a droplet with Laplace law (or other constitutive laws in the case of elastic capsules or vesicles [51]). Furthermore, by using equation (2.17), we can calculate the interface velocity as

$$4\pi(\mu_2 + \mu_1) u_j(\mathbf{x}_0) = 8\pi\mu_2 u_j^\infty - \int_S G_{ji}(\mathbf{x}_0, \mathbf{x}) (\sigma_{ik}^{(2)}(\mathbf{x}) - \sigma_{ik}^{(1)}(\mathbf{x})) n_k(\mathbf{x}) dS(\mathbf{x}) + (\mu_2 - \mu_1) \int_S^{PV} u_i(\mathbf{x}) T_{ijk}(\mathbf{x}, \mathbf{x}_0) n_k(\mathbf{x}) dS(\mathbf{x}). \quad (2.26)$$

Note that equation (2.26) can be readily used for bounded domain by simply adding an integral for the external boundary.

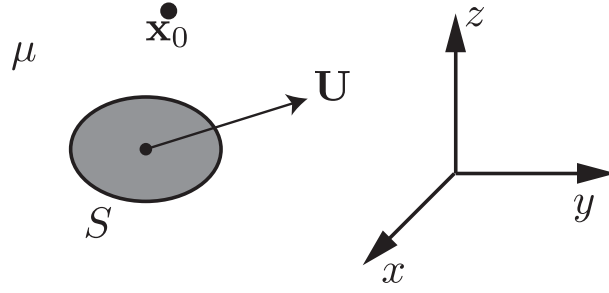


Figure 2.3 – Physical domain: Particle moving with velocity \mathbf{U} in an unbounded fluid domain.

2.1.4 BIE for the flow generated by a moving rigid particle

Let's consider a rigid particle which is moving with velocity $\mathbf{U} = \mathbf{V} + \boldsymbol{\Omega} \times \mathbf{x}$ in Stokes flow (see figure 2.3). The fluid velocity in a point \mathbf{x}_0 of the domain is given by equation (2.16) integrated on the surface S . However, since the velocity on the particle surface is uniform we can take it out of the integration. Therefore the double layer vanishes using equation (2.19) because \mathbf{x}_0 lies outside the surface S . Therefore the boundary integral equation writes

$$8\pi\mu u_j(\mathbf{x}_0) = - \int_S G_{ji}(\mathbf{x}_0, \mathbf{x}) \sigma_{ik}(\mathbf{x}) n_k(\mathbf{x}) dS(\mathbf{x}). \quad (2.27)$$

For a point \mathbf{x}_0 on the particle surface, the double layer vanishes using (2.17) & (2.19)

$$U_i \int_S T_{ijk}(\mathbf{x}, \mathbf{x}_0) n_k(\mathbf{x}) dS(\mathbf{x}) = 4\pi U_i \delta_{ij} + \underbrace{U_i \int_S T_{ijk}(\mathbf{x}, \mathbf{x}_0) n_k(\mathbf{x}) dS(\mathbf{x})}_{-4\pi \delta_{ij}} = 0. \quad (2.28)$$

Therefore, since $u_j(\mathbf{x}_0) = U_j$, we obtain

$$8\pi\mu U_j = - \int_S G_{ji}(\mathbf{x}_0, \mathbf{x}) \sigma_{ik}(\mathbf{x}) n_k(\mathbf{x}) dS(\mathbf{x}). \quad (2.29)$$

To conclude, the flow due to rigid particle is described only by the single layer potential. In section 2.2.3 we will see that this might cause numerical problems and we will discuss how to avoid those issues.

2.1.5 Axisymmetric Stokes flow

When the flow is axisymmetric, it is possible to integrate equation (2.16) in the azimuthal direction (see section (2.4) of [49] for the detailed derivation), obtaining the boundary integral equation in the cylindrical coordinate system (r, θ, z)

$$8\pi\mu u_j(\mathbf{x}_0) = \int_l M_{ji}(\mathbf{x}_0, \mathbf{x}) f_i(\mathbf{x}) dS(\mathbf{x}) + \mu \int_l u_i(\mathbf{x}) q_{jik}(\mathbf{x}_0, \mathbf{x}) n_k(\mathbf{x}) dS(\mathbf{x}) \quad \text{for } i, j, k = z, r. \quad (2.30)$$

2.1. The boundary integral equation for Stokes flows

where \mathbf{M} and \mathbf{q} are the Green's functions after azimuthal integration and $f_i = \sigma_{ik} n_k$. Physically, \mathbf{M} represents the flow in \mathbf{x}_0 due to a ring of point forces in \mathbf{x} and \mathbf{q} represents a flow due to a ring of point sources and point dipoles. Note that the integration is performed now on the line l , that describes the axisymmetric surface shape in the plane containing the axis.

Proceeding by analogy, we can integrate equation (2.18) in the azimuthal direction in order to find the boundary velocity of an axisymmetric boundary

$$4\pi u_j(\mathbf{x}_0)\mu = - \int_l M_{ji}(\mathbf{x}_0, \mathbf{x}) \Delta f_i(\mathbf{x}) dS(\mathbf{x}) + \mu \int_l u_i(\mathbf{x}) Q_{ji}(\mathbf{x}_0, \mathbf{x}) dS(\mathbf{x}), \quad (2.31)$$

where we have introduced $Q_{ji} = q_{jik} n_k$. The last passage will be important in the numerical implementation illustrated in section 2.2.1, since Q_{ji} is actually non-singular (note that the double layer is not PV), as will be later explained in section 2.4.1. Similarly, the expression for the fluid motion due to an axisymmetric droplet and a background flow \mathbf{u}^∞ is found by integrating equation (2.26) in the azimuthal direction

$$4\pi u_j(\mathbf{x}_0)(\mu_1 + \mu_2) = 8\pi u_j^\infty - \int_l M_{ji}(\mathbf{x}_0, \mathbf{x}) \Delta f_i(\mathbf{x}) dS(\mathbf{x}) + (\mu_2 - \mu_1) \int_l u_i(\mathbf{x}) Q_{ji}(\mathbf{x}_0, \mathbf{x}) dS(\mathbf{x}), \quad (2.32)$$

and for a particle is found by integrating equation (2.29) in the azimuthal direction

$$8\pi U_j(\mathbf{x}_0)\mu = - \int_l M_{ji}(\mathbf{x}_0, \mathbf{x}) \Delta f_i(\mathbf{x}) dS(\mathbf{x}), \quad (2.33)$$

note that particles in axisymmetric flows can only move along the axis, meaning that $U_r = 0$. The main analogies between the boundary integral equations in $3D$ and in axisymmetric domain are summed up in Figure 2.4.

The mathematical expression for the Stokeslet reads

$$\mathbf{M} = r \begin{pmatrix} I_{10} + \hat{z}^2 I_{30} & \hat{z}(r I_{30} - r_0 I_{31}) \\ \hat{z}(r I_{31} - r_0 I_{30}) & I_{11} + (r^2 + r_0^2) I_{31} - r r_0 (I_{30} + I_{32}) \end{pmatrix} \quad (2.34)$$

where $\hat{z} = z - z_0$ and

$$I_{mn}(\hat{z}, r, r_0) = \frac{4k^m}{(4r r_0)^{m/2}} \int_0^{\pi/2} \frac{(2 \cos^2 \omega - 1)^n}{(1 - k^2 \cos^2 \omega)^{m/2}} d\omega, \quad (2.35)$$

and

$$k^2 = \frac{4r r_0}{\hat{z}^2 + (r + r_0)^2}. \quad (2.36)$$

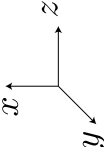
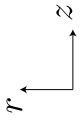
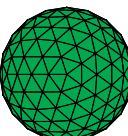
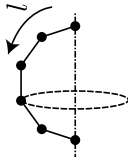
	3D	Axisymmetric
Coordinate system		
Mesh for a sphere		
Background flow	$\mathbf{u}_\infty(\mathbf{x}) = u_x(\mathbf{x})\mathbf{e}_x + u_y(\mathbf{x})\mathbf{e}_y + u_z(\mathbf{x})\mathbf{e}_z$	$\mathbf{u}_\infty(\mathbf{x}) = u_z(\mathbf{x})\mathbf{e}_z + u_r(\mathbf{x})\mathbf{e}_r$
Integral equation for droplets	$4\pi u_j(\mathbf{x}_0)(\mu_1 + \mu_2) = 8\pi u_j^\infty - \int_S G_{ji}(\mathbf{x}_0, \mathbf{x}) \Delta f_i(\mathbf{x}) dS(\mathbf{x}) + (\mu_2 - \mu_1) \int_S^{P,V} u_i(\mathbf{x}) T_{ijk} n_k(\mathbf{x})(\mathbf{x}_0, \mathbf{x}) dS(\mathbf{x}),$ $i, j, k = x, y, z$	$4\pi u_j(\mathbf{x}_0)(\mu_1 + \mu_2) = 8\pi u_j^\infty - \int_l G_{ji}(\mathbf{x}_0, \mathbf{x}) \Delta f_i(\mathbf{x}) dl(\mathbf{x}) + (\mu_2 - \mu_1) \int_l u_i(\mathbf{x}) Q_{ji}(\mathbf{x}_0, \mathbf{x}) dl(\mathbf{x}),$ $i, j, k = z, r$
Integral equation for particle	$8\pi \mu U_j = - \int_S G_{ij}(\mathbf{x}, \mathbf{x}_0) f_i(\mathbf{x}) dS(\mathbf{x})$ $i, j, k = x, y, z$	$8\pi \mu U_j = - \int_l M_{ji}(\mathbf{x}_0, \mathbf{x}) f_i(\mathbf{x}) dS(\mathbf{x})$ $i, j, k = z, r$

Figure 2.4 – Analogies between full 3D and axisymmetric flows.

2.1. The boundary integral equation for Stokes flows

The integration of I_{mn} results in elliptic integrals of the first and second kind, for instance

$$M_{zz} = 2k\sqrt{\frac{r}{r_0}} \left(F(k) + \frac{\hat{z}^2}{d^2} E(k) \right), \quad (2.37)$$

where $d = \sqrt{\hat{z}^2 + (r - r_0)^2}$ and

$$F(k) = \int_0^{\pi/2} \frac{d\omega}{\sqrt{1 - k^2 \cos^2 \omega}}, \quad E(k) = \int_0^{\pi/2} \sqrt{1 - k^2 \cos^2 \omega} d\omega, \quad (2.38)$$

are the complete elliptic integral of the first and second kind. Using the same notation, the Stresslet is written as

$$\begin{pmatrix} q_{zzz} \\ q_{zzr} = q_{zrz} \\ q_{zrr} \end{pmatrix} = -6r\hat{z} \begin{pmatrix} \hat{z}^2 I_{50} \\ \hat{z}(rI_{50} - r_0 I_{51}) \\ r_0^2 I_{52} + r^2 I_{50} - 2r r_0 I_{51} \end{pmatrix}, \quad (2.39)$$

and

$$\begin{pmatrix} q_{rzz} \\ q_{rzz} = q_{rzz} \\ q_{rrr} \end{pmatrix} = -6r \begin{pmatrix} \hat{z}^2(rI_{51} - r_0 I_{50}) \\ \hat{z}[(r^2 + r_0^2)I_{51} - r r_0(I_{50} + I_{52})] \\ r^3 I_{51} - r^2 r_0(I_{50} + 2I_{52}) + r r_0^2(I_{53} + 2I_{51}) - r_0^3 I_{52} \end{pmatrix}. \quad (2.40)$$

The BEMLIB library [50] provides these integrals in a form suitable for computer implementation. Furthermore we point out two important features which are crucial for carrying on an accurate numerical implementation: the diagonal term of the Stokeslet are weakly singular $\sim \log d$, and the Stresslet is strongly singular $\sim 1/d$.

Similarly, when computing the pressure we integrate equation (2.20) in the azimuthal direction obtaining

$$8\pi p(\mathbf{x}_0) = - \int_l L_i(\mathbf{x}_0, \mathbf{x}) f_i(\mathbf{x}) dl(\mathbf{x}) + \mu \int_l u_i(\mathbf{x}) N_{ij}(\mathbf{x}_0, \mathbf{x}) n_j(\mathbf{x}) dl(\mathbf{x}), \quad (2.41)$$

where \mathbf{L} represents the pressure in \mathbf{x}_0 due to a ring of point forces in \mathbf{x} and \mathbf{N} represents the pressure due to a ring of point sources and point dipoles. Following the same procedure as before we find

$$\mathbf{L}(\mathbf{x}_0, \mathbf{x}) = -2r \begin{pmatrix} \hat{z} I_{30} \\ r I_{30} - r_0 I_{31} \end{pmatrix}, \quad (2.42)$$

and

$$\mathbf{N}(\mathbf{x}_0, \mathbf{x}) = -4r \begin{pmatrix} -I_{30} + 3\hat{z}^2 I_{50} & 3\hat{z}(rI_{50} - r_0 I_{51}) \\ 3\hat{z}(rI_{50} - r_0 I_{51}) & -I_{30} - 6r_0 r I_{51} + 3r_0^2 I_{52} + 3r^2 I_{50} \end{pmatrix}. \quad (2.43)$$

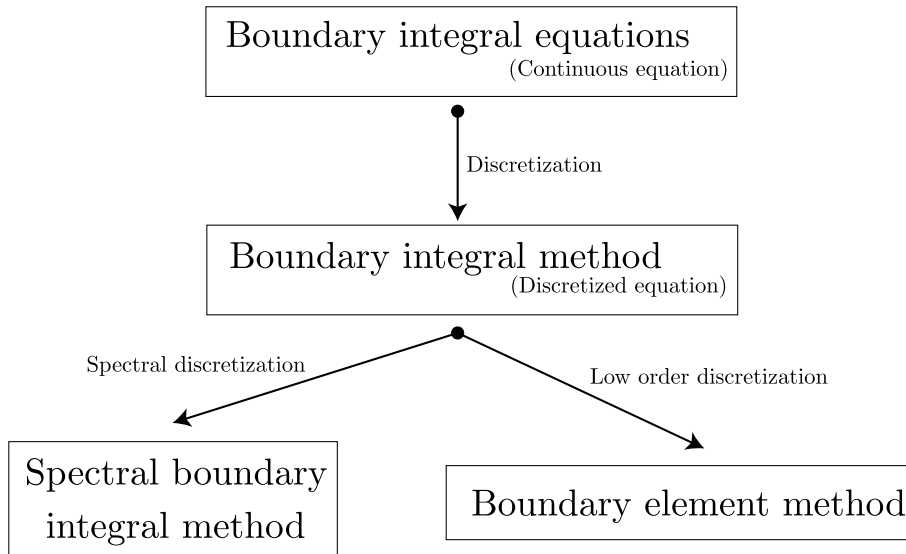


Figure 2.5 – Names of equations and numerical methods.

2.2 The axisymmetric Boundary Integral Method

In this section we illustrate classical discretization methods for numerically solving boundary integral equations [50]. We will refer only to the class of axisymmetric problems. Terminology wise, the discretized form of the boundary integral equation is called Boundary Integral Method (BIM) and low and higher order discretization are called Boundary Element Method (BEM) and Spectral Boundary Integral Method (Spectral BIM) respectively (see Figure 2.5). Note that in the following we will refer to non-dimensional integral equation, therefore we introduce the viscosity ratio $\lambda = \mu_1 / \mu_2$, the capillary number Ca and Bond number Bo introduced in section 1.1. Ca and Bo set the intensity of the externally applied external flow and of the gravity forces respectively, as shown in equation (1.3).

2.2.1 Boundary Element Method implementation

Moving boundary problems require the discretization of the boundary geometry and the approximation of the variables along the boundary itself. Referring to the sketch in figure 2.6, four cases are most common:

- **(a) Straight constant (P0) elements.** The boundary is split into N straight elements and the variables are assumed to be constant along the elements. The functions for the velocities and stresses become $2N \times 1$ vectors, corresponding to the values in the midpoints of the elements.
- **(b) Straight linear (P1) elements.** The boundary is split into N straight elements and the variables are assumed to vary linearly along the element. The functions for the

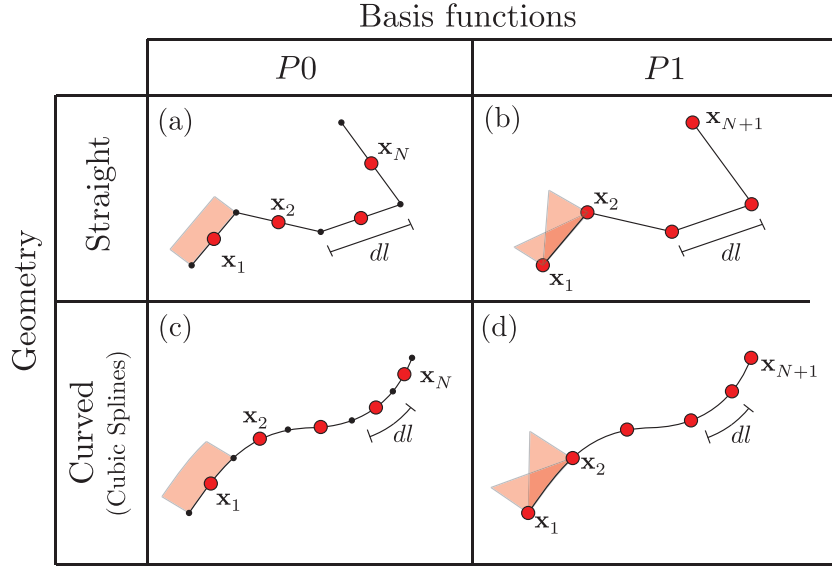


Figure 2.6 – Schematic representation of different discretization for the geometry and the dependent variables: (a) Constant straight elements. (b) Linear straight elements. (c) Curved constant elements (d) Curved linear elements. Lines represent a boundary split into the mesh elements and large red circles the collocation points.

velocities and stresses become $(2N + 2) \times 1$ vectors, corresponding to the values at the end-points of the elements.

- **(c) Curved constant (P_0) elements.** The boundary is split into N curved elements, for example cubic splines, and the variables are assumed to be constant along the element. The functions for the velocities and stresses become $2N \times 1$ vectors, corresponding to the values in the midpoints of the elements.
- **(d) Curved linear (P_1) elements.** The boundary is split into N curved elements, for example cubic splines, and the variables are assumed to vary linearly along the element length. The functions for the velocities and stresses become $(2N + 2) \times 1$ vectors, corresponding to the values at the end-points of the elements.

In the case of P_0 elements, the discretized functions write

$$\mathbf{x} = \begin{pmatrix} \mathbf{x}_1 \\ \mathbf{x}_2 \\ \vdots \\ \mathbf{x}_N \end{pmatrix}, \quad \mathbf{u} = \begin{pmatrix} \mathbf{u}(\mathbf{x}_1) \\ \mathbf{u}(\mathbf{x}_2) \\ \vdots \\ \mathbf{u}(\mathbf{x}_N) \end{pmatrix}, \quad \mathbf{f} = \begin{pmatrix} \mathbf{f}(\mathbf{x}_1) \\ \mathbf{f}(\mathbf{x}_2) \\ \vdots \\ \mathbf{f}(\mathbf{x}_N) \end{pmatrix}, \quad (2.44)$$

where

$$\mathbf{x}_n = \begin{pmatrix} z_n \\ r_n \end{pmatrix}, \quad \mathbf{u}_n = \begin{pmatrix} u_z(\mathbf{x}_n) \\ u_r(\mathbf{x}_n) \end{pmatrix}, \quad \mathbf{f}_n = \begin{pmatrix} f_z(\mathbf{x}_n) \\ f_r(\mathbf{x}_n) \end{pmatrix}. \quad (2.45)$$

Chapter 2. Numerical method

Generally, it is convenient to use $P1$ elements for deformable objects (drops or capsules), because the solution already provides the node velocity itself, while it is more convenient to implement $P0$ for non deformable objects. Considering the simplest implementation (straight $P0$ elements), the geometry is divided in N elements of length Δl_n , hence the discretized boundary integral equations (2.31), for the velocity on the m th element rewrites in non-dimensional form as

$$4\pi\mathbf{u}_m = \sum_{n=1}^N \left[-\mathbf{f}_n \int_{\Delta l_n} \mathbf{M}(\mathbf{x}_m, \mathbf{x}) dl(\mathbf{x}) + \mathbf{u}_n \int_{\Delta l_n} \mathbf{Q}(\mathbf{x}_m, \mathbf{x}) dl(\mathbf{x}) \right] \quad \text{for } m = 1, \dots, N. \quad (2.46)$$

where the integrals are computed with a six point Gauss-Legendre quadrature rule [52]. When $n = m$ the diagonal terms of \mathbf{M} are singular, therefore Gauss-Legendre integration might become inaccurate. To prevent this, we use standard techniques for singular treatment, for instance one can verify that $M_{zz}(\mathbf{x}_0, \mathbf{x}) \rightarrow -2\log d$ as $\mathbf{x} \rightarrow \mathbf{x}_0$. Following [50], we split the singular integral into two parts, namely

$$\int_{\Delta l_n} M_{zz}(\mathbf{x}_m, \mathbf{x}) dl(\mathbf{x}) = \int_{\Delta l_n} (M_{zz}(\mathbf{x}_m, \mathbf{x}) + 2\log d) dl(\mathbf{x}) - 2\Delta l_n (\log(\Delta l_n/2) - 1), \quad (2.47)$$

doing so, the first integral on the right hand side is not singular and can be integrate with standard techniques. Grouping the integrals on the discretized elements, we obtain the single and double layer operators

$$S_{mn} = \int_{\Delta l_n} \mathbf{M}(\mathbf{x}_m, \mathbf{x}) dl(\mathbf{x}), \quad (2.48)$$

$$D_{mn} = \int_{\Delta l_n} \mathbf{Q}(\mathbf{x}_m, \mathbf{x}) dl(\mathbf{x}), \quad (2.49)$$

$$(2.50)$$

and equation (2.46) rewrites

$$4\pi\mathbf{u} = -\mathbf{Sf} + \mathbf{Du}. \quad (2.51)$$

Depending whether \mathbf{u} or \mathbf{f} is known, equation (2.51) results in the discretized Fredholm integral of first or second kind respectively. For example, knowing \mathbf{f} , leads to

$$\underbrace{(\mathbf{D} - 4\pi\mathbf{I})}_{2N \times 2N} \underbrace{\mathbf{u}}_{2N \times 1} = \underbrace{\mathbf{Sf}}_{2N \times 1} \rightarrow \mathbf{Au} = \mathbf{b}, \quad (2.52)$$

which can be solved by inverting the influence matrix \mathbf{A} for the unknown velocities \mathbf{u} . Similarly, one can prescribe the velocity and solve for the stresses. Other geometry or variables discretizations lead to similar matrices, the reader interested in the details of the implementation can refer to Ref. [50].

2.2.2 Deformable droplets and bubbles

In our numerical implementation for deformable droplets and bubbles we always use curved (cubic splines) $P1$ elements, as in [53, 6, 7], where the interface coordinates $z(s)$ and $r(s)$ are parametrized by the independent variable s . This implementation has the main advantage that all geometrical quantities vary smoothly along the discretized interface. For example, the unit normal vector and the interface curvature, appearing in the interface boundary condition (1.3), can be directly computed using the analytical formula

$$\mathbf{n} = \frac{1}{\sqrt{z'^2 + r'^2}} \begin{pmatrix} r' \\ -z' \end{pmatrix}, \quad \nabla_s \cdot \mathbf{n} = \frac{z' r'' - z'' r'}{(z'^2 + r'^2)^{3/2}} - \frac{z'}{r \sqrt{z'^2 + r'^2}}. \quad (2.53)$$

After discretization, equation (2.32) writes in non-dimensional form as

$$4\pi\mathbf{u}(1 + \lambda) = 8\pi\mathbf{u}^\infty - \mathbf{S}\mathbf{f} + (1 - \lambda)\mathbf{D}\mathbf{u}, \quad (2.54)$$

where \mathbf{S} and \mathbf{D} were defined in (2.48) & (2.49) respectively. In order to validate our implementation, we compare our numerical results with the literature. A simple case to start with is a droplet rising in an quiescent heavier fluid due to gravity. It is well know that a spherical droplet is a solution of this flow [54, 3]. Rearranging equation (2.54), the influence matrix writes

$$\mathbf{A} = 4\pi(1 + \lambda)\mathbf{I} - (1 - \lambda)\mathbf{D}, \quad (2.55)$$

and the right hand side

$$\mathbf{b} = -\mathbf{S}\mathbf{f}. \quad (2.56)$$

Clearly, when $\lambda = 1$, equation (2.54) is greatly simplified because the double layer potential cancels out. Otherwise, since \mathbf{f} is given by the droplet geometry by equation (1.3) and imposing no external flow ($\text{Ca} = 0$), we can find the interface velocities by matrix inverting the influence matrix. In Figure 2.7 we show the numerical solution for $N = 100$ compared to the analytical result, finding good agreement, and we verify the convergence over the number of elements.

Furthermore, we want to validate the transient evolution of the droplet shape. Therefore, we impose the non-dimensional extensional flow $\mathbf{u}^\infty(\mathbf{x}) = \text{Ca}\mathbf{e}_z - \text{Ca}/2\mathbf{e}_r$, where Ca is the capillary number setting the strength of the flow ($\text{Bo} = 0$). The influence matrix is given by

$$\mathbf{A} = 4\pi(1 + \lambda)\mathbf{I} - (1 - \lambda)\mathbf{D}, \quad (2.57)$$

with right hand side

$$\mathbf{b} = 8\pi\mathbf{u}^\infty - \mathbf{S}\mathbf{f}. \quad (2.58)$$

Imposing \mathbf{f} with equation (1.3) the interface velocity is found by matrix inversion. Afterward,

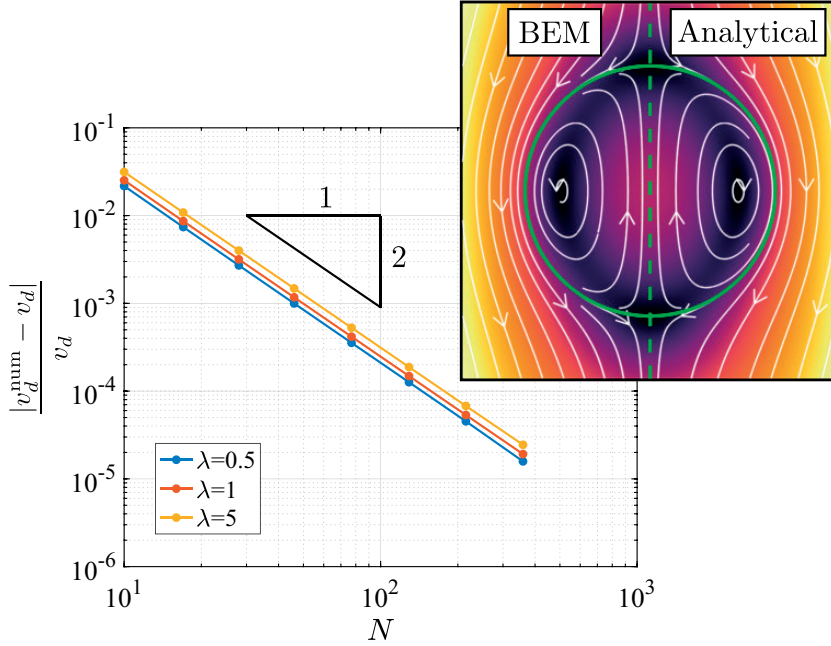


Figure 2.7 – Convergence study for the rising velocity of a spherical droplet in a gravitational field compared to the analytical result, for $Bo = 1$ and varying the viscosity. The inset shows streamlines and intensity of the velocity field of the numerical solution (half-left) and the analytical solution (half-right), isoviscosity case.

the interface is advanced in time with its own velocity (see equation (1.6)) with a second order explicit Runge Kutta solver. Figure 2.8a shows the time evolution of the deformation parameter $D = (a - b)/(a + b)$ (where a is the major axis and b the minor axis) for $Ca = 0.05$. Starting from initially spherical droplet, the droplet shape settles on a steady state after a certain time. As expected, the dynamics of a more viscous droplets is slower. In Figure 2.8b, we show the deformation parameter of the steady state D_f for different capillary numbers and viscosity ratios. Our simulation are validated with the results in [53]. As a final note, we would like to point out that the time integration introduces errors as mesh distortion and unphysical volume variation due to numerical error. Therefore, remeshing algorithms and other techniques are often necessary in order to maintain good accuracy throughout the simulation. These techniques will be described in detail in section 2.2.4, 2.2.5 and 2.2.6.

2.2.3 Rigid particles in flows

When solving for a flow around a rigid non-moving boundary, we make non-dimensional and discretize equation (2.33) and set the particle velocity equal to zero, and write

$$0 = 8\pi\mathbf{u}^\infty - \mathbf{Sf}, \quad (2.59)$$

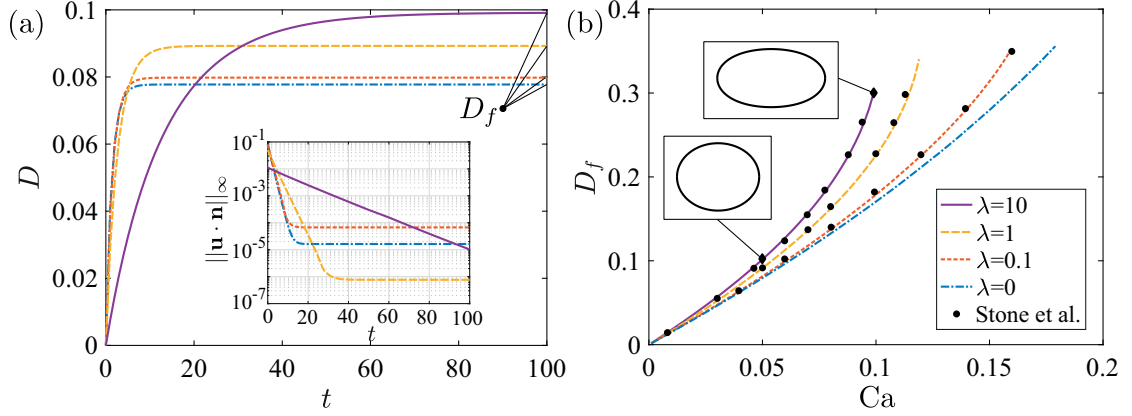


Figure 2.8 – (a) Deformation parameter versus time starting from spherical droplets for different viscosity ratio, $\lambda = [0, 0.1, 1, 10]$ (see inset in Figure 2.8b). The inset shows the L_∞ norm of the velocity normal to the interface. (b) Deformation parameter of the steady shape versus Ca for different viscosity ratios, the dots are the results from [53]. The inset shows droplet shapes for $Ca = 0.05, 0.1$ and $\lambda = 10$.

where \mathbf{u}^∞ is an axial uniform velocity, such that $\mathbf{u}^\infty = U\mathbf{e}_z$. Note that this is equivalent to a moving particle with velocity $-\mathbf{u}^\infty$. We can find stresses acting on the surface by inverting the influence matrix $\mathbf{A} = \mathbf{S}$ with right hand side $\mathbf{b} = 8\pi\mathbf{u}^\infty$. In Figure 2.9 we show the comparison with analytically known flow around a sphere when $U = 1$, and the convergence of the force exerted on the sphere $F_s = 6\mu UR$ on the number of elements.

A crucial feature of the flow around rigid particles is that the integral equation is ill-posed and might result in an infinite number of solutions. Mathematically, this comes from the fact that the single layer operator contains a neutral eigenvalue [50]. Interestingly, we have noticed this problem does not arise for a spherical particle (it seems not to arise for front-back symmetric particles). Therefore we focus on the flow around a non front-back symmetric particle and we observe that the normal stress $f_n = \mathbf{f} \cdot \mathbf{n}$ from the solution undergoes huge variations when changing the discretization (see Figure 2.10a) as a consequence of the neutral eigenvalue. Physically, this might be interpreted as an arbitrary uniform pressure inside the particle. We can avoid this indetermination and the existence of infinite solutions following [50], by imposing the solvability condition

$$\int_l f_n dl = C, \quad (2.60)$$

where C is an arbitrary constant. In principle, considering the linear system $\mathbf{A}\mathbf{f} = \mathbf{b}$, one could simply replace one line of \mathbf{A} with the discretized solvability condition. Unfortunately, this would not result in an accurate solution because \mathbf{A} is not precisely singular due to discretization errors (the "neutral" eigenvalue is not exactly zero). Again following [50], we perform so called singular preconditioning. Namely, we build the preconditioning matrix with the neutral

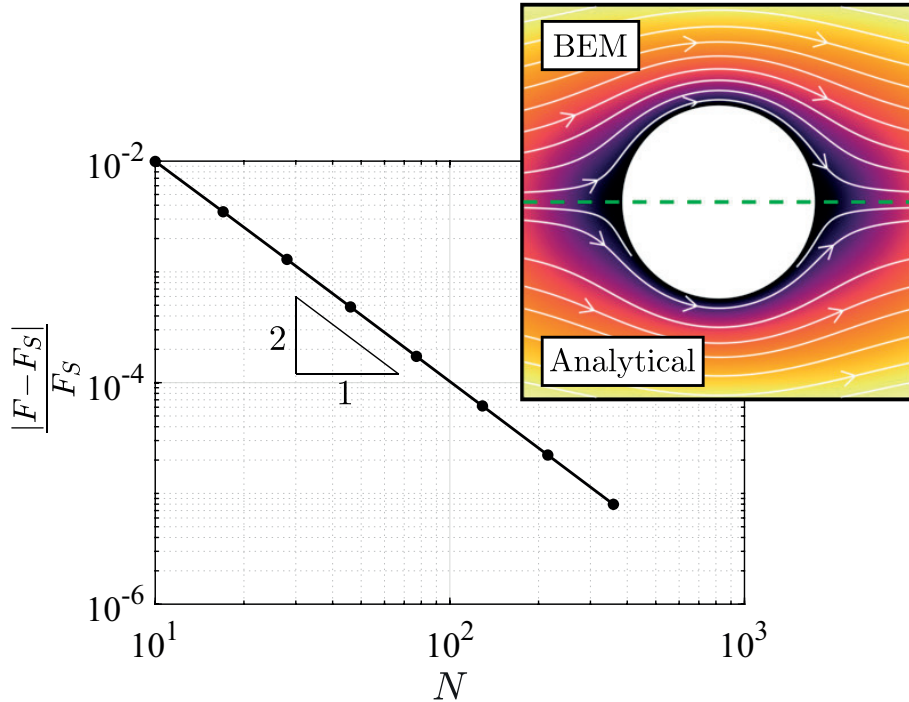


Figure 2.9 – Convergence study for a spherical particle immersed in a flow compared to the analytical result. The inset shows streamlines and intensity of the velocity field of the numerical solution (upper-half) and the analytical solution (lower-half).

eigenvector \mathbf{v}

$$\mathbf{P} = \mathbf{I} - \mathbf{v}\mathbf{v}^T, \quad (2.61)$$

and we modify the discretized equation by applying \mathbf{P} on both sides

$$\mathbf{A}_P \mathbf{f} = \mathbf{b}_P, \quad (2.62)$$

where $\mathbf{A}_P = \mathbf{P}\mathbf{A}$ and $\mathbf{b}_P = \mathbf{P}\mathbf{b}$. Now the influence matrix \mathbf{A}_P has a zero eigenvalue to machine precision. Therefore we substitute a line of the linear system \mathbf{A}_P with the integral constraint (2.60). With this treatment, the influence matrix is not singular anymore and an accurate solution is possible. For example, we can immediately verify that the result does not change with the discretization (see Figure 2.10b).

2.2.4 Remeshing algorithms

Changing the number and distribution of mesh elements is necessary in order to maintain good accuracy during a simulation. This procedure is fairly easy for axisymmetric geometries because the mesh is simply constituted by a line. However, from the developer point of view, this is still one of the most time consuming routine to implement, mostly because of the large

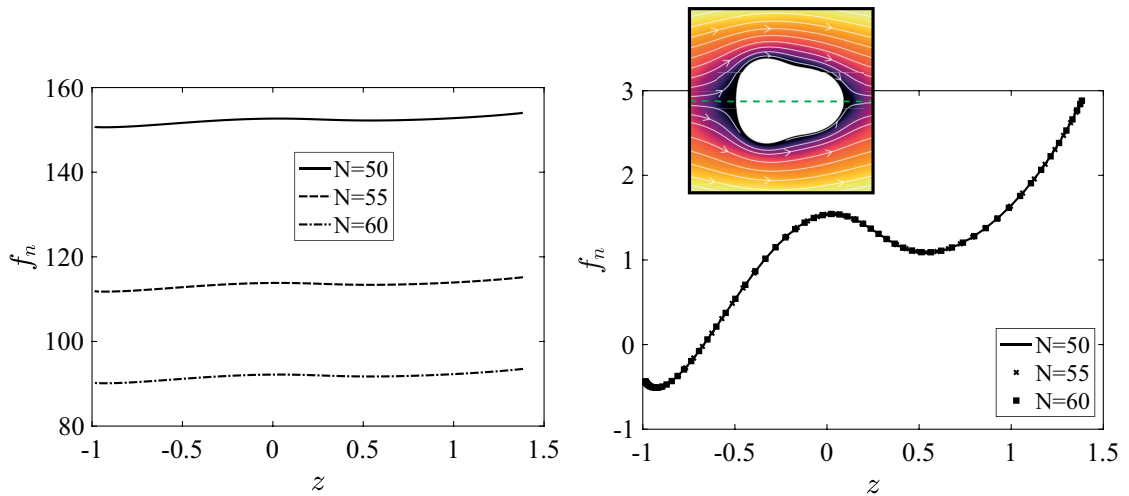


Figure 2.10 – Stresses normal to the particle surface for different number of mesh elements. (a) Without solvability condition. (b) With singular preconditioning and solvability condition (2.62). The inset shows streamlines and intensity of the velocity field.

amount of different algorithms that one can adopt and the need of tailoring an algorithm to the specific simulation case. Based on our experience, we hereby sum up our opinions on the most suited remeshing algorithms for different situations. First of all, boundary geometries can be divided in two subgroups:

- Geometries whose shape is known analytically (for example lines and circles).
- Geometries whose shape is not known analytically (i.e. deformable objects like droplets or capsules).

In the first case, we have observed that the best choice seems to be an adaptive criterion based on the proximity of two objects. Namely, when two objects come close, the facing mesh elements are split into two. In figure 2.11 a we report an example for a sphere in a pipe, where the number of nodes are increased (by splitting the elements) for the portion of the sphere close to the pipe wall.

In the case of deformable droplets the situation is more complicated as the mesh node can move tangentially along the interface. For example, in the case of buoyant droplet, the nodes will tend to cluster in the bottom part of the droplet and sparsen in the upper part. An easy way to reduce mesh deformation is to advect the nodes with their normal velocity only as in equation (1.6), thus minimizing the clustering. However this is not always sufficient and it is often necessary to resort to an active modification of the mesh. We mostly follow classic methods, for example moving the nodes along an interpolating line (for example a cubic spline) in order to maintain a given distribution or to increase the node density in specific regions, for example the curvature value can be used as distribution weight in order to cluster

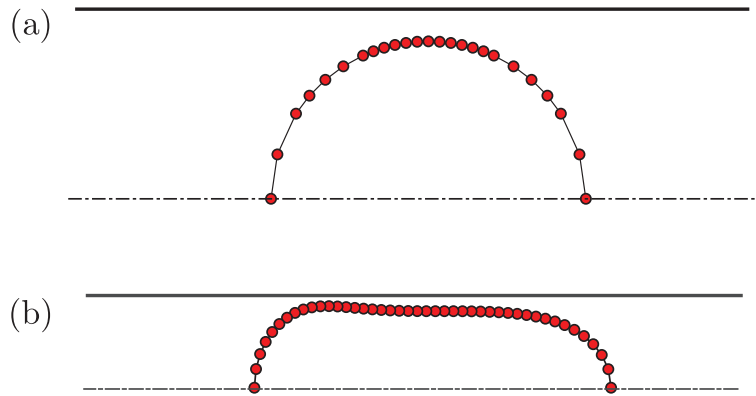


Figure 2.11 – Our remeshing strategies (the wall-mesh is not shown). (a) Sphere in a pipe: elements are split into two when are close to other objects. (b) Deformable droplet in a pipe: elements size follows a distribution based on the wall-drop distance.

nodes in high curvature regions. In Figure 2.11b the mesh elements of a droplet in a pipe is distributed based on the wall-drop distance. We have noticed that, for deformable objects, it is detrimental in term of accuracy to have abrupt changes in mesh size and therefore we use smooth distributions.

In some cases we have used more sophisticated techniques, so called passive mesh stabilization, where an artificial velocity field is added on top of the physical one in order to minimize mesh distortions [55, 56]. The artificial velocity field is chosen in such a way to modify the mesh displacement along the interface, hence maintaining the physical interface displacement unchanged.

2.2.5 Volume correction

When the simulation lasts for a long (physical) time, the droplet volume might change as a result of the summation of small errors accumulated during the time integration. In order to remove this error, we resize the droplet at every iteration by uniformly displacing the nodes along the direction normal to the interface, similar to Refs. [57, 58]. In our implementation, the value of such displacement is found by Newton iterations. This method does not influence the physical time evolution as long as the resizing is much smaller than the characteristic interface motion. At every time step, the volume change is typically less than 10^{-8} times the droplet volume. In figure 2.12 we compare a simulation with/without volume correction algorithm. The simulation is the same as that shown is figure 2.8 for the isoviscosity case.

2.2.6 Deflation technique for inviscid droplets

When $\lambda = 0$, the double layer potential present a neutral eigenmode which will change the volume of the bubble unphysically [49, 59]. A solution to this is proposed in [59] with a

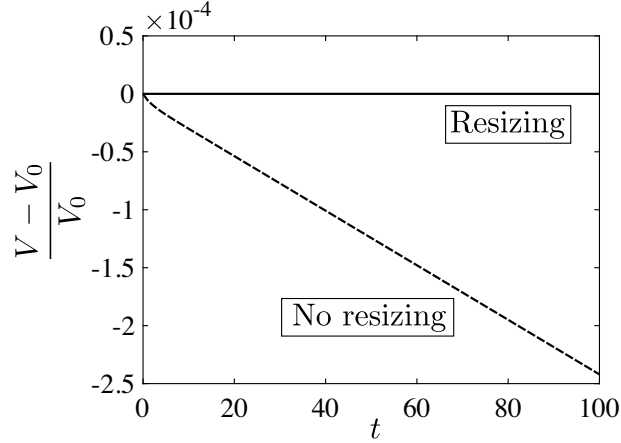


Figure 2.12 – Volume variation for a droplet in extensional flow, $Ca = 0.1$ and $\lambda = 1$. The dashed line is the error when the volume correction is not activated while the solid one when is activated.

deflation technique. In practice, we add

$$n_j(\mathbf{x}_0) \left(\int_l u_i(\mathbf{x}) n_i(\mathbf{x}) dl(\mathbf{x}) - Q \right) = 0 \quad (2.63)$$

to the right hand side of equation (2.32), where Q is the bubble rate of inflation. For the extensional flow we set $Q = 0$. In figure 2.13 we can see that if the deflation is not actuated, the droplet volume changes unphysically already after 2 units of time. This technique might be employed for obtaining inflating/deflating bubbles by imposing $Q \neq 0$.

2.2.7 Spectral Boundary Integral Method

In this section we illustrate higher order discretization methods, so called Spectral Boundary Integral Method (Spectral BIM). In particular, we implement a spectral collocation method, where the interface location $z(s)$ and $r(s)$, velocity $\mathbf{u}(s)$ and stresses $\mathbf{f}(s)$ are parametrized by $s \in [0, 1]$ along the interface (see Figure 2.14). We first consider the isoviscosity droplet case $\lambda = 1$ in order to simplify the boundary integral equation. The boundary integral equation for the interface velocity (2.32) in non-dimensional form writes

$$8\pi u_j(\mathbf{x}_0) = 8\pi u_j^\infty(\mathbf{x}_0) - \int_0^1 M_{ji}(\mathbf{x}_0, \mathbf{x}) \Delta f_i(\mathbf{x}) h(\mathbf{x}) ds. \quad (2.64)$$

where $h = \sqrt{z'^2 + r'^2}$ is the metrics term. As shown in figure 2.14, the interface is discretized with Gauss-Legendre nodes [52, 60] mapped on $s \in [0, 1]$. Choosing N collocation points, the integration along s reads

$$8\pi \mathbf{u}_m = 8\pi \mathbf{u}_m^\infty - \sum_{n=1}^N \mathbf{M}(\mathbf{x}_m, \mathbf{x}_n) \cdot \Delta \mathbf{f}_n w_n h_n \quad (2.65)$$

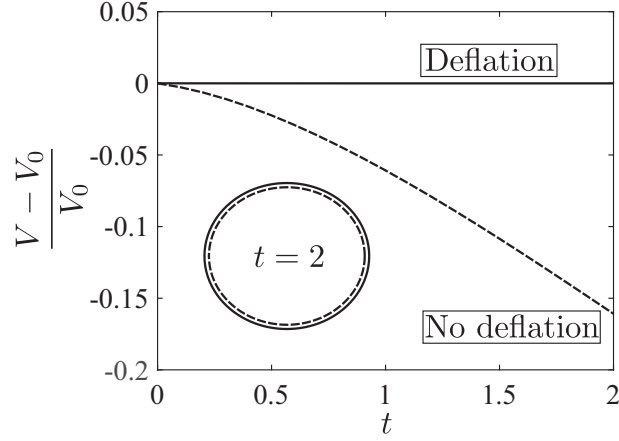


Figure 2.13 – Volume error for a bubble in an extensional flow, $Ca = 0.1$ and $\lambda = 0$. The solid line refers to the error when the deflation technique is applied and the dashed line when is not applied. The inset shows the corresponding bubble shapes at $t = 2$.

where \mathbf{x}_n is the coordinate of the n th node and w_n is the corresponding integration weight [52, 60]. Written in matrix form, equation (2.65) writes

$$8\pi\mathbf{u} = 8\pi\mathbf{u}_m^\infty - \mathbf{S}\Delta\mathbf{f}, \quad (2.66)$$

where

$$S_{mn} = w_n h_n \begin{pmatrix} M_{zz}(\mathbf{x}_m, \mathbf{x}_n) & M_{zr}(\mathbf{x}_m, \mathbf{x}_n) \\ M_{rz}(\mathbf{x}_m, \mathbf{x}_n) & M_{rr}(\mathbf{x}_m, \mathbf{x}_n) \end{pmatrix}. \quad (2.67)$$

Contrary to low orders methods, here velocities and stresses (as well the droplet shape itself) are represented by high order polynomials, giving higher accuracy. Problems arise when $n = m$ since the Green's function become singular (and contrary to low order methods, in this case the grid point for \mathbf{x}_0 and \mathbf{x} really coincide!), we will therefore remove the singularity with the integral identity

$$\int_0^1 \mathbf{M}(\mathbf{x}_0, \mathbf{x}) \cdot f(s)\mathbf{n} h(s) ds = \int_0^1 \mathbf{M}(\mathbf{x}_0, \mathbf{x}) \cdot \mathbf{n} [f(\mathbf{x}) - f(\mathbf{x}_0)] h(s) ds + f(\mathbf{x}_0) \underbrace{\int_0^1 \mathbf{M}(\mathbf{x}_0, \mathbf{x}) \cdot \mathbf{n} h(s) ds}_0, \quad (2.68)$$

where $\Delta\mathbf{f} = f(s)\mathbf{n}$ and the second integral on the right hand side is zero because \mathbf{M} is a divergence free field [61] (note that this singular treatment works only when the traction difference tangent to the interface is zero). The first integral on the right hand side is non-singular and can be integrated accurately (when $\mathbf{x} = \mathbf{x}_0$ the value of the integrand is zero). Therefore equation (2.66) becomes

$$8\pi\mathbf{u} = 8\pi\mathbf{u}_m^\infty - \mathbf{S} \circ \Delta\mathbf{f}', \quad (2.69)$$

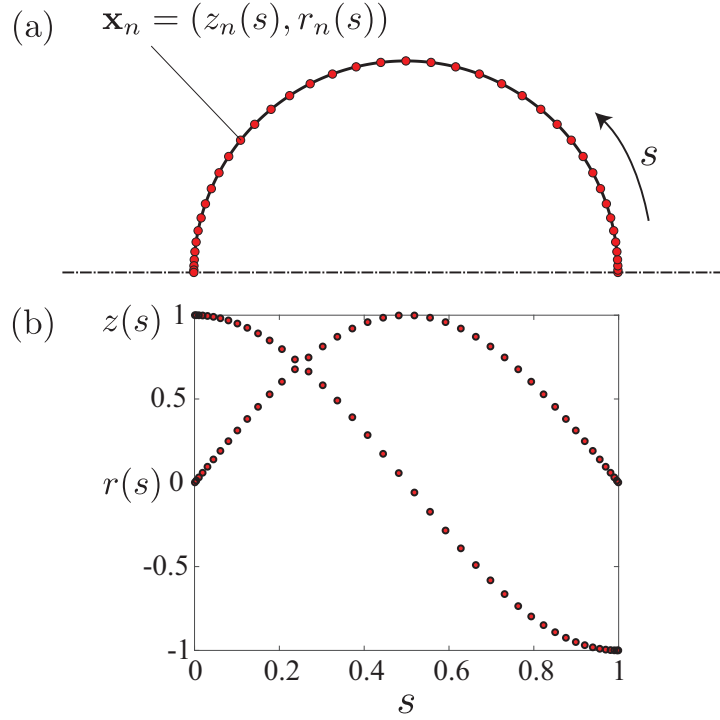


Figure 2.14 – A sphere meshed with Gauss-Legendre nodes in the axisymmetric domain. (a) Physical and (b) parametric domain.

where \circ indicates the Hadamard product and

$$\Delta f'_{mn} = [f(\mathbf{x}_n) - f(\mathbf{x}_m)] \begin{pmatrix} n_z(\mathbf{x}_n) & n_r(\mathbf{x}_n) \\ n_z(\mathbf{x}_n) & n_r(\mathbf{x}_n) \end{pmatrix}, \quad (2.70)$$

and the term on the diagonal of $\mathbf{S} \circ \Delta \mathbf{f}'$ are directly set to zero.

What described for the single layer operator can be directly used to compute the double layer operator. Namely, the discretized double layer operator read

$$D_{mn} = w_n h_n \begin{pmatrix} Q_{zz}(\mathbf{x}_m, \mathbf{x}_n) & Q_{zr}(\mathbf{x}_m, \mathbf{x}_n) \\ Q_{rz}(\mathbf{x}_m, \mathbf{x}_n) & Q_{rr}(\mathbf{x}_m, \mathbf{x}_n) \end{pmatrix}. \quad (2.71)$$

Technically, the only difference lies in the singularity of the double layer potential. In fact, the kernel q_{jik} of the double layer contains a strong singularity that is regularized by the normal vector, meaning that $Q_{ji} = q_{jik} n_k$ is non-singular. Therefore the integral can be computed without any special treatment. However, it is necessary to evaluate the non-singular kernels in $\mathbf{x} = \mathbf{x}_0$. This is not completely trivial and we refer to 2.4.1 for a detailed explanation. In figure 2.15a we validate the code implementation with the analytical solution for a rising droplet and the results in figure 2.7 with low order discretization. Note that the error does not converge exponentially because the integrand in the single layer, even if it is non singular, is not smooth because of singularities in higher order terms (this was already observed in

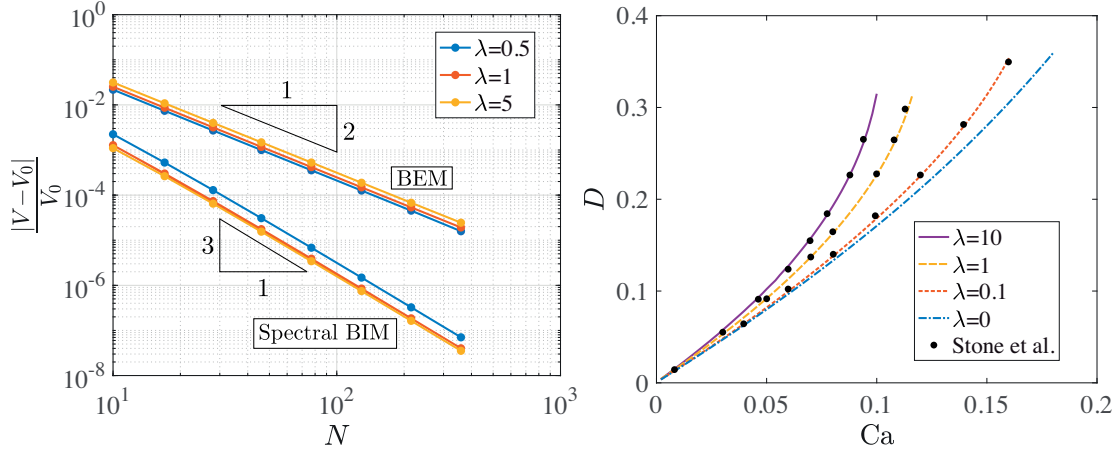


Figure 2.15 – Validation Spectral BIM. (a) Convergence of the velocity of a rising spherical droplet and compared to BEM of figure 2.7. (b) Validation of a droplet in extensional flow with Ref.[53].

previous studies [58]). In figure 2.15b we validate also for a droplet in extensional flow.

2.2.8 Remeshing in the Spectral BIM

As explained before in section 2.2.4, remeshing is needed in order to prevent nodes from clustering. This is a problem because it means that the metrics term $h(s)$ in equation (2.64), relating the physical space to the spectral grid, becomes a high order (or even non-smooth) function, leading to a loss in accuracy. The metric term is physically represented as the arc-length derivative and the most favorable situation is when the arc-length discretization is coincident with the spectral grid discretization and therefore $h(s) = 1$. This in general is not the case, for example when drawing an ellipse

$$z = a \cos(\pi s), \tag{2.72}$$

$$r = b \sin(\pi s), \tag{2.73}$$

the arc-length does not correspond exactly to the spectral grid, as shown in figure 2.16. Replacing the points in the right place while maintaining the spectral accuracy is not a trivial task. The proposed strategy is to displace the grid point in order to satisfy the nonlinear equation

$$h(s) - 1 = 0, \tag{2.74}$$

This equation can be solved with Newton method. In figure 2.16 we compare an ellipsoidal shape before and after remeshing. As shown in the graph, the satisfaction of equation (2.74) is excellent after remeshing. This remeshing strategy is typically applied when the L_2 norm of equation (2.74) is greater than 10^{-4} .

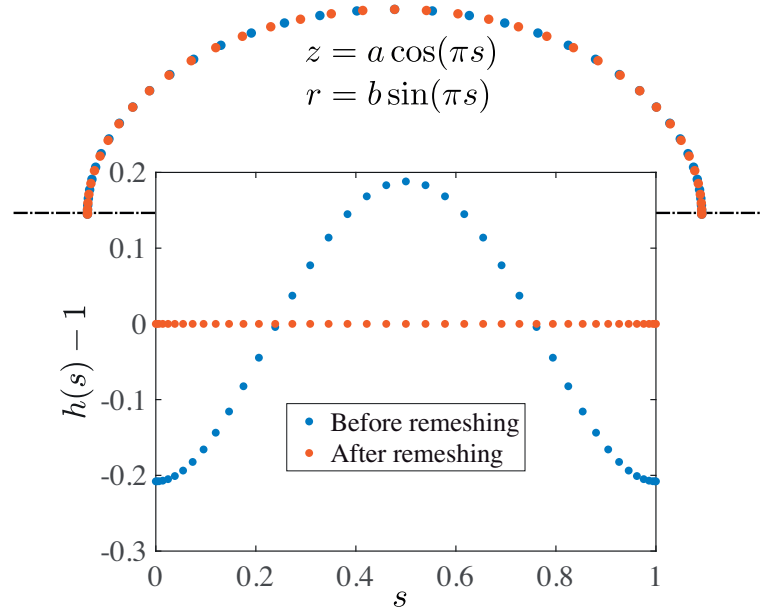


Figure 2.16 – Remeshing of an ellipsoid. The remeshing algorithm acts in order to optimize the mapping between the arc-length and the spectral grid.

2.3 Newton method and linear stability analysis

Newton method is useful in order to identify solutions of a set of nonlinear differential equations, it is also possible to identify unstable solutions which are not observable in a DNS. This is usually employed together with continuation method, in order to identify bifurcations and different solution branches. We implement Newton method in the framework of BIM, as done already in the literature [62, 63, 64].

As a recap, the Newton method solves numerically a nonlinear $\mathbb{R} \rightarrow \mathbb{R}$ equation $f(x) = 0$ by iteratively solving the linearized equation. Namely, starting from an initial guess x_0 the linearized equation writes

$$f(x_0 + dx) \approx f(x_0) + \underbrace{\frac{df}{dx}}_J dx, \quad (2.75)$$

where we have neglected higher order terms. Setting equation (2.75) to zero, we can find the solution to the linearized system as

$$dx = -J^{-1} f(x_0), \quad (2.76)$$

and a new solution is found as $x_1 = x_0 + dx$. Iterating this procedure, the method rapidly converges to the nonlinear solution, provided that the initial guess is close enough. The method is readily generalizable to a system of nonlinear equations.

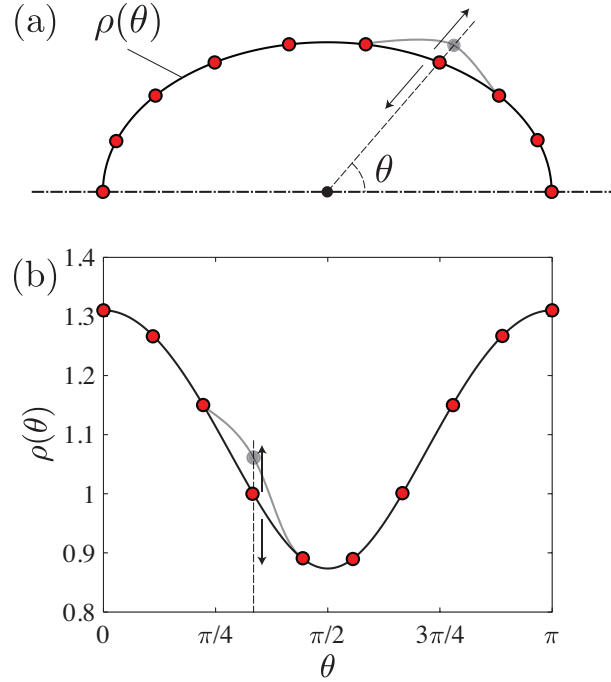


Figure 2.17 – Uniform discretization in $\theta \in [0, \pi]$. Every mesh point has one degrees of freedom for the position along the direction set by θ . (a) Physical domain with a sketch of the displacement of one mesh point and (b) correspondent interface position versus θ .

2.3.1 A well posed Newton method for deformable droplets

A steady shape of the droplet is reached when the velocity normal to the interface $u^{(n)} = \mathbf{u} \cdot \mathbf{n}$ vanishes, this comes from the impermeability condition (1.6). Discretizing the interface in N collocation points, this condition gives N equations

$$u_i^{(n)} = 0, \quad i = 1, \dots, N. \quad (2.77)$$

At first, it might seem that we will not have enough equations for the degrees of freedom of the problem. In fact, for every mesh point we have two degrees of freedom, axial and radial position. It is therefore important to use a parametrization of the interface having only one degree of freedom per point. For this purpose we will first use polar coordinates, where every mesh point is allowed to move only in one direction (see Figure 2.17). However, it is not always possible to describe the droplet shape in polar coordinate, we will discuss this issue in section 2.3.4.

At this stage, the reader might get confused between the parametrization used to solve the boundary integral equations and the one used in the Newton method. Here we clarify this point: the Newton method requires a problem with N equations and N unknowns, hence the need for the polar coordinate parametrization. However, the nonlinear function (in this case the normal velocity) can be computed by any mean or numerical method (in our case

Boundary Integral Method in curvilinear coordinates). Our algorithm performs the following operations:

1. Choose an initial droplet shape and discretize it in N points. This results in a vector $\boldsymbol{\rho}^0 = (\rho_1, \dots, \rho_N)$.
2. Compute the residuals of the nonlinear function $\mathbf{R} = \mathbf{u}^{(n)}$ (normal velocity) with a numerical method. In our case we use the Boundary Integral Method but one could use another numerical method either (for example finite element methods).
3. Compute the Jacobian \mathbf{J} . As we will see, the Jacobian is computed numerically by finite differences and requires special treatment in order to enforce the conservation of the droplet volume. Computing \mathbf{J} requires N evaluations of the nonlinear function (again, one can use his favorite numerical method to compute the nonlinear function, we use the Boundary Integral method).
4. Solve the linearized equation $\mathbf{d}\boldsymbol{\rho} = \mathbf{J}^{-1}\mathbf{R}$ in order to find the droplet shape variation $\mathbf{d}\boldsymbol{\rho}$.
5. Update the droplet shape $\boldsymbol{\rho}^1 = \boldsymbol{\rho}^0 + \mathbf{d}\boldsymbol{\rho}$ and restart from (2) with this new guess. Usually we consider that the solution has converged when $\|\mathbf{R}\|_\infty < 10^{-10}$. Less than 10 iterations are normally sufficient in order to satisfy this criterion.

2.3.2 BEM based Newton method with singular preconditioning

As previously explained in section 2.3.1, the aim of our Newton method is to find the zeros of (2.77), which is a nonlinear function of the interface position ρ , taking N mesh point we write the normal velocity $u^{(n)} = \mathbf{u} \cdot \mathbf{n}$ as

$$u_i^{(n)} = \mathcal{F}_i(\rho_1, \dots, \rho_N) = 0, \quad i = 1, \dots, N. \quad (2.78)$$

The Jacobian (computed using finite differences with $\Delta h = 10^{-5}$) thus write as

$$J_{ij} = \frac{\partial u_i^{(n)}}{\partial \rho_j} \approx \frac{u_i(\rho_1, \dots, \rho_j + \Delta h, \dots, \rho_N) - u_i(\rho_1, \dots, \rho_N)}{\Delta h} \quad i, j = 1, \dots, N. \quad (2.79)$$

However, solving the nonlinear system with this Jacobian will not work, because there are infinitely many droplets of different volumes which are a solution of (2.78). Mathematically this means that the \mathbf{J} has a neutral eigenvalue, whose associated eigenmode corresponding to shapes spanning the family of possible solutions with different volumes. Therefore, following [62], we fix the volume of the droplet

$$V = \frac{2}{3}\pi \int_0^\pi \rho^3 \sin\theta d\theta, \quad (2.80)$$

and we get to the following system of equations

$$\mathcal{F}_i(\rho_1, \dots, \rho_N) = u_i^{(n)} = 0, \quad i = 1, \dots, N, \quad (2.81)$$

$$\mathcal{G}(\rho_1, \dots, \rho_N) = \frac{2}{3}\pi \int_0^\pi \rho^3 \sin\theta d\theta - V = 0. \quad (2.82)$$

This system has more equations than unknowns and it is therefore overdetermined. However as we have mentioned before, since there is one neutral eigenmode, we can simply replace one equation for the normal velocity with volume conservation. Writing the problem in terms of residuals we get

$$R_i(\rho) = u_i^{(n)} = 0, \quad i = 1, \dots, N-1, \quad (2.83)$$

$$R_N(\rho) = \frac{2}{3}\pi \int_0^\pi \rho^3 \sin\theta d\theta - V = 0. \quad (2.84)$$

and the Jacobian where one line has been replaced with the linearized volume constraint $\frac{\partial \mathcal{G}}{\partial \rho_j}$ now writes as

$$J_{ij}^V = \frac{\partial R_i}{\partial \rho_j} \quad i, j = 1, \dots, N. \quad (2.85)$$

While this was the strategy implemented in [62], it seems not to work well in our case. In figure 2.18 we show results from this implementation for a droplet in extensional flow. From a mathematical point of view, the Newton method works correctly, after few iterations the L_∞ norm of the residuals is less than 10^{-10} and a droplet shape of the correct volume is obtained (see Figure 2.18a). However, if we now look closer at the droplet shape, we can notice a bump in the curvature K (see Figure 2.18b) corresponding to the matrix line where the volume constraint has been replaced. Consequently, the normal velocity is not very small in this node (see inset of Figure 2.18b). This situation is mathematically analogous to finding the stresses on a rigid particle described in section 2.2.3, in fact we want to eliminate a neutral eigenvalue with an integral condition but we run into trouble because the eigenvalue is not precisely zero due to discretization errors. We propose therefore the same treatment, namely we precondition the Jacobian in such a way that the eigenvalue becomes zero and then we replace one line with the Jacobian of (2.84). Denoting \mathbf{v} the column vector containing the neutral eigenvector, we build the preconditioning matrix $\mathbf{P} = \mathbf{v}\mathbf{v}^T$ and define

$$\mathbf{J}_P = \mathbf{P}\mathbf{J}, \quad \mathbf{R}_P = \mathbf{P}\mathbf{R} \quad (2.86)$$

as the preconditioned Jacobian and residuals. Now the Jacobian is singular to machine precision and we can add the volume constraint, thus obtaining the Jacobian \mathbf{J}_P^V . The results using this method are reported in Figure 2.19. The converged shape looks almost identical to the one in figure 2.18, however a closer look at the curvature (see figure 2.19c) reveals that there are no bumps. Also the normal velocity of the converged shape, despite only being converged around a value of 10^{-6} and not to machine precision, is smooth.

2.3. Newton method and linear stability analysis

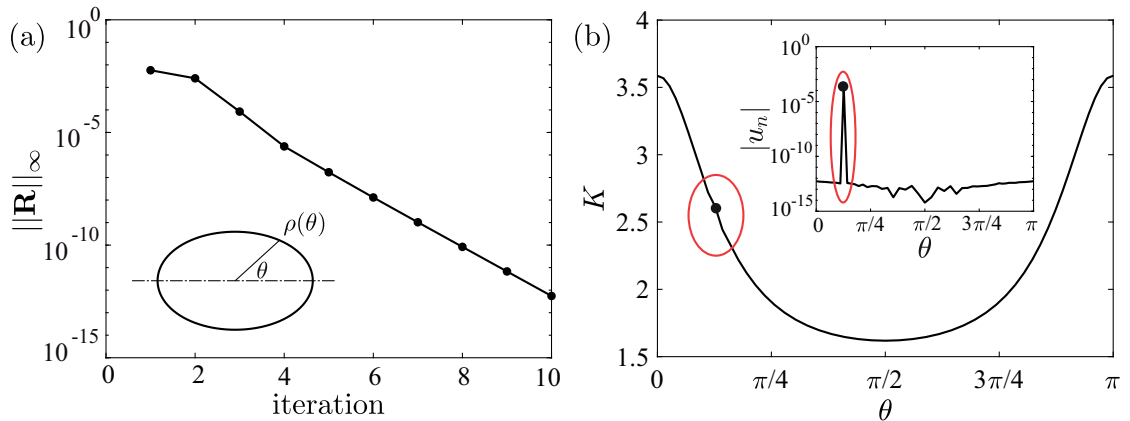


Figure 2.18 – Newton method based on BEM. The volume conservation constraint causes a discontinuity in the interface shape highlighted by an unphysical bump in the curvature. (b) Infinity norm of the residuals versus number of Newton Method iteration. The inset shows the converged droplet shape. (b) Curvature of the converged shape, the circle highlight a bump in the curvature. The inset shows the velocity normal to the interface.

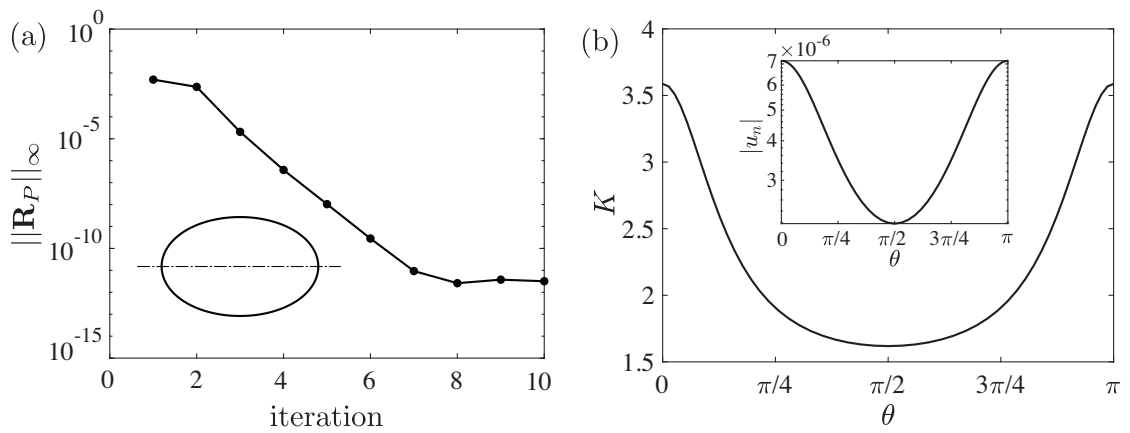


Figure 2.19 – Newton method based on BEM with singular pre-conditioning of the Jacobian for a droplet in extensional flow, $Ca = 0.1$, $\lambda = 1$ and $N = 50$. The volume conservation constraint does not cause any discontinuity in the interface shape. (a) Infinity norm of the residuals versus number of Newton method iteration. The inset shows the converged droplet shape. (b) Curvature of the converged shape. The inset shows the velocity normal to the interface.

To conclude, we have used a BEM based Newton method, computing the Jacobian by finite difference and using singular preconditioning. This method is able to converge to smooth physical solutions for a droplet in extensional flow, although the velocity normal to the interface remains of the order of 10^{-6} and converges slowly only when increasing the number of elements. In next sections we will describe a more accurate implementation based on the Spectral Boundary Integral Method.

2.3.3 Spectral BIM based Newton method

In this section we adapt the implementation of [51], developed for vesicles, to our deformable droplet case. Namely, we represent the droplet shape with N Legendre modes $(\hat{\rho}_1, \dots, \hat{\rho}_N)$ and usually $2N$ collocation points for dealiasing [58, 65, 51]. Motivated by the fact that the system seems to be overdetermined when imposing drop volume V , we solve the system of $N - 1$ degrees of freedom imposing the 1st mode amplitude in order to conserve volume. Our discretized system of the equation is

$$\hat{u}_i^{(n)} = \mathcal{F}_i(\hat{\rho}_0, \dots, \hat{\rho}_{N-1}) = 0, \quad i = 0, \dots, N-1 \quad (2.87)$$

and it would have therefore N degrees of freedom but we can fix one with volume conservation

$$\hat{\rho}_0 = \mathcal{G}(V, \hat{\rho}_1, \dots, \hat{\rho}_{N-1}). \quad (2.88)$$

In this way the system has now $N - 1$ degrees of freedom, namely

$$\hat{u}_i^{(n)} = \mathcal{F}_i(\hat{\rho}_1, \dots, \hat{\rho}_{N-1}, \mathcal{G}(V, \hat{\rho}_1, \dots, \hat{\rho}_{N-1})) = 0, \quad i = 1, \dots, N-1 \quad (2.89)$$

The Jacobian of the nonlinear system of equations is now given as

$$J_{ij} = \frac{\partial \hat{u}_i}{\partial \hat{\rho}_j}, \quad i, j = 1, \dots, N-1, \quad (2.90)$$

and computed with finite differences as before. With this strategy, the Newton method works extremely well and the residuals converge rapidly to machine precision (see Figure 2.20a), obtaining a very smooth shape and consequently smooth curvature (see Figure 2.20b). Note that we include in the residuals also \hat{u}_0 which does not explicitly appear in the Newton method but still converges to machine precision (see inset of Figure 2.20b). The physical reason for this is that, once $(\hat{u}_1, \dots, \hat{u}_{N-1})$ are zero, than \hat{u}_0 has to be zero in order to respect volume conservation.

2.3.4 The novelty: Newton method for overturning droplet geometries

As we have mentioned before, it is not always possible to describe the droplet shape in polar coordinates (see Figure 2.21a), still we need a representation where the Newton method

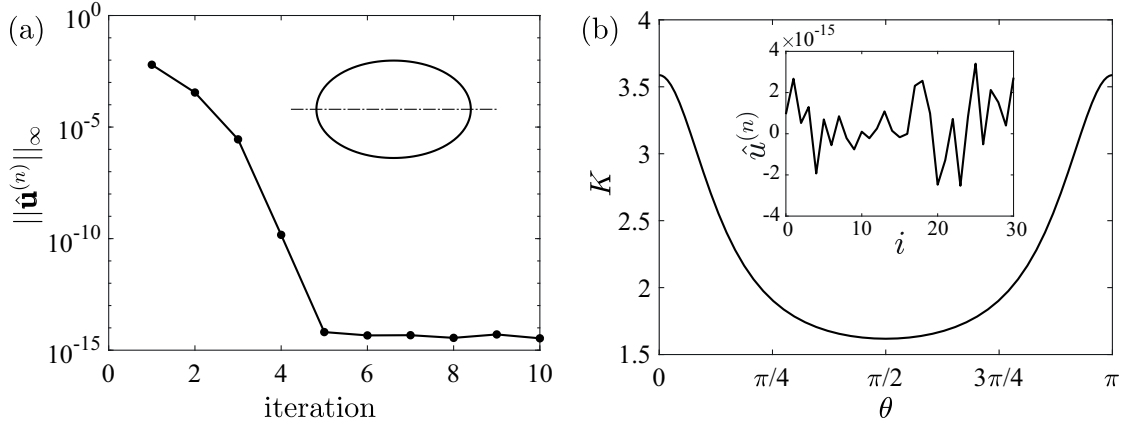


Figure 2.20 – Newton method based on Spectral BIM for a droplet in extensional flow, $Bo = 1$, $\lambda = 1$ and $N = 30$. The volume conservation constraint does not cause any discontinuity in the interface shape. (a) Infinity norm of the normal velocity modes versus number of Newton method iteration. The inset shows the converged solution. (b) Curvature of the converged shape. The inset shows the normal velocity modes.

is well posed. In this section we introduce an implementation that we have developed to overcome this issue. Namely, the droplet shape is described as a perturbation of the initial guess (base shape \mathbf{x}_B). Such perturbation is applied only in the normal direction $\mathbf{n}_B(s)$, the only direction causing a modification of the droplet shape. Namely, considering a base shape $\mathbf{x}_B = [z_B(s), r_B(s)]$, parametrized by s as in section 2.2.7, a perturbation $\delta(s)$ will be applied as $\mathbf{x}_B(s) + \delta(s)\mathbf{n}_B(s)$ (see Figure 2.21b). By doing so, it is possible to describe any droplet shape, provided that it does not overturn compared to the base shape \mathbf{x}_B , meaning that the interface points of the final shape have to be identified uniquely by a normal displacement of the interface points of the initial guess.

The discretized system of the equations, including the volume conservation as in previous section, is

$$\hat{u}_i^{(n)} = \mathcal{F}_i(\hat{\delta}_1, \dots, \hat{\delta}_{N-1}, \mathcal{G}(V, \hat{\delta}_1, \dots, \hat{\delta}_{N-1})) = 0, \quad i = 1, \dots, N-1 \quad (2.91)$$

The Jacobian of the nonlinear system of equations is now given as

$$J_{ij} = \frac{\partial \hat{u}_i}{\partial \hat{\delta}_j}, \quad i, j = 1, \dots, N-1, \quad (2.92)$$

and computed with finite differences as before. As in the previous section, the Newton method converges rapidly to machine precision (see Figure 2.22a), with the advantage of being able to describe overtuning shapes.

As a final note, we would like to point out that the same strategy for conserving the droplet volume might be employed to impose other physical quantities. In the following we make an example for a rising spherical droplet (as the case studied in section 2.2.2). The moving

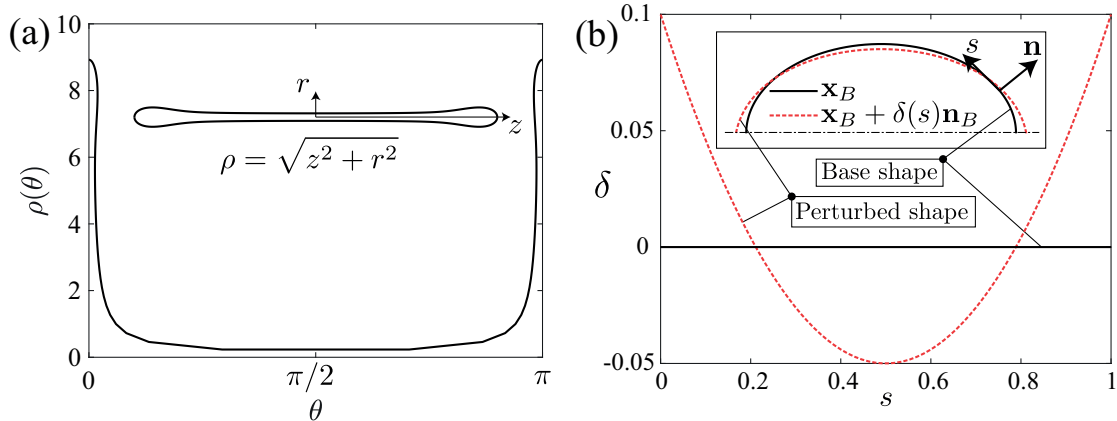


Figure 2.21 – (a) Elongated droplet where the representation in polar coordinates fails, $\rho(\theta)$ is not a function of θ because it overturns. (b) Sketch of perturbation of the base shape by displacing the interface in the normal direction.

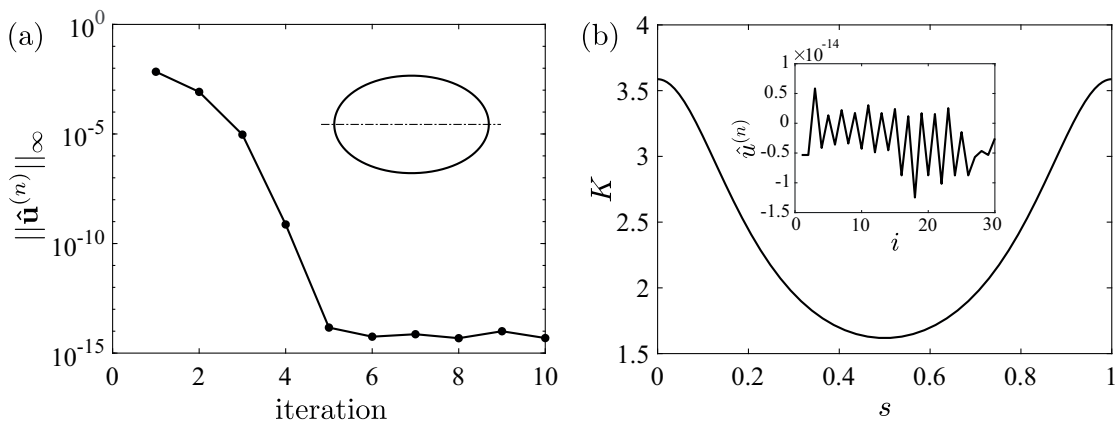


Figure 2.22 – Newton method based on Spectral BIM for a droplet in extensional flow, $Ca = 0.1$, $\lambda = 1$ and $N = 30$. The representation in the direction normal to the interface allows for computing overturning shapes. (a) Infinity norm of the normal velocity modes versus number of Newton method iteration. The inset shows the converged solution. (b) Curvature of the converged shape. The inset shows the normal velocity modes.

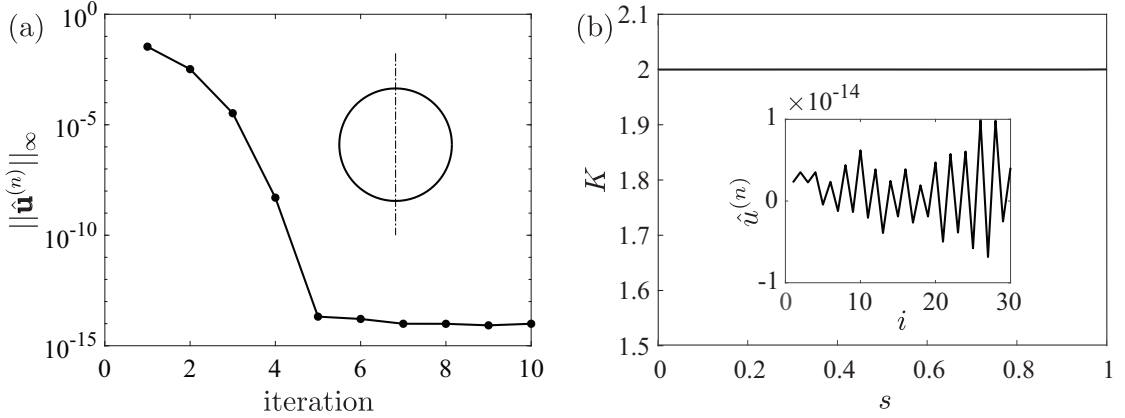


Figure 2.23 – Newton method for a rising droplet, $Ca = 1$, $\lambda = 1$ and $N = 30$. The center of mass is constrained to the origin. (a) Infinity norm of the normal velocity modes versus number of Newton method iteration. The inset shows the converged solution. (b) Curvature of the converged shape. The inset shows the normal velocity modes.

spherical droplet is a solution of the system of equation, however, in order to obtain a fixed (non-moving shape) as a solution one can solve the equations in the co-moving frame of reference of the droplet. In this case, there are infinite many solutions of the different axial position of the droplet and in order to have a converging Newton method we have to impose the axial location. We employ a similar strategy to what done before for the droplet volume, namely we suppress one degree of freedom in order to impose the axial location of the droplet z_{cm} . Therefore, $\hat{\delta}_0$ and $\hat{\delta}_1$ are found imposing volume conservation and center of mass location

$$\hat{\delta}_0 = \mathcal{G}(V, \hat{\delta}_1, \dots, \hat{\delta}_{N-1}), \quad (2.93)$$

$$\hat{\delta}_1 = \mathcal{H}(z_{\text{cm}}, \hat{\delta}_0, \hat{\delta}_2, \dots, \hat{\delta}_{N-1}). \quad (2.94)$$

We show the results in figure 2.23, where starting from an ellipsoidal droplet, the Newton method converge rapidly to the spherical solution.

2.3.5 Linear stability analysis

Linear stability analysis is necessary to investigate the stability of the steady solutions obtained for instance with Newton method. Having already computed the linearized operator (the Jacobian), we can now proceed to linear stability analysis simply by computing the eigenvalues of \mathbf{J} . We use the ansatz $\eta = \hat{\eta}(s) \exp(\sigma t)$ for the interface perturbations in the normal direction, obtaining from perturbing (2.91), the eigenvalue problem

$$\sigma \hat{\eta} = \mathbf{J} \hat{\eta}. \quad (2.95)$$

The real part of σ determines the temporal evolution of the eigenmode (unstable when is positive and stable when negative) while the imaginary one the spatial evolution. In figure 2.24

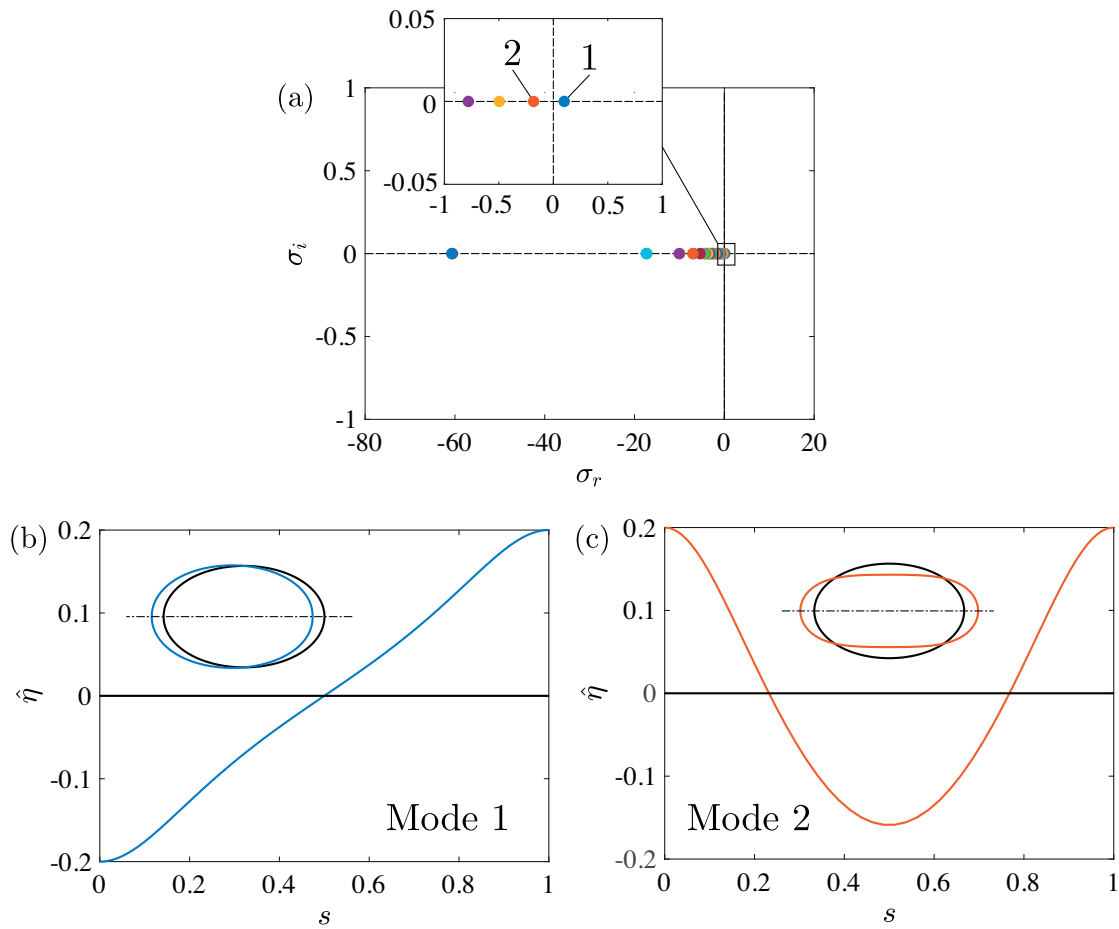


Figure 2.24 – Stability analysis for a droplet in an extensional flow, $Ca = 0.1$ and $\lambda = 1$. (a) Eigenvalue spectra: there is one unstable eigenvalue. (b) Eigenmode associated to the unstable eigenvalue. The inset shows the eigenmode superimposed to the base state. (c) Eigenmode associated to the least stable eigenvalue. The inset shows the eigenmode superimposed to the base state.

we plot the results of the linear stability analysis from the previously computed steady state solution. The eigenvalue spectra reveals (see Figure 2.24a) the existence of one unstable eigenvalue. Physically, the unstable eigenmode is a rigid body displacement (see Figure 2.24b) that is known to exist in extensional flow [66]. Therefore, strictly speaking about shape instabilities, this droplet is stable. We show also the least stable mode (see Figure 2.24c) which elongates the droplet.

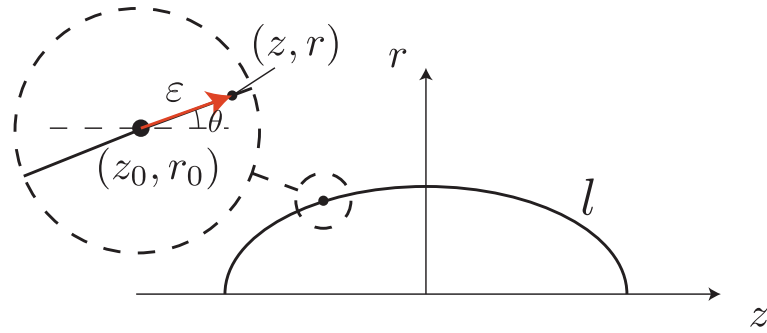


Figure 2.25 – Sketch of the domain. As $(z, r) \rightarrow (z_0, r_0)$, the Green's functions become singular.

2.4 Appendix

2.4.1 Appendix I: Study of the leading order singularity of Stokes kernels

We inspect the singularities of the Green's function of axisymmetric Stokes flow. Considering the sketch in figure 2.25, the function become singular when $(z, r) \rightarrow (z_0, r_0)$. The knowledge on the behavior of the function close to (z_0, r_0) is crucial especially when using spectral method, due to details that have been explained in section 2.2.7. Considering figure 2.25 we zoom on the boundary of the domain (for example the droplet interface) and we go from cartesian to a local polar coordinate where $\hat{z} = z - z_0 = \varepsilon \cos \theta$, $r = r_0 + \varepsilon \sin \theta$ and $\varepsilon = \sqrt{\hat{z}^2 + (r - r_0)^2}$. The boundary can be locally considered a straight line, as $\varepsilon \rightarrow 0$ the Green's functions become singular.

Special functions

As explained in section 2.1.5, the Green's function for axisymmetric Stokes flows contain special functions, the so called elliptic integrals of first and second kind $F(k)$ and $E(k)$, defined in equation (2.38). In order to study the leading order singularities it is necessary to know the expansion of $F(k)$ and $E(k)$ as $k \rightarrow 1$

$$F(k) = \log\left(\frac{1}{\sqrt{1-k^2}}\right) + \psi(1/2) + O(k^2) \quad E(k) = 1 + O(k^2)$$

where ψ denotes the digamma function and $\psi(0.5) = \log(4)$. The corresponding expansions as $\varepsilon \rightarrow 0$ are given by

$$F(k(\varepsilon)) = -\log \varepsilon + \log(8r_0) + \frac{\sin \theta}{2r_0} \varepsilon + O(\varepsilon^2), \quad E(k(\varepsilon)) = 1 + O(\varepsilon^2). \quad (2.96)$$

Stokeslet

The extended form of equation (2.34) reads

$$M_{zz} = 2k\sqrt{\frac{r}{r_0}} \left(F(k) + \frac{\hat{z}^2}{\varepsilon^2} E(k) \right), \quad (2.97)$$

$$M_{zr} = k \frac{\hat{z}}{(r r_0)^{1/2}} \left[F(k) - (r_0^2 - r^2 + \hat{z}^2) \frac{E(k)}{\varepsilon^2} \right], \quad (2.98)$$

$$M_{rz} = -k \frac{\hat{z}}{r_0} \left(\frac{r}{r_0} \right)^{1/2} \left[F(k) + (r_0^2 - r^2 - \hat{z}^2) \frac{E(k)}{\varepsilon^2} \right], \quad (2.99)$$

$$M_{rr} = \frac{k}{r_0 r} \sqrt{\frac{r}{r_0}} \left\{ (r_0^2 + r^2 + 2\hat{z}^2) F(k) - [2\hat{z}^4 + 3\hat{z}^2(r_0^2 + r^2) + (r_0^2 - r^2)^2] \frac{E(k)}{\varepsilon^2} \right\}. \quad (2.100)$$

As $\varepsilon \rightarrow 0$ the Stokeslet becomes

$$M_{zz} = -2 \log \varepsilon + \log(8r_0) + \cos^2 \theta + O(\varepsilon), \quad (2.101)$$

$$M_{zr} = \sin(2\theta) + O(\varepsilon), \quad (2.102)$$

$$M_{rz} = \sin(2\theta) + O(\varepsilon), \quad (2.103)$$

$$M_{rr} = -2 \log \varepsilon + 2 \log(8r_0) - 2(\cos^2 \theta + 2) + O(\varepsilon). \quad (2.104)$$

These expansions give us the leading order of the singularity and also the value of the non-singular functions in (z_0, r_0) . For example, the zeroth order of M_{zz} is needed in order to evaluate the non-singular function $M_{zz} + 2 \log \varepsilon = \log(8r_0) + \cos^2 \theta + O(\varepsilon)$ in (z_0, r_0) .

Stresslet

We now proceed in a similar way for the Stresslet, the Green's function appearing in the double layer potential. The extended form of equations (2.39) and (2.40) read

$$q_{zzz} = -\frac{\hat{z}^3 r k^5}{4(r r_0)^{5/2}} \left[\frac{2(2-k^2)}{(1-k^2)^2} E(k) - \frac{F(k)}{1-k^2} \right], \quad (2.105)$$

$$q_{zzr} = q_{zrz} = \frac{r \hat{z}^2 k^5}{4(r r_0)^{5/2}} \left[\left(\frac{r}{1-k^2} - \frac{r_0(2-k^2)}{(1-k^2)k^2} \right) F(k) - \left(2r \frac{2-k^2}{(1-k^2)^2} - 2r_0 \frac{1-k^2+k^4}{(1-k^2)^2 k^2} \right) E(k) \right], \quad (2.106)$$

$$q_{zrr} = \frac{r \hat{z} k^5}{4(r r_0)^{5/2}} \left[\left(r_0^2 \frac{k^4+8k^2-8}{k^4(1-k^2)} + 2r^2 \frac{1}{1-k^2} - 2r r_0 \frac{2-k^2}{k^2(1-k^2)} \right) F(k) + \left(r_0^2 \frac{2k^6-12k^2+8}{k^4(1-k^2)^2} - 2r^2 \frac{2-k^2}{(1-k^2)^2} + 2r r_0 \frac{2-2k^2+2k^4}{k^2(1-k^2)^2} \right) E(k) \right], \quad (2.107)$$

$$q_{rzz} = \frac{r \hat{z} k^5}{4(r r_0)^{5/2}} \left[\left(r \frac{2-k^2}{(1-k^2)k^2} - r_0 \frac{1}{1-k^2} \right) F(k) + \left(-r \frac{2-2k^2+2k^4}{k^2(1-k^2)^2} + 2r_0 \frac{2-k^2}{(1-k^2)^2} \right) E(k) \right], \quad (2.108)$$

$$q_{r zr} = q_{r rz} = \frac{r \hat{z} k^5}{4(r r_0)^{5/2}} \left[\left((r_0^2 + r^2) \frac{2-k^2}{k^2(1-k^2)} - r r_0 \frac{2k^4+8k^2-8}{(1-k^2)k^4} \right) F(k) + \left(-(r^2 + r_0^2) \frac{2-2k^2+2k^4}{k^2(1-k^2)^2} + r r_0 \frac{4k^6-4k^4-12k^2+8}{k^4(1-k^2)^2} \right) E(k) \right], \quad (2.109)$$

$$q_{rrr} = \frac{k^5}{4(r r_0)^{5/2}} \left[\left(r^3 \frac{2-k^2}{(1-k^2)k^2} - r^2 r_0 \frac{3k^4+16k^2-16}{k^4(1-k^2)} + r r_0^2 \frac{-3k^6-26k^4+96k^2-64}{k^2(1-k^2)} - r_0^3 \frac{k^4+8k^2-8}{k^4(1-k^2)} \right) F(k) + \left(r^3 \frac{-2+2k^2-2k^4}{k^2(1-k^2)^2} - r^2 r_0 \frac{6k^6-4k^4-24k^2+16}{k^4(1-k^2)^2} - r r_0^2 \frac{6k^8-2k^6-62k^4+128k^2-64}{k^6(1-k^2)^2} - r_0^3 \frac{2k^6-12k^2+8}{(1-k^2)^2 k^4} \right) E(k) \right]. \quad (2.110)$$

Chapter 2. Numerical method

As $\varepsilon \rightarrow 0$, the leading order terms are

$$q_{zzz} = -8 \frac{\cos^3 \theta}{\varepsilon} - 4 \frac{\cos^3 \theta \sin \theta}{r_0} + O(\varepsilon), \quad (2.111)$$

$$q_{zzr} = q_{zrz} = -8 \frac{\cos^2 \theta \sin \theta}{\varepsilon} + 2 \cos^2 \theta \frac{1 + 2 \sin^2 \theta}{r_0} + O(\varepsilon), \quad (2.112)$$

$$q_{zrr} = -8 \frac{\cos \theta \sin^2 \theta}{\varepsilon} + 12 \frac{\cos \theta \sin^3 \theta}{r_0} - 4 \frac{\cos \theta \sin \theta (1 + 4 \sin^2 \theta)}{r_0} + O(\varepsilon), \quad (2.113)$$

$$q_{rzz} = -8 \frac{\cos^2 \theta \sin \theta}{\varepsilon} + 12 \frac{\cos^2 \theta \sin^2 \theta}{r_0} + 2 \cos^2 \theta \frac{1 - 8 \sin^2 \theta}{r_0} + O(\varepsilon), \quad (2.114)$$

$$q_{rzt} = q_{rtz} = -8 \frac{\cos \theta \sin^2 \theta}{\varepsilon} - 4 \frac{\cos \theta \sin^3 \theta}{r_0} + O(\varepsilon), \quad (2.115)$$

$$q_{rrr} = -8 \frac{\sin^3 \theta}{\varepsilon} - 4 \frac{\sin^4 \theta}{r_0} + \frac{6}{r_0} - 2 \frac{\sin^2 \theta}{r_0} + O(\varepsilon). \quad (2.116)$$

As expected, the leading order singularity of the Stresslet is $1/\varepsilon$. However, we have to consider that the integrand is actually a sum of Stresslets, namely $Q_{ji} = q_{jik} n_k$. Therefore, considering the expression of the normal vector to a curve

$$n_z = -\sin \theta - \frac{\cos \theta}{\varepsilon'(0)} \varepsilon + O(\varepsilon^2),$$

$$n_r = \cos \theta - \frac{\sin \theta}{\varepsilon'(0)} \varepsilon + O(\varepsilon^2),$$

one can see that the integrand is actually non-singular

$$Q_{zz} = q_{zzz} n_z + q_{zzr} n_r = 2 \cos^2 \theta \frac{4r_0 - \varepsilon'(0) \cos \theta}{r_0 \varepsilon'(0)} + O(\varepsilon), \quad (2.117)$$

$$Q_{zr} = q_{zrz} n_z + q_{zrr} n_r = \sin(2\theta) \frac{4r_0 - \varepsilon'(0) \cos \theta}{r_0 \varepsilon'(0)} + O(\varepsilon), \quad (2.118)$$

$$Q_{rz} = q_{rzz} n_z + q_{rzt} n_r = \sin(2\theta) \frac{4r_0 - \varepsilon'(0) \cos \theta}{r_0 \varepsilon'(0)} + O(\varepsilon), \quad (2.119)$$

$$Q_{rr} = q_{rrz} n_z + q_{rrr} n_r = \frac{16r_0 \sin^2 \theta + \varepsilon'(0) (11 \cos \theta + \cos(3\theta))}{2r_0 \varepsilon'(0)} + O(\varepsilon). \quad (2.120)$$

More often, the domain boundaries are represented in curvilinear coordinates $[z(s), r(s)]$. For this reason it is necessary to express $\cos \theta$, $\sin \theta$ and $\varepsilon'(0)$ in the more general $z(s), r(s)$ curvilinear system of coordinates, with $s \in [0, 1]$. After developing the calculations we obtain

$$\cos \theta = \frac{-z'}{\sqrt{z'^2 + r'^2}}, \quad (2.121)$$

$$\sin \theta = \frac{-r'}{\sqrt{z'^2 + r'^2}}, \quad (2.122)$$

$$\left. \frac{d\varepsilon}{d\theta} \right|_0 = 2 \frac{(z'^2 + r'^2)^{3/2}}{z'' r' - r'' z'}. \quad (2.123)$$

Function Name	Simulation time	Calls	Total Time	Self Time*	Total Time Plot (dark band = self time)
main_oneDropBEM		1	23.237 s	0.029 s	
runTimeSteppingBEM		1	23.189 s	0.001 s	
RK2mostGeneralBubbleVolCorr		1	23.183 s	0.063 s	
...var)computeVelocityDrop(t,var.PARAM)		2001	19.739 s	0.059 s	
computeVelocityDrop	Build single and double layer potential		19.680 s	0.179 s	
BEM_Stokes			18.194 s	0.705 s	
computeKernelsOperatorsAxis		2001	14.998 s	0.170 s	
computeKernelStokesAxisLinearSpline		2001	14.560 s	3.996 s	
sgf_ax_fs_vect3		2001	7.588 s	5.503 s	
spline_symmetric	Computation of the Green's functions	24938	3.240 s	3.240 s	

Figure 2.26 – Time spent in the first ten (from longer to shorter time) subroutines of the code.

This expressions allow the calculation of equation (2.117) (2.118) (2.119) (2.120) in curvilinear coordinates.

2.4.2 Appendix II: Computational efficiency of BIM

We hereby make a few considerations about the computational efficiency of the Boundary Integral Method. We focus in particular on the simulation reported in figure 2.8a for $\lambda = 10$, which represents well a typical simulation. In Figure 2.26 we show the time spent in every routine of the code. First of all, the total time of the simulation is ≈ 23 s. Interestingly, most of the time is spent to build the single and double layer operators (≈ 14 s) and not to solve the linear system. Even more surprising, a considerable amount of time (≈ 7.5 s) is spent to compute the (analytically known!) Green's functions. This is because of the complexity of the Green's functions that include elliptic integrals.

The consideration that we make are general to most of the simulation that we have performed. The only exception is that, when the geometry is extremely complicated, the remesh algorithm can take a significant amount of computational time although it never exceeds 20% of the total duration of the simulation.

Droplet breakup in simple domains Part I

3 The stability of a rising droplet: an inertialess non-modal growth mechanism

G. Gallino¹, L. Zhu^{1,2,3} and F. Gallaire¹

¹Laboratory of Fluid Mechanics and Instabilities, EPFL, CH1015 Lausanne, Switzerland

²Linné Flow Centre and Swedish e-Science Research Centre (SeRC), KTH Mechanics, SE 10044 Stockholm Sweden

³Department of Mechanical and Aerospace Engineering, Princeton University, NJ 08544, USA

Journal of Fluid Mechanics, 786 (2016): R2.

Prior modal stability analysis [4] predicted that a rising or sedimenting droplet in a viscous fluid is stable in the presence of surface tension no matter how small, in contrast to experimental and numerical results. By performing a non-modal stability analysis, we demonstrate the potential for transient growth of the interfacial energy of a rising droplet in the limit of inertialess Stokes equations. The predicted critical capillary numbers for transient growth agree well with those for unstable shape evolution of droplets found in the direct numerical simulations of [6]. Boundary integral simulations are used to delineate the critical amplitude of the most destabilizing perturbations. The critical amplitude is negatively correlated with the linear optimal energy growth, implying that the transient growth is responsible for reducing the necessary perturbation amplitude required to escape the basin of attraction of the spherical solution.

3.1 Introduction

The instability of capillary interfaces has long been an intriguing topic in fluid mechanics. Perhaps one of the earliest investigated interfacial instability phenomena is the Rayleigh-Taylor instability, where a denser fluid located above a lighter one protrudes into the latter due to any arbitrary small perturbation of the initially flat interface. However, this protrusion is not always observed when a droplet rises or sediments into another density-contrasted

Chapter 3. The stability of a rising droplet: an inertialess non-modal growth mechanism

fluid. According to [67] and [54], a spherical translating droplet is a solution of this problem in the Stokes regime, regardless of the presence or magnitude of the surface tension. What remains unknown, however, is the existence of other equilibrium shapes of the droplet and the influence of surface tension on the stability of the spherical solution.

Experiments were conducted by [4] to examine this issue. Two patterns of shape instability were observed: depending on the viscosity ratio λ , a protrusion or an indentation at the rear of droplet was seen to grow with time. [4] also performed a linear stability analysis assuming that the droplet underwent small deformations. A linear operator depending on the viscosity ratio λ and capillary number Ca (inversely scaling with the surface tension) was derived which governs the linearised droplet shape evolution. It was found that, irrespective of the value of Ca , i.e. even for arbitrary small surface tension, the eigenvalues of the operator had negative real part, pointing to a linearly stable shape. The authors recognized that this linear stability study contradicted their experiments showing instabilities with finite surface tension; Direct numerical simulations (DNS) [6] also reported the unstable shape evolution of slightly disturbed droplets in the presence of sufficient surface tension ($Ca < 10$). Recent numerical work has examined the effect of surfactants [68] and viscoelasticity [69] on this scenario.

The contradiction between the theory and experiments/DNS is somewhat reminiscent of the case of the fingering instability of a film flowing down an inclined plane: the experimentally-measured [70, 71] critical inclination angle triggering instability was found to be well below that obtained from the linear theory. [72] discovered that the traditional spectrum analysis failed to capture the short-time but significant energy amplification of the perturbations near the contact line. They pinpointed the missing mechanism by performing a so-called non-modal analysis, borrowed from the transient growth theory founded and developed in the early 1990s for hydrodynamic stability analysis [25, 73, 74], to identify and interpret the short-time energy amplification.

The non-modal tools of stability theory have been used to explain the discrepancies between the theoretically computed critical Reynolds number and the experimentally-observed counterpart in a variety of wall-bounded shear flows [75]. The traditional eigenvalue analysis as also used in [4], i.e. the so-called modal approach, can sometimes fail to interpret real flow dynamics as the spectrum of the linear operator only dictates the asymptotic fate of the perturbations *without* considering their *short-term* dynamics [26]. The non-modal analysis, in contrast, is able to capture the short-time perturbation characteristics and determine the most dangerous initial conditions leading to the optimal energy growth. In addition to its great success in the traditional hydrodynamic stability analysis, it has been also used to elucidate complex flow instability problems including capillary interfaces [76], thermal-acoustic interactions [77, 78] and viscoelasticity [79].

In this paper, we perform a non-modal analysis to investigate the shape instability of a rising droplet in an ambient fluid, neglecting inertial effects. After introducing the linearised equations and operator in Sec. 3.2 and the non-modal approaches in Sec. 3.3, we demonstrate the

existence of transient growth and predict the critical capillary numbers required for instability to become possible in Sec. 3.4. In Sec. 3.5, we conduct in-house DNS to compute the nonlinear shape evolutions of the droplets initiated with the linear optimal perturbations and identify the minimal amplitudes leading eventually to instability. We further analyse the relationship between the optimal growth and the critical amplitude of perturbation. We finally examine how the instability pattern is related to the viscosity ratio and propose a phenomenological explanation in Sec. 3.6.

3.2 Governing equations and linearisation

We study the dynamics of a buoyant droplet rising in an ambient fluid in the Stokes regime. The droplet is assumed to be axisymmetric and the axis is along the z direction with gravity $\mathbf{g} = -g\mathbf{e}_z$. The two Newtonian immiscible fluids, one carrying the droplet (fluid 2), and the other constituting the droplet (fluid 1) are characterized by different densities $\rho_2 > \rho_1$, inducing (without loss of generality) an upward migration of the droplet. Likewise, their viscosities are μ_2 and μ_1 respectively, with a ratio $\lambda = \mu_1/\mu_2$. The interface between the two fluids has a uniform and constant surface tension coefficient γ . The undeformed state of the droplet is a sphere of radius a and terminal velocity $U_{\text{ter}} = \frac{a^2 g (\rho_2 - \rho_1)}{\mu_2} \frac{1 + \lambda}{3(1 + 3\lambda/2)}$ [24]. We use a and U_{ter} as the reference length and velocity scales, and $\mu_2 U_{\text{ter}}/a$ as the reference scale for p and σ , the modified pressure (removing the hydrostatic part) and the corresponding stress tensor respectively [16]. Hence, the governing equations for the non-dimensional velocity and pressure field inside the droplet (\mathbf{u}_1, p_1) and that outside the droplet (\mathbf{u}_2, p_2) are written as

$$\begin{aligned} \nabla \cdot \mathbf{u}_1 &= 0, -\nabla p_1 + \lambda \nabla^2 \mathbf{u}_1 = 0, \\ \nabla \cdot \mathbf{u}_2 &= 0, -\nabla p_2 + \nabla^2 \mathbf{u}_2 = 0, \end{aligned} \quad (3.1)$$

where the velocity is zero at infinity and the boundary conditions on the interface are

$$\begin{aligned} \mathbf{u}_1 &= \mathbf{u}_2, \\ \sigma_2 \cdot \mathbf{n} - \sigma_1 \cdot \mathbf{n} &= [\nabla_s \cdot \mathbf{n} / \text{Ca} + 3z(1 + 3\lambda/2) / (1 + \lambda)] \mathbf{n}. \end{aligned} \quad (3.2)$$

Here, \mathbf{n} is the unit normal vector pointing from the interface towards the carrier fluid and $\text{Ca} = \mu_2 U_{\text{ter}}/\gamma$ is the capillary number indicating the ratio of the viscous effect with respect to the surface tension effect.

Following [4], the interface of an axisymmetric droplet undergoing small deformation can be expressed in polar coordinates as

$$R(\theta) = 1 + \delta \sum_{n=2}^{\infty} (2n+1) f_n P_n(\cos\theta), \quad (3.3)$$

where θ is the polar angle measured from the rear of droplet, $R(\theta)$ is the polar distance (see figure 7.1), δ indicates the amplitude of the deformation, the P_n are the n th-order Legendre

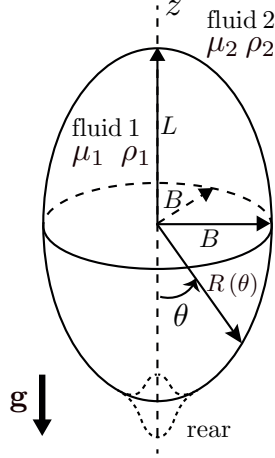


Figure 3.1 – An axisymmetric droplet rising in the quiescent fluid, along the axial (z) direction. The fluid inside and outside is labelled as fluid 1 and fluid 2 respectively, so as their dynamic viscosities (μ_1, μ_2) and densities (ρ_1, ρ_2). The polar coordinates $R(\theta)$ are used to represent its shape, where θ is measured from its rear stagnation point. L and B is the axis length along the revolution axis and orthogonal directions.

polynomials and the f_n are the corresponding coefficients. The first two terms P_0 and P_1 are removed such that the volume of the droplet is conserved and its centroid stays at the origin [4]. To advance the interface, the kinematic condition $\partial R(\theta, t)/\partial t = \mathbf{u}(\theta, t) \cdot \mathbf{n}$ is applied.

Following [4] and linearising the governing equations and truncating the series expansion, the evolution of the droplet can be obtained by solving a system of ordinary differential equations,

$$d\mathbf{f}/dt = \mathbf{A}\mathbf{f}, \quad (3.4)$$

where the shape coefficient $\mathbf{f} = (f_2, f_3, \dots, f_{m+1})^T$ is a truncated vector and \mathbf{A} is an $m \times m$ matrix depending on λ and Ca . It should be noted that the shape of the droplet can be expressed by a unique series of coefficients $\mathbf{f}\delta$ and vice versa; for a certain \mathbf{f} , the effective shape varies significantly with the amplitude and sign of δ . For the truncation of \mathbf{f} we use $m = 1000$ throughout our study: extensive tests using larger values of m confirm that our results are independent of this truncation level.

3.3 Non-modal analysis: Theory

As shown by the modal analysis of [4], the operator \mathbf{A} has a stable spectrum with all of its eigenvalues having negative real parts, irrespective of the magnitude of the surface tension, as long as the capillary number is finite. This modal analysis predicts the long-term behaviour of the disturbance but in the short-term limit it is only valid if the linear operator \mathbf{A} is normal, i.e. its eigenvectors are orthogonal. In the case of a non-normal operator, even though

the amplitudes of all eigenmodes decay exponentially, their nonorthogonality can lead to a transient energy growth over a short time. We indeed found that \mathbf{A} was non-normal. The optimal growth G^{\max} of the initial energy (L_2 norm) over a chosen time interval $[0, T]$ [75] is

$$G^{\max}(T) = \max_{\mathbf{f}(0)} \left[G(T) = \frac{\|\mathbf{f}(T)\|_2}{\|\mathbf{f}(0)\|_2} \right] = \|\exp(T\mathbf{A})\|_2, \quad (3.5)$$

where $\mathbf{f}(0)$ denotes the initial perturbation. $G^{\max}(T)$ represents the maximum amplification of the initial energy at a target time (the so-called horizon) T where the optimization has been performed over all possible perturbations $\mathbf{f}(0)$. The optimal initial perturbation for horizon T will be denoted $\mathbf{f}_{[T]}^{\text{opt}}(0)$. The quantity G^{\max} is the envelope of all individual gain profiles, indicating the presence of transient growth when $G^{\max}(T) > 1$ for some T .

Compared with the L_2 norm in equ. 3.5, it is natural to introduce a physically-driven form of energy, designed for the physical problem at hand. In the present study, the variation of surface area of the droplet ΔS is chosen as the target energy, since $\gamma\Delta S$ indicates the interfacial energy throughout the evolution: ΔS is zero only for a spherical droplet and is positive otherwise. The surface area is $S = 2\pi \int_0^\pi R^2 \sin\theta \sqrt{1 + [(1/R)(\partial R/\partial\theta)]^2} d\theta$. Assuming small deformation and thus $\frac{1}{R} \frac{\partial R}{\partial\theta} \ll 1$, a Taylor expansion yields

$$S = 2\pi \int_0^\pi R^2 \sin\theta \left(1 + \frac{1}{2R^2} \left(\frac{\partial R}{\partial\theta} \right)^2 \right) d\theta. \quad (3.6)$$

Plugging 3.3 into 3.6, the area variation $\Delta S = S - 4\pi$ is found to be

$$\Delta S / (2\pi\delta^2) = \mathbf{f}^T \mathbf{M}_{\Delta S} \mathbf{f} + o(\delta^2), \quad (3.7)$$

where $\mathbf{M}_{\Delta S}$ is the so-called weight matrix [26] of size $m \times m$, with entries

$$\mathbf{M}_{\Delta S}(i, j) = 2\delta_{ij}^K (2i+1) + \frac{1}{2} (2i+1)(2j+1) \int_0^\pi P'_i(\cos\theta) P'_j(\cos\theta) \sin^3\theta d\theta. \quad (3.8)$$

The optimal growth of ΔS can now be defined as

$$G_{\Delta S}^{\max}(T) = \max_{\mathbf{f}(0)} \left[G_{\Delta S}(T) = \frac{\sqrt{\Delta S(T)}}{\sqrt{\Delta S(0)}} \right] = \max_{\mathbf{f}(0)} \left[G_{\Delta S}(T) = \frac{\sqrt{\mathbf{f}^T \mathbf{M}_{\Delta S} \mathbf{f}}}{\sqrt{\mathbf{f}^T(0) \mathbf{M}_{\Delta S} \mathbf{f}(0)}} \right]. \quad (3.9)$$

By Cholesky decomposition $\mathbf{M}_{\Delta S} = \mathbf{F}^T \mathbf{F}$, the above equation is formulated as

$$G_{\Delta S}^{\max}(T) = \max_{\mathbf{f}(0)} \left[G_{\Delta S}(T) = \frac{\|\mathbf{F}\mathbf{f}(T)\|_2}{\|\mathbf{F}\mathbf{f}(0)\|_2} \right]. \quad (3.10)$$

In a similar way to how the asymptotic stability ($t \rightarrow \infty$) is determined by the eigenvalues of the evolution operator \mathbf{A} , the maximum instantaneous growth rate of the perturbation energy at $t = 0^+$ can be determined algebraically, expanding the matrix exponential $\exp(t\mathbf{A}) \approx I + t\mathbf{A}$

Chapter 3. The stability of a rising droplet: an inertialess non-modal growth mechanism

at $t = 0^+$. The growth rate of the excess area ΔS is then

$$\frac{1}{\Delta S} \frac{d\Delta S}{dt} \Big|_{t=0^+} = \frac{\mathbf{f}^T(0) [\mathbf{A}^T \mathbf{F}^T \mathbf{F} + \mathbf{F}^T \mathbf{F} \mathbf{A}] \mathbf{f}(0)}{\mathbf{f}^T(0) \mathbf{F}^T \mathbf{F} \mathbf{f}(0)}. \quad (3.11)$$

By introducing $\mathbf{h} = \mathbf{F} \mathbf{f}(0)$, the maximum growth rate of ΔS is formulated as

$$\max_{\mathbf{h}} \frac{1}{\Delta S} \frac{d\Delta S}{dt} \Big|_{t=0^+} = \max_{\mathbf{h}} \frac{\mathbf{h}^T [\mathbf{F} \mathbf{A} \mathbf{F}^{-1} + (\mathbf{F} \mathbf{A} \mathbf{F}^{-1})^T] \mathbf{h}}{\mathbf{h}^T \mathbf{h}}, \quad (3.12)$$

which becomes the optimization of a Rayleigh quotient with respect to \mathbf{h} . Because $\mathbf{F} \mathbf{A} \mathbf{F}^{-1} + (\mathbf{F} \mathbf{A} \mathbf{F}^{-1})^T$ is a symmetric operator, the maximum is given by its largest eigenvalue,

$$\max \frac{1}{\sqrt{\Delta S}} \frac{d\sqrt{\Delta S}}{dt} \Big|_{t=0^+} = s_{\max} \left[\frac{1}{2} (\mathbf{F} \mathbf{A} \mathbf{F}^{-1} + (\mathbf{F} \mathbf{A} \mathbf{F}^{-1})^T) \right], \quad (3.13)$$

where $s_{\max}[\cdot]$ denotes the largest eigenvalue. This maximum instantaneous growth rate is commonly called the numerical abscissa [80], which is closely linked to the numerical range $W_{\Delta S}(\mathbf{A}, \mathbf{F})$ defined as the set of all Rayleigh quotients,

$$W_{\Delta S}(\mathbf{A}, \mathbf{F}) \equiv \{z : z = (\mathbf{F} \mathbf{A} \mathbf{F}^{-1} \mathbf{p}, \mathbf{p}) / (\mathbf{p}, \mathbf{p})\}. \quad (3.14)$$

The numerical range is the convex hull of the spectrum for a normal operator (and is therefore always in the stable half plane $z_r < 0$ for a stable operator), but can extend significantly to even protrude into the unstable half-plane $z_r > 0$ for stable non-normal operators. Its maximum protrusion is equal to the numerical abscissa and thus determines the maximum energy growth rate at $t = 0^+$.

3.4 Non-modal analysis: results

3.4.1 Transient growth and numerical range

In figure 3.2, we show the optimal growth of the interfacial energy $G_{\Delta S}^{\max}(T)$ for viscosity of ratios $\lambda = 0.5$ and 5, varying the capillary number Ca . The threshold value of Ca to yield transient growth is between 4 and 5, in accordance with the rightmost boundary of the numerical range (see inset) depicted in the complex plane (z_r, z_i). The boundary is almost tangent to $z_r = 0$ at $Ca \approx 4.9$ for $\lambda = 0.5$ and $Ca \approx 4.53$ for $\lambda = 5$ representing the critical capillary number Ca_c above which the maximum energy growth rate at $t = 0$, $\max_{\mathbf{f}(0)} \frac{1}{\sqrt{\Delta S}} \frac{d\sqrt{\Delta S}}{dt} \Big|_{t=0^+}$, is positive, guaranteeing transient growth.

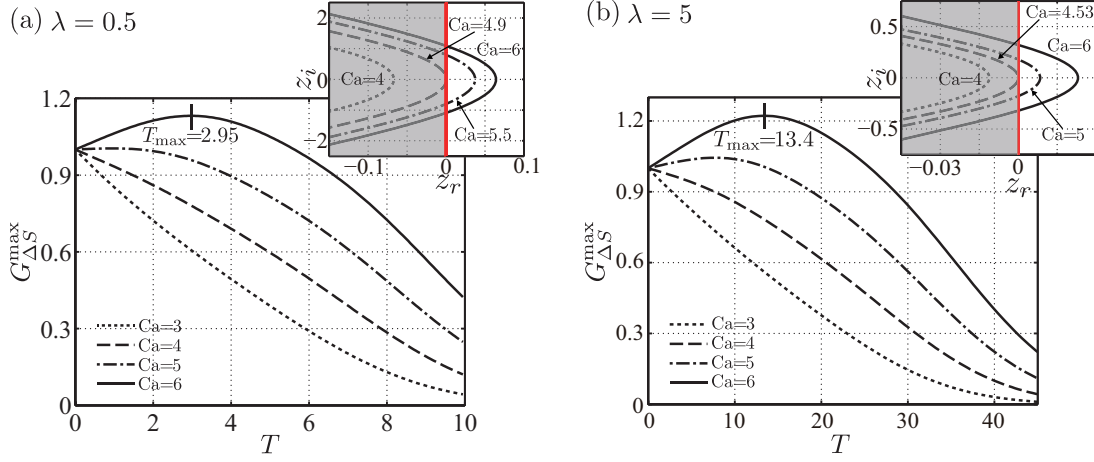


Figure 3.2 – The optimal growth of the interfacial energy $G_{\Delta S}^{\max}(T)$ versus the nondimensional time T , for viscosity ratio $\lambda = 0.5$ (a) and $\lambda = 5$ (b); for each case, four capillary number Cas are shown and for the highest Ca , the time T_{\max} corresponding to the peak energy growth is marked. The inset shows the boundary of the numerical range (z_r, z_i) .

3.4.2 Linear growth and shape evolutions

Non-modal analysis not only predicts the maximum energy growth over a particular time interval, but also provides the optimal perturbation, i.e. the initial shape coefficients $\mathbf{f}_{[T]}^{\text{opt}}(0)$ that ensure the optimal gain at horizon T . Figure 3.3 depicts the individual energy gains $G_{\Delta S}$ for four optimal initial conditions $\mathbf{f}_{[T]}^{\text{opt}}(0)$ corresponding to $T = 0.2, 1.05, 3.95$ and 5.45 , with $\lambda = 0.5$ and $Ca = 6$. Their gain profiles are tangent to $G_{\Delta S}^{\max}(T)$ at $t = T$. The optimal perturbation targeting $T = T_{\max} = 2.95$ coincides with the optimal growth $G_{\Delta S}^{\max}$ at its peak.

Assuming small deformation amplitude and integrating equ. 3.4 in time, the linear shape evolution is readily reconstructed for the droplets with the four optimal initial conditions, depicted in figure 3.3, at time $t = 0$ (dashed), $2.5, 5, 7.5, 10$ (light solid) and the target time $t = T$ (solid); the evolution is shown for negative/positive δ in (a)/(c). For both signs, the initial perturbation is mainly introduced near the tail ($\theta = 0$) of the droplet where the interface is respectively flattened for $\delta < 0$ and stretched for $\delta > 0$ while the front part of the droplet remains spherical. In accordance with the modal analysis implying a linearly stable evolution, the perturbations eventually decay and the droplets finally recover a spherical shape.

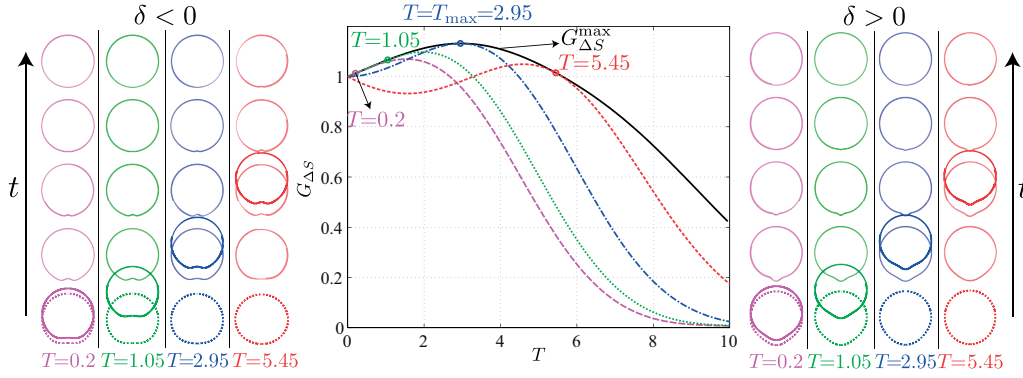


Figure 3.3 – Linear growth $G_{\Delta S}$ of the interfacial energy of the droplets with an optimal initial perturbation $\mathbf{f}_{[T]}^{\text{opt}}(0)$ for the target times $T = 0.2, 1.05, 2.95$ and 5.45 ; the solid curve indicates the optimal growth $G_{\Delta S}^{\max}(T)$ and it reaches its peak at $T = T_{\max} = 2.95$. The linear shape evolution of the perturbations are shown for negative and positive δ , on the left and right panel respectively.

3.5 Nonlinear analysis

3.5.1 Nonlinear energy growth and shape evolution using DNS

As the droplets deform more and more on increasing the initial perturbation amplitude, nonlinearities become significant and the droplet evolution cannot be adequately described by the linearised equations. We resort to DNS to address the non-linear dynamics using a three-dimensional axisymmetric boundary integral implementation, following the standard approach of [6].

We focus on the droplets of $\lambda = 0.5$ and $\text{Ca} = 6$ with the optimal perturbation $\mathbf{f}_{[T_{\max}]}^{\text{opt}}(0)$ achieving the peak of the optimal energy growth $G_{\Delta S}^{\max}$ at T_{\max} . Two slightly different magnitudes of perturbation $\delta = 0.0496, 0.0505$ are chosen for the positive δ and similarly $\delta = -0.122, -0.126$ for the negative case. Their energy growth $G_{\Delta S}(t) = \sqrt{\frac{\Delta S(t)}{\Delta S(0)}}$ is plotted in figure 3.4a, together with the linear counterpart $G_{\Delta S}(t)$ using equ. 3.7. The linear and non-linear energy growth share the same trend in the initial growing phase $t < 3$, but differ as the former is approximated by a truncated Taylor expansion. For the two values of δ with the same sign but slightly different magnitude, the energy growth curves almost collapse before reaching their peaks at $t \approx 4$, but diverge afterwards; $G_{\Delta S}$ decays for the smaller magnitudes $\delta = -0.122$ and $\delta = 0.0496$ indicating stable evolutions but maintains a sustained value around 1 for larger initial amplitudes $\delta = -0.126$ and $\delta = 0.0505$, implying the onset of instability.

The shape evolutions of droplets are shown in figure 3.4b. For $\delta = -0.122$ and -0.126 , no significant difference is observed for $0 < t < 7.5$: an inward cavity develops at the rear and sharpens; it is subsequently smoothed out and disappears for $\delta = -0.122$ while it keeps

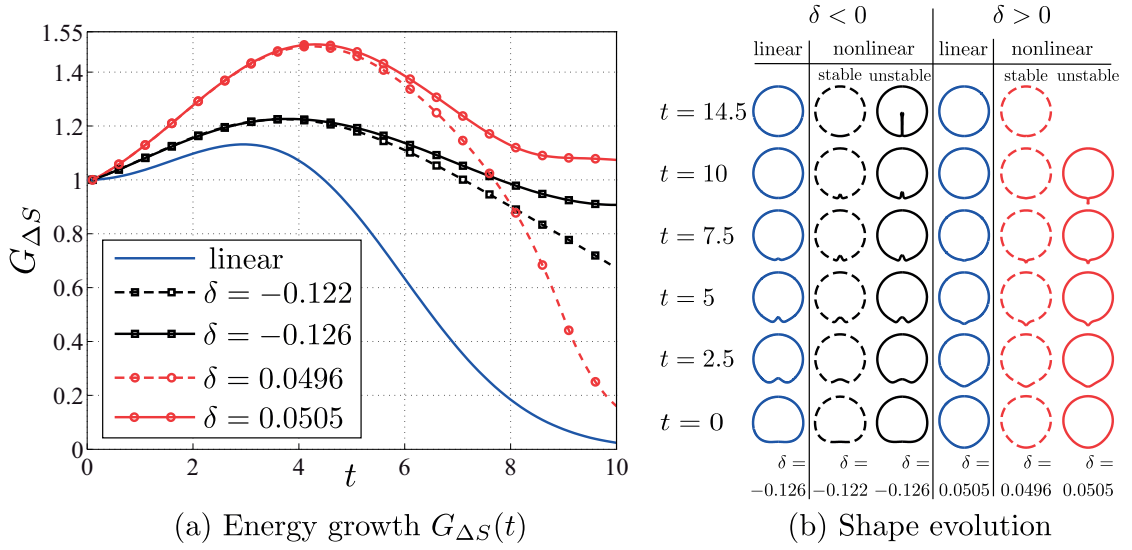


Figure 3.4 – (a): Nonlinear energy growth $G_{\Delta S}$ of the droplets with the optimal perturbation $\mathbf{f}_{[T]}^{\text{opt}}(0)$ for the target time $T = T_{\text{max}} = 2.95$; the solid curve indicates the linear energy growth. For positive δ , $G_{\Delta S}$ of droplets with $\delta = 0.0496$ and 0.0505 are shown, the former/latter being stable/unstable; for negative δ , the chosen value leading to stable and unstable evolution is $\delta = -0.122$ and $\delta = -0.126$ respectively. (b): The shape evolutions of the corresponding droplets.

growing to form a long indentation for $\delta = -0.126$. These two values of δ bound a threshold initial amplitude required to excite nonlinear instabilities. A similar trend is found for positive values of δ , while the instability arises through the formation of a dripping tail.

It becomes natural to introduce δ_c , the critical magnitude of the perturbation above/below which the evolution of the drop is unstable/stable. Parametric computations are conducted to identify δ_c^\pm within a confidence interval (for instance $\delta_c^+ \in [0.0496, 0.0505]$ and $\delta_c^- \in [-0.122, -0.126]$) as in figure 3.4). Searching in both directions, the critical amplitude is then defined as $\delta_c = \min(|\delta_c^+|, |\delta_c^-|)$. When $\lambda = 0.5$ and $\text{Ca} = 6$, $|\delta_c^-| > |\delta_c^+|$, implying that the instability tends to favour an initially stretched tail with respect to a flattened bottom; otherwise when $\lambda = 5$ the situation reverses ($|\delta_c^-| < |\delta_c^+|$), as discussed in next section.

3.5.2 Critical amplitude of the perturbation δ_c

Following the description of the previous paragraph, the critical deformation amplitude $\delta_c(T)$ can be determined for any targeting time T and associated optimal initial perturbation $\mathbf{f}_{[T]}^{\text{opt}}(0)$. The critical deformation amplitude $\delta_c(T)$ is plotted in figure 3.5 for $\text{Ca} = 6$ and both $\lambda = 0.5$ and $\lambda = 5$, together with the optimal growth $G_{\Delta S}^{\text{max}}$. The critical deformation amplitude δ_c is negatively correlated with $G_{\Delta S}^{\text{max}}$ and corresponds to a target time T slightly larger than T_{max} where the peak transient growth is reached. This shows that the transient growth reduces the threshold non-linearity needed to trigger instabilities and consequently the critical magnitude

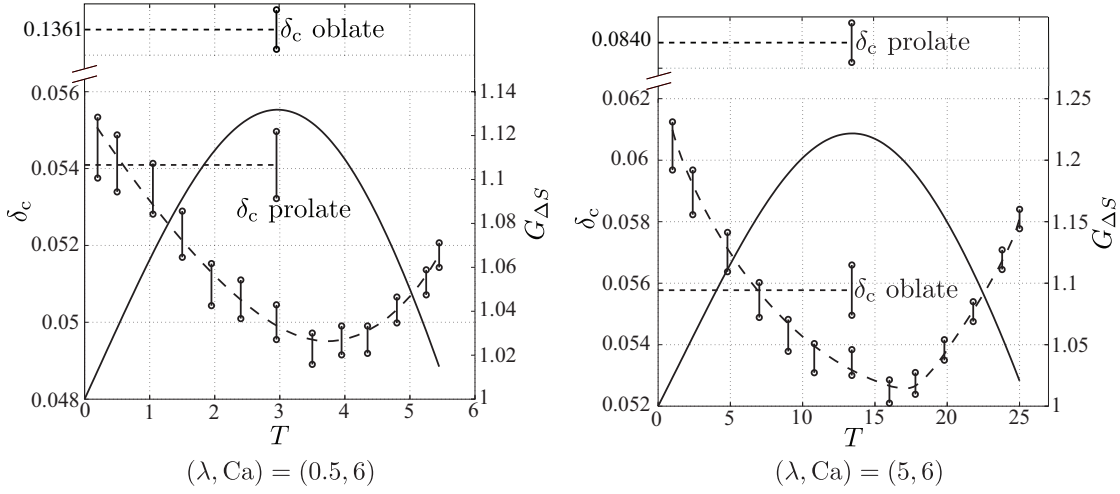


Figure 3.5 – The critical perturbation magnitude δ_c for: (a): $(\lambda, Ca) = (0.5, 6)$ and (b): $(\lambda, Ca) = (5, 6)$. The upper and lower limits of δ_c (measured by the left scale) are plotted versus the target time T , with a curve fitted to show the trend. Accordingly, the linear energy growth $G_{\Delta S}$ (measured by the right scale) is provided. δ_c^P and δ_c^O is the critical magnitude for an initially prolate and oblate respectively.

of the initial perturbation.

We also determined the critical amplitude $\delta_c^{P/O}$ for an initially prolate (P) / oblate (O) ellipsoidal droplet to be unstable, as reported in figure 3.5. When the fluid inside the droplet is less viscous than the one outside, i.e. $\lambda < 1$, an initially prolate droplet is more unstable, δ_c^P is less than half that of an oblate droplet δ_c^O ; the trend reverses as $\lambda > 1$. Such an observation is in agreement with the results of [6] using DNS (see fig. 11 of their paper). As expected, the minimum δ_c using the optimal perturbations is smaller than $\min(\delta_c^P, \delta_c^O)$ based on the limited family of ellipsoidal shapes.

So far, we have analysed the critical amplitude δ_c of perturbations exhibiting transient energy growth. We would like to know how it varies as the transient growth decreases and even disappears as it is suppressed by high surface tension. In addition to $Ca = 6$, the time-dependence of δ_c is shown in figure 3.6 for $Ca = 4, 5$. As expected, δ_c increases with decreasing Ca , by a factor of approximately 3, varying from the highest to the lowest Ca . With respect to T , δ_c varies non-monotonically for $Ca = 5, 6$ showing transient growth. In the absence of transient growth, like for $Ca = 4$, δ_c increases with T monotonically. Indeed, without transient growth, the energy decays monotonically and $T_{\max} = 0$, hence the minimum δ_c appears at $T \approx 0$.

3.6 Conclusion and discussions

In this paper, we have performed non-modal analysis and DNS to investigate the shape instabilities of an inertialess rising droplet which tends to recover the spherical shape, the

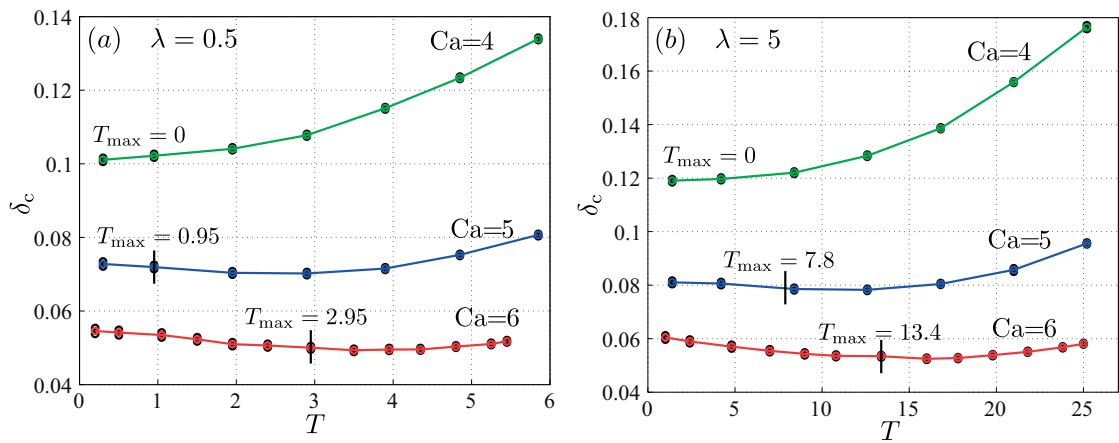


Figure 3.6 – Akin to figure 3.5, adding δ_c of two smaller Ca s for (a): $\lambda = 0.5$ and (b): $\lambda = 5$.

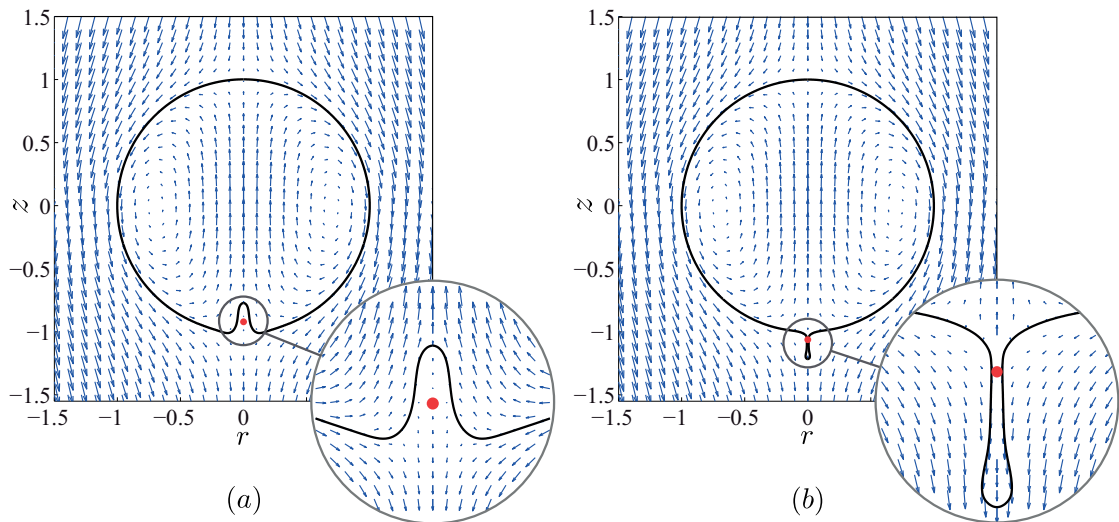


Figure 3.7 – The flow field co-moving with the droplet, using the optimal initial coefficient $\mathbf{f}_{[T_{\max}]}^{\text{opt}}(0)$, when $(\lambda, Ca) = (0.5, 6)$, (a): $\delta = -0.126$ and (b): $\delta = 0.0505$. The red dot indicates the stagnation point of the flow.

Chapter 3. The stability of a rising droplet: an inertialess non-modal growth mechanism

attractor solution, due to surface tension. For sufficiently low surface tension, transient growth of the interfacial energy arises and leads to a bypass transition. This reduces the initial disturbance amplitude required to trigger instability, hence significantly decreasing the threshold magnitude of perturbation for the droplet to escape the basin of attraction. This magnitude is negatively correlated to the optimal growth of the interfacial energy.

We now compare our results with the work of [6] who employed DNS to identify the critical capillary number Ca_c leading to shape instabilities of an initially prolate or oblate ellipsoidal sedimenting droplet; the magnitude of perturbation is $\Delta = \frac{L-B}{L+B}$ (see figure 7.1). For their lowest magnitude $|\Delta| = 1/21$ considered, $Ca_c \in (4, 5)$ for $\lambda = 0.1, 0.5$ and 5 , indeed close to our prediction: $Ca_c \approx 5.42, 4.9$ and 4.53 respectively for the same λ . Additionally, [6] observed that for a viscosity ratio $\lambda < 1/\lambda > 1$, the first unstable pattern appears as a protrusion/indentation developing near the tail of the droplet that is initially a prolate/oblate. The trend holds in our case even though we search over all possibilities for the most 'dangerous' initial perturbation instead of using an initially ellipsoidal shape. This is also reflected from the initial shapes: as $\lambda < 1/\lambda > 1$, the optimal shape shares a common feature with an oblate/prolate ellipsoid, namely its rear interface is compressed/stretched.

To explain the dependence of the instability patterns on the viscosity ratio λ , let us focus on the velocity field near the tail of the droplet (see figure 3.7), where the flow resembles a uniaxial extensional flow, drawing the tip into the drop on the top side and pulling it outwards on the other side. We suggest that this imbalance induces the onset of the shape instability. The internal (respectively external) viscous force on the tip is $\mu_1 \partial u_z^{\text{tip}} / \partial z$ (respectively $\mu_2 \partial u_z^{\text{tip}} / \partial z$). When $\mu_1 < \mu_2$, i.e. $\lambda < 1$, the external viscous effect overcomes the internal one, hence the perturbation tends to be stretched outward to form a protrusion; otherwise, when $\lambda > 1$, it is prone to be sucked inwards to form an indentation.

Developed originally for hydrodynamic stability analysis, non-modal tools have here demonstrated the predictive capacity for the inertialess shape instabilities of capillary interfaces. This work might stimulate the application of non-modal analysis for complex multiphase flow instabilities even at low Reynolds number.

Acknowledgements

L.Z. thanks Francesco Viola for the helpful discussions. We thank the anonymous referee for pointing out an incorrect coefficient in our previous derivation. Computer time from SCITAS at EPFL is acknowledged, and the European Research Council is acknowledged for funding the work through a starting grant (ERC SimCoMiCs 280117).

4 Edge states control droplet breakup in subcritical extensional flows

G. Gallino¹, T. M. Schneider² and F. Gallaire¹

¹Laboratory of Fluid Mechanics and Instabilities, EPFL, 1015 Lausanne, Switzerland

²Emergent Complexity in Physical Systems Laboratory, EPFL, 1015 Lausanne, Switzerland

Accepted in *Physical Review Fluids*.

A fluid droplet suspended in an extensional flow of moderate intensity may break into pieces, depending on the amplitude of the initial droplet deformation. In subcritical uniaxial extensional flow the nonbreaking base state is linearly stable, implying that only a finite-amplitude perturbation can trigger breakup. Consequently, the stable base solution is surrounded by its finite basin of attraction. The basin boundary, which separates initial droplet shapes returning to the non-breaking base state from those becoming unstable and breaking up, is characterized using edge tracking techniques. We numerically construct the edge state, a dynamically unstable equilibrium whose stable manifold forms the basin boundary. The edge state equilibrium controls if the droplet breaks and selects a unique path towards breakup. This path physically corresponds to the well-known end-pinching mechanism. Our results thereby rationalize the dynamics observed experimentally [H. A. Stone and L. G. Leal, *J. Fluid Mech.* 206, 223 (1989)].

4.1 Introduction

The shape of a droplet in low-Reynolds-number flows results from two competing effects, the viscous forces stretching the droplet and the surface tension forces reducing its deformation in order to minimize the droplet surface area. When the ratio between viscous forces and surface tension forces, defined as the capillary number Ca , is large, the droplet may deform until breaking into smaller droplets [81, 66, 82].

Taylor was the first to systematically study this phenomenon, by placing a liquid drop in flow fields generated by counter-rotating rollers [1]. Imposing a hyperbolic flow, he observed that when the capillary number exceeds a critical value Ca_{crit} , the droplet always breaks. Consistent results were later obtained in experimental [83, 84] and numerical [85] studies. At the critical capillary number, the nonbreaking equilibrium state, or *base state*, undergoes a saddle-node bifurcation [86, 87] and no longer exists for $Ca > Ca_{\text{crit}}$. Interestingly, the droplet can break up even for a subcritical value of Ca , depending on its initial shape [11, 53, 5]. The dependence of the droplet stability upon the initial shape indicates the existence of a finite basin of attraction surrounding the base state. Initial droplet shapes evolving towards the base state are separated from those breaking apart by the basin boundary, a co-dimension one manifold in the state space spanned by all possible droplet shapes.

Due to the high dimensionality of the state space and the infinite number of possible initial shapes, it is challenging to characterize the basin of attraction and predict if a droplet breaks up. The situation is however analogous to other high-dimensional nonlinear dynamical systems characterized by a finite basin of attraction, such as in pipe flow and plane Couette flow, where the laminar base flow is linearly stable and a finite-amplitude perturbation is needed to trigger turbulence. In the latter cases, recent studies have demonstrated the relevance of unstable equilibrium states embedded in the basin boundary. Of specific importance are *edge states* [28, 88], unstable equilibria in the basin boundary with only a single unstable direction. These edge states are attracting for the dynamics confined to the basin boundary but unstable in the direction perpendicular to the boundary. Their significance lies in their guiding role for the transition between laminar and turbulent flows.

In this letter we show that an unstable edge state equilibrium embedded in the basin boundary of the base state governs the break-up dynamics of a droplet in a subcritical uniaxial extensional flow. In fact, the unstable direction of the edge state selects an almost unique path towards droplet breakup.

4.2 Numerical method

We consider a droplet of fluid 1 and unperturbed radius R suspended in fluid 2, the viscosity ratio between the two fluids is $\lambda = \mu_1 / \mu_2$ and the surface tension γ . The characteristic length scale of the problem is R and the velocity scale γ / μ_2 . After nondimensionalization, the axisymmetric droplet shape is expressed in cylindrical coordinates as $\mathbf{x} = [z(t, s), r(t, s)]$, with z the axial and r the radial coordinates, t the time, and $s \in [0, 1]$ the spatial curvilinear coordinate along the droplet's meridian (see figure 7.1).

The unknown interface velocity $\mathbf{u} = [u_z(t, s), u_r(t, s)]$ on a point of the interface \mathbf{x}_0 is determined by solving the Stokes equations in fluids 1 and 2. The creeping flow equations can be recast into a boundary integral equation [66, 49]. Consequently, the interface velocity is given by an integration along the droplet interface of arc length l ,

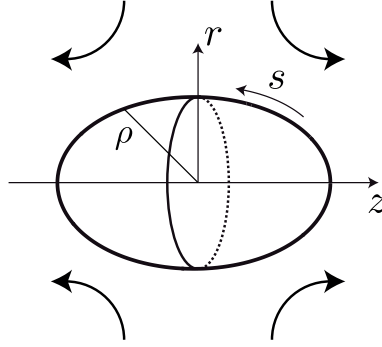


Figure 4.1 – Sketch of the axisymmetric droplet, its parametrization, and the coordinate system. The arrows indicate the direction of the extensional flow.

$$4\pi(1 + \lambda)\mathbf{u}(\mathbf{x}_0) = 8\pi\mathbf{u}_\infty - \int_0^l \mathbf{M}(\mathbf{x}, \mathbf{x}_0) \cdot \Delta\mathbf{f}(\mathbf{x}) dl(\mathbf{x}) + (1 - \lambda) \int_0^l \mathbf{u}(\mathbf{x}) \cdot \mathbf{q}(\mathbf{x}, \mathbf{x}_0) \cdot \mathbf{n}(\mathbf{x}) dl(\mathbf{x}), \quad (4.1)$$

where \mathbf{M} and \mathbf{q} are the velocity and stress Green's functions of axisymmetric Stokes flow respectively [50], \mathbf{n} is the normal vector pointing into the suspending fluid and $\Delta\mathbf{f}(\mathbf{x}) = (\nabla_s \cdot \mathbf{n})\mathbf{n}$ is the discontinuity in normal stresses scaled by γ/R . In the far field we impose vanishing pressure $p \rightarrow 0$ and the uniaxial extensional flow $\mathbf{u}_\infty = \Gamma \cdot \mathbf{x}_0$ where, in cylindrical coordinates (z, r) and omitting the θ direction,

$$\Gamma = \frac{\text{Ca}}{2} \begin{pmatrix} 2 & 0 \\ 0 & -1 \end{pmatrix}.$$

The capillary number $\text{Ca} = \mu_2 GR/\gamma$ and G are, respectively, the nondimensional and dimensional velocity gradients. The droplet interface evolves in time under the impermeability condition

$$\frac{d\mathbf{x}}{dt} = [(\mathbf{u} - \mathbf{u}_{\text{drop}}) \cdot \mathbf{n}] \mathbf{n}, \quad (4.2)$$

where \mathbf{u}_{drop} is the velocity of the center of mass of the droplet. Focusing on shape deformations, we describe the system in the frame of reference comoving with the droplet, thus enforcing z -translational symmetry [66].

Equation (4.1) is discretized using a pseudospectral scheme in which the interface coordinates $\mathbf{x}(s)$, velocity $\mathbf{u}(s)$ and normal stresses $\Delta\mathbf{f}(s)$ are represented by Legendre polynomials. For direct numerical simulations (DNS), we integrate equation (4.2) with a second-order Runge-Kutta scheme. Typically, 100 modes are sufficient for the spatial discretization and the time step is $\Delta t = 2 \times 10^{-3}$. Similar to previous studies [62, 51], we develop a Newton solver in order to find the roots of equation (4.2), which allows for the computation of unstable steady states and rigorous linear stability analysis. The code has been validated against Refs. [53, 6, 7, 89].

4.3 Results

4.3.1 Edge tracking

To follow orbits in the basin boundary and compute the edge state we adapt the edge tracking techniques used in shear flows [88] and other fields [90, 91]: We consider two slightly different initially ellipsoidal droplets for $Ca = 0.1$ and $\lambda = 1$. One labeled a_0 in figure 4.2a approaches the base state and another one, labeled b_0 , eventually breaks apart. Consequently, the two droplets, both of identical volume, define two initial conditions on either side of the basin boundary. For fixed volume, the shape of an ellipsoidal droplet is uniquely defined by the droplet half-length L , so iterative bisection in L allows to construct a pair of arbitrarily close initial conditions on opposite sides of the basin boundary. Orbits starting from those initial conditions bracket and approximate an *edge orbit* that neither returns to the base state nor evolves towards breakup but remains in the basin boundary. When the distance between the bracketing orbits becomes larger than a set threshold (usually 10^{-4} measured in the difference of surface area), the approximation of the edge orbit is refined and a new initial condition is created by bisecting between the current shapes ¹. Iterating this procedure allows us to numerically follow an edge orbit in the basin boundary for arbitrary time. Two iterations are reported in figure 4.2 with initial conditions c_0 (long-dashed) and d_0 (dashed-dotted).

After short time the edge orbit settles to a shape of constant L , indicating that a locally attracting equilibrium state in the basin boundary, the edge state, has been reached. We have verified the existence of the nonlinear edge state equilibrium by Newton iteration, reaching convergence to machine precision in a few iterations. The bracketing orbits transiently approach the edge state (shape a_1 , b_1 , c_0 and d_0), as evidenced by the low values of the residuals shown in figure 4.2b, before evolving towards breakup or approaching the base state. As expected, the growth rate of the residuals shows an exponential behavior close to the edge state and to the base state. For both bracketing orbits, the least stable eigenvalue σ_2^E of the edge state governs the attractive dynamics, while its unstable eigenvalue σ_1^E drives the dynamics when departing from it. Likewise, when the droplet approaches the stable base state, the decay of the residuals is dictated by its least stable eigenvalue σ_1^B . It is noteworthy that the exponential growth (or decay) is maintained also far from the equilibrium states.

The flow fields associated to the equilibrium states are qualitatively similar to each other (see figure 4.3a-b). Namely, the external flow induces a fluid motion along the interface toward the droplet caps, which is compensated by a recirculation along the axis driven by a pressure gradient (decreasing from the caps toward the droplet center). The equilibrium states exist when the flow along the interface is equal to the recirculating one, although they might be stable or unstable. If a slight droplet elongation increases/decreases the recirculating flow, the droplet is stable/unstable.

¹Technically, a convex combination followed by resizing to enforce volume conservation is used to interpolate between the shapes along the two previous orbits. Iterative bisection in the weight parameter of the convex combination yields a new initial condition for bracketing the orbit.

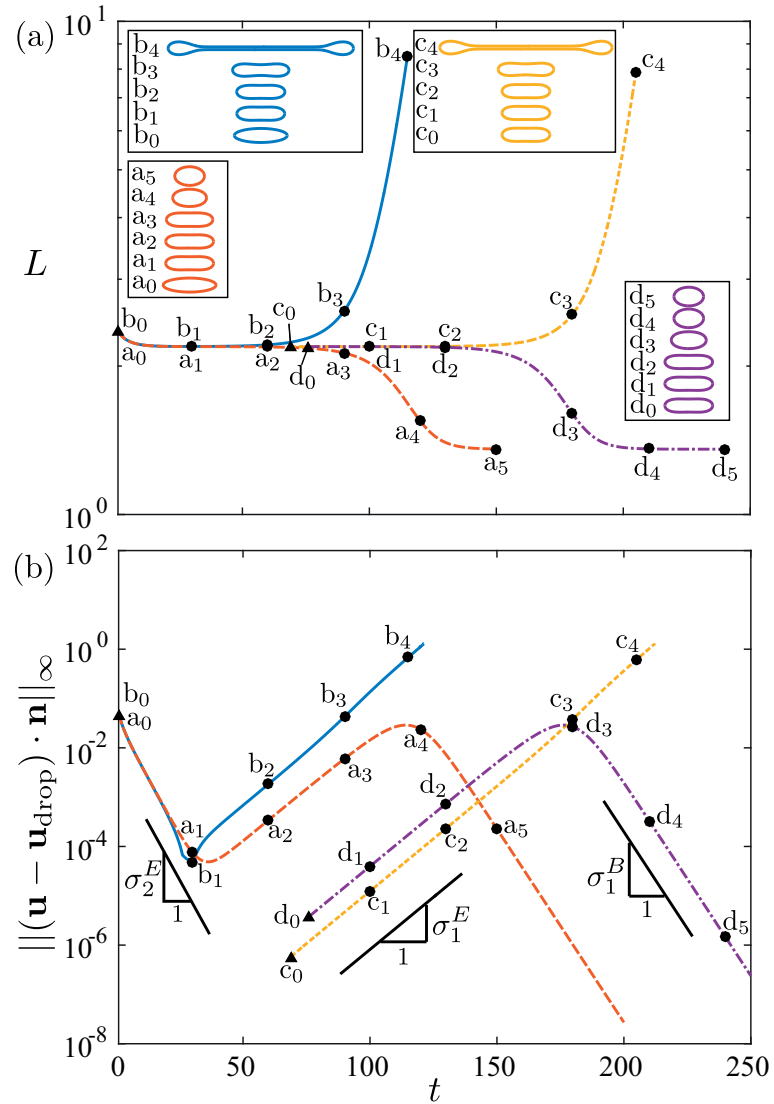


Figure 4.2 – Edge tracking orbits for $Ca = 0.1$ and $\lambda = 1$. (a) Droplet elongation versus time, the orbits reach the stable base state or break up through the end-pinching mechanism. Triangles denote the initial shapes and dots subsequent snapshots. (b) Corresponding normal velocity residuals measured in the L_{∞} norm versus time, the growth and decay rates are given by the most unstable and least stable eigenvalues of the edge state and the base state σ_1^E , σ_2^E and σ_1^B respectively.

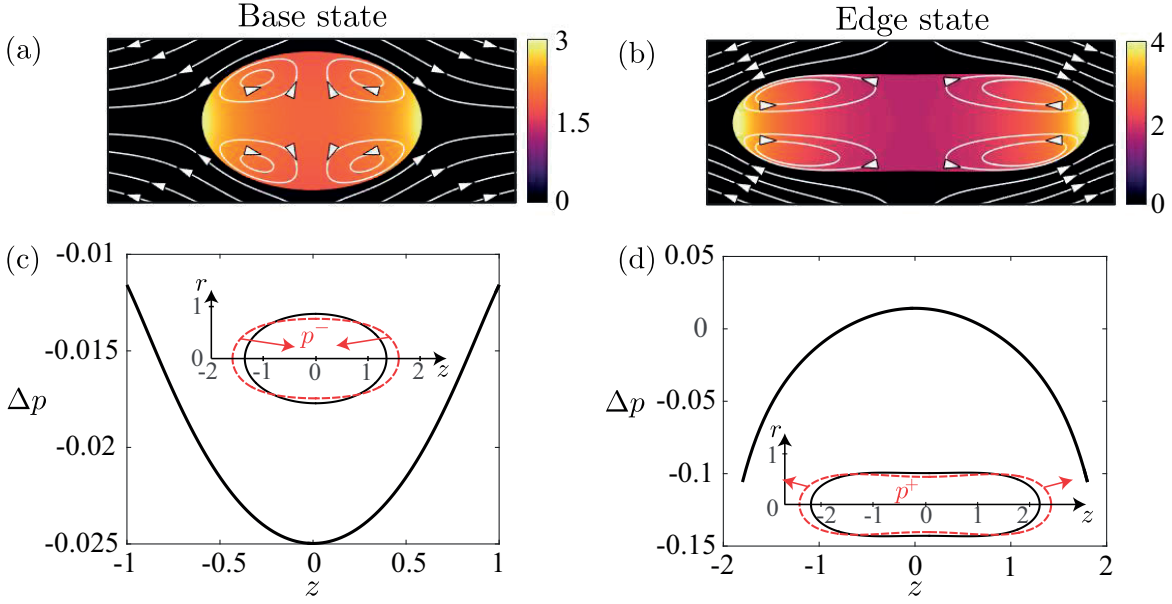


Figure 4.3 – Pressure field and velocity streamlines for the base state (a) and the edge state (b) for $Ca = 0.1$ and $\lambda = 1$. (c-d) Change in pressure along the z -axis when the base state is perturbed with its least stable eigenmode (c) and the edge state with its most unstable eigenmode (d), the insets show the shape of the base state and the edge state (solid line) and their shapes after the modes are superimposed (dashed line). The interface motion is depicted by the arrows.

When the base state is perturbed with its least stable eigenmode, the pressure along the axis decreases more in the center than at the caps (see figure 4.3c), therefore the recirculation becomes stronger due to the lower pressure in the droplet center, producing an interface displacement that restores the base state shape. When the edge state is perturbed with its most unstable eigenmode, the pressure along the axis increases in the center and decreases at the caps (see figure 4.3d), therefore the recirculation becomes weaker due to the higher pressure in the droplet center, producing an unstable droplet elongation that leads to breakup.

To demonstrate the dynamical relevance of the edge state, we consider a two dimensional cut of the state space, following [87, 92]. To this end, we project the local droplet radius $\rho(s) = \sqrt{z^2 + r^2}$ onto the second and fourth Legendre polynomials, obtaining the coefficients f_2 and f_4 . The state-space representation of the orbits in figure 4.2 is plotted in figure 4.4.

All orbits are attracted towards the edge state along its stable manifold, which forms the basin boundary. After passing close to the edge state, the orbit leaves along the one-dimensional unstable manifold. Depending on which side of the basin boundary the initial condition is located, the orbit either approaches the base state or evolves towards breakup along an almost unique path. The state-space visualization thus shows the guiding role of the edge state and its stable manifold which controls if a droplet undergoes breakup.

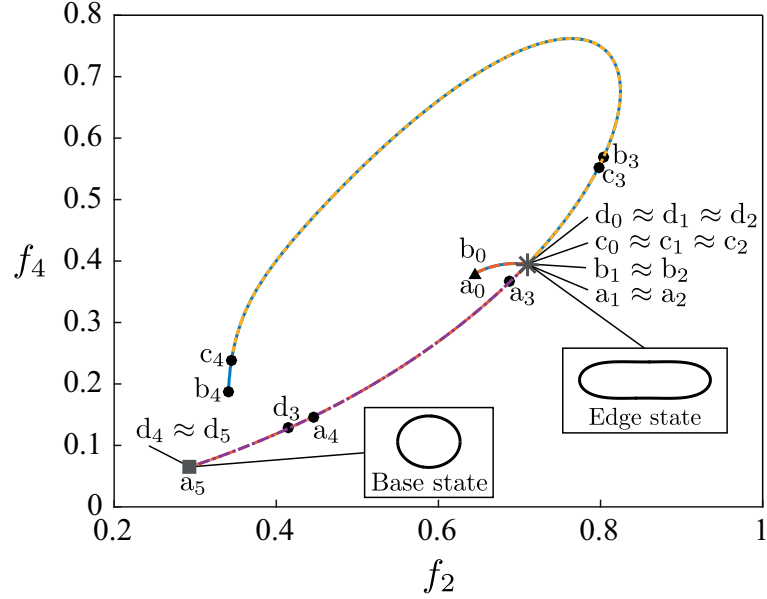


Figure 4.4 – Edge tracking orbits in state space (f_2, f_4) for the cases shown in figure 4.2, where f_2 and f_4 are the droplet radius projections onto the second and fourth Legendre polynomials. The star and the square symbols indicate the locations of the edge state and stable base state respectively.

4.3.2 Bifurcation diagram

In order to track equilibrium solutions (i.e. the base state and the edge state) when varying the capillary number, we apply a continuation method based on our Newton algorithm. In particular, we implement pseudo arc-length continuation, which consists in adding the continuation parameter, in our case the capillary number, as unknown in the Newton iteration and constraining the solution along the tangent to the solution branch curve [93, 94]. The bifurcation diagram is shown in Figure 4.5: starting from the edge state for $Ca = 0.1$ and decreasing Ca , the droplet elongation of the equilibrium state first increases and then decreases, with a concavity developing in the central part of the droplet. When $Ca < 0.07$, a second unstable eigenvalue appears, see for instance the eigenvalue spectra for the edge state at $Ca = 0.1$ compared to $Ca = 0.05$ which are shown in the top-right and top-left inset of figure 4.5 respectively. These states have more than one unstable eigendirection, and are thus not edge states in the strict sense of being an attractor for the dynamics within the basin boundary. However, the states dynamically still act like edge states for two reasons: first, the second unstable eigenvalue is very small compared to the first one with the ratio being less than 10^{-2} , second, the eigenmode associated to the second unstable eigenvalue is asymmetric and therefore it is not excited by the symmetric initial shapes hereby considered (eigenvalues associated to symmetric/non-symmetric modes are denoted by circles/crosses in the inset of figure 4.5). When the capillary number is increased, the edge state droplet elongation decreases. A saddle node bifurcation is encountered when $Ca_{\text{crit}} = 0.1203$, as already discussed in previous studies [95, 86, 87]. The saddle node bifurcation connects the stable solution branch

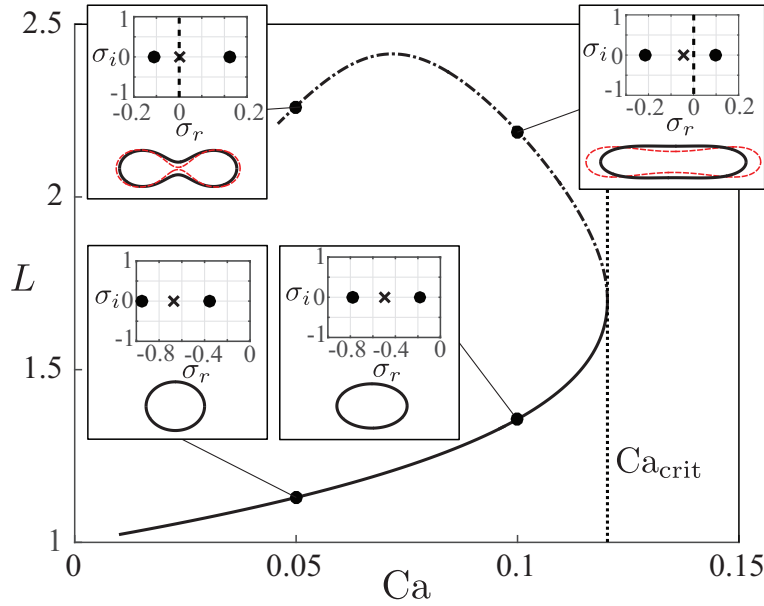


Figure 4.5 – Elongation of the droplet versus the capillary number for $\lambda = 1$, the solid and dashed lines indicate the stable and unstable branches respectively. Stable and unstable droplet shapes are plotted for $Ca = 0.05$ and $Ca = 0.1$ (solid line), superimposing the most unstable mode (dashed line). The eigenvalue spectra is also reported, circles indicate eigenvalues corresponding to symmetric modes while crosses to asymmetric modes. The translational symmetry is canceled by constraining the droplet center of mass in the origin.

(solid line) with the unstable branch of the edge states (dashed-dotted line). The bifurcation diagram shows that, for every subcritical capillary number, there exists an edge state sharing similar properties with the one found for $Ca = 0.1$. We omit edge states for very low capillary numbers since their computations become challenging due to the increasing concavity of the droplet neck. Calculation attempts at increased numerical resolution suggest that the concavity always increases as the capillary number decreases, leading us to speculate that in the limit of $Ca = 0$ the edge state may develop a cusp and correspond to two equally-sized spherical droplets in contact.

4.3.3 Numerical experiment: sudden change in flow conditions

In experiments, the breakup of droplets in subcritical conditions is often a consequence of a sudden change in the flow [11, 53, 5]. For instance, an elongated droplet can result from a supercritical flow, which selects the initial condition for a subsequent subcritical flow. We address this situation by repeating the numerical experiment performed in Stone and Leal (1989) and we verify the relevance of the edge state for the dynamics (see Supplemental Material video ²). Namely, a droplet is placed in a slightly supercritical flow set by $Ca_{\text{super}} =$

²See Supplemental Material for the animation of the numerical experiment illustrated in figure 4.6, from left to right: droplet elongation versus time, state space orbits and droplet shapes

0.125 and evolved in time with equation (4.2). Since no base state exists for the selected capillary number, the droplet elongates until it breaks. However, if one applies a step change on the flow by setting $Ca_{\text{sub}} = Ca_{\text{super}}/2$, the droplet approaches a steady state or becomes unstable, depending on its initial elongation. This is illustrated in figure 4.6a, with the blue solid line representing the droplet elongation for Ca_{super} and the dashed lines for $Ca_{\text{sub}} = Ca_{\text{super}}/2$ (in order of increasing initial elongation: orange long-dashed, yellow dotted, purple short-dashed, green dotted-dashed). We demonstrate the relevance of the edge state in figure 4.6b by showing the orbits in state space. All the orbits are transiently attracted to the edge state, which selects an almost unique path towards breakup. The path along the unstable manifold of the edge state evolves towards an elongated droplet whose ends eventually pinch off (see for instance state h_3 in figure 4.6b).

The unique path thereby explains the robustness of the end-pinching mechanism for droplet breakup commonly observed in experiments. Repeating the Stone & Leal experiment thus stresses the relevance of the edge state and also shows that its shape was indeed already observed experimentally and named the "dogbone" shape [5].

It is worth-noting that the edge state, while it explains the robustness of the end-pinching mechanism, does not yield a critical value for the droplet elongation. In fact, the critical elongation depends on the droplet shape itself: some initial droplet shapes are stable when more elongated than the edge state (for instance e_0 and f_0 in figure 4.6) while others become unstable when less elongated, as reported in figure 4.7a. At the same time this shows that one scalar parameter (here the droplet elongation) is not sufficient to describe the basin boundary of this high-dimensional system. However, even if these initial droplet shapes differ in term of initial elongation, they undergo a similar time evolution which is guided by the edge state and leads to the base state or break up through the end-pinching mechanism (see figure 4.7b).

4.3.4 Influence of the viscosity ratio

We verify that the guiding role of the edge state is robust when the viscosity ratio is varied. Continuation of nonlinear equilibrium states in the capillary number for different viscosity ratios are shown in figure 4.8. The critical capillary number increases with decreasing viscosity ratio [96, 84] allowing for more elongated stable base states [66]. For slender droplets, the critical capillary number depends on the viscosity ratio as $Ca_{\text{crit}} = 0.148\lambda^{-1/6}$, based on slender body theory [96]. We find a compatible scaling based on our fully nonlinear computations, as shown in the inset of figure 4.8. The dynamics at subcritical Ca discussed above is robust for all non-zero viscosity ratios: A finite deformation of the stable base state is required to trigger the breakup and its dynamics is controlled by the edge state, which remains connected to the base state via a saddle-node bifurcation at Ca_{crit} . In the $\lambda \rightarrow 0$ limit corresponding to an ideal bubble with vanishing viscosity there is no finite critical capillary number but the base state remains stable for all Ca and a finite deformation is required to trigger the breakup dynamics. Remarkably, the unstable upper branch of edge states still exists although it stays separated

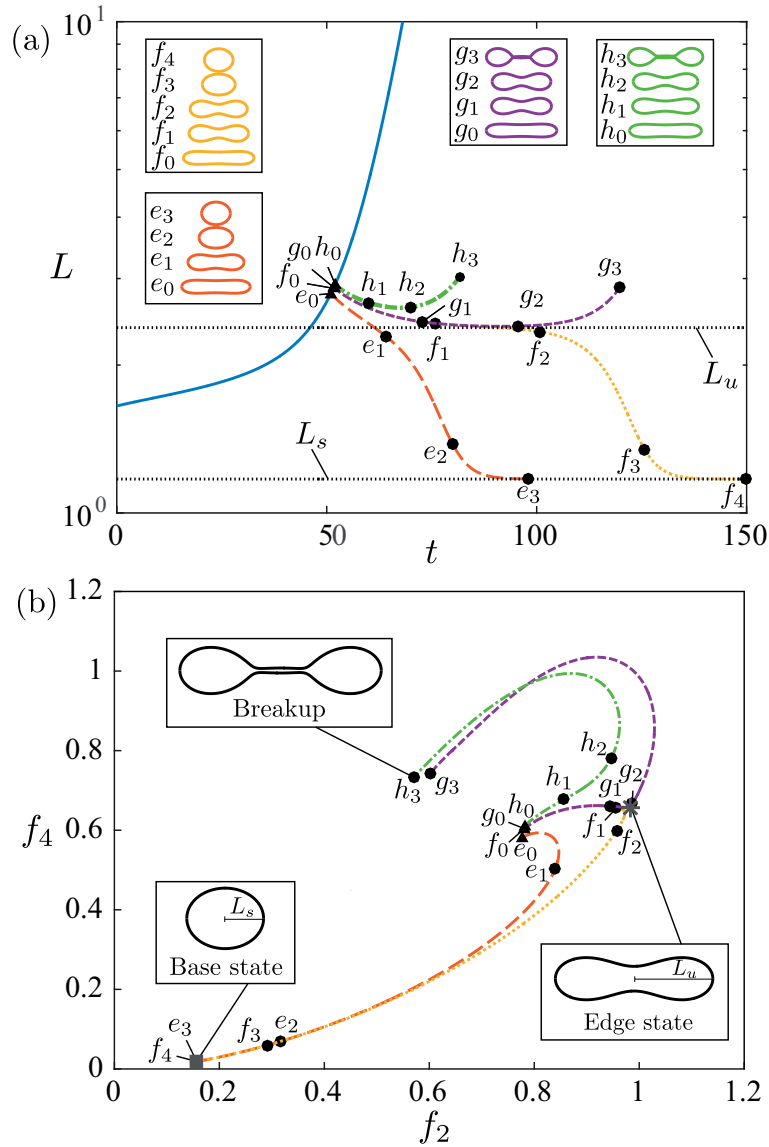


Figure 4.6 – Step change from a supercritical flow $Ca_{\text{super}} = 0.125$ (solid line) to a subcritical flow $Ca_{\text{sub}} = Ca_{\text{super}}/2$ (dashed lines), $\lambda = 1$. (a) Elongation of the droplet versus time and corresponding shapes, the horizontal lines indicate the elongation of the unstable equilibrium (edge state) L_u and stable equilibrium (base state) L_s for $Ca_{\text{sub}} = Ca_{\text{super}}/2$. (b) State space orbits, the edge state selects the path towards the base state or end-pinching. The edge state and the base state are plotted and indicated respectively by the star and square symbols.

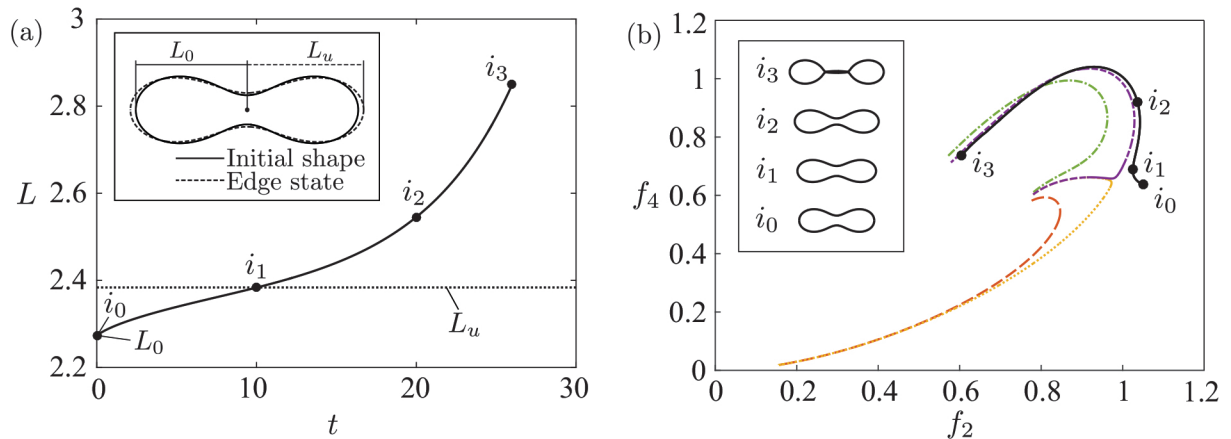


Figure 4.7 – Breakup of a droplet whose initial elongation L_0 is smaller than the edge state elongation L_u , for $Ca = 0.0625$ and $\lambda = 1$. (a) Droplet elongation versus time (solid line) and edge state elongation (dotted line). The inset shows the initial shape at $t = 0$ and the edge state. (b) State space orbit plotted together with the orbits in figure 4.6. The inset shows snapshots corresponding to the markers.

from the stable lower branch of base states. This separation persists at arbitrary large Ca .

4.4 Conclusions

In summary, let us reiterate that at subcritical capillary numbers, the edge state equilibrium located within the basin boundary of the stable base state controls whether an initial droplet deformation leads to breakup. If the breakup is triggered, the dynamical evolution is attracted towards the edge state along its stable manifold and then repelled along the one-dimensional unstable manifold. Thereby the edge state selects an almost unique breakup path which physically corresponds to the well-known end-pinching mechanism. It is worth noting that the guiding role of the edge state is robust for varying capillary numbers and viscosity ratios. In the ideal bubble limit, there is no saddle-node bifurcation and the edge state plays a key role in selecting the breakup mechanism for arbitrary large Ca .

Our results rationalize previous studies about the mechanism responsible for droplet breakup in subcritical extensional flows. Moreover, we answer previous conjectures regarding the existence of unstable states, finding that the "dogbone" shape, already observed in experiments, is an edge state. Future work should complement the identification of the basin boundary by a nonlinear optimal growth analysis [97, 98], which provides the minimal perturbation amplitude triggering breakup.

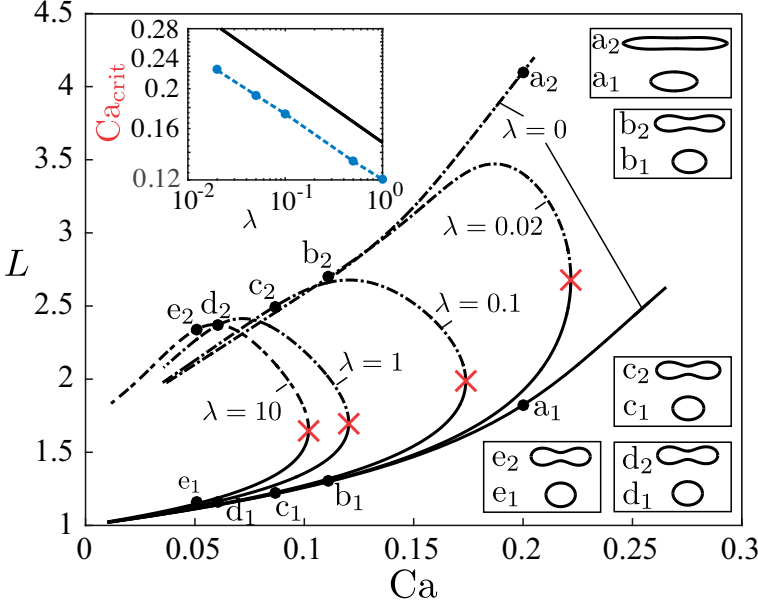


Figure 4.8 – Droplet elongation L versus capillary number Ca . Each line corresponds to a different viscosity ratio λ , crosses indicate the critical capillary number. Inset: log-log plot of Ca_{crit} versus $\lambda \in [0.02, 1]$ (dashed line) compared with the theoretical prediction of [96] (solid line).

5 Further exploration of the parameter space of a droplet in an extensional flow

5.1 Introduction

The objective of this chapter is to extend the study of a droplet in an extensional flow, carried out in chapter 4. In particular, we want to investigate the regions of the bifurcation diagram, which remained unexplored. Considering figure 5.1, three cases are of interest:

- When the number of unstable eigenvalues, along the unstable branch in Figure 4.5, passes from one to two, a second bifurcation happens. In section 5.2, we will investigate the new solution branch, where droplet shapes become non-symmetric. The symmetry breaking associated to this second bifurcation leads to droplet shape resembling droplets undergoing the well known tip-streaming [99, 82, 100, 101, 102]. We conjecture that these unstable shapes, that were, to our best knowledge, never observed before, might contribute in tip streaming.
- When the externally applied flow is suddenly halted ($Ca = 0$) the droplet relaxes in an otherwise quiescent flow. Droplet relaxation has been studied theoretically [23] experimentally [11] and numerically [53]. More recently, droplet relaxation has been employed to measure forces at the microscale [103]. The objective of section 5.3 is to investigate whether the theory of ellipsoidal relaxation holds for droplets that are initially elongated by an extensional flow.
- When the capillary number is negative, the flow is called biaxial extensional flow and it corresponds to a compression of the droplets along the axial direction. This flow has been studied numerically in [104] and theoretically in [105]. The aim of section 5.4 is to draw the bifurcation diagram for negative capillary numbers and to study its influence on the dynamics.

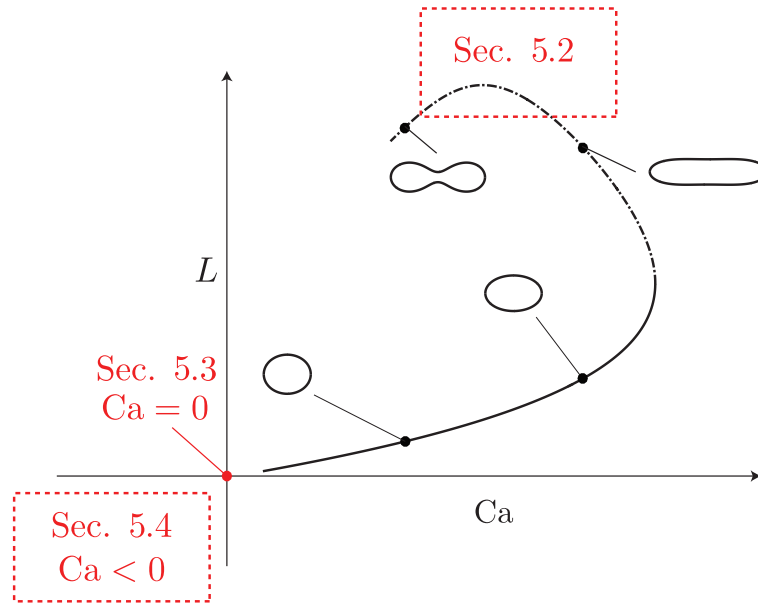


Figure 5.1 – Reproduction of Figure 4.5 highlighting the unexplored regions of the bifurcation diagram and the corresponding sections.

5.2 Symmetry breaking bifurcation

In section 4.3 we have briefly mentioned that for $Ca \approx 0.05$, the number of unstable eigenvalue of the unstable branch in Figure 4.5 changes (from 1 to 2 in the direction of decreasing capillary number). Usually, a change in the number of unstable eigenvalues changes corresponds to a bifurcation [94]. In order to follow this new branch of solution we proceed as follows: passing from one to two unstable eigenvalues, there is solution for which this second eigenvalue is neutral (less than 10^{-3} in our numerical procedure), when this happens we superimpose the associated neutral eigenmode to the current solution, thus switching branch. We show the results in Figure 5.2: the droplet shapes belonging to the new branch are still axisymmetric but they are $z \rightarrow -z$ non-symmetric. Interestingly, these non-symmetric droplets are steady solutions in a symmetric driven flow. Studying the number of eigenvalue of the different branches, we conclude that this is a subcritical pitchfork bifurcation, which is best observable when plotting the droplet center of mass position z_{cm} versus the capillary number Ca (see Figure 5.2). The inset of Figure 5.2 shows the eigenvalue spectra for $Ca = 0.09$, and the droplet shape with the two unstable eigenmodes superimposed.

The new solution branch subsequently goes through a series of folds (see Figure 5.3a). At each fold the number of unstable eigenvalue increases by one and, physically, the droplet develops a sharper tip until we stop our calculations because of the prohibitive resolution required to resolve it numerically. Figure 5.3b shows the droplet tip at the folds, and an almost fractal structure is observed: at every fold the droplet either elongates (shapes b and d) or develops a new concavity (shapes c and e). Tentatives to rescale the droplet tip, in order to investigate whether the droplet shape might be self-similar were unsuccessful. An attempt is shown in

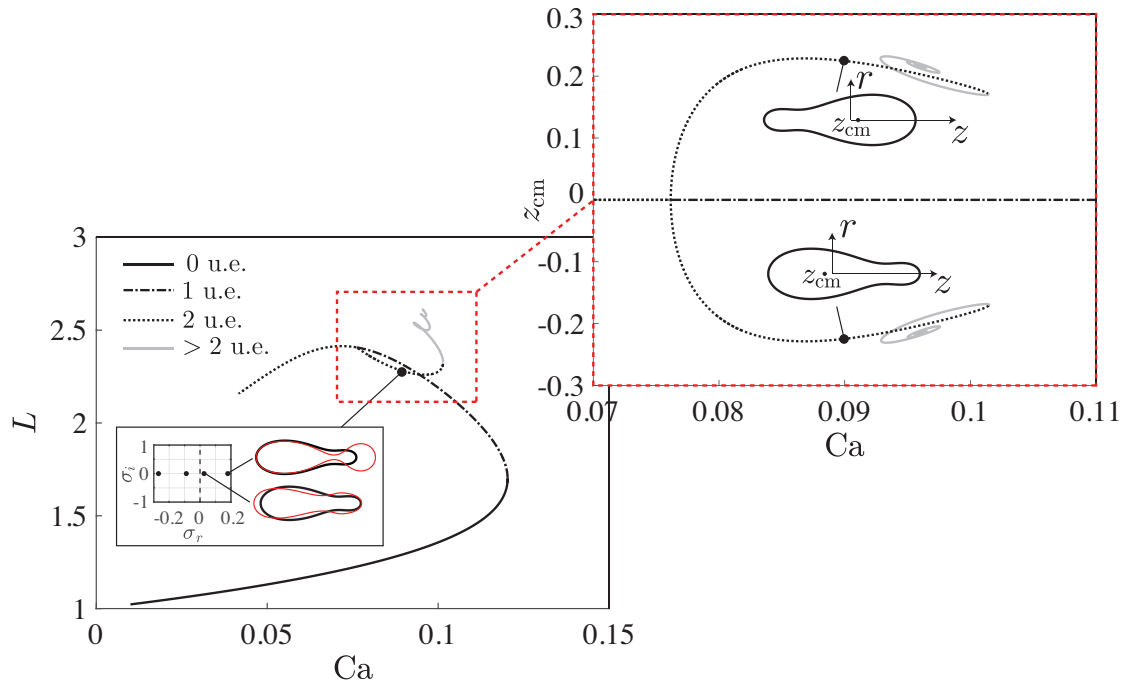


Figure 5.2 – Bifurcation diagram (L and center of mass location z_{cm} versus Ca) for a droplet in an extensional flow with a pitchfork bifurcation occurring at $Ca \approx 0.078$, plotting z_{cm} reveals the pitchfork bifurcation. The inset shows the eigenvalue spectra. The line style corresponds to the number of unstable eigenvalues: solid line (0 unstable eigenvalue), dashed-dotted line (1 unstable eigenvalue), dashed line (2 unstable eigenvalues), grey line (more than 2 unstable eigenvalues).

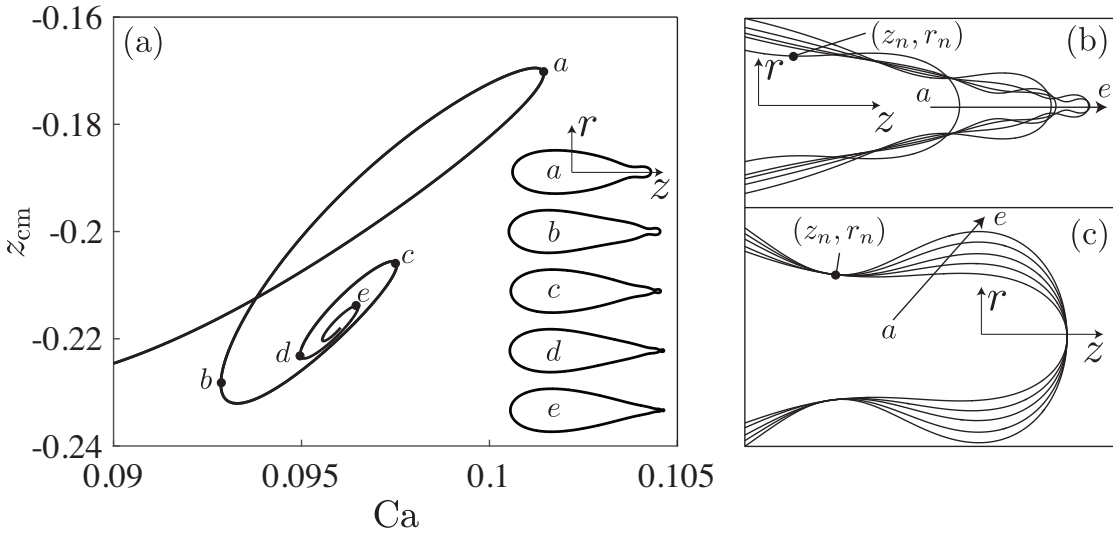


Figure 5.3 – (a) Solution branch of the non-symmetric solution, the inset shows the droplet shapes at the folds. (b) Zoom of the droplet right tip. (c) Rescaled droplet tip such that the first neck coincides.

Figure 5.3c, where z and r are rescaled by the coordinate of the first neck (z_n, r_n) .

To conclude, we have found (for the first time, to our knowledge) a pitchfork bifurcation in the bifurcation diagram of a droplet in a uniaxial extensional flow. The second bifurcation is a symmetry breaking bifurcation (subcritical pitchfork). Since this new branch is always unstable (having 2 or more unstable eigenvalues), such solutions are not expected to prevail in real experiments. However, these unstable states strongly resemble droplets undergoing tip streaming [99, 82, 100, 101, 102], a complex phenomenon which remains not entirely understood. We conjecture that these unstable states might eventually help in the understanding of the tip streaming phenomenon.

5.3 The relaxation of a droplet in a quiescent flow

We consider two droplet relaxation situations. In the first setting the droplet is initially ellipsoidal (or only slightly different from an ellipsoid) and in the second it is an initially very elongated thread. The former well represents when the droplet is transiently extended by a subcritical extensional flow and the latter when the droplet is extended by a supercritical extensional flow. In this section we will use the deformation parameter $D = (a - b)/(a + b)$, where a and b are respectively the major and minor axis of the droplet.

5.3.1 Relaxation of initially ellipsoidal droplets

Let us first consider a large initial ellipsoidal deformation. Our objective is first to see whether initially ellipsoidal droplet relax as axisymmetric ellipsoid, i.e. ellipses in the (z, r) plane. In

5.3. The relaxation of a droplet in a quiescent flow

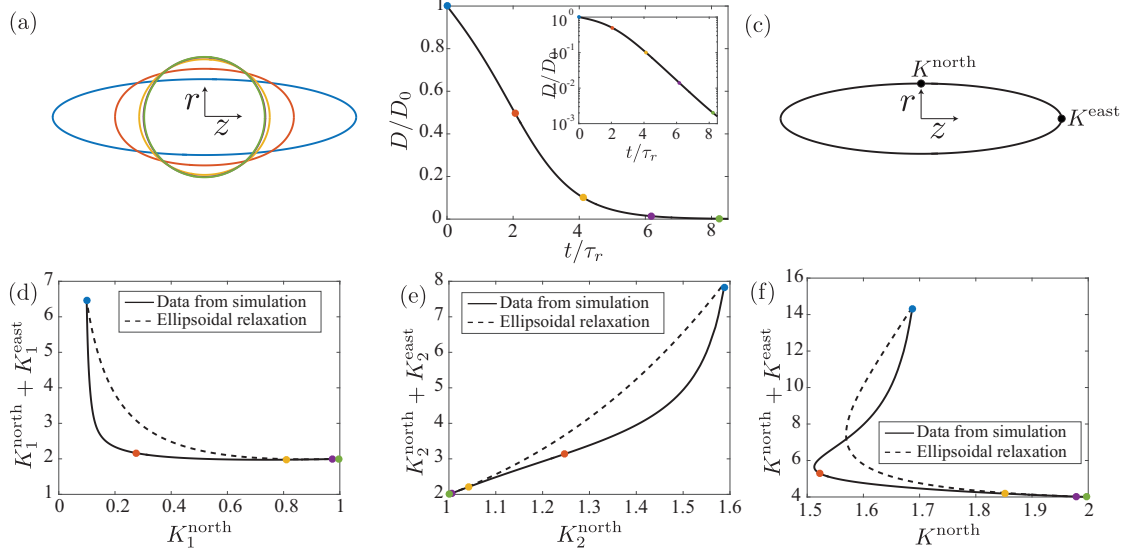


Figure 5.4 – Relaxation of an initially ellipsoidal droplet $D_0 = 0.6$ and $\lambda = 1$. (a) Droplet relaxation over time and (b) corresponding deformation parameter, dots correspond to shapes of the same color. (c) Sketch showing the locations where the curvature is measured. Relaxation path in the state space of the (d) in plane curvature K_1 , (e) azimuthal curvature K_2 and (f) their sum K respectively.

order to check if the droplet relax as an ellipsoid, we plot the curvature values at specific locations of the droplet interface. In particular, as in [106], we monitor the curvature K at precise locations, namely K^{east} and K^{north} (see sketch in figure 5.4c). In the following, we will monitor the droplet relaxation in the state space defined by $(K^{\text{north}}, K^{\text{east}} + K^{\text{north}})$. Since the ellipsoidal path in the state space is known analytically, we can directly check if the droplet relaxes as an ellipsoid. An example of this comparison is reported in figure 5.4d-e-f. Because of the axisymmetric geometry of the drop, the curvature (see Figure 5.4f) can be decomposed into the in-plane curvature K_1 and the azimuthal curvature K_2 . See equation (2.53) for the in-plane and azimuthal curvatures formula. These contributions are add up in Figure| 5.4 which shows that an initially elongated droplet does not relax as an ellipse. Moreover, since $K_1^{\text{east}} + K_1^{\text{north}}$ is always smaller than in the case of ellipsoidal relaxation, and $K_2^{\text{east}} + K_2^{\text{north}}$ is larger, the resulting $K^{\text{east}} + K^{\text{north}}$ transiently crosses the ellipsoidal path.

We now consider far less deformed initial states. Obviously, the small deformation theory from [24] works extremely well for small D_0 (see Figure 5.5a-b), and the time scale or relaxation is given by

$$\tau_r = \frac{(2\lambda + 3)(19\lambda + 16)}{40(1 + \lambda)}. \tag{5.1}$$

As expected, as the initial deformation becomes larger (see Figure 5.6a), the time evolution

Chapter 5. Further exploration of the parameter space of a droplet in an extensional flow

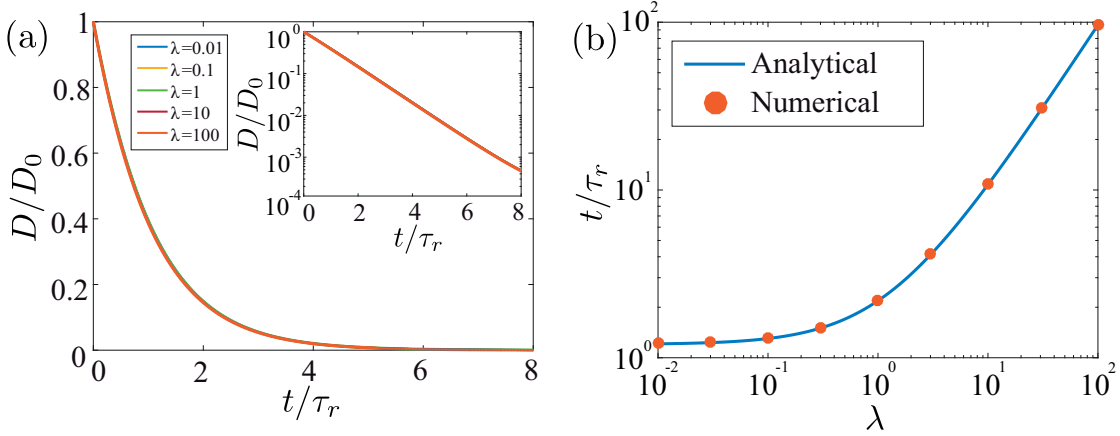


Figure 5.5 – Relaxation of initially slightly ellipsoidal droplet ($D_0 = 0.091$) for $\lambda \in [0.01, 100]$. (a) Time evolution of $D(t)$ and (b) comparison between relaxation time τ_r obtained numerically and from theory [23, 24].

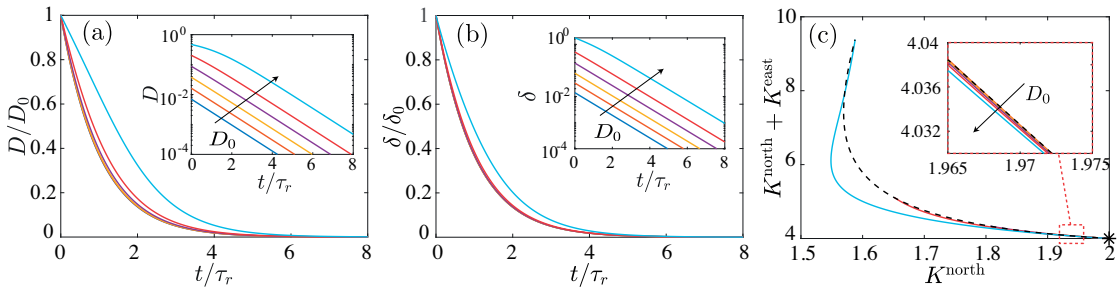


Figure 5.6 – Relaxation of initially ellipsoidal droplets $\lambda = 1$. Time evolution of (a) $D(t)$ and (b) $\delta(t)$ for different $D_0 \in [0.007, 0.47]$. (c) Corresponding trajectories in the $(K^{\text{north}}, K^{\text{north}} + K^{\text{east}})$ state space, the black dashed line indicate the family of ellipsoids.

of D departs from the exponential relaxation predicted by the theory. Interestingly, using the deformation parameter $\delta = b/a - 1$ (as in [103]) the exponential relaxation holds for larger D_0 (see Figure 5.6b). This highlights the problematics that might arise in choosing one deformation parameter instead of another one (for example δ or D) and the consequent difficulty in picking up the parameter which makes the problem most linear. In figure 5.6c, we report the graphs in the $(K^{\text{north}}, K^{\text{east}} + K^{\text{north}})$ plane for the $\lambda = 1$ case. There is a departure from the ellipsoidal path drop having initial deformation $D_0 = 0.47$. This results shows that when the droplet is initially quite elongated, the departure from the ellipsoidal relaxation path is considerable.

In real experiments, the initial shape is not an ellipse but is dictated by the flow history. Here, we consider the case where a droplet is elongated by extensional flow that is subsequently halted. In figure 5.7 we select the initial shape by choosing the steady droplet shape in an extensional flow at different capillary number. As shown in Figure 4.5, higher deformations correspond to higher capillary number. Interestingly, droplet trajectories do not to follow the

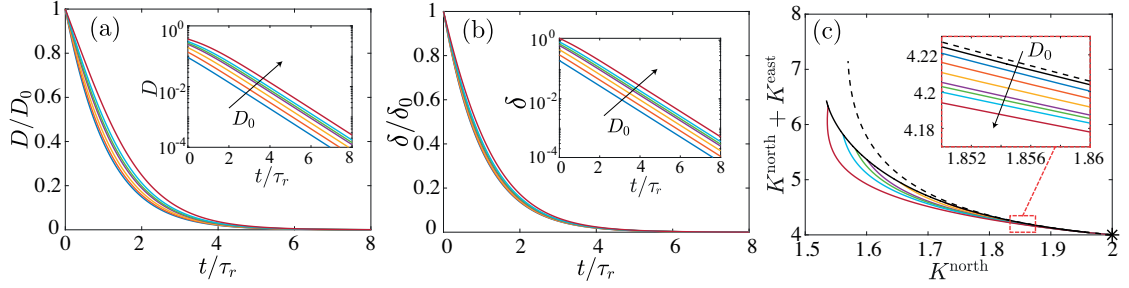


Figure 5.7 – Droplet relaxation starting from steady state of a droplet in an extensional flow, higher initial deformation corresponds to higher capillary number. Time evolution of (a) $D(t)$ and (b) $\delta(t)$. (c) Droplet relaxation in the $(K^{\text{north}}, K^{\text{north}} + K^{\text{east}})$ state space. The solid black line indicates the steady state for a droplet in extensional flow for $Ca \in [0.05, 0.12]$ and the dashed line the family of ellipsoid.

ellipsoidal relaxation path but, even for small initial deformations, first depart from it until converging to the spherical shape (see Figure 5.7c).

In conclusion, when D_0 is large, initially ellipsoidal droplet deviate from the ellipsoidal relaxation path. In addition, more natural initial shapes selected by the steady states in extensional flow are not precisely elliptical and therefore their path always differ from the elliptic relaxation.

5.3.2 Relaxation of initially non-ellipsoidal droplets

When the droplet is put in a supercritical extensional flow, the initial droplet shape can be very elongated and lead to breakup, which is fundamentally different from the cases considered in previous section, where the spherical droplet shape was always recovered. We hereby perform the same numerical experiment of figure 4.6, where the initial droplet shape is selected by halting a supercritical extensional flow at a certain time. This numerical experiment is similar to the one carried out in section 4.3.3, where the flow was halved. In figure 5.8 we see that whether the extensional flow is halted at $t = 58$ or $t = 60$, the droplet retrieves the spherical shape or breaks-up. The interface dynamics is as follows: first the elongated thread shrinks and the caps move toward the axis droplet center and then, depending if the droplet is stable or unstable, the spherical shape is retrieved or breakup happens. In the case of stable drops, we can distinguish two different regimes (see Figure 5.8b): first the deformation parameter D is of $O(1)$ and the caps move toward the droplet center. Afterwards, D decreases exponentially and this second phase is similar to the relaxation of an initially ellipsoidal droplets.

5.4 Biaxial extensional flow

In this section we study the case when the capillary number is negative in the extensional flow. This flow is called biaxial extensional flow [104, 107]. In this flow conditions, the droplet

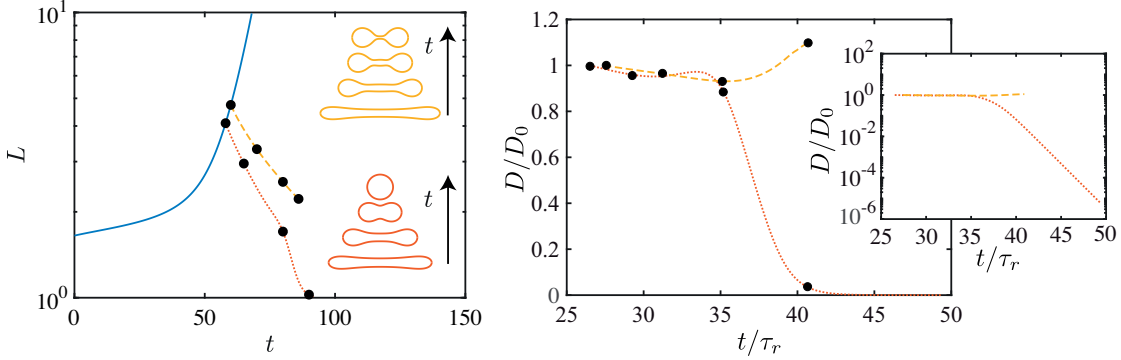


Figure 5.8 – Droplet relaxation from initial shapes which are selected by a supercritical extensional flow. (a) Droplet elongation versus time. The insets show snapshots denoted by the black circles. (b) Deformation parameter D versus rescaled time.

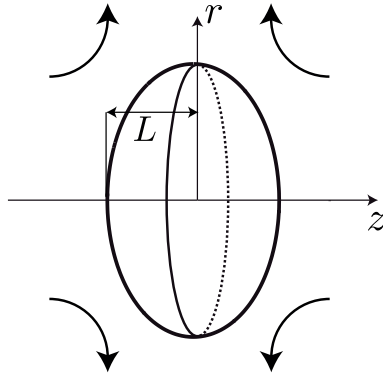


Figure 5.9 – Sketch of a droplet in a biaxial extensional flow.

is compressed along the axis of symmetry and acquires an oblate-like shape (see Figure 5.9). Prior studies [104, 105] have investigated the bifurcation diagram: similarly (but reversed) to uniaxial extensional flow, the droplet compresses in a disk-like shape as the intensity of the flow increases. Beyond a critical capillary number, no steady solution is found and the droplet breaks, no matter which initial condition was chosen. In Figure 5.10 we report the bifurcation diagram for $\lambda = 1$, as in chapter 4, we are able to turn around the saddle node bifurcation and to explore an unstable branch, which was, to our knowledge, never reported in the literature. A qualitatively different feature from the uniaxial extensional flow is that the unstable branch cannot be continued when L becomes zero. We conjecture that this might be related to a change in topology of the droplet interface, which points to the idea that for $Ca > -0.36$ the unstable branch is constituted by toroidal droplets. Currently we are not able to investigate this hypothesis because our algorithm is designed only for a simply connected domain.

In Figure 5.11 we investigate the effect of a sudden variation of the imposed flow, as in Figure 4.5 for the uniaxial extensional flow. Namely, we impose a supercritical flow where $Ca = -0.4$ and we change the flow condition at a different time, setting the initial droplet shape for the subsequent subcritical flow. For the latter, we investigate two subcritical capillary number:

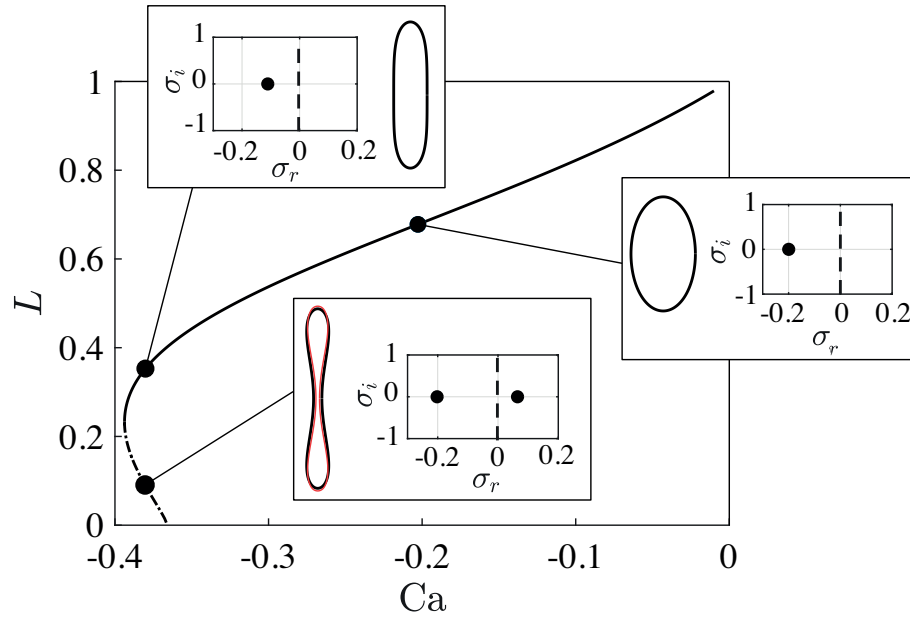


Figure 5.10 – Bifurcation diagram of a droplet in a biaxial extensional flow, $\lambda = 1$. The solid line shows the stable solution branch and the dashes-sotted line the unstable branch. The inset show droplet shapes for $Ca = -0.2$ and $Ca = -0.38$ (stable and unstable) with the most unstable mode superimposed in red.

one for which there exists an unstable state ($Ca = -0.38$) and the other one ($Ca = -0.35$) for which we are not able to find the unstable state (that we speculate might be a toroidal droplet). As expected, when the capillary number is smaller, it is necessary to start from a more squeezed initial shape in order to trigger breakup. From this numerical experiment, it appears the the droplet half width L has to be much smaller in order to trigger breakup when $Ca = -0.35$ as compared to $Ca = -0.38$ (almost 10 times smaller). We conjecture that this difference might come from the different unstable shapes belonging to the unstable branch, elongated droplet for $Ca = -0.38$ and (maybe) toroidal droplet for $Ca = -0.35$. This aspect surely calls for further investigations.

In Figure 5.12, we investigate the influence of the viscosity ratio upon the bifurcation diagram. In the range that we study, where $\lambda \in [0.1, 10]$, the bifurcation diagram is qualitatively similar. The critical capillary number decreases (i.e. the flow intensity increases) as the viscosity ratio decreases. Interestingly, the droplet shape at the critical capillary number does not vary much (see inset in figure 5.12), contrary to what happens for uniaxial extensional flow, as already noted in [104, 105]. Considering future developments, we would like to verify whether there exists a fold in the $\lambda = 0$ case. Numerically, we didn't find any fold by numerical continuation, even if we couldn't study extremely large flow intensities due to numerical challenges (the droplet squeezes a lot and becomes very thin). This problem might maybe tackled theoretically, although, in contrast to the case of uniaxial extensional flow, where slender body theory shows that there is no fold in the inviscid droplet case [96], we are not aware of theoretical frameworks

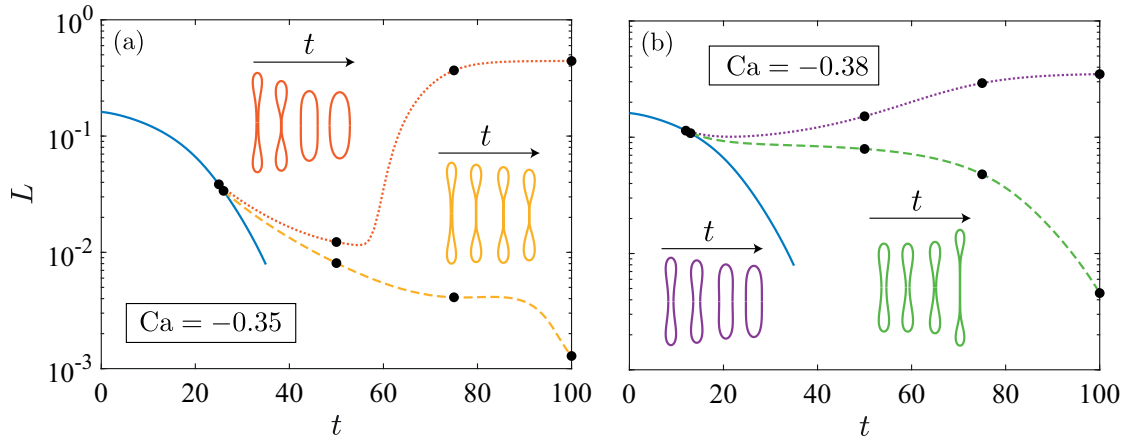


Figure 5.11 – Step change in the flow condition from supercritical flow $Ca = -0.4$ (solid blue line) to subcritical flow at (a) $Ca = -0.35$ and (a) $Ca = -0.38$, $\lambda = 1$. Dotted lines denote trajectories leading to the steady stable state while dashed lines to breakup. The insets show snapshots of the droplet shape corresponding to the black circles.

to compute the flow due to a sheet-like droplet.

5.5 Conclusions

Even in the extremely simple case where a droplet is suspended in an unbounded domain where a linear extensional flow is imposed, the non-linearity embedded in the interface conditions gives rise to a rich dynamics and an intricate bifurcation diagram. This has been first shown in chapter 4 and has been further investigated here. In particular, we have investigated a symmetry breaking occurring in uniaxial extensional flow (section 5.2), showing that the droplet shapes undergoes a seemingly fractal thinning of the droplet tip which resembles droplets undergoing tip streaming. In section 5.3 we have investigated the relaxation of an initially extended droplet in a quiescent flow. We have compared our results with the theory of ellipsoidal droplet relaxation and verified its validity for initial droplet shapes set by a uniaxial extensional flow. In the last section, we have considered the case when the capillary number of the extensional flow is negative, so called biaxial extensional flow or compressional flow. In this flow the droplet is squeezed along its axis and becomes oblate. We have studied the bifurcation diagram and observed that for high (but still subcritical) intensity of the flow there are two possible solutions, one stable and the second, more elongated, unstable. For low flow intensity, we conjecture that the unstable shape, if it continues to exist, might be a toroidal droplet. This qualitative difference might lead to a different transient dynamics of the droplet shape between strong and weak subcritical flows. In future work, we would also like to address the validity on the assumptions of considering an axisymmetric droplet, as one could imagine that instabilities might develop along the azimuthal direction, similarly to the Saffman-Taylor instability.

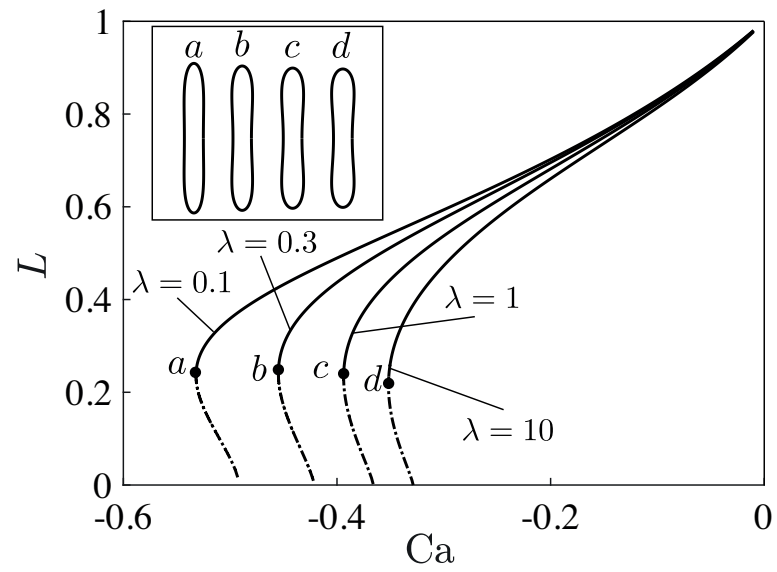


Figure 5.12 – Bifurcation diagram of a droplet in a biaxial for different viscosity ratios. Solid/dashes-dotted lines correspond to stable/unstable branches. The inset shows the droplet shape at the turning point.

Conical microswimmers **Part II**

6 Physics of Bubble-Propelled Micro-rockets

G. Gallino^{1,2}, F. Gallaire¹, E. Lauga² and S. Michelin^{2,3}

¹Laboratory of Fluid Mechanics and Instabilities, EPFL, CH1015 Lausanne, Switzerland

²Department of Applied Mathematics and Theoretical Physics, University of Cambridge
CB3 0WA, United Kingdom

³LadHyX – Département de Mécanique, CNRS – Ecole Polytechnique,
91128 Palaiseau Cedex, France

Advanced Functional Materials, 1800686 (2018).

A popular method to induce synthetic propulsion at the microscale is to use the forces created by surface-produced gas bubbles inside the asymmetric body of a catalytic swimmer (referred to in the literature as microrocket). Gas bubbles nucleate and grow within the catalytic swimmer and migrate toward one of its openings under the effect of asymmetric geometric confinement, thus generating a net hydrodynamic force which propels the device. In this paper we use numerical simulations to develop a joint chemical (diffusive) and hydrodynamic (Stokes) analysis of the bubble growth within a conical catalytic microrocket and of the associated bubble and microrocket motion. Our computational model allows us to solve for the bubble dynamics over one full bubble cycle ranging from its nucleation to its exiting the conical rocket and therefore to identify the propulsion characteristics as function of all design parameters, including geometry and chemical activity of the motor, surface tension phenomena, and all physicochemical constants. Our results suggest that hydrodynamics and chemistry partially decouple in the motion of the bubbles, with hydrodynamics determining the distance travelled by the microrocket over each cycle while chemistry setting the bubble ejection frequency. Our numerical model finally allows us to identify an optimal microrocket shape and size for which the swimming velocity (distance travelled per cycle duration) is maximized.

6.1 Introduction

Artificial microswimmers have recently attracted much attention across many scientific disciplines: from a fundamental point of view, they represent alternatives to biological systems (e.g. bacteria, algae) to characterize and control individual propulsion at the micron scale and collective organization in so-called active fluids. They also present many opportunities for engineering applications, in particular in the biomedical context to perform such tasks as drug delivery [108, 109], nanosurgery [110], cell sorting [111, 34]. Two of the main challenges are to overcome the restrictions inherent to propulsion in highly-viscous environments such as reversibility and symmetry-breaking [36] as well as miniaturization.

Proposed designs can currently be classified into two broad categories, namely (i) *actuated* systems which rely on an externally-imposed forcing, most often at the macroscopic level, in order to self-propel (e.g. an unsteady magnetic or acoustic field [112, 113, 114]) and (ii) *catalytic* (or fuel-based) systems which rely on local physico-chemical processes (e.g. chemical reactions at their surface) to convert chemical energy into a mechanical displacement [115, 116, 117, 118]. For the latter, this energy conversion may follow different routes, a popular one being the generation of gas bubbles whose growth and dynamics enable propulsion [119].

These so-called microrockets represent one of the most promising designs for applications. In contrast with active phoretic colloids [120, 121, 122, 123] that swim exploiting local physico-chemical gradients in order to generate hydrodynamic forcing [124], microrockets move due to the production of gas bubbles inside the asymmetric body of the swimmer. More precisely, bubbles nucleate and grow within the catalytic motor and migrate toward one of its opening under the effect of the asymmetric geometric confinement, thus generating a net hydrodynamic force which propels the device.

Such configuration has been studied experimentally, focusing primarily on the rocket velocity and resulting trajectory [125, 126, 127]. In parallel, the first in-vivo application of this technology for drug delivery was recently conducted [47]. Fundamental understanding is still needed of the role played by the different hydrodynamic and chemical mechanisms involved as well as their couplings, in order to identify optimal design rules for such microrockets. Several studies have proposed partial modeling of the problem, focusing more specifically on the motion of the bubble inside the rocket [128, 129] or during and after its ejection [130, 131].

The purpose of the present work is to propose a detailed chemical and hydrodynamic analysis of the bubble growth within the catalytic microrocket, and associated bubble and microrocket motion, in order to identify the role of the different design parameters in setting the propulsion speed. To this end, we propose an accurate numerical simulation of the dissolved gas diffusion and fluid motion both inside and outside a conical catalytic microrocket, assuming that the predominance of capillary effects ensures that the bubble remains spherical while translating inside the conical body. Focusing specifically on the bubble growth within the motor, we monitor the bubble dynamics over one bubble cycle ranging from its nucleation to its exiting the conical rocket. The propulsion characteristics are clearly identified in terms of the design

characteristics (i.e. geometry and chemical activity of the motor, surface tension phenomena, ambient conditions).

The bubble dynamics is observed to be composed of two different phases, which are characterized in detail in terms of bubble and microrocket motion as well as hydrodynamic signature, an information of particular importance which conditions the hydrodynamic interaction of the artificial swimmer with its environment (e.g. boundaries or other swimmers) and critically influences its trajectory and its control. Our results further suggest that for such bubbles, hydrodynamics and chemistry partially decouple, the former determining the distance travelled by the microrocket over each cycle, while the latter determines the cycle duration or bubble ejection frequency. Moreover, we are able to identify an optimal microrocket shape and size for which the swimming velocity is maximized.

6.2 Model

The dynamics of an isolated microrocket is considered here in a fluid of density $\rho = 10^3 \text{ kg m}^{-3}$ and dynamic viscosity $\mu = 10^{-3} \text{ Pa s}$ (i.e. water). The axisymmetric microrocket geometry is that of a cone of radius $R = 1 \mu\text{m}$, aspect ratio $\xi = L/R$, thickness h/R and opening angle θ (see Figure 6.1). Throughout this study we use cylindrical coordinates (r, z) measured in units of cone radius R , and set $\xi = 10$ and $h/R = 0.2$, which are compatible with experimental designs [128, 130, 119]. The inner surface of the cone is chemically-active and catalyses a chemical reaction. One of the products of this reaction is a soluble gas. We pick O_2 as a specific example, produced by the decomposition of hydrogen peroxide on platinum, which diffuses in the liquid with molecular diffusivity $D = 2 \times 10^{-9} \text{ m}^2 \text{ s}^{-2}$; note that our modeling approach is generic and easily applicable to other chemical situations. The production of oxygen on the surface of the catalyst is modelled here as a fixed molar flux $\mathcal{A} = 10^{-2} \text{ mol m}^{-2} \text{ s}^{-1}$ (considering the experimental data in [128]). The rate of production of the gas is large enough that the fluid is saturated so that a spherical gas bubble of radius $r_b(t)$ grows within the rocket. Throughout this study, we consider the dynamics of a bubble on the axis of symmetry (see Section 6.3.1 for more details). The viscosity and density of the gas are negligible compared to that of the liquid, and, although in experimental conditions the surface tension value is often affected by the presence of surfactants, we initially consider $\gamma = 7.2 \times 10^{-2} \text{ N m}^{-1}$. In section 6.3.5, we will then systematically vary the value of γ in order to study the effect of surfactants, which play a crucial role in real applications by stabilizing the bubble.

Based on the above characteristics and the experimentally-measured microrocket velocity $U_c \sim 5 \times 10^{-4} \text{ m s}^{-1}$ [128, 130, 119], the effect of inertia and gravity can be neglected (the Reynolds $\text{Re} = \rho U_c R / \mu \sim 5 \times 10^{-4}$ and Bond numbers $\text{Bo} = g R^2 \rho / \gamma \sim 10^{-6}$ are both small). The Peclet number $\text{Pe} = R U_c / D \sim 0.2$ is less than one and we may neglect gas advection and unsteady diffusion within the rocket as a first approximation. Finally, because the typical hydrodynamic stresses are negligible compared to those due to surface tension (the capillary number $\text{Ca} = \mu U_c / \gamma \sim 10^{-5}$ is small), the bubble is expected to remain spherical during its

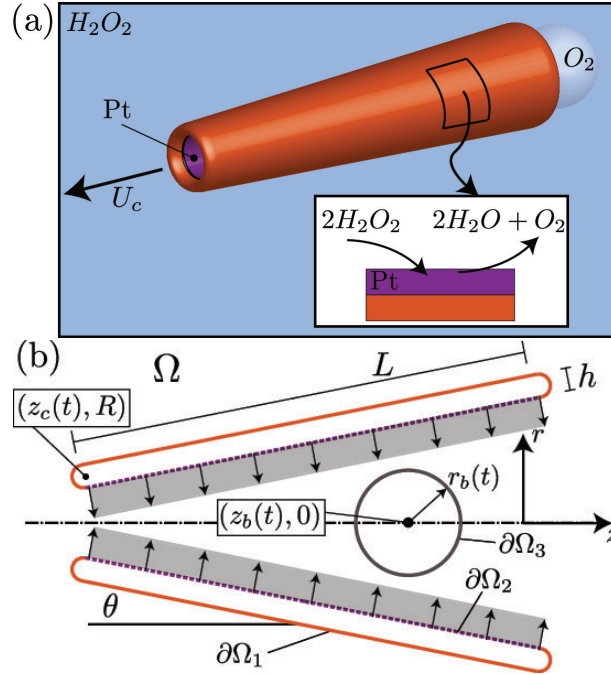


Figure 6.1 – Microrocket: (a) Dissolved oxygen (O_2) is produced by the decomposition of hydrogen peroxide onto a platinum-coated surface. The saturated oxygen environment in the confined motor leads to bubble nucleation and growth. Bubbles exit from the larger opening while the microrocket is propelled in the opposite direction. (b) Schematic of the problem and side view of the axisymmetric microrocket in a plane containing the central axis. Red solid surfaces are inert (no oxygen production) while reactive surface where oxygen emission occurs are shown as dashed purple lines.

entire evolution and hydrodynamic effects do not contribute to the bubble inner pressure.

6.2.1 Gas diffusion

Following these dimensional considerations, the non-dimensional dissolved gas concentration $c(\mathbf{x})$, relative to its far-field concentration and measured in units of $\mathcal{A}R/D$, satisfies the steady diffusion equation in the liquid domain Ω ,

$$\nabla^2 c = 0, \tag{6.1}$$

and decays in the far-field ($c \rightarrow 0$ for $\mathbf{x} \rightarrow \infty$). The dissolved gas is produced through chemical reaction on the inner surface of the cone, and $c(\mathbf{x})$ therefore also satisfies

$$-\mathbf{n} \cdot \nabla c = 0 \quad \text{for } \mathbf{x} \in \partial\Omega_1, \tag{6.2}$$

$$-\mathbf{n} \cdot \nabla c = 1 \quad \text{for } \mathbf{x} \in \partial\Omega_2. \tag{6.3}$$

where $\partial\Omega_1$ and $\partial\Omega_2$ refer to the inert and active cone surfaces respectively (see Figure 6.1b). At the bubble surface, the dissolved gas is in thermodynamic equilibrium with the gas pressure inside the bubble, and c is therefore given by Henry's law $c = H^{cc} p_b$, where $H^{cc} = H^{cp} D\gamma/R^2 \mathcal{A}$ is the non-dimensional volatility constant and p_b is the pressure inside the bubble measured in units of γ/R . The volatility constant is an intrinsic property of the dissolved gas (e.g. $H^{cp} = 4 \times 10^{-7} \text{kg m}^{-3} \text{Pa}^{-1}$ for oxygen in water [132]). The bubble pressure p_b is given by Laplace law ($\text{Ca} \ll 1$), so that in non-dimensional form

$$c = H^{cc} \left(\beta + \frac{2}{r_b} \right) \quad \text{for } \mathbf{x} \in \partial\Omega_3, \quad (6.4)$$

where $\beta = \bar{p}_0 R/\gamma$ is the ratio between the dimensional ambient pressure \bar{p}_0 and capillary pressure. Equations (6.1)–(6.4) determine $c(\mathbf{x})$ uniquely. Using this solution, the flux of dissolved gas into the bubble is computed as

$$Q = \int_{\partial\Omega_3} (\mathbf{n} \cdot \nabla c) dS. \quad (6.5)$$

Using mass conservation of the gas species and the ideal gas law, the time evolution of the bubble radius is finally determined in non-dimensional form as

$$\frac{dr_b}{dt} = \frac{Q}{3\beta r_b^2 + 4r_b}, \quad (6.6)$$

where the time is measured in units of $4\pi\gamma/3\mathcal{A}\mathcal{R}T_0$, $\mathcal{R} = 8.314 \text{ J mol}^{-1} \text{K}^{-1}$ is the universal gas constant and $T_0 \sim 293 \text{ K}$ is the ambient (room) temperature.

6.2.2 Hydrodynamics

The change in bubble size imposed by the chemical reaction and gas diffusion dynamics, equation (6.6), sets the fluid into motion within the rocket. Since $\text{Re} \ll 1$, the non-dimensional fluid velocity \mathbf{u} and hydrodynamic pressure field p (now measured in units of $3\mathcal{A}\mathcal{R}T_0R/4\pi\gamma$ and $3\mu\mathcal{A}\mathcal{R}T_0/4\pi\gamma$, respectively) satisfy the incompressible Stokes' equations in the liquid domain Ω

$$-\nabla p + \nabla^2 \mathbf{u} = 0, \quad \nabla \cdot \mathbf{u} = 0. \quad (6.7)$$

The cone and bubble are translating along the axis of symmetry with respective velocities $\mathbf{U}_c = \dot{z}_c \mathbf{e}_z$ and $\mathbf{U}_b = \dot{z}_b \mathbf{e}_z$, with $z_c(t)$ and $z_b(t)$ the axial positions of the cone's narrow opening and of the bubble center, respectively. One of the main purposes of this paper is to compute the time-dependent values of both \mathbf{U}_c and \mathbf{U}_b . At the surface of the solid cone, the no-slip boundary condition imposes the boundary condition

$$\mathbf{u} = \mathbf{U}_c \quad \text{for } \mathbf{x} \in \partial\Omega_1, \partial\Omega_2, \quad (6.8)$$

and the hydrodynamic flow decays in the far-field ($\mathbf{u} \rightarrow 0$ and $p \rightarrow p_0$ as $\mathbf{x} \rightarrow \infty$). The bubble is inflating while translating, and its surface is free of any tangential stress, so that mixed boundary conditions must be satisfied

$$\mathbf{u} \cdot \mathbf{n} = \mathbf{U}_b \cdot \mathbf{n} + \frac{dr_b}{dt} \quad \text{and} \quad (\mathbf{I} - \mathbf{nn}) \cdot \boldsymbol{\sigma} \cdot \mathbf{n} = \mathbf{0} \quad \text{for} \quad \mathbf{x} \in \partial\Omega_3, \quad (6.9)$$

with \mathbf{n} the normal unit vector to the bubble surface. The coupling between chemistry and hydrodynamics enters only in equation (6.9) through the inflation rate. The problem is closed by imposing that the cone and the bubble are each force-free during their axisymmetric translation along the axis (inertia is negligible here, as explained previously)

$$\int_{\partial\Omega_1 + \partial\Omega_2} (\mathbf{n} \cdot \boldsymbol{\sigma} \cdot \mathbf{e}_z) dS = \int_{\partial\Omega_3} (\mathbf{n} \cdot \boldsymbol{\sigma} \cdot \mathbf{e}_z) dS = 0, \quad (6.10)$$

a closure relationship which implicitly determines the instantaneous values of the bubble and cone velocities.

6.2.3 Numerical method and validation

Both the diffusion (Laplace) and hydrodynamic (Stokes) equations are solved numerically using axisymmetric Boundary Element Methods. The boundary integral equation for the axisymmetric solute concentration on the boundaries is classically written for $\mathbf{x}_0 \in \partial\Omega$ as (see equation (4.5.5) in Ref. [50])

$$c(\mathbf{x}_0) = -2 \int_{\partial\Omega} G(\mathbf{x}, \mathbf{x}_0) [\mathbf{n}(\mathbf{x}) \cdot \nabla c(\mathbf{x})] r(\mathbf{x}) dl(\mathbf{x}) + 2 \int_{\partial\Omega}^{PV} c(\mathbf{x}) [\mathbf{n}(\mathbf{x}) \cdot \nabla G(\mathbf{x}, \mathbf{x}_0)] r(\mathbf{x}) dl(\mathbf{x}), \quad (6.11)$$

where $G(\mathbf{x}, \mathbf{x}_0)$ is the axisymmetric Green's function of the Laplace equation (see equation (4.5.6) in Ref. [50]), PV denotes the principal-value integral and \mathbf{n} is the normal vector pointing into the liquid domain Ω , whose boundaries $\partial\Omega$ consists in the cone and bubble surfaces. Discretizing these boundaries into N piecewise constants elements, and applying boundary conditions, equations (6.2) and (6.3), equation (6.11) provides a $N \times N$ linear system for the value of the concentration on each element, which is solved using classical matrix inversion techniques.

Similarly, using the fundamental integral representation of Stokes flows [49], the fluid velocity \mathbf{u} is expressed on the boundaries $\partial\Omega$ as

$$4\pi\mathbf{u}(\mathbf{x}_0) = - \int_{\partial\Omega} \mathbf{M}(\mathbf{x}, \mathbf{x}_0) \cdot \mathbf{f}(\mathbf{x}) dl(\mathbf{x}) + \int_{\partial\Omega}^{PV} \mathbf{n}(\mathbf{x}) \cdot \mathbf{q}(\mathbf{x}, \mathbf{x}_0) \cdot \mathbf{u}(\mathbf{x}) dl(\mathbf{x}), \quad (6.12)$$

where \mathbf{M} and \mathbf{q} are the axisymmetric Stokeslet and associated stress respectively (we follow the notation in Ref. [49]) and $\mathbf{f} = \boldsymbol{\sigma} \cdot \mathbf{n}$ is the traction acting on the boundaries. Equation (6.12) can be rewritten more conveniently on the cone and bubble surface respectively, by using the

no-slip and mixed boundary conditions respectively, equations (6.8) and (6.9), as [133, 134]

$$4\pi\mathbf{u}_{\text{rel}}(\mathbf{x}_0) = - \int_{\partial\Omega} \mathbf{M}(\mathbf{x}, \mathbf{x}_0) \cdot \mathbf{f}(\mathbf{x}) dl(\mathbf{x}) + \int_{\partial\Omega_3}^{PV} \mathbf{n}(\mathbf{x}) \cdot \mathbf{q}(\mathbf{x}, \mathbf{x}_0) \cdot \mathbf{u}_{\text{rel}}(\mathbf{x}) dl(\mathbf{x}) - 8\pi\mathbf{U}_b \quad (6.13)$$

for $\mathbf{x}_0 \in \partial\Omega_3$,

$$0 = - \int_{\partial\Omega} \mathbf{M}(\mathbf{x}, \mathbf{x}_0) \cdot \mathbf{f}(\mathbf{x}) dl(\mathbf{x}) + \int_{\partial\Omega_3} \mathbf{n}(\mathbf{x}) \cdot \mathbf{q}(\mathbf{x}, \mathbf{x}_0) \cdot \mathbf{u}_{\text{rel}}(\mathbf{x}) dl(\mathbf{x}) - 8\pi\mathbf{U}_c \quad (6.14)$$

for $\mathbf{x}_0 \in \partial\Omega_1 + \partial\Omega_2$,

where \mathbf{u}_{rel} is the relative velocity of the bubble surface to its center of mass whose normal component is set by the bubble growth rate, $\mathbf{u}_{\text{rel}} \cdot \mathbf{n} = \dot{r}_b$. The principal value integral appears only in equation (6.13), when \mathbf{x}_0 belongs to the integration path $\partial\Omega_3$.

When discretizing the boundaries into N piecewise constant elements, equations (6.13) and (6.14), together with the force-free conditions equation (6.10), provide a $(2N + 2) \times (2N + 2)$ for (i) the axial and radial components of the fluid traction on the cone surface, (ii) the tangential relative fluid velocity and normal traction on the bubble surface and (iii) the bubble and cone axial velocities. A particular technical point deserves special attention: when $\mathbf{x} \rightarrow \mathbf{x}_0$ the Green's function in equations (6.11), (6.12), (6.13) and (6.14) become singular and special (but classical) treatment is needed in order to maintain good accuracy [50, 49].

The Laplace and Stokes solvers described above were validated by computing the chemical field around a Janus particle and its swimming velocity due to diffusiophoretic effects and a good agreement was found with the analytical solution [135].

The bubble is growing within a confined environment. As observed in Section 6.3, the liquid gap between the bubble and cone may become small during the bubble formation and expulsion. Adaptive mesh refinement is therefore needed to maintain sufficient numerical accuracy: the elements are split into two when their size is larger than the gap. However, accurately resolving the hydrodynamic stresses when the bubble approaches the cone wall would require a prohibitive number of mesh elements for thin gaps. The physical effect of these hydrodynamic lubrication stresses is however essential to prevent overlap between the bubble and cone surfaces. We therefore introduce short-ranged repulsive forces to prevent such overlap numerically. The force-free conditions along the axial direction now write

$$F = 2\pi \int_{\partial\Omega_1 + \partial\Omega_2} r(\mathbf{n} \cdot \boldsymbol{\sigma} \cdot \mathbf{e}_z) dl = -2\pi \int_{\partial\Omega_3} r(\mathbf{n} \cdot \boldsymbol{\sigma} \cdot \mathbf{e}_z) dl, \quad (6.15)$$

where, similarly to what was done in Ref. [57], the axial repulsive force F is defined as

$$F = \begin{cases} B \frac{e^{\delta-d} - 1}{e^\delta - 1} \frac{|\mathbf{d} \cdot \mathbf{e}_z|}{d} & \text{for } d \leq \delta \\ 0 & \text{for } d > \delta \end{cases} \quad (6.16)$$

where \mathbf{d} is the minimum distance vector between the bubble and the cone and $d = \|\mathbf{d}\|$.

This simply adds a repulsive interaction between the bubble and cone and the global system remains overall force-free. In the following, $B = 10^7$ and $\delta = 0.1$ are used; varying these parameters does not significantly affect the numerical results. The system of first order differential equations for $r_b(t)$, $z_c(t)$ and $z_b(t)$ is marched in time using Matlab's ODE23t routine, which uses a semi-implicit, adaptive time-stepping scheme.

6.3 Results

6.3.1 Dissolved gas distribution and bubble growth

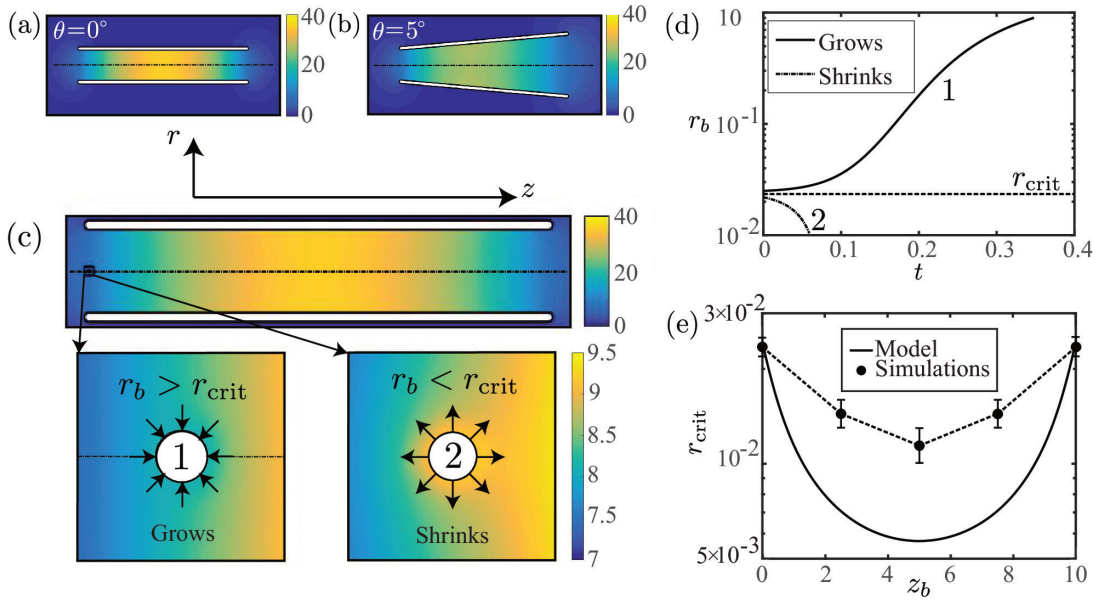


Figure 6.2 – Dissolved gas concentration inside and around the microrocket for (a) $\theta = 0^\circ$ and (b) $\theta = 5^\circ$. (c) Effect of the presence of the bubble on the local dissolved gas concentration for $\theta = 0^\circ$. The top panel is the concentration with no bubble while the central and bottom panels show the concentration around a growing (1) or shrinking (2) bubble, and (d) the associated evolution of the bubble radius. The black arrows indicate the direction of the diffusive flux of dissolved gas. (e) Critical radius as a function of bubble position along the axis for $\theta = 0^\circ$ obtained numerically results (with error bars) or from the estimation $r_{crit} = 2H^{cc}/(c(z,0) - \beta H^{cc})$. For all panels, $H^{cc} = 0.1$ and $\beta = 1$.

When $\theta = 0^\circ$, the microrocket is cylindrical and the concentration of dissolved gas is left-right symmetric with a maximum in the center of the microrocket due to the geometric confinement (Figure 6.2a). When $\theta \neq 0^\circ$, the left-right symmetry is broken and the maximum concentration moves toward the smaller cone opening (Figure 6.2b). It is worth noting that the overall concentration level becomes smaller due to the increased dissolved gas diffusion out of the cone resulting from the weaker confinement.

We are now interested in understanding how the chemical field generated by the microrocket

impacts and controls the growth of a bubble. To this end, it should be reminded that a gas bubble placed in a uniform concentration of dissolved gas shrinks (resp. grows) when its surface concentration c_b is higher (resp. lower) than the background concentration c_∞ . Namely, when $c_b < c_\infty$ the diffusive flux of gas species is oriented toward the bubble and vice versa. Since c_b decreases as the bubble radius r_b increases, see equation (6.4), large bubbles are more likely to grow than small bubbles.

In the microrocket geometry, a bubble located outside the cone will shrink more easily than one located inside, due to the lower level of gas concentration outside the rocket. But even when a bubble is inside the conical microrocket, it is still expected to shrink if its concentration is higher than the background concentration established by the microrocket (e.g. for small enough bubbles). The concentration of the bubble surface is set by the thermodynamic equilibrium at the bubble surface (Henry's law, equation 6.4) and it increases when H^{cc} (inversely proportional to the surface flux \mathcal{A}) or β increase. Based on experimental estimates [128, 131], we set $H^{cc} = 0.1$ and $\beta = 1$ and numerically compute the net flux of dissolved gas into the bubble in order to determine whether a bubble will grow or shrink depending on its radius and axial position. For each bubble position, a critical radius $r_{\text{crit}}(z_b)$ is identified as the minimum radius for which bubble growth is observed at a fixed location (Figure 6.2e).

Throughout this study, an axisymmetric problem is considered where the bubble center is located on the axis of symmetry. This assumption seems reasonable when considering an inertialess bubble translating in a channel [136], although it neglects the initial bubble migration from the catalyst surface, where it most likely nucleates, toward the axis. Bubble nucleation on a catalyst surface considered in some recent studies [132] is a complex physico-chemical phenomenon which is beyond the scope of the present study, that focuses on the coupling of gas diffusion and hydrodynamics resulting in the rocket propulsion.

Figure 6.2c shows the dissolved gas concentration for a bubble of radius slightly larger (resp. smaller) than r_{crit} , corresponding to a growing (resp. shrinking) bubble. The gas concentration around the bubble is locally lower (resp. higher) due to the bubble presence, as a result of the diffusive flux of gas toward (resp. away from) the bubble (the flux direction is indicated with arrows in the lower panels of Figure 6.2c).

The critical radii found numerically are small compared to the cone size. Assuming further that the bubble is small compared to the local length scale for the gas concentration changes with no bubble, the bubble is expected to grow if its surface concentration, equation (6.4), is lower than the local background concentration (i.e. when the bubble is not present). This provides an estimate of the critical radius as $r_{\text{crit}} = 2H^{cc}/(c(z, 0) - \beta H^{cc})$. This estimate agrees qualitatively with the numerical solution (see Figure 6.2e): the estimated critical radius is of the same order as the numerical solution, and is smaller in the middle of the motor, where the concentration is higher. The quantitative discrepancy most likely arises from finite-size effects of the bubble: while critical radii are small compared to the cone radius, they are not negligible over the characteristic length scale introduced by the local gas concentration gradients within

the conical motor.

In the following simulations, the initial bubble conditions (radius and position) are chosen as those for the smallest bubble that can grow: its position $z_b(0)$ and radius $r_b(0)$ are identified by the location of the minimum of the critical radius r_{crit} along the axis and the corresponding critical radius. A small constant $C_0 = 0.1$ is added to $r_b(0)$ in order to ensure bubble growth and avoid spurious bubble shrinking due to numerical inaccuracy.

6.3.2 Definition and dynamics of the bubble cycle

Starting from the initial conditions described in the previous section, the diffusion and hydrodynamic equations are solved numerically, and the bubble and motor displacements are investigated during a single *bubble cycle*, i.e. the growth of a single bubble. This bubble cycle is defined starting from the initial condition described previously (nucleation) and finishing when the bubble center exits the cone (Figure 6.3a). The bubble cycle is shown in video #1 of the Supporting Information.

The evolution of the bubble and cone displacements $z_b(t)$ and $z_c(t)$, as well as that of the bubble radius $r_b(t)$, are shown over one bubble cycle in Figure 6.3b-c for fixed H^{cc} , β and cone geometry. The bubble is initially small and not confined by the cone geometry. It is growing, thanks to the absorption of dissolved gas by diffusion at its surface, thereby lowering the concentration in its vicinity. In this first, not geometrically-confined phase, the bubble growth pushes fluid out through the small and large openings of the cone and both the cone and bubble displacements are small. Hydrodynamically, the microrocket is a so-called “pusher” during this phase (see Figure 6.3f). Like swimming bacteria, it pushes fluid away along its axis of symmetry while pumping fluid toward it in the equatorial plane [36].

A transition to a second phase is observed for $t \approx 0.12$ when the bubble has grown sufficiently for the confinement by the walls of the motor to become significant. As it continues growing under the effect of the dissolved gas diffusion, the bubble translates rapidly toward the larger opening. Figure 6.3b shows that most of the cone displacement occurs during this second phase. Because of the fast relative translation of the confined bubble with respect to the motor, fluid is sucked in from the smaller opening and pushed out of the rocket at the larger opening (Figure 6.3e). Overall, the hydrodynamic signature of the microrocket is reversed in this phase as it now acts as a so-called “puller” although higher-order contributions to the hydrodynamic signature create more complex flow structures in the vicinity of the rocket such as the recirculation zone in the back (see Figure 6.3g). We conjecture that these different (and unsteady) flow signatures might play an important role in the flow-mixing generated by the displacement of the microrocket [137]. When the bubble exits the cone, the bubble cycle ends. Following the bubble motion toward the exit, the concentration of dissolved gas within the microrocket recovers its initial levels, allowing for a new bubble cycle (Figure 6.3d).

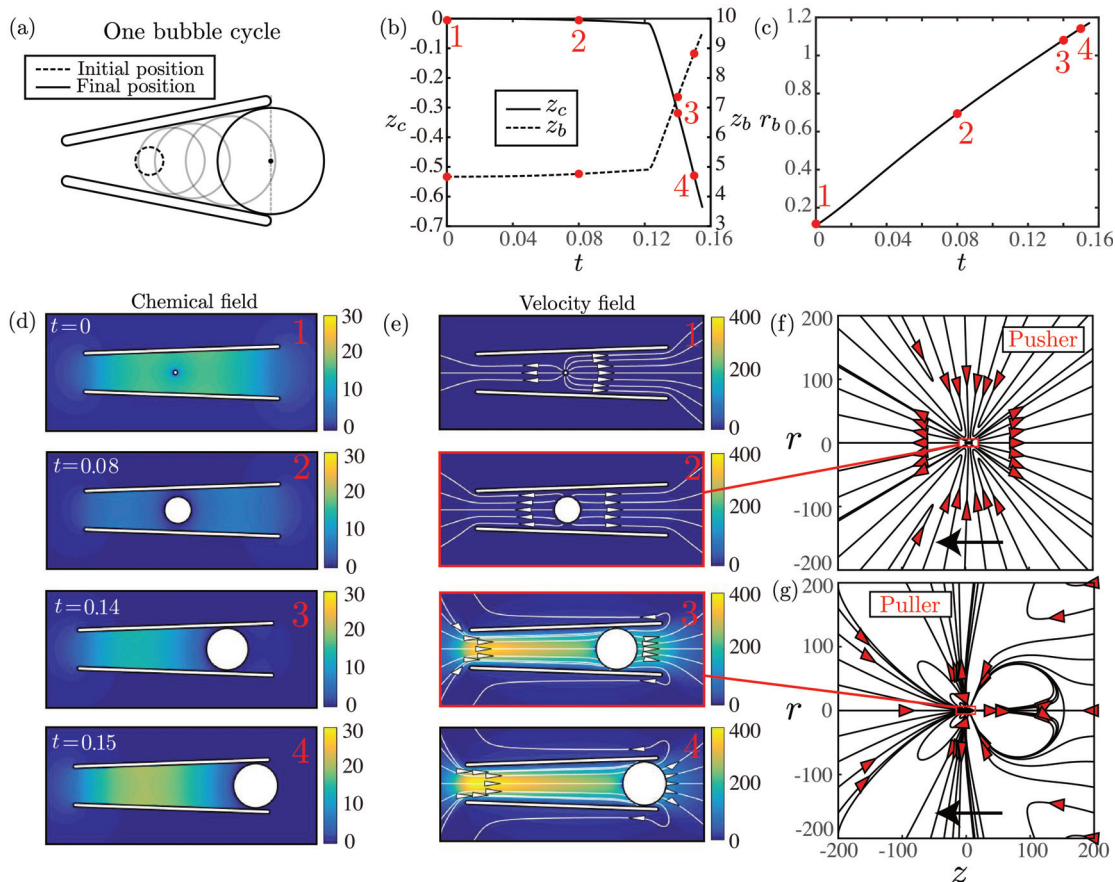


Figure 6.3 – Chemical and bubble dynamics over one bubble cycle for $H^{cc} = 0.1$, $\beta = 1$ and $\theta = 2^\circ$: (a) Sketch of one bubble cycle, starting when the bubble is in the initial position and ending when it exists the cone. (b,c) Time-dependence of the cone and bubble positions. (d) Time-dependence of the bubble radius r_b . (d,e) Snapshots of the dissolved gas concentration and velocity field (streamlines and intensity) for the four instants in panels (b,c). (f,g) Large scale velocity field which is a pusher/puller when the bubble is non-confined/confined while the arrows indicate the swimming direction.

6.3.3 Influence of physico-chemical properties on the microrocket displacement

As emphasized above, the chemical properties of the catalyst and gas species (e.g. the flux of dissolved gas \mathcal{A} or its volatility H^{cp}) and the background pressure \tilde{p}_0 influence the magnitude of the dissolved gas concentration within the microrocket and at the bubble surface. The effect of such quantities, and of their non-dimensional counterpart H^{cc} and β , on the motor and bubble dynamics is investigated in Figure 6.4 for a given rocket geometry.

Increasing the value of H^{cc} (see Figure 6.4a and 6.4c) is equivalent to reducing the chemical activity of the catalyst, \mathcal{A} , or increasing the gas volatility. For instance, recent experimental studies have shown that enhanced surface activity can be achieved by varying the roughness of the catalysts [138, 139]. Although we consider in our model only smooth surfaces, such

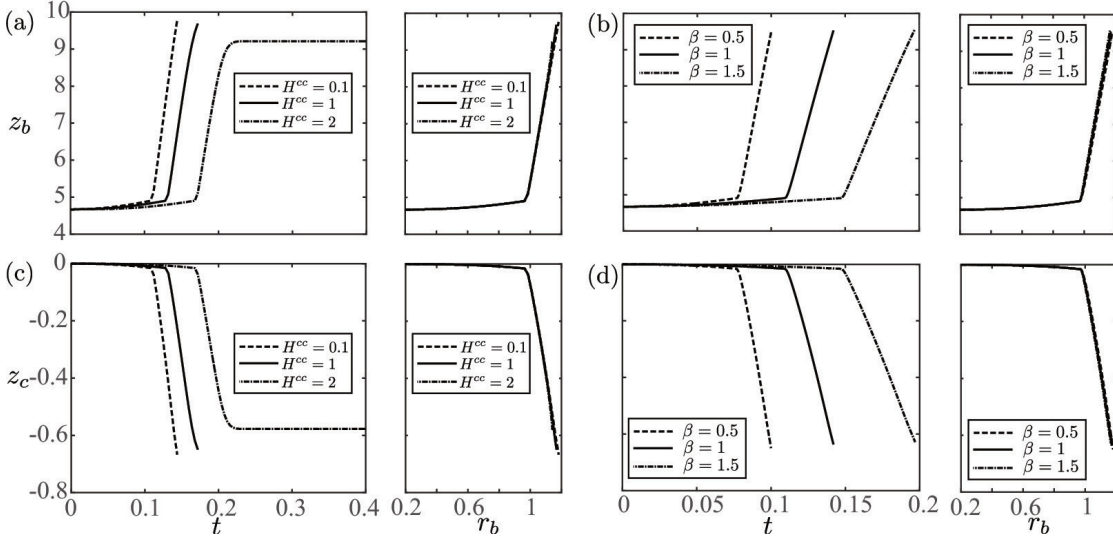


Figure 6.4 – Influence of the physico-chemical parameters for $\theta = 2^\circ$. Evolution in time of (a,b) the bubble position $z_b(t)$ and (c,d) the cone position $z_c(t)$ for different values of (a,c) H^{cc} and (b,d) β . In (a,c) $\beta = 1$ and in (b,d) $H^{cc} = 0.1$. In each panel, the figure on the right show the evolution of z_b or z_c with respect to r_b .

effects could be described, as a first approximation, by a decrease of the effective value of H^{cc} . Figure 6.4a and c show that the total displacement of the bubble over one cycle is almost unchanged when H^{cc} is varied. Changing H^{cc} modifies however the duration of the bubble cycle. Moreover, for $H^{cc} = 2$, the bubble stops inflating before leaving the cone (the diffusive flux of gas at its boundary is not sufficiently large); in that case, the bubble cycle is not closed and the microrocket will not be able to reach a continuous motion. Similarly, the time required for a full bubble cycle is observed to increase with β , but this does not significantly affect the total displacement (Figure 6.4b,d).

This independence of the kinematic displacement from the chemical characteristics is an illustration of the decoupling between the chemical and hydrodynamic problems due to the negligible deformation of the spherical bubble. The shape of the bubble is here solely described by the growth of its radius, and because the bubble grows monotonously, a bubble cycle can be parameterized by the bubble size (rather than time) starting from the initial critical radius and up to its final radius at the exit. At leading order, the latter is solely determined by the cone geometry since the bubble surface is very close to the wall in the second part of the cycle. Starting from given initial conditions, the subsequent bubble and motor displacements depend only on the bubble radius (see figures on the right of each panel of Figure 6.4), and hydrodynamics and geometry are observed to fully determine the total displacement of the motor, Δz_c .

In contrast, the chemical problem, set by the properties H^{cc} and β , does affect the bubble growth rate by setting the amplitude of the dissolved gas flux, Q , and the duration of the bubble cycle, ΔT , is therefore set by the chemical and diffusion dynamics. This decoupling

between the hydrodynamic and chemical problems obviously breaks down when the bubble is unable to exit the cone (e.g. for large values of H^{cc}).

6.3.4 Microrocket displacement and average velocity for different opening angles

With this understanding, we now turn to the role of motor geometry and study the dependence of the average velocity, $\bar{U} = \Delta z_c / \Delta T$, on the opening angle, fixing the values $H^{cc} = 0.1$ and $\beta = 1$. The cone displacement is plotted as a function time for different opening angles θ on Figure 6.5. The total displacement achieved over one bubble cycle is observed to increase with the opening angle, θ , whereas the ejection frequency defined as $1/\Delta T$ decreases with θ (Figure 6.5b). As a result, the average velocity \bar{U} becomes negligible for small and large opening angles, because either the displacement is too small (small angles) or the cycle period diverges (large angles). As a result, an optimal opening angle $\theta_{\text{opt}} = 10^\circ$ is identified for which \bar{U} is maximum, as shown in Figure 6.5c.

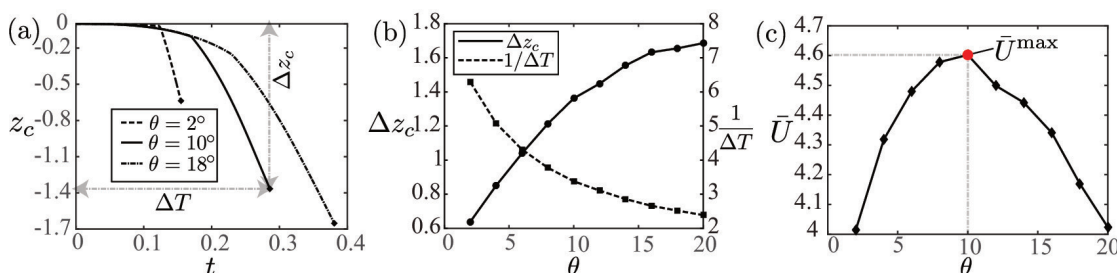


Figure 6.5 – Impact of the value of the opening angle, θ , on the propulsion over one cycle for $H^{cc} = 0.1$ and $\beta = 1$. (a) Evolution with time of the microrocket displacement for different opening angles. (b) Influence of the opening angle, θ , on the total cone displacement over the cycle, Δz_c , and bubble ejection frequency, $1/\Delta T$. (c) Corresponding evolution of the average cone velocity, $\bar{U} = \Delta z_c / \Delta T$. The maximum value is reached for $\theta = 10^\circ$.

6.3.5 Optimal microrocket design

In Figure 6.6a we extend the results of Section 6.3.3 and plot the variation of the average velocity with the physico-chemical parameters H^{cc} and β . Given the results of Figure 6.4, it comes as no surprise that the average velocity is a decreasing function of both H^{cc} and β , since an increase in either of those parameters effectively increases the bubble cycle period until it becomes infinite (i.e. the bubble stops inflating before reaching the cone exit).

Although this map provides useful information and physical insight, since both H^{cc} and β combine different parameters that are critical in experimental applications, it is not sufficient to disentangle the role of dimensional characteristics such as the cone radius, R , the chemical activity, \mathcal{A} , or surface tension, γ , which can be tuned during the fabrication process of the motor (R , \mathcal{A}) or by using surfactants (γ). In Figure 6.6a, we overlap lines following the variations R , γ and \mathcal{A} , respectively, all other parameters being held constants and equal to

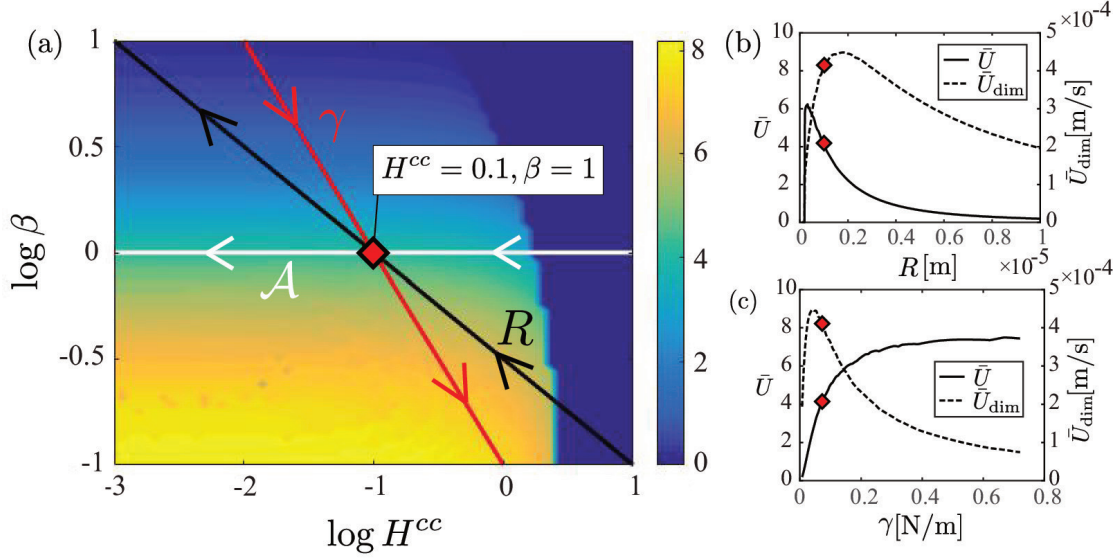


Figure 6.6 – Effect of the microrocket radius, R , chemical activity, \mathcal{A} , and surface tension, γ , on the propulsion: (a) Average microrocket velocity (non-dimensional) versus H^{cc} and β ; the red diamond corresponds to the reference conditions $H^{cc} = 0.1$ and $\beta = 1$, and coloured lines correspond to variations of the indicated dimensional parameter, all other remaining fixed. (b,c) Evolution of the average microrocket velocity, non-dimensional, \bar{U} , and dimensional, \bar{U}_{dim} , with (b) motor radius R and (c) surface tension, γ , around the reference conditions denoted by a red diamond (see panel a).

those introduced in section 6.2, starting from $H^{cc} = 0.1$ and $\beta = 1$ for which a motor radius $R = 1 \mu\text{m}$ and surface tension $\gamma = 7.2 \times 10^{-2} \text{ N m}^{-1}$ lead to an average dimensional velocity $\bar{U}_{dim} = 4.2 \times 10^{-4} \text{ m s}^{-1}$ (we refer to this in the following as the “reference conditions”). The variations of the corresponding average velocity, \bar{U} , along these lines are shown in Figure 6.6b-c, together with the corresponding dimensional velocity, \bar{U}_{dim} . One should note that the motor radii maximizing the non-dimensional and dimensional average velocities differ slightly, the former reaching its peak for a radius slightly larger than the reference configuration, while the latter peaks at lower values of R . Similarly, the non-dimensional velocity increases monotonically with surface tension γ , while the dimensional velocity presents a maximum at intermediate values of γ . This is a result of the reference velocity scale chosen here, namely $3R\mathcal{A}\mathcal{R}T_0/4\pi\gamma$ so that $\bar{U}_{dim} \sim (R/\gamma)\bar{U}$. Similarly, since \bar{U} remains almost constant with \mathcal{A} (see figure 6.6a), $\bar{U}_{dim} \sim \mathcal{A}\bar{U}$ increases monotonically with \mathcal{A} as is observed experimentally [130].

Focusing on the influence of the microrocket size, an increase of R leads to a decrease in the non-dimensional velocity \bar{U} as it inhibits bubble growth (β is increased, corresponding to an increase in the relative influence of the ambient pressure on the bubble inner pressure and surface concentration). But increasing R also leads to a larger dimensional velocity for fixed H^{cc} and β . The competition of these two mechanisms results to negligible values of the dimensional velocity for both small and large R , and in the existence of an optimal motor

radius.

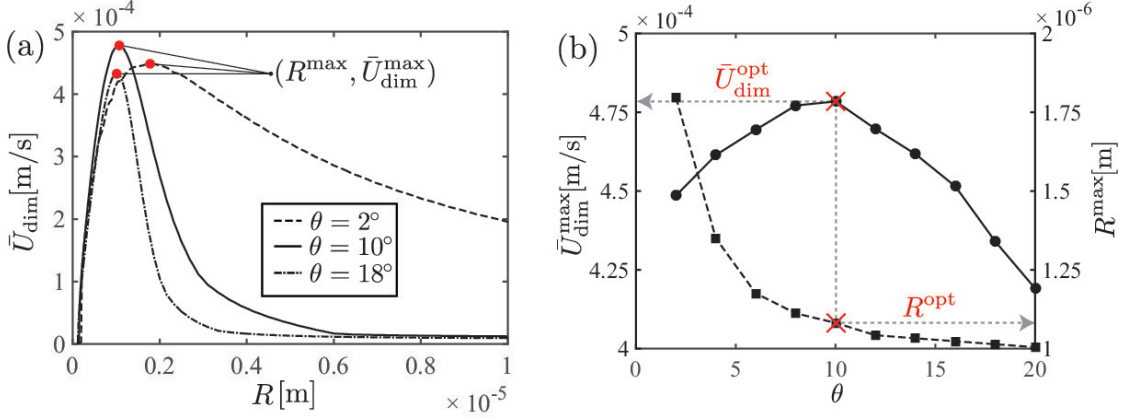


Figure 6.7 – Optimal microrocket design: (a) Evolution of the average dimensional velocity with the cone radius around the reference conditions for different opening angles. (b) Evolution with cone opening angle θ of the average velocity, $\bar{U}_{\text{dim}}^{\text{max}}$, and corresponding cone radius at which the maximum is attained, R^{max} .

We now repeat such a numerical experiment for different opening angles θ , retrieving a family of curves $(R, \bar{U}_{\text{dim}})$ (Figure 6.7a) and identifying for each value of θ , the optimal dimensional velocity, $\bar{U}_{\text{dim}}^{\text{max}}$, and the optimal radius, R^{max} . As the cone angle increases, the maximum average velocity $\bar{U}_{\text{dim}}^{\text{max}}$ is reached for a smaller cone radius, i.e. R^{max} is a decreasing function of θ (Figure 6.7b). In order to work in optimal conditions, larger microrockets are thus required for smaller opening angles. Furthermore, a global optimum $\bar{U}_{\text{dim}}^{\text{max}} = 4.78 \times 10^{-4} \text{ m/s}$ is identified for $\theta = 10^\circ$, to which corresponds a cone radius $R^{\text{opt}} \approx 1.2 \times 10^{-6} \text{ m}$.

6.3.6 Perspectives: many bubbles interaction

In this section, we show preliminary results for the propulsion of the microrocket in the case where many bubbles are present in the cone. This scenario is of interest for real applications where a train of closely spaced bubbles is observed to exit the microrocket.

The results presented below use the same parameters as in section 6.3.2 and more systematic investigations will be addressed in our future work. In order for the problem to remain tractable, we also enforce two additional rules:

- After the nucleation of the first bubble, which occurs as explained in section 6.3.1, subsequent bubbles nucleate on the axis when the concentration exceeds a threshold value, c_N , with radius $r_b(0) = 2H^{cc}/(c_N - \beta H^{cc}) + 0.1$, similarly to section 6.3.1. The value $c_N = 20$ was chosen as an illustration; note that this value does not derive from thermodynamic considerations, as it is challenging to precisely determine how bubble nucleation occurs on catalyst surfaces [132]. Instead, the value of c_N is a tuning parameter selected in order to obtain a bubble ejection frequency compatible with the one

observed in experiments [128].

- The presence of multiple bubbles increases significantly the computational complexity of the system, thus the number of coexisting bubble is limited to two. Namely, when a third bubble nucleates, we eliminate the bubble farthest away from the cone. We expect that this assumption will not strongly affect these preliminary results, because eliminated bubbles have already exited the cone and therefore weakly contribute to the cone displacement and the chemical environment within the cone. In fact, when out of the cone, bubbles receive a small chemical flux (or even shrink, see Figure 6.8b) which leads to a small fluid displacement (see intensity of the fluid velocity in Figure 6.8d, snapshots 3 and 4).

Under these two rules, we illustrate our computational results for $\theta = 2^\circ$, $H^{cc} = 0.1$ and $\beta = 1$ in Figure 6.8. The first part of the simulation is identical to the results illustrated in section 6.3.2, namely a slow cone displacement when the first bubble B1 is not confined followed by a sharp cone acceleration during the confined phase. At time $t = 0.152$ a second bubble B2 nucleates because $\max(c(z, 0)) > c_N$. Running very long simulations, we observe that from this instant the dynamics repeats periodically roughly every 0.16 unit of time (see video #2 in the Supporting Information). In order to investigate the microrocket dynamics, we can therefore focus on the periodic dynamics that defines the bubble cycle (shaded region in Figure 6.8a-b and corresponding snapshots in Figure 6.8c-d).

The nucleation of bubble B2 lowers the local concentration but does not strongly affect the flow because of its small size compared to B1. In fact, B1 keeps translating toward the larger opening, generating a flow that drags B2 along. Subsequently, B1 exits the cone and B2 inflates but it does not yet feel the confinement: in this phase the cone displaces slowly because none of the two bubbles are geometrically confined. When B2 becomes larger, it translates because of the geometrical confinement and pushes B1 out of the cone. Because B1 is now completely outside the cone, it absorbs less chemical flux and eventually shrinks. Finally, B2 keeps inflating and translating while the concentration in the left part of the cone recovers its original higher level. Shortly after $t = 0.31$, a third bubble B3 nucleates and the bubble cycle starts again. The computed average microrocket velocity is $\bar{U} \approx 4.6$, which is larger than that obtained in section 6.3.2, where $\bar{U} \approx 4$. This difference is mostly due to the fact that, when B2 is inside the cone but is not geometrically confined (see snapshot 2 in Figure 6.8c-d), B1 is still partially confined and provides thrust to the microrocket. This situation is considerably different from the one-bubble case, where almost no thrust is provided while the bubble is not confined. In fact, the displacement attained when the bubbles are not strongly confined is considerably smaller in the one-bubble case ($\Delta z_c = 0.017$ from $t = 0$ to $t \approx 0.12$) compared to the two-bubble case ($\Delta z_c = 0.163$ from $t = 0.155$ to $t \approx 0.29$).

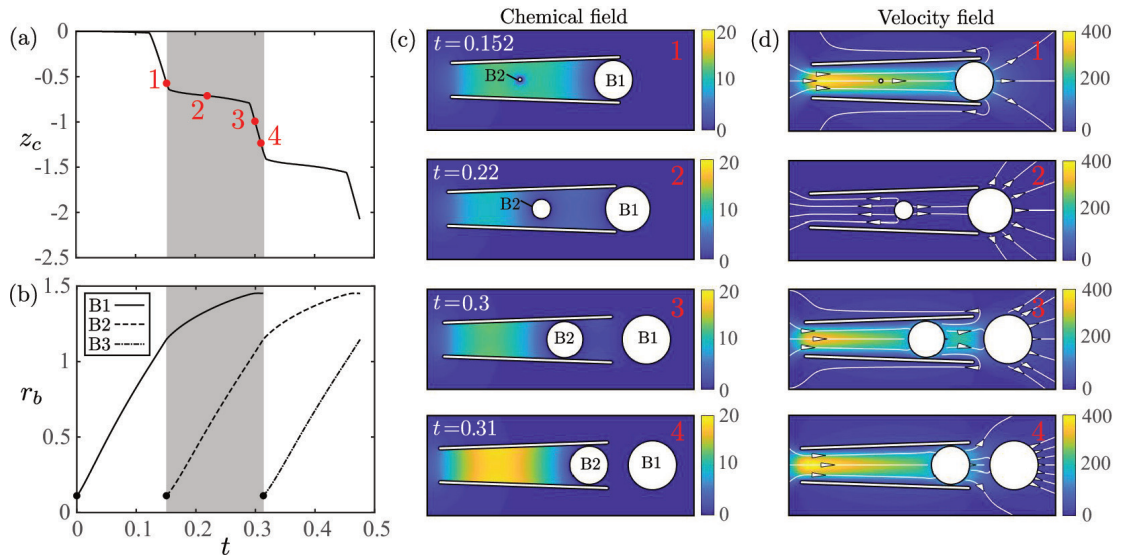


Figure 6.8 – Chemical concentration and bubble dynamics when many bubble are present in the cone for the parameters $H^{cc} = 0.1$, $\beta = 1$ and $\theta = 2^\circ$: (a) Time-dependence of the cone position, with the shaded region highlighting one bubble cycle; (b) Time-dependence of the bubble radius, r_b , with each line describing a different bubble; (c,d) Snapshots of the dissolved gas concentration and velocity field (streamlines and intensity) at the four instants shown in panels (a)

6.4 Conclusions

In summary, in this paper we have used numerical simulations to develop a joint chemical and hydrodynamic analysis of the bubble growth within a conical catalytic microrocket and of the associated bubble and microrocket motion. Our computations have revealed number of important physical features. First, we have found that most of the displacement of the microrocket is attained when the bubble is strongly confined by the conical-shaped swimmer. Second, we have shown that the chemical and the hydrodynamic problem can be decoupled: the chemical problem determines the bubble ejection frequency while the hydrodynamic problem determines the microrocket displacement. Finally, we have systematically studied the microrocket swimming velocity, finding the optimal cone shape and size which maximize it.

In our future work, we plan to explore the relevance of the bubble deformation and the interaction between many bubbles, both relevant to real applications where a lot of bubbles are seen to be emitted close to each other. Preliminary computational results seem to indicate that, although the presence of many bubbles slightly modify the quantitative performance of the motor, it does not alter the qualitative picture obtained for the one-bubble case where a periodic bubble cycle establishes and essentially all the microrocket displacement is obtained when bubbles are geometrically confined by the conical-shaped swimmer. Overall, our results shed light on the fundamental chemical and hydrodynamic processes of the propulsion of

Chapter 6. Physics of Bubble-Propelled Microrockets

catalytic conical swimmers and will allow the experimental design of optimal bubble-propelled microrockets.

Acknowledgements

This project has received funding from the Swiss National Science Foundation (SNFS) with the Doc.Mobility Fellowship P1ELP2_172277 (G.G.) and the European Research Council (ERC) under the European Union's Horizon 2020 research and innovation program under grant agreements 714027 (S.M.), 682754 (E.L.) and 280117 (E.G.). The computer time has been provided by SCITAS at EPFL.

Keywords

microswimmer, microrocket, self-propulsion, catalytic swimmer, numerical simulations

7 The hydrodynamics of a microrocket propelled by a deformable bubble

G. Gallino^{1,2}, L. Zhu^{1,2,3} and F. Gallaire¹

¹Laboratory of Fluid Mechanics and Instabilities, EPFL, CH1015 Lausanne, Switzerland

²Linné Flow Centre and Swedish e-Science Research Centre (SeRC), KTH Mechanics, SE 10044 Stockholm Sweden

³Department of Mechanical and Aerospace Engineering, Princeton University, NJ 08544, USA

In preparation.

7.1 Introduction

Self-propelling artificial micro-swimmers have attracted the attention of the researchers for their utilization in a number of biomedical applications, for example drug delivery [108, 109, 119], nanosurgery [31] and cell sorting [111, 34]. Among the most promising micro-swimmers are those converting chemical energy into propulsion energy, via a catalytic decomposition of fuel (usually oxygen peroxide); the chemical reaction produces oxygen bubbles that propel the swimmer. We consider a conical-shaped swimmer, where the bubbles forming inside the cone move toward its larger opening to minimize the interfacial energy. This configuration has been studied experimentally, focusing on the swimmer speed and the trajectory attained, while the first in vivo use of this technology for drug delivery has been conducted [47]. An important aspect is the modeling of the micro-swimmer motion, some studies concentrate on the movement of the bubble when still inside the cone [128], others consider mainly the locomotion due to the bubble exiting the cone [130, 131]. In contrast to Chapter 6, we relax the assumption on the bubble sphericity, considering a deformable bubble. This enables us to study in detail the hydrodynamics of the swimmer motion. In particular we underline the nontrivial dependency of the swimming velocity on the characteristics of the bubble (deformability and nucleation position) and on the geometry of the swimmer. We identify three distinct periods during the bubble evolution: immediately after nucleation the bubble is

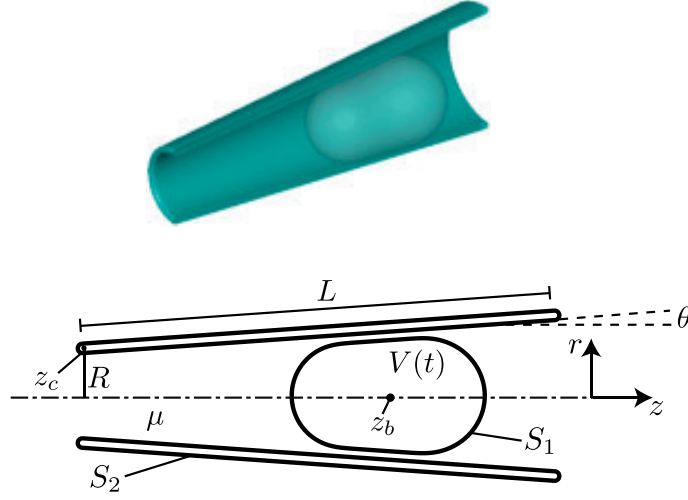


Figure 7.1 – Sketch of the geometrical configuration.

spherical and its inflation barely affects the swimming speed; then the bubble starts to deform due to the confinement gradient generating a pressure that propels the swimmer; in the last period it exits the cone producing an increase in the swimmer velocity. Our results shed light on the fundamental hydrodynamics of the propulsion of catalytic conical swimmers and may help to improve the efficiency of these machines.

7.2 Model

We compute the motion of a conical shaped microswimmer due to the inflation of a deformable bubble of volume $V_B(t)$. The cone geometry is measured in unit of the cone opening radius R (see Figure 7.1) and its shape is defined by its opening angle θ and aspect ratio $\xi = L/R$. In this study we fix $\xi = 10$, which is the most common design in experiment [111, 130, 128], and study the microrocket velocity for different θ . The molar flux emitted from the catalyst is $\dot{n} = \mathcal{A} \xi R^2$, where $\mathcal{A} = 10^2 \text{ mol m}^{-2} \text{ s}^{-1}$ [128] is the molar flux per surface area and it is a material property of the catalyst. In order to simplify the problem, we consider that \mathcal{A} is constant throughout the simulation and that all chemical flux is direct to a growing bubble inside the cone. The motion of the suspending fluid of viscosity μ is triggered by the bubble growth and it is found by solving Stokes equations [36], because inertia and gravity are negligible ($\text{Re} \approx 10^{-4}$ and $\text{Bo} \approx 10^{-6}$ based on the average cone velocity of $\bar{U} = 10^{-4}$ m/s, measured experimentally in [128]). The viscosity of the bubble is negligible compared to the one of the suspending fluid and the surface tension for the air-water interface is $\gamma = 7.2 \times 10^{-2}$ N/m. In this study, we will investigate the influence of the cone geometry (varying the opening angle θ) and the bubble deformability on the swimming velocity.

7.2.1 Hydrodynamics

In order to find the swimming velocity of the microrocket, we solve for the fluid motion by resolving the Stokes equation. Considering the following reference scales,

$$[U] = \frac{\gamma}{\mu} \quad [L] = R \quad [T] = \frac{R\mu}{\gamma} \quad [P] = \frac{\gamma}{R}. \quad (7.1)$$

the non-dimensional Stokes equations, for fluid velocity \mathbf{u} and pressure p , write as

$$-\nabla p + \nabla^2 \mathbf{u} = 0, \quad \nabla \cdot \mathbf{u} = 0, \quad (7.2)$$

imposing, on the cone surface S_2 , a rigid body translation with velocity $\mathbf{U}_c = \dot{z}_c \mathbf{e}_z$ in the axial direction

$$\mathbf{u} = \mathbf{U}_c, \quad \text{for } \mathbf{x} \in S_2. \quad (7.3)$$

On the bubble surface S_1 , we impose the discontinuity of normal stress due to surface tension and disjoining pressure $\mathbf{\Pi}$

$$\boldsymbol{\sigma} \cdot \mathbf{n} - p_B \mathbf{n} = (\nabla_s \cdot \mathbf{n}) \mathbf{n} + \mathbf{\Pi}(\mathbf{x}) \quad \mathbf{x} \in S_1 \quad (7.4)$$

where $\boldsymbol{\sigma}$ is the stress tensor, p_B is the gas pressure inside the bubble, \mathbf{n} is the normal vector pointing into the suspending fluid and $\nabla_s = (\mathbf{I} - \mathbf{nn})\nabla$ is the surface gradient operator. The disjoining pressure at the location $\mathbf{x} \in S_1$ of the bubble interface due to the proximity to the cone surface is modeled as in [57], namely

$$\mathbf{\Pi}(\mathbf{x}) = \begin{cases} \int_{S_2} B \frac{e^{\delta-r} - 1}{e^\delta - 1} \frac{\mathbf{x} - \mathbf{y}}{d} dS(\mathbf{y}) & \text{for } d \leq \delta \\ 0 & \text{for } d > \delta \end{cases} \quad (7.5)$$

where $d = |\mathbf{x} - \mathbf{y}|$ and δ and B are the range and the magnitude of the force. This law mimics the repulsion due to an electric double layer potential [140]. The bubble volume V_B is imposed as a global constraint and varies following the ideal gas law (variables indicated by tilde denote dimensional quantities)

$$\frac{d(\tilde{p}_B \tilde{V}_B)}{d\tilde{t}} = \dot{n} \mathcal{R} T_0, \quad (7.6)$$

$$= \mathcal{A} \xi R^2 \mathcal{R} T_0, \quad (7.7)$$

where \dot{n} is the molar flow rate, \mathcal{R} is the ideal gas constant and $T_0 = 300K$ is the ambient room temperature. When imposing the molar flux, the volume increase is found by assuming that the internal bubble pressure is the one of a spherical bubble of equivalent volume

$$\tilde{p}_B = \tilde{p}_0 + \frac{2\gamma}{(\frac{3}{4\pi} \tilde{V}_B)^{1/3}}, \quad (7.8)$$

Chapter 7. The hydrodynamics of a microrocket propelled by a deformable bubble

Substituting equation (7.8) into (7.6) and making the variables non dimensional, we obtain

$$\frac{dV_B}{dt} = \frac{Ca}{\beta + CV_B^{-1/3}} \quad (7.9)$$

where $Ca = \frac{\mathcal{A}\xi R\mathcal{R}T_0}{\gamma} \frac{\mu}{\gamma}$ is the capillary number and $\beta = \frac{p_0 R}{\gamma}$ and the constant $C = \frac{4}{3(\frac{3}{4\pi})^{1/3}}$. Physically the capillary number is the ratio between the velocity $\frac{\mathcal{A}\xi R\mathcal{R}T_0}{\gamma}$ coming from the bubble inflation due to the chemical influx and the characteristic velocity of deformation of the interface γ/μ . Finally the cone velocity is found by imposing that the system is globally force free (as expected in Stokes flow), implying that the net force on the bubble due to the repulsive forces is applied back on the cone

$$\int_{S_2} \mathbf{f} \cdot \mathbf{e}_z dS + \int_{S_1} \mathbf{\Pi} \cdot \mathbf{e}_z dS = 0. \quad (7.10)$$

For a given geometry (cone-bubble shape and position), equations from (7.2) to (7.10) can be solved numerically (see next section for details of the numerical implementation). This gives the cone velocity \mathbf{U}_c and the bubble interface velocity. The time evolution of the system is found by solving

$$\frac{dz}{dt} = \mathbf{U}_c \cdot \mathbf{e}_z, \quad (7.11)$$

$$\frac{d\mathbf{x}}{dt} = \mathbf{u} \quad \text{for } x \in S_1 \quad (7.12)$$

The initial conditions is a bubble of size R_0 placed in z_0 , the non-dimensional number of the problem are the capillary number Ca , the intensity B and activation distance δ of the disjoining pressure and the pressure ratio β . The capillary number $Ca = \mathcal{A}\xi R\mathcal{R}T_0\mu/\gamma^2$, based on the molar flow rate, lies approximately in the range $Ca \in 10^{-5} - 10^{-4}$, at most $Ca \in [10^{-4} - 10^{-3}]$. We consider $Ca \in [10^{-3}, 5 \times 10^{-1}]$, larger than in real applications, due to the increasing stiffness of the problem for smaller capillary numbers. However, large capillary numbers might be of interest when considering enhanced catalysts [138] resulting in larger \mathcal{A} . Similarly the intensity of the disjoining pressure is set to $B = 10$ and the activation distance to $\delta = 0.2$, both larger than typical experimental values, in order to ease the numerical simulation by having a thicker film. Finally, we fix $\beta = 1$, which is considered a representative value of this system [141]. We expect these choices to slightly influence the quantitative results of our study but still provide physical insights into this system.

7.2.2 Numerical method

Assuming axisymmetric flow, we re-write equation (7.2) as a boundary integral equation [49] on the domain contour in the meridional plane: l_1 and l_2 corresponding to S_1 and S_2 respec-

7.3. Velocity field and microrocket velocity over one bubble cycle

tively. The velocity on a point \mathbf{x}_0 lying on the interface is given as

$$4\pi\mathbf{u}(\mathbf{x}_0) = - \int_{l_1} \mathbf{M}(\mathbf{x}_0, \mathbf{x}) \cdot \Delta\mathbf{f}(\mathbf{x}) dl + \int_{l_1}^{\text{PV}} \mathbf{n}(\mathbf{x}) \cdot \mathbf{q}(\mathbf{x}_0, \mathbf{x}) \cdot \mathbf{u}(\mathbf{x}) dl - \int_{l_2} \mathbf{M}(\mathbf{x}_0, \mathbf{x}) \cdot \mathbf{f}(\mathbf{x}) dl + \mathbf{n}(\mathbf{x}_0) \left(\int_{l_1} \mathbf{u}(\mathbf{x}) \cdot \mathbf{n}(\mathbf{x}) dl - \dot{V}_B \right), \quad (7.13)$$

where $\Delta\mathbf{f} = \boldsymbol{\sigma} \cdot \mathbf{n} - p_B \mathbf{n}$. When \mathbf{x}_0 lies on the cone wall

$$8\pi\dot{z}_c \mathbf{e}_z = - \int_{l_1} \mathbf{M}(\mathbf{x}_0, \mathbf{x}) \cdot \Delta\mathbf{f}(\mathbf{x}) dl + \int_{l_1} \mathbf{n}(\mathbf{x}) \cdot \mathbf{q}(\mathbf{x}_0, \mathbf{x}) \cdot \mathbf{u}(\mathbf{x}) dl - \int_{l_2} \mathbf{M}(\mathbf{x}_0, \mathbf{x}) \cdot \mathbf{f}(\mathbf{x}) dl + \mathbf{n}(\mathbf{x}_0) \left(\int_{l_1} \mathbf{u}(\mathbf{x}) \cdot \mathbf{n}(\mathbf{x}) dl - \dot{V}_B \right). \quad (7.14)$$

The Green's functions \mathbf{M} and \mathbf{q} are the axisymmetric velocity and stress fields obtained from a ring of point forces acting in \mathbf{x} , as explained in detail in Chapter 2 and Ref. [49, 50]. The third term on the right hand side of (7.13) & (7.14) has to be treated in order to remove a neutral mode in the operator [50] (by applying an integral constraint after singular preconditioning, as explained in Chapter 2 and Ref. [50]). The last term on the right hand side is responsible for the bubble inflation [59]. The force free condition (7.10) writes as

$$\int_{l_2} r \mathbf{f} \cdot \mathbf{e}_z dl + \int_{l_1} r \boldsymbol{\Pi} \cdot \mathbf{e}_z dl = 0. \quad (7.15)$$

The cone geometry is then discretized into N_w straight constant elements and the bubble into N_b curved linear elements. Discretization of equation (7.13), (7.14) & (7.15), employing P_0 elements of the cone surface and P_1 elements on the bubble surface [50], gives a $(2N_w + 2N_b + 3) \times (2N_w + 2N_b + 3)$ linear system that can be solved numerically for the stresses on the cone surface, the interface velocity and the cone velocity. Converged results are reached by choosing $N_w = 124$ and $N_b = 20$ for a bubble of initial radius $R_0 = 0.5$. Subsequently, due to the bubble inflation and deformation, mesh elements are added both on the deformable bubble and on the wall, in order to keep high accuracy in the lubrication film region, see Chapter 2 for detailed explanations. The time evolution of the system is found by solving equations (7.11) & (7.12) with second order Runge-Kutta scheme.

7.3 Velocity field and microrocket velocity over one bubble cycle

A typical bubble evolution and associated cone motion is depicted in figure 7.2 for $\text{Ca} = 0.01$ and $\theta = 1^\circ$. The bubble cycle starts when the bubble is inside the microrocket and it ends when it exists, recovering a spherical shape (see snapshots in Figure 7.2a-d). Intuitively, since the bubble tends to recover a spherical shape in order to minimize its surface energy, we can propose the interpretation that a deformed bubble is *storing* energy that will be released into propulsion energy at a certain point. In particular we monitor the excess surface area $\Delta A = A - A_B$ (the current surface area A minus the surface area A_0 of a spherical bubble of

same volume), which is scalar quantity describing the degree of bubble deformation: ΔA is zero for spherical bubbles and larger than zero for deformed ones. The behavior of ΔA along the bubble cycle allows us to define three different phases:

- Phase *I* (Spherical phase): the bubble is spherical and not confined (from $t = 0$ to $t \approx 700$). As shown in Figure 7.2a, the fluid is expelled from opening of the cone, due to the inflation of the bubble. During this phase ΔA is almost equal to zero and the cone-bubble displaces very slowly.
- Phase *II* (Migration phase): the bubble is geometrically confined and squeezed inside the cone (from $t \approx 700$ to $t \approx 2100$). As shown in Figure 7.2b-c, the bubble starts to translate fast due to the geometrical confinement, this causes the fluid to be sucked from the smaller cone opening. During this phase the bubble becomes more and more squeezed, as ΔA increases (see Figure 7.2e). The cone and bubble velocity increase (see Figure 7.2f-g) due to the increasing geometrical confinement.
- Phase *III* (Recoil phase): finally, the bubble exits the cone and during what we call recoil phase, from $t \approx 2100$ to $t \approx 2600$, when the bubble rapidly restores its spherical shape (see Figure 7.2d). This phase clearly starts when ΔA is maximum and continues when ΔA decreases recovering the spherical shape. During this phase, the rapid *release of energy* due to bubble relaxation leads to the maximum cone and bubble velocity (i.e maximum slope of cone and bubble displacement in figure 7.2f and 7.2g).

The cone velocity behavior over one bubble cycle that we have reported seems to provide an explanation to the unsteady cone velocity observed experimentally [128]. Namely, the cone displaces relatively slow during phase *I* and *II* while it displaces much faster during phase *III* due to the large release of surface energy. In Figure 7.3 we report the far field velocity, created by (a) the cone, (b) the bubble and (c) the sum of the two at $t = 1000$. The cone and bubble contribute to the velocity field with a Stokeslet contribution [36], because they are not force free due the disjoining pressure term in (7.4) (see Figure 7.3a-c-d-f). However, the microswimmer is globally force free due to equation (7.15), leading to a stresslet-like velocity field (see Figure 7.3c-f).

7.4 Influence of the opening angle

7.4.1 Direct numerical simulations

The opening angle of the cone is an important design parameter. In this section we vary it and look at its effect on the average microrocket velocity \bar{U} . We first fix $Ca = 0.01$ and vary θ , Figure 7.4a shows snapshots of the time evolution for different opening angle. We can observe that the bubble cycle duration Δt is smaller for $\theta = 1^\circ$, pointing to the fact that there might be some non-monotonic behavior when varying the opening angle. First, we notice

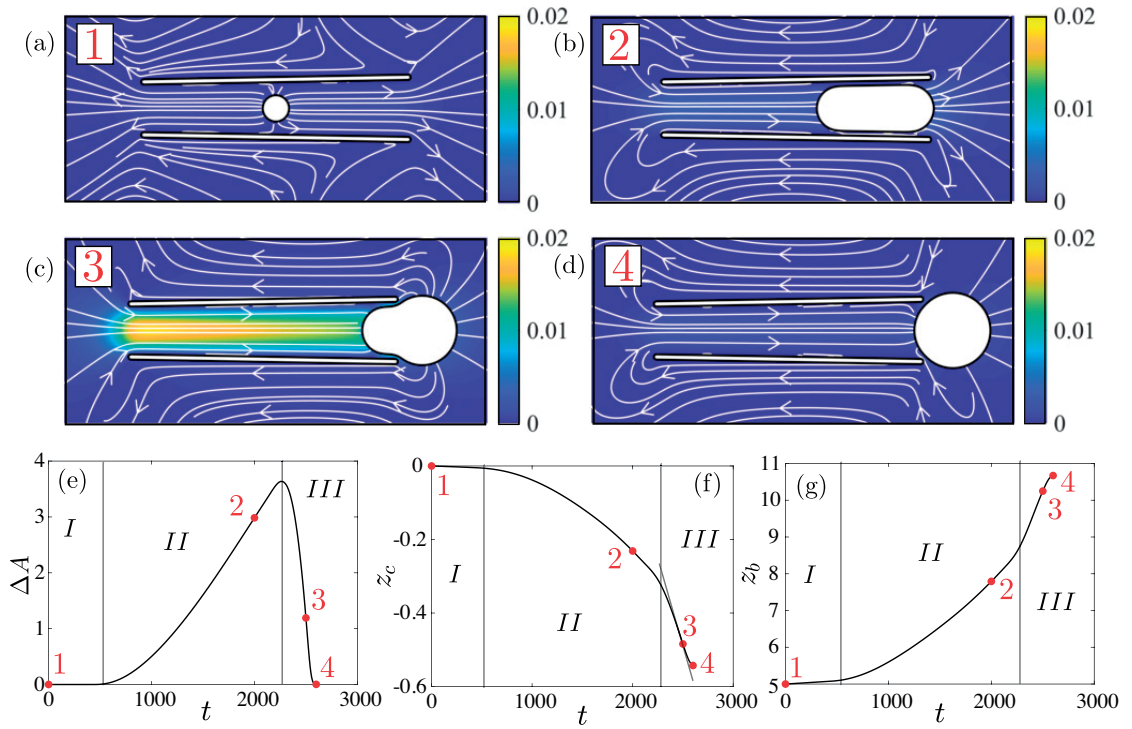


Figure 7.2 – Bubble cycle for $Ca = 0.01$ and $\theta = 1^\circ$. (a-b-c-d) Snapshots along the bubble cycle, velocity magnitude and streamlines from bubble nucleation to when the bubble exists the cone. (e) Cone and (f) bubble position. (g) Excess surface area. Vertical lines show the separation between phase *I*, *II* and *III*.

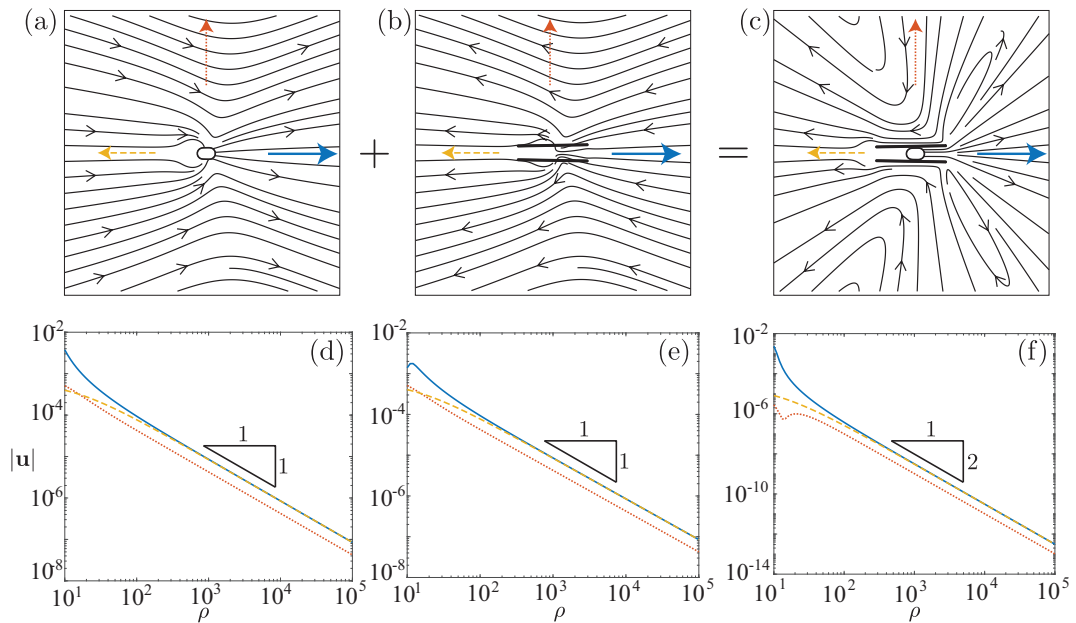


Figure 7.3 – Far field streamlines and velocity intensity at $t = 1000$, $Ca = 0.01$, $\theta = 1^\circ$. (a-b-c) Cone, bubble and cone-bubble generated velocity field respectively and (d-e-f) corresponding far field decay.

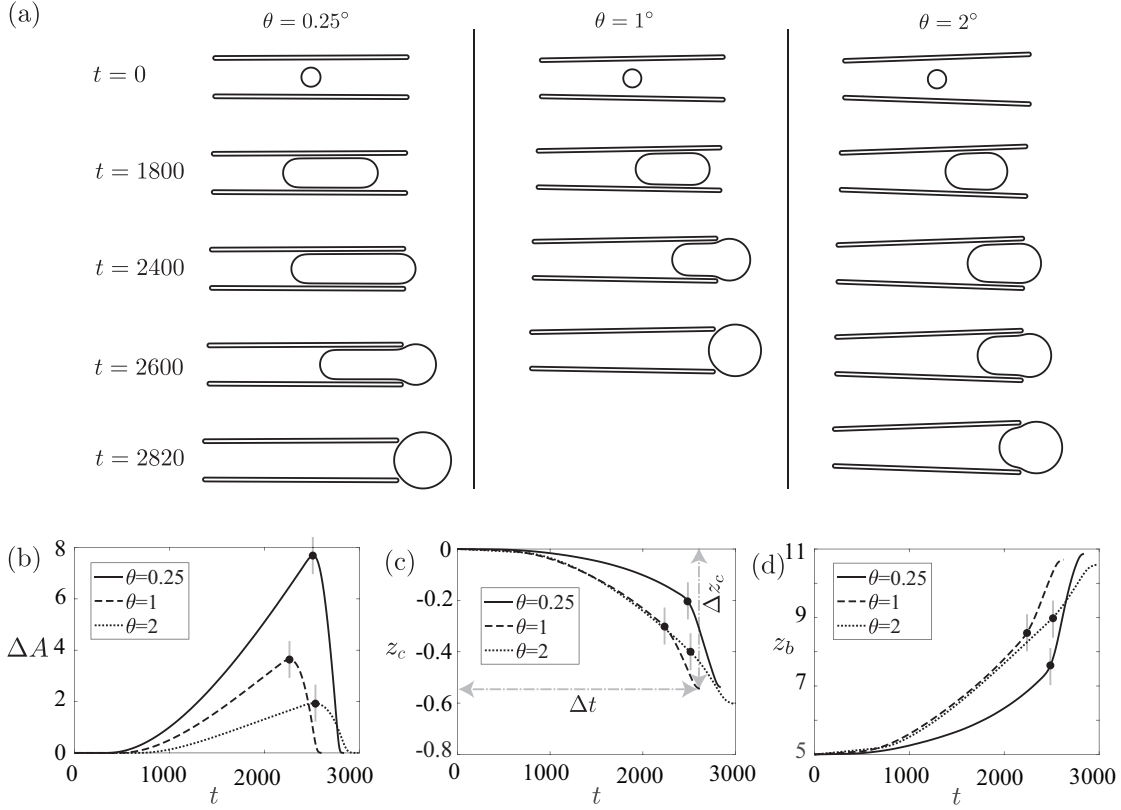


Figure 7.4 – (a) Snapshots of the time evolution for three opening angle $\theta = [0.25, 1, 2]$, $Ca = 0.01$, and corresponding (b) excess surface area (c) cone position and (d) bubble position.

that the excess surface area at the beginning of the recoiling phase is larger for smaller θ , because the geometrical confinement is larger for smaller θ (see Figure 7.4b). Therefore, while recoiling, bubble releases more energy for smaller θ which leads to higher fluid velocity (in fact, both bubble and cone displace faster, see Figure 7.4c-d). Therefore, it seems that the non-monotonic behavior of the bubble cycle duration comes from phase *I* and *II*, as suggested by the non-monotonic start-point of the recoiling phase as shown in Figure 7.4b.

In Figure 7.5, we investigate more in depth where the non-monotonicity comes from. First of all, the average velocity $\bar{U} = \Delta z_c / \Delta t$ shows indeed an optimum for $\theta \approx 1^\circ$. This optimum is dictated by a minimum in Δt , while Δz_c increases almost monotonically, as shown in Figure 7.5a-b. More specifically, the minimum in Δt is given by a minimum in Δt_{I+II} (the duration of phase *I* and *II*), while Δt_{III} (the duration of phase *III*) increases monotonically. Therefore, the non-monotonic average velocity, with a maximum for $\theta \approx 1^\circ$ shown in figure 7.5c, is dictated almost exclusively by phase *I* and *II*. In fact, while the third phase exhibits a monotonic decrease of the average velocity $\bar{U}_{III} = \Delta z_c^{III} / \Delta t_{III}$ in θ (Δt_{III} monotonically increases and Δz_c^{III} monotonically decreases), the first two phases show an optimum for $\bar{U}_{I+II} = \Delta z_c^{I+II} / \Delta t_{I+II}$. This optimum is non-trivial to explain and we will attempt an investigation with a simplified model in next section.

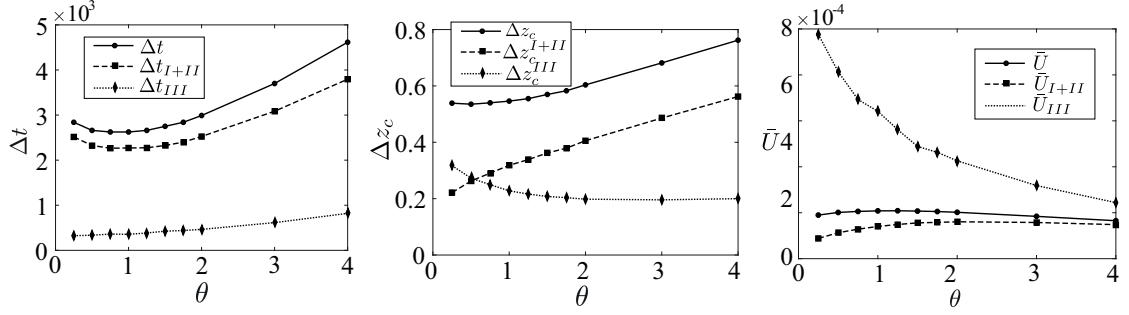


Figure 7.5 – Relevance of the two phases over one bubble cycle: (a) Bubble cycle duration Δt and duration of first and second phase Δt_{I+II} and third phase Δt_{III} , respectively. (b) Cone displacement over one bubble cycle Δz_c , cone displacement over the first and second phase Δz_c^{I+II} and third phase Δz_c^{III} . (c) Microrocket average velocity over one bubble cycle \bar{U} , average velocity over the first and second phase \bar{U}_{I+II} and third phase \bar{U}_{III} .

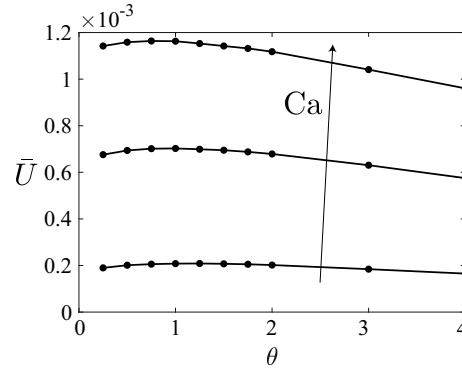


Figure 7.6 – Microrocket average velocity versus cone angle θ for $Ca = [0.01, 0.05, 0.1]$.

In figure 7.6 we plot the average velocity versus the opening angle for different capillary numbers. The optimum exists for all capillary numbers considered and it is attained approximately for $\theta \approx 1^\circ$. Interestingly, the average velocity does not vary much (at least keeping $\theta < 4^\circ$), pointing to the idea that, when increasing θ , a reduced performance of the second phase is somehow counterbalanced by an improved performance of the first phase. This might explain the robustness in the microrocket swimming velocity observed in experiments, even when using different fabrication techniques that might result in different opening angles.

7.4.2 An empirical spring-like model for confined bubbles

The objective of this section is to understand why there is an optimal angle for the swimming velocity. We focus on the modeling of the phase *II*, where the optimum originates, while phase *I* is probably not important because it appears as independent of θ . We proceed empirically, by drawing an analogy between a simple spring, where the force is proportional to the displacement due to Hooke's law $F \sim dx$, and a bubble where we impose that a restoring force is exerted when the bubble is deformed and that this force is proportional to the excess

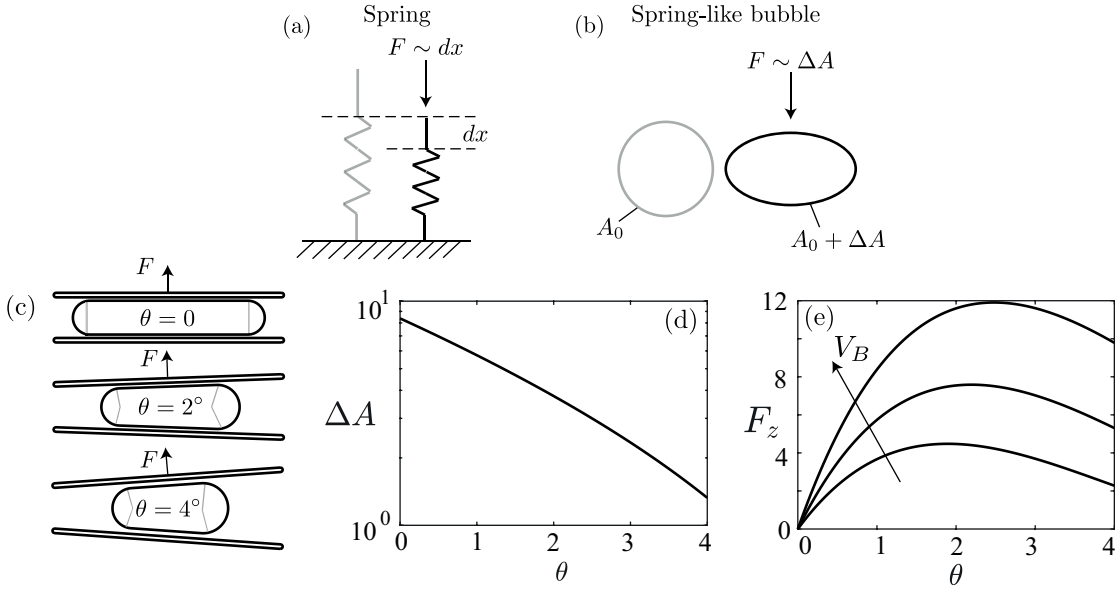


Figure 7.7 – Spring-bubble empirical model. (a) Sketch of Hooke's law. (b) Sketch of the analogy to Hooke's law for bubbles where $F \sim \Delta A$. (c) Bubble of volume V_0 squeezed in cones of different opening angles. (d) Excess area ΔA versus θ assuming that the droplet is made of a conical section and two spherical caps. (e) Axial forces F_z versus θ for different bubble volumes $V_B = [1.3, 1.4, 1.5]$.

area $F \sim \Delta A$ (see figure 7.7a). Note that by assuming this linear behavior we are neglecting all the details of the lubrication film that could modify this scaling. Assuming small θ , the force acting on the cone wall in the axial direction due to the restoring force of the bubble (see Figure 7.7b) writes

$$\frac{F_z}{\theta} \sim \Delta A \rightarrow F_z \sim \Delta A \theta. \quad (7.16)$$

For a given volume, the excess area decreases when the opening angle increases because the geometrical confinement decreases. In figure 7.7d we compute numerically the excess area assuming that the bubble is made by a cone section closed by spherical caps whose center of mass is placed in the middle on the cone. Fixing the volume and film thickness, the bubble shape is uniquely determined. For small θ the excess surface area seems to decrease exponentially, although we have not yet attempted to show it analytically. Therefore, F_z shows a non-monotonic behavior as a function of θ . Namely, $F_z(0) = 0$ because the projection of the force in the axial direction is null and it is small for sufficiently large θ because the exponential decrease of ΔA dominates over the linear increase of the projection angle (see Figure 7.7e). Thus, assuming that the microrocket velocity scales linearly with F_z and that its drag is constant when varying θ , these two effects explain the non-monotonic behavior of the microrocket velocity observed in the previous section. As will become clear in next section, we can take into account the variation of capillary number by imposing different bubble volumes, as shown in figure 7.7e.

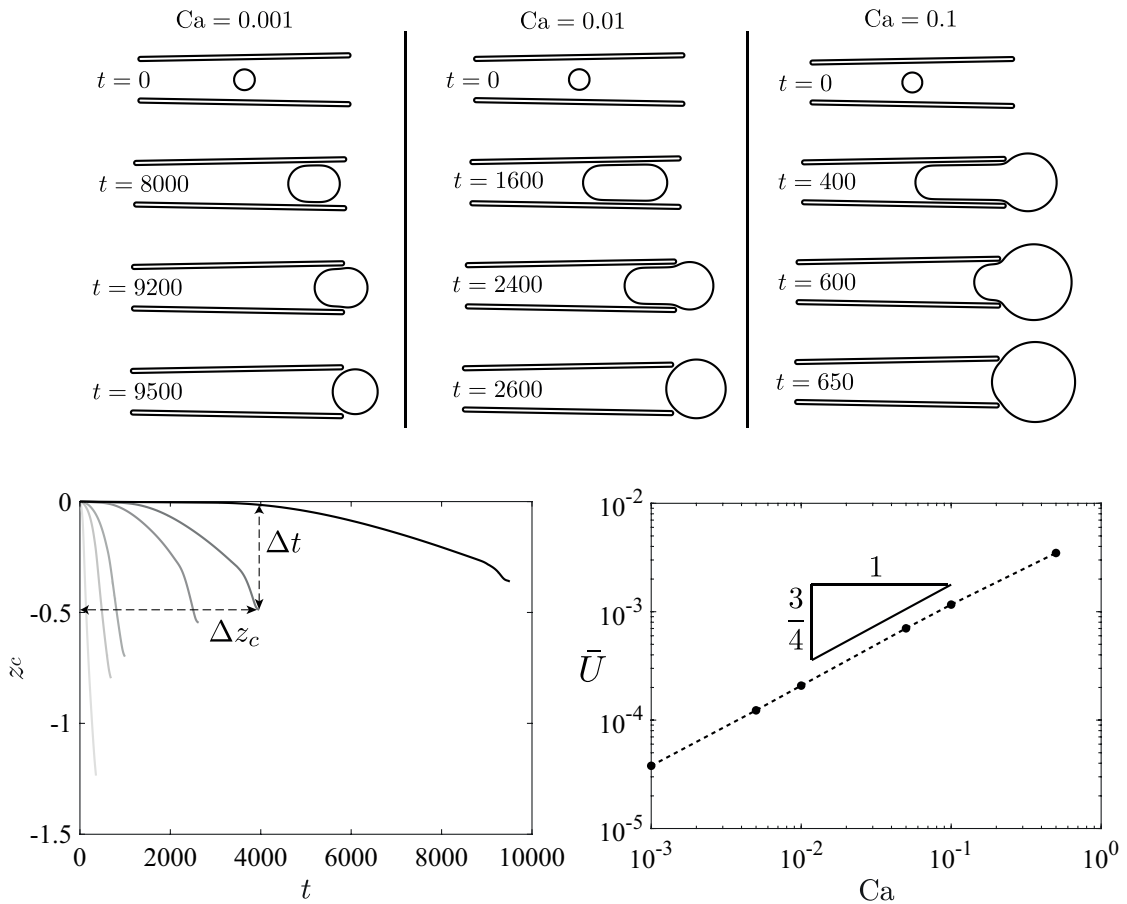


Figure 7.8 – (a) Snapshots for the time evolution at different capillary numbers, $\theta = 1^\circ$. (b) Cone position versus time, black to light grey line for increasing capillary numbers $Ca = [0.001, 0.005, 0.01, 0.05, 0.1, 0.5]$. (c) Average velocity versus capillary number.

7.5 Influence of the capillary number

In Figure 7.8a we show the results of many simulations at different capillary numbers. When increasing the capillary number, the bubble inflates more rapidly. The consequence are two-fold: the bubble cycle is shorter and the cone displacement is larger. Both effects contribute to the increase of the average velocity as a function of the capillary number (see Figure 7.8b), seemingly with a scaling $\bar{U} \sim Ca^{0.75}$. Results for different opening angles (i.e $\theta = 2^\circ$) show apparently the same scaling. As a consequence, a change in chemical flux (say ten times) will not result in the same variation of the swimming velocity due to the slight sublinearity of the scaling. We have not yet been able to explain the physical origin of this scaling.

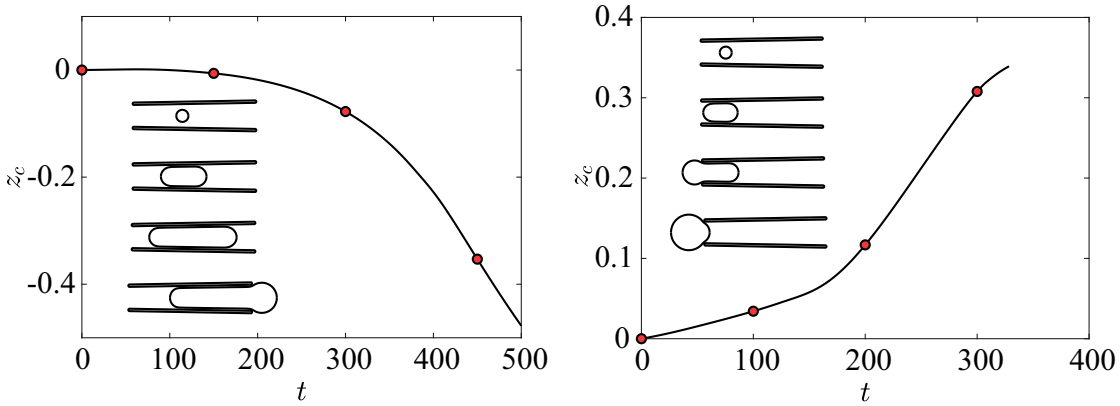


Figure 7.9 – Cone position versus time when (a) $z_b(0) = 4$ and (b) $z_b(0) = 2$. The insets show snapshots corresponding to the circles.

7.6 Critical threshold for sustained bubble ejection

In this section we study the influence of the initial bubble position on the bubble cycle. Focussing this time on $Ca=0.1$, we report two cases where $z_b(0) = 4$ and $z_b(0) = 2$. When $z_b(0) = 4$ the bubble cycle is similar to what previously observed ($z_b(0) = 5$ in all previous simulations, corresponding to the middle of the cone), but when $z_b(0) = 2$ the bubble exits from the smaller opening, as shown in figure 7.9. This situation might reproduce an issue reported in experiments, where the bubble exits from the smaller opening and a unidirectional motion is not attained [130]. In fact, when the bubble exits from the smaller opening, the microrocket displaces from right to left. For smaller capillary number this problem is less present because bubbles deform less and soon start to translate toward the larger opening. Since the capillary number increases for higher chemical fluxes $\dot{n} = \mathcal{A}\xi$, using enhanced catalysts or longer microrockets might worsen this phenomenon and become a serious challenge to achieve a sustained bubble cycle.

7.7 Conclusions

We have investigated numerically the motion of a catalytic microrocket due to the inflation of a deformable bubble. We have identified a physical quantity, the excess surface area, which defines three phases of the bubble growth and corresponding microrocket motion. The different phases correspond to low microrocket velocity, when the bubble is confined, and to high microrocket velocity, when the bubble exits and recoils. By studying the influence of the different phases when varying the design parameters (as the opening angle of the cone), we have identified optimal working condition and we have concluded that these conditions are robust for small opening angles. This leads to the conclusion that as long as the opening angle is small ($\theta < 4^\circ$), there is no particular need of optimizing this parameter from the hydrodynamic point of view. This weak optimum has been physically explained with an empirical model. Moreover, we have observed a sublinear scaling of the average

swimming velocity with the capillary number. As a consequence, enhanced catalysts, which are extensively studied, would possibly lead to an increase of velocity but a decrease of efficiency. Finally, we have analyzed the dependence of the swimming velocity upon the initial bubble position: in particular, when a bubble is close to the smaller opening it might exit from there causing a microrocket motion in the "wrong" direction. This phenomenon, that has been observed in the literature [130], is more likely to happen at high capillary number, which might pose technological problems when increasing Ca with enhanced catalysts surfaces [138]. In future work, we plan to couple the chemical problem treated already in Chapter #, with non-trivial hydrodynamics introduced by the bubble deformability and studied here.

8 The motion of a bubble inflating next to a wall

G. Gallino^{1,2}, F. Gallaire¹, E. Lauga² and S. Michelin^{2,3}

¹Laboratory of Fluid Mechanics and Instabilities, EPFL, CH1015 Lausanne, Switzerland

²Department of Applied Mathematics and Theoretical Physics, University of Cambridge
CB3 0WA, United Kingdom

³LadHyX – Département de Mécanique, CNRS – Ecole Polytechnique,
91128 Palaiseau Cedex, France

In preparation.

8.1 Introduction

The motion of spherical objects close to boundaries is a classical problem in fluid mechanics [142, 143, 48] and it is relevant to many disciplines, for example sedimentation of blood cells in biology [144] or the rise of bubbles toward the free surfaces of the sea, which is crucial for the marine-atmospheric ecosystem [145, 146]. Since the dynamics is dominated by the lubrication film established in the sphere-boundary gap, lubrication theory is the right tool to analyze these problems. In particular, lubrication theory is able to answer the question: is there sphere-boundary contact in finite time? In the aforementioned cases, there is no contact in finite time for a sedimenting spheres [24] while there is for bubble moving towards the sea free surface [147].

In this study we investigate a slightly different problem, where a spherical bubble inflates close to a wall. This situation is relevant for applications, for example boiling and bubble-propelled microswimmers studied in Chapter 6 & 7. Contrary to the aforementioned cases, where the film drainage and contact with the wall is generated by imposing an external force, here the driving mechanism is the bubble growth and the resistance of surrounding fluid that compresses the lubrication film. The small scales at which the phenomena happen justify the

assumptions of considering a spherical bubble, assuming that surface tension dominates over viscous dissipation.

We proceed by first solving numerically the governing equations and then we develop the lubrication analysis. We identify different regimes in which the bubble-wall gap closes or not in finite time depending on the bubble boundary conditions.

8.2 Description of the problem

We consider here the fluid motion and resulting displacement of a growing or shrinking gas bubble near a fixed flat infinite boundary $\partial\Omega_w$ (see Figure 8.1). The bubble radius $a(t)$ and the sphere-wall distance $d(t)$ are measured in unit of initial bubble radius a_0 . The fluid has density ρ and dynamic viscosity η . The rate of change of the bubble \dot{a} , measured in units of initial rate \dot{a}_0 , is prescribed here and may result from gas dissolution within the bulk fluid or phase transition (e.g. evaporation) at the liquid-gas interface. Inertial effects and bubble deformation are neglected (i.e. $Re = \dot{a}_0 a_0 / \nu \ll 1$ and $Ca = \eta \dot{a}_0 / \gamma \ll 1$). Using a time scale $T = a_0 / \dot{a}_0$ of the variations in bubble radius, the hydrodynamic problem can be written in non-dimensional form as

$$\nabla^2 \mathbf{u} = \nabla p, \quad \nabla \cdot \mathbf{u} = 0. \quad (8.1)$$

The impermeability condition at the surface of the bubble can be written

$$\mathbf{u} \cdot \mathbf{n} = \mathbf{U} \cdot \mathbf{n} + \dot{a} \quad \text{on } \partial\Omega_b, \quad \mathbf{u} = 0 \quad \text{on } \partial\Omega_w \quad (8.2)$$

with \mathbf{n} the local unit normal vector pointing into the fluid domain and $\mathbf{U} = (\dot{a} + \dot{d})\mathbf{e}_z$ the translation velocity of the center of the bubble.

To close the problem for $(\mathbf{u}, p, \mathbf{U})$, an additional condition must be applied on each boundary to describe the nature of the surface (e.g. perfect slip, no-slip...). To account for impurity of the bubble and keep the most general framework, we consider in the following a slip-length model, i.e.

$$(\mathbf{I} - \mathbf{nn}) \cdot (\mathbf{u} - \mathbf{u}_{\text{ref}}) = \lambda (\mathbf{I} - \mathbf{nn}) \cdot (\nabla \mathbf{u} + \nabla \mathbf{u}^T) \cdot \mathbf{n} \quad \text{on } \partial\Omega_b, \quad (8.3)$$

where λ is the slip-length on the bubble, and characterize the purity of the interface: $\lambda = \infty$ corresponds to a perfect slip condition and a “clean” bubble, while $\lambda = 0$ is equivalent to an inflating spherical shell (e.g. armored bubble with large surface concentration of surfactants). In the following, it will also be referred to as the “rigid shell” limit: for an inflating sphere, this should be understood as a system for which the relative tangential velocity is strictly zero while the normal relative velocity is given by \dot{a} .

In the previous equation, $\mathbf{u}_{\text{ref}} = \mathbf{U} + \dot{a}\mathbf{n}$ is the reference velocity of the rigid shell from which the slip length model is defined. Finally, the flow velocity must satisfy the no-slip boundary

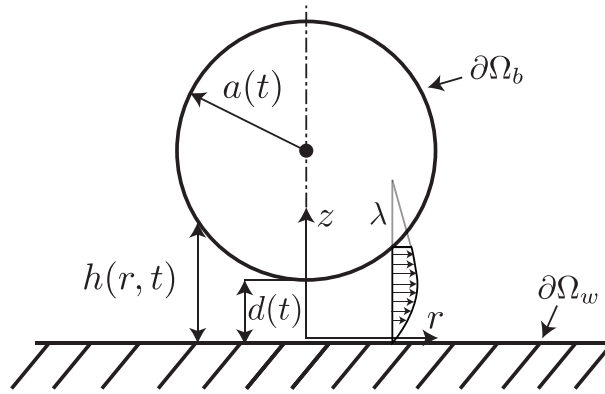


Figure 8.1 – Sketch of a sphere inflating next to a solid wall.

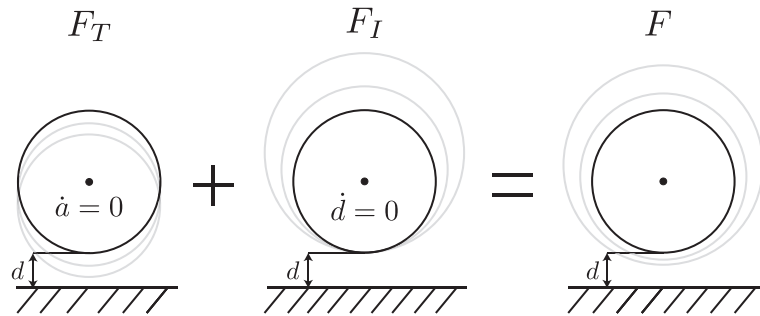


Figure 8.2 – Schematic representation of the different components of the force acting on an inflating sphere: F_T is the force from the translation and F_I from an inflation while the gap is kept constant.

condition $\mathbf{u} = 0$ on the wall, $\partial\Omega_w$.

Once the velocity and pressure field have been obtained by solving the previous hydrodynamic problem, the total hydrodynamic force on the bubble can be computed by integrating the hydrodynamic stress on the bubble surface. Because of the axisymmetry of the problem, $\mathbf{F} = F\mathbf{e}_z$ and using the linearity of Stokes flow, it can be written at each time:

$$F = \mathbf{e}_z \cdot \int_{\partial\Omega_b} \boldsymbol{\sigma} \cdot \mathbf{n} dS = F_T + F_I, \tag{8.4}$$

where F_T and F_I are the forces associated with the translation of the bubble and the increase of its radius holding the minimum bubble-wall distance constant, as sketched in Figure 8.2.

8.3 Numerical results

We solve equations from (8.1) to (8.3) numerically with the boundary element method, together with the force free condition. The implementation is explained in detail in Chapter 2 & 6. The only technical difference is that we use special Green's functions that take into account

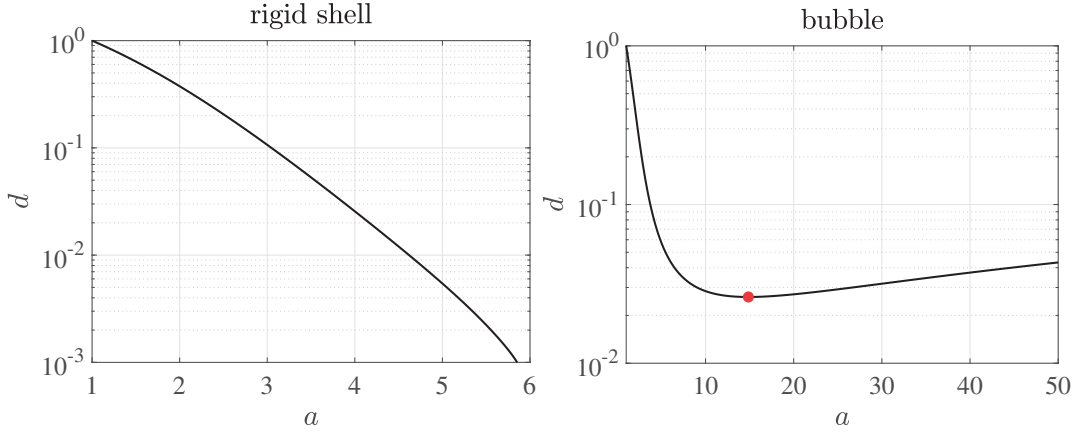


Figure 8.3 – Sphere-wall gap evolution versus sphere size calculated numerically starting from the initial condition $d(0) = 1$. (a) A rigid shell and (b) a bubble.

the presence of the wall, as done in [148]. This allows us to avoid meshing the wall. With this numerical method we are restricted to the case of "clean bubble", $\lambda = \infty$, and "rigid shell", $\lambda = 0$.

The results for these two cases are shown in Figure 8.3, where we plot the gap size d versus the bubble radius a . Therefore, given the linearity of Stokes equation, these curves are valid for every \dot{a} . Interestingly, we obtain a very different behavior in the rigid shell case and in the bubble case. In the first case, the sphere-wall distance decreases monotonically, at least until we are able to carry on our numerical simulation (simulations become computationally more expensive for smaller d). In the second case, d is non-monotonic, meaning that when the gap is small, the wall starts to repel the bubble interface. This unexpected behavior is investigated in detail in next section by lubrication theory.

8.4 Lubrication theory

In the limit of small gap width $\varepsilon \ll 1$, lubrication theory can be used to solve for the flow field within the thin layer of fluid separating the inflating bubble from the wall. This thin film is described in polar coordinates by the position of the bubble's surface $z = h(r, t)$.

Without any approximation on the thickness of the film, the impermeability condition at the bubble surface write

$$u_z(r, h) = \frac{\partial h}{\partial t} + u_r(r, h) \frac{\partial h}{\partial r}. \tag{8.5}$$

Similarly, using the definition of the tangential and normal unit vectors \mathbf{t} and \mathbf{n} ,

$$\mathbf{t} = \frac{\mathbf{e}_r + h' \mathbf{e}_z}{\sqrt{1 + h'^2}}, \quad \mathbf{n} = \frac{h' \mathbf{e}_r - \mathbf{e}_z}{\sqrt{1 + h'^2}} \tag{8.6}$$

and that of the reference surface velocity $\mathbf{u}^{\text{ref}} = (\dot{a} + \dot{d})\mathbf{e}_z + \dot{a}\mathbf{n}$, Eq. (8.3) can be written here in the general case as

$$\lambda \left[(1 - h'^2) \left(\frac{\partial u_z}{\partial r} + \frac{\partial u_r}{\partial z} \right) + 2h' \left(\frac{\partial u_z}{\partial z} + \frac{\partial u_r}{\partial r} \right) \right] + (u_r + h' u_z) \sqrt{1 + h'^2} = h' \sqrt{1 + h'^2} (\dot{d} + \dot{a}). \quad (8.7)$$

In the lubrication assumption, the typical film thickness h is much smaller than the scale of its variations in the radial direction and so is its slope. In that limit,

$$h(r, t) = d(t) + a(t) - \sqrt{a(t)^2 - r^2} = d + \frac{r^2}{2a(t)} + O(\varepsilon^{3/2}), \quad (8.8)$$

and the lubrication framework is only valid within a $O(\sqrt{ad})$ region located near the axis of symmetry [24]. Therefore, in the lubrication limit $h \sim d$ and $r \sim d\varepsilon^{-1/2}$.

The lubrication problem considered here is in fact composed of two different problems, the first one for translation (forced by \dot{d}) and the second one for inflation (forced by \dot{a}). Because of the incompressibility of the fluid, noting V the vertical velocity scale, at leading order $u_z \sim V$ and $u_r \sim V\varepsilon^{-1/2}$. The impermeability condition, Eq. (8.5), sets the velocity scale in each problem, respectively as $V \sim \dot{d}$ (translation) and $V \sim \varepsilon\dot{a}$ (inflation). Keeping only dominant contributions for each problem, the dynamic boundary condition (8.7) can be finally written at leading order as

$$\lambda \frac{\partial u_r}{\partial z} + u_r = h' \dot{a}. \quad (8.9)$$

At leading order in ε , the equations of motion for the fluid write in non-dimensional form:

$$\frac{1}{r} \frac{\partial(r u_r)}{\partial r} + \frac{\partial u_z}{\partial z} = 0, \quad (8.10)$$

$$\frac{\partial p}{\partial r} = \frac{\partial^2 u_r}{\partial z^2}, \quad (8.11)$$

$$\frac{\partial p}{\partial z} = 0, \quad (8.12)$$

In the following, we focus on the leading order problem remembering that second order contributions are $O(\varepsilon)$ smaller. Solving the previous system follows then the classical approach. Since p is independent of z , the radial and vertical velocities profile are obtained as

$$u_r = \frac{z^2}{2} \frac{\partial p}{\partial r} + \alpha z, \quad u_z = -\frac{z^3}{6r} \frac{\partial}{\partial r} \left(r \frac{\partial p}{\partial r} \right) - \frac{z^2}{2r} \frac{\partial(r\alpha)}{\partial r}, \quad (8.13)$$

where $\alpha(r, t)$ is determined by the dynamic boundary condition, Eq. (8.9),

$$\alpha = -\frac{h(h+2\lambda)}{2(h+\lambda)} \frac{\partial p}{\partial r} + \frac{\dot{a}}{h+\lambda} \frac{\partial h}{\partial r}. \quad (8.14)$$

Using these results, as well as Eqs. (8.5) and (8.8), the Reynolds equation is obtained at leading

Chapter 8. The motion of a bubble inflating next to a wall

order as

$$\frac{\partial h}{\partial t} = \frac{1}{12r} \frac{\partial}{\partial r} \left[rh^3 \left(\frac{h+4\lambda}{h+\lambda} \right) \frac{\partial p}{\partial r} - \frac{6rh^2 \dot{a}}{h+\lambda} \frac{\partial h}{\partial r} \right] = \dot{d} - \frac{(h-d)\dot{a}}{a}. \quad (8.15)$$

This equation can be integrated in r (since $\frac{\partial p}{\partial r} = 0$ on the axis by symmetry), and using $\frac{\partial h}{\partial r} = r/a + O(\varepsilon^{3/2})$, we obtain at leading order

$$\frac{\partial p}{\partial r} = \left[\frac{6a(h+\lambda)\dot{d}}{h^3(h+4\lambda)} + \frac{3\dot{a}[h^2 + (d-\lambda)h + \lambda d]}{h^3(h+4\lambda)} \right] \frac{\partial h}{\partial r}. \quad (8.16)$$

Integrating once more in r , the dominant pressure profile is obtained within the thin lubricating film as

$$p(r) = p_\infty + \frac{3\dot{a}}{64\lambda^2} \left[(3d-20\lambda) \log \left(1 + \frac{4\lambda}{h} \right) - \frac{8d\lambda^2}{h^2} + \frac{4\lambda(4\lambda-3d)}{h} \right] + \frac{3a\dot{d}}{32\lambda^2} \left[3 \log \left(1 + \frac{4\lambda}{h} \right) - \frac{8\lambda^2}{h^2} - \frac{12\lambda}{h} \right] \quad (8.17)$$

with p_∞ an $O(1)$ function of time only related to the pressure outside the lubricating film. In particular, in the two limit cases of a rigid shell or clean bubble, this profile simplifies as

$$p(r) = p_\infty - \frac{3a\dot{d}}{h^2} - \frac{3(d+2h)\dot{a}}{2h^2} \quad \lambda = 0 \text{ (rigid shell)}, \quad (8.18)$$

$$p(r) = p_\infty - \frac{3a\dot{d}}{4h^2} + \frac{3(2h-d)\dot{a}}{8h^2} \quad \lambda = \infty \text{ (clean bubble)}. \quad (8.19)$$

The dominant contribution to the vertical force on the bubble from the lubrication film is given by the pressure contribution and can be evaluated by integrating the pressure force over the region $0 \leq r \leq R$ with $\sqrt{ad} \ll R \ll a$:

$$F_{\text{lub}} = 2\pi \int_0^R r p(r) dr = 2\pi a \int_d^{h(R)} p(h) dh = \left[\frac{3\pi a \dot{a}}{8\lambda} \left\{ (3d-20\lambda) \left[\left(1 + \frac{h}{4\lambda} \right) \log \left(1 + \frac{4\lambda}{h} \right) - 1 \right] + \frac{2d\lambda}{h} - 16\lambda \log h \right\} + \frac{3\pi a^2 \dot{d}}{4\lambda} \left\{ 3 \left[\left(1 + \frac{h}{4\lambda} \right) \log \left(1 + \frac{4\lambda}{h} \right) - 1 \right] + \frac{2\lambda}{h} \right\} \right]_d^{h(R)} + O(1). \quad (8.20)$$

The dominant terms in the previous expression arise from the central region ($r = 0$ and $h = d$). Expanding equation (8.20), when $\varepsilon = d/a$ is small, yields the leading order contribution of the lubrication force. The leading order force due to the translation of the sphere is found by expanding the second term on the right hand side of (8.20)

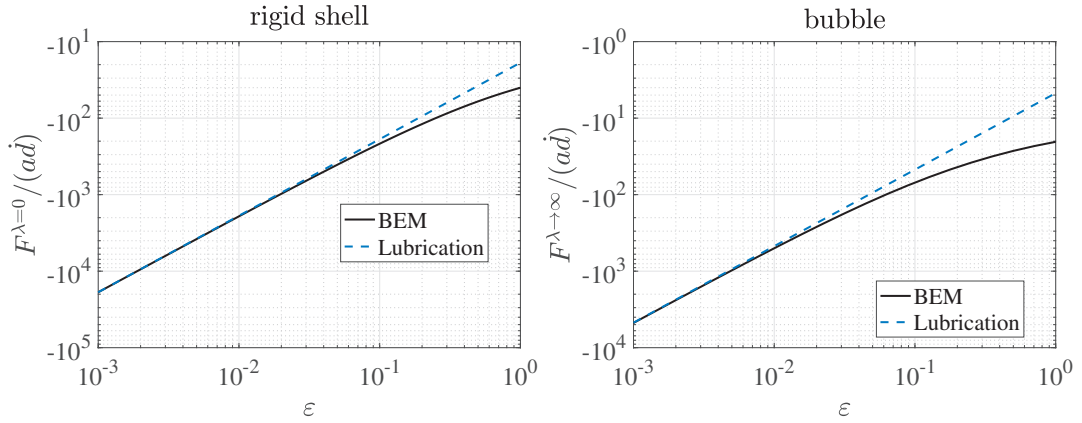


Figure 8.4 – Force due to pure translation for a rigid shell and for a bubble. Lubrication theory and BEM simulation.

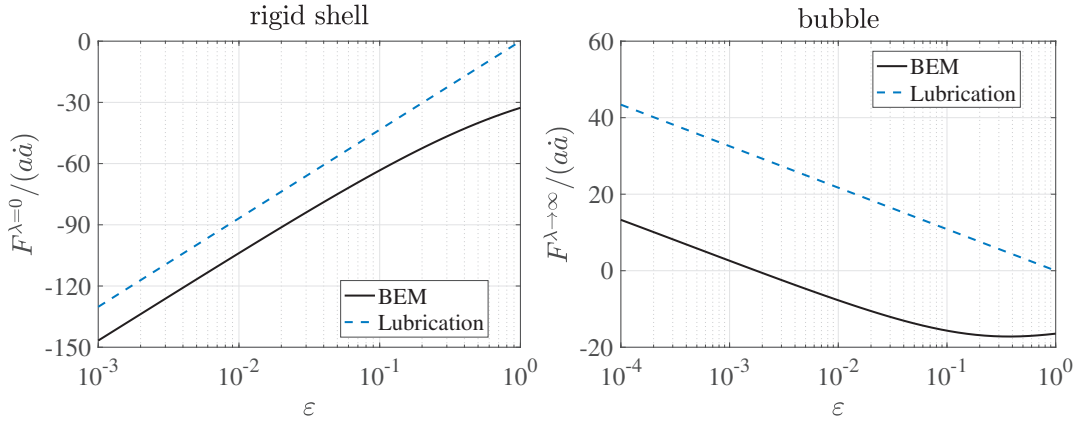


Figure 8.5 – Force due to pure inflation (fixed gap) for a rigid shell and for a bubble. Lubrication theory and BEM simulation.

$$\frac{F_T^{\lambda>0}}{a\dot{d}} = -\frac{3\pi}{2\varepsilon}\pi + O(\log\varepsilon) \quad \lambda > 0, \quad (8.21)$$

$$\frac{F_T^{\lambda=0}}{a\dot{d}} = -\frac{6\pi}{\varepsilon} + O(\log\varepsilon) \quad \lambda = 0, \quad (8.22)$$

respectively for non-zero and zero slip length. Expanding the first term on the right hand side of (8.20), we obtain the leading order force due to inflation as

$$\frac{F_I^{\lambda>0}}{a\dot{a}} = -\frac{3}{2}\pi \log\varepsilon + O(1) \quad \lambda > 0, \quad (8.23)$$

$$\frac{F_I^{\lambda=0}}{a\dot{a}} = 6\pi \log\varepsilon + O(1) \quad \lambda = 0, \quad (8.24)$$

respectively for non-zero and zero slip length. Interestingly, for non-zero slip length the scaling does not depend on λ , meaning that spheres with $\lambda \neq 0$ behave similarly for small ε . The

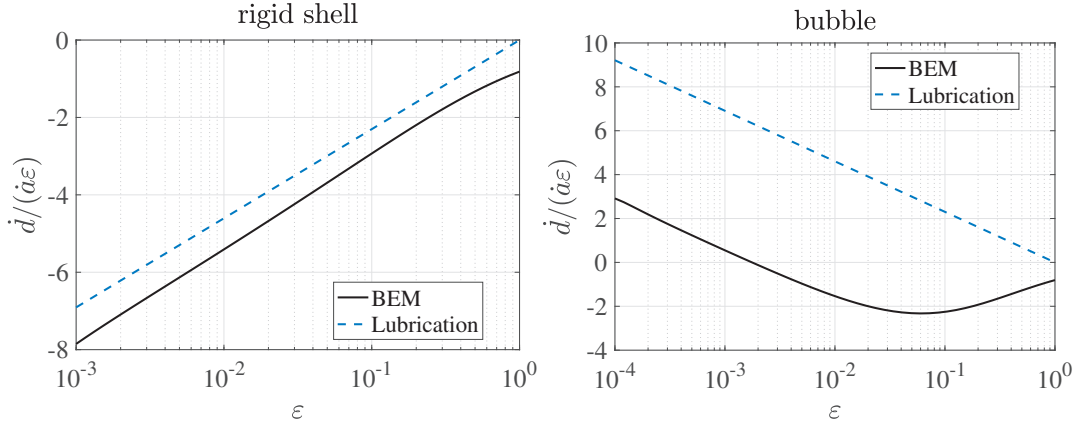


Figure 8.6 – Normalized gap velocity for a rigid shell and a bubble. Lubrication theory and BEM simulation.

scalings for a rigid shell and a bubble compare well with the results from the full solution obtained numerically, as shown in Figure 8.4 and 8.5.

We use equations from (8.21) to (8.24) to find the gap velocity by applying the force free condition $F_T + F_I = 0$. Thus, we obtain the gap velocity as

$$\frac{\dot{d}}{a\dot{\epsilon}} = -\log \epsilon + O(1) \quad \lambda > 0, \quad (8.25)$$

$$\frac{\dot{d}}{a\dot{\epsilon}} = \log \epsilon + O(1) \quad \lambda = 0, \quad (8.26)$$

for a bubble or a rigid shell respectively. For inflating spheres, the gap velocity is positive in the case of a bubble ($\log \epsilon < 0$) while it is negative for a rigid shell. In figure 8.6 we report the comparison between lubrication theory and numerical simulations. The discrepancy between numerics and lubrication theory is due to the $O(1)$ error in the logarithmic scaling of the force for pure inflation (see Figure 8.5). As a direct consequence of this, the absolute error on the gap velocity in Figure 8.6 does not decrease when ϵ is smaller. Nevertheless, the qualitative features of the system are captured by the lubrication analysis, with a rigid shell approaching the wall and a clean bubble being repelled.

8.5 Physical explanation: flow field within the gap

The main (and somewhat surprising) outcome of the previous analysis is that the force experienced by a growing bubble near a wall *when the fluid gap width is held fixed* can reverse sign depending on the wall proximity and slip length; as a result, and for a thin lubrication gap and a clean bubble, a force-free growing bubble is repelled by the confining wall in contrast with what happens for a rigid shell or for weaker confinement. This reversal stems from a fundamentally-different behavior of the flow field within the thin gap ($d \ll a$) for a rigid interface and for a stress-free one. This difference in the flow properties is described on

8.5. Physical explanation: flow field within the gap

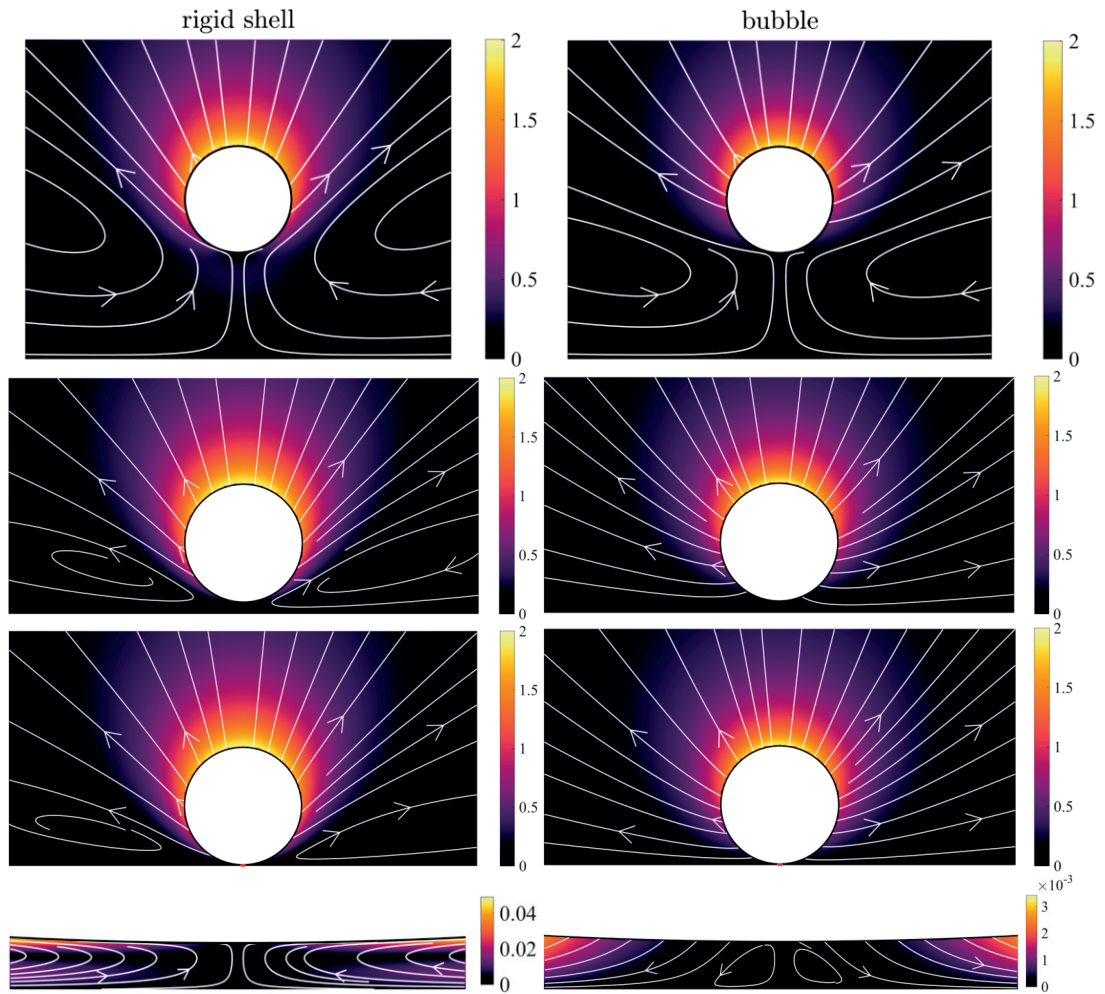


Figure 8.7 – Velocity field during inflation when the gap is kept fixed at $\varepsilon = [2, 0.2, 0.02]$. The left/right column is for a rigid shell/bubble. Bottom figures show a zoom of the velocity field in the gap for $\varepsilon = 0.02$. In all cases $\dot{a} = 1$.

Figure 8.7 where the streamlines and velocity magnitude are shown for the two limit cases of surfaces with zero and infinite slip length (respectively, no-slip and free surfaces) and varying gap width. Far from the wall, the inflation of the bubble while holding its bottom pole fixed leads in both cases to the formation of a recirculation torus around the axis of symmetry of the problem (closed streamlines). More precisely, the fluid domain can be divided into two different regions: (i) an expanding region where the streamlines leave the bubble surface outward, as a result of the bubble inflation and (ii) a recirculating region where fluid is pumped in from below the bubble and expelled out on the side (recirculating torus). Far from the wall, the topology of the recirculating regions is roughly similar for both $\lambda = 0$ and $\lambda = \infty$, with the main difference being only a weaker flow velocity behind a clean surface which allows for fluid slip and is therefore less efficient in driving a tangential fluid motion.

The two limits $\lambda = 0$ and $\lambda = \infty$ differ however fundamentally in the behaviour of this recircu-

lation zone when the distance to the wall is reduced. In the case of a no-slip boundary ($\lambda = 0$), a recirculation torus whose size scales with the radius of the bubble is maintained around the bubble and within the thin lubricating film when $\varepsilon \rightarrow 0$. This is only possible because the sphere's surface can sustain a net shear stress and continue driving the fluid tangentially to its surface and out of the gap. This reversal of direction in the flow within the lubrication gap is only possible if the pressure gradient within the lubrication film is oriented outward (i.e. the pressure within the film is lower than the outer pressure), which is consistent with the lubrication analysis, Eq. (8.18). This leads to the attraction of the inflating shell by the wall.

In contrast, in the case of a no-stress boundary ($\lambda = \infty$), the recirculation torus still exists but scales with the lubrication gap, as the bubble's surface can only exert normal stress on the fluid. In the limit $\varepsilon \rightarrow 0$, it is therefore confined to the immediate vicinity of the axis and its impact essentially vanishes. The pressure gradient within the lubrication gap is then oriented inward as predicted by the lubrication analysis, Eq. (8.19), leading to a larger pressure than in the outer region and a repulsion of the bubble from the wall.

8.6 Conclusions

In summary, we have studied numerically and theoretically the flow due to a bubble inflating close to a rigid wall. We have found that the flow in the lubrication film is fundamentally different for a "rigid shell" and for a "clean bubble". This difference causes the sphere-wall gap to decrease in time in the rigid shell case, contrary to the "clean bubble" case where the gap size increases in time.

These findings shed light on the dynamics of bubbles inflating close to boundaries and might provide insights to guide the theoretical exploration of more complex geometry as conical microswimmers, studied in Chapter 6 & 7. In future work, we would like to address the influence of bubble deformability on this system.

9 Conclusions and perspectives

In this Thesis we have first studied the breakup of droplets in canonical low Reynolds number flows, where we have proceeded by adapting theories developed to study laminar-turbulent transition to our problem. This transfer of knowledge across different communities has led to new findings and insights, and in particular in the exploration of the basin of attraction separating droplets that break from those reaching a stable state. Secondly, we have studied the propulsion of conical catalytic microswimmers. This has allowed us to gain insights about the propulsion mechanism of these microswimmers and to find the optimal parameters for maximum swimming velocity. In the following, we sum up the main results of Part I and Part II and we propose future developments of this work.

In **Part I** we have considered a droplet in an extensional flow and a buoyant droplet translating in an otherwise quiescent fluid. Considering simple domains has allowed us to reduce the physical ingredients at play and to rigorously adapt theories initially designed to study laminar-turbulent transition, to droplet breakup in low Reynolds number flows. In particular, our effort has been devoted to the exploration of the state space in which the basin boundary is defined. In Chapter 3, we have shown that the surface deformation of **a droplet rising in a quiescent fluid exhibits transient growth** due to non-normal effects. The results from nonmodal analysis have revealed the region of state space where the *distance* between the basin boundary and the base state is (locally) minimal and small perturbations are sufficient to trigger breakup. Therefore, we have been able to design optimal initial droplet shapes that undergo breakup with smaller initial perturbation energy, compared for example to ellipsoidal initial conditions. Furthermore, these results provide a proof of concept about the relevance of linear nonmodal analysis in droplet breakup at low Reynolds number. In Chapter 4, we have pursued the basin boundary exploration by identifying edge states of a droplet in an extensional flow, resorting to the edge tracking technique. We have shown that **edge states guide droplet breakup** and lead to the well known end-pinching mechanism. The exploration of the bifurcation diagram, also complemented in **Chapter 5**, has allowed us to conclude that these findings are robust for every subcritical capillary number, even when the flow compresses the droplet along its axis instead of stretching it. These results are summed up in

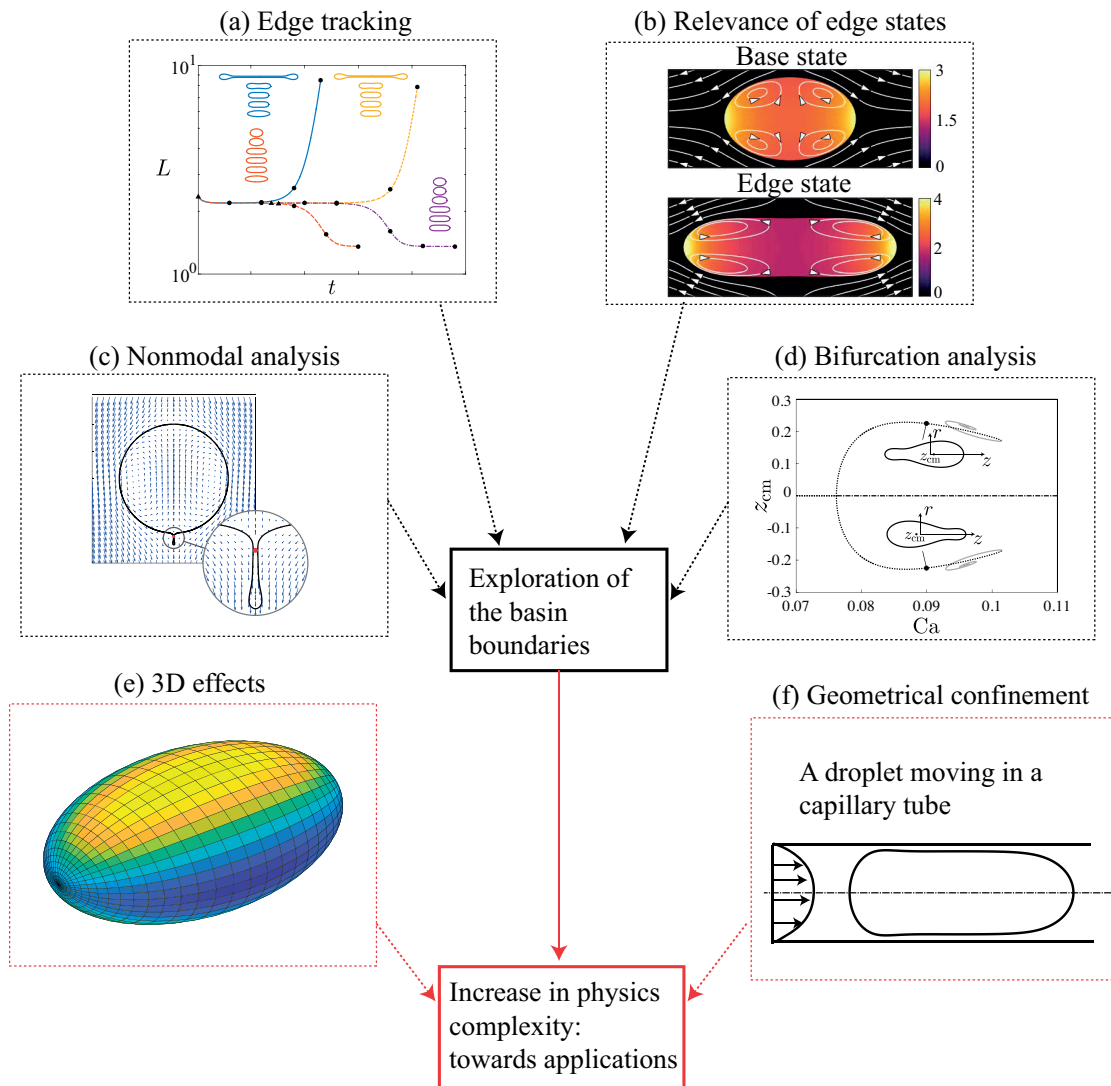


Figure 9.1 – Schematic representation of the studies carried out in Part I on the exploration the state space of droplets breaking-up in low Reynolds number flows: from building blocks to more realistic flow configurations. (a-b-c-d) Reprint of results from chapter 3, 4 & 5: edge states and bifurcation diagram for a droplet in an extensional flow and nonmodal analysis for a rising droplet. Future perspectives include considering (e) 3D effects and (f) geometrical confinement, which are relevant in applications.

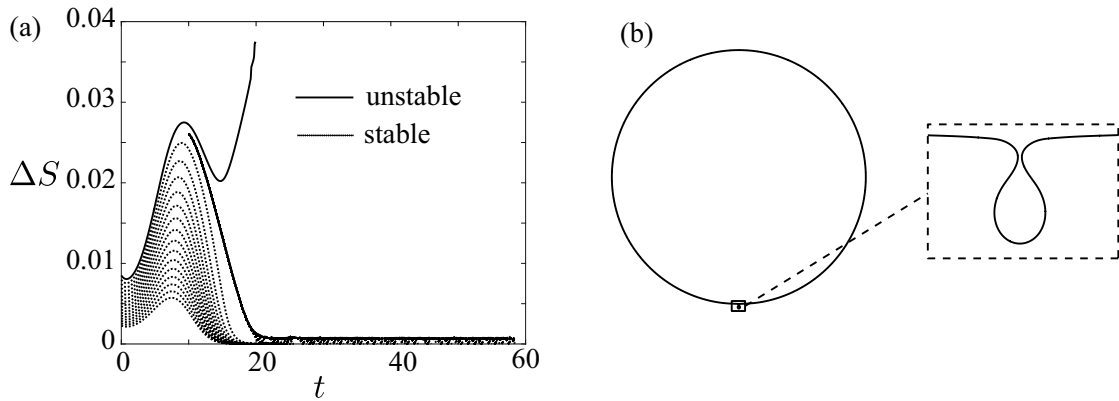


Figure 9.2 – Edge tracking for a rising droplet, $Ca = 6$ and $\lambda = 1$. (a) Edge tracking trajectories, excess surface area ΔS versus time. (b) Edge state shape, where a small tail develops in the rear part of the droplet.

Figure 9.1, where we also underline our research approach employed in this part. In fact, we have proceeded by considering simple flow configurations that, in our view, should constitute the building blocks for applying these methods in more complex physical situations. Our effort is therefore currently directed in two directions: on the fundamental side, we wish to focus on the study and the exploration of the basin boundary in simple flow configurations. On the applications side, we would like to start including physical ingredients that are important in real configurations, for example by studying the role of geometrical confinement and 3D effects both playing an important role in applications like microfluidics [149]. Currently, we are working on finding the edge state of a rising droplet. This is challenging because of the small structures that form and require very high mesh resolution. Preliminary results are shown in Figure 9.2, where we show the edge tracking trajectories and the edge state shape. This case is of particular interest because, contrary to the extensional flow, the spherical shape is a stable solution for every capillary number [4]. Therefore, like in Couette or plane Poiseuille flow, there is no simple branch-tracking approach that allow to connect unstable branches to this unconditionally linear stable base state.

In **Part II** we have studied the motion of an isolated catalytic conical microswimmer. This system is rich of physical ingredients as it includes hydrodynamics of confined inflating bubbles, chemistry and bubble nucleation. In fact, we have conducted this study in an almost opposite approach when compared to Part I. We have started in Chapter 6 by studying a spherical bubble inflating inside a cone, due to an influx of chemical species generated on the cone wall. We have proceeded by retaining most of the physical ingredients and formulate some assumptions (i.e. constraining the spherical bubble geometry and imposing a nucleation criterion) in order to make the problem tractable. This study has led to the interesting finding that the chemistry sets the characteristic time scale of the microswimmer motion while the hydrodynamics sets the displacement attained within this time. Furthermore, we have been able to determine parameter values that optimize the swimming velocity. Since the physics here is complicated and there is an interplay between many aspects of it, our approach in

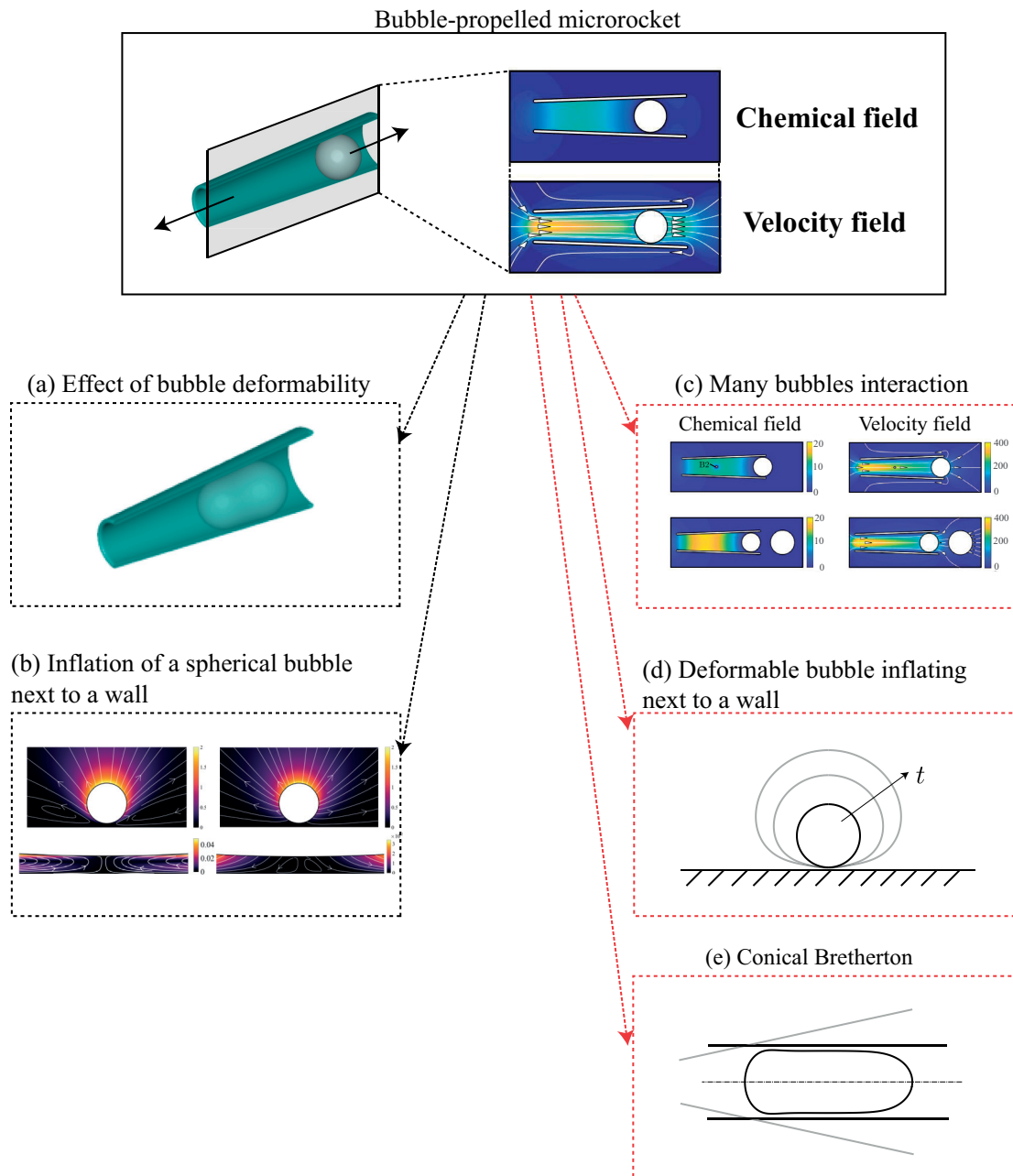


Figure 9.3 – Schematic representation of the studies carried out in Part II on the motion of a conical microswimmer: from a general but simplified investigation to considering sub-problems. (a-b-c) Reprint of results from chapter 6, 7 & 8. Future perspectives include considering many (c) bubble interactions, (d) the inflation of deformable bubble close to boundaries and (e) a theoretical approach to the motion of bubbles in conical tubes.

future work will be to simplify this problem in sub-problems. We have already started this process in Chapter 7 & 8, where we have first considered the effect of the bubble deformability upon the propulsion and then considered the inflation of spherical bubble next to a wall. These are the first steps to build a more fundamental understanding of these microswimmers, as sketched in Figure 9.3. Next steps would be to consider the motion of a bubble inside a non-moving cone, in analogy with the Bretherton problem [150]. A similar study has been carried out in [151] in Hele-Shaw configuration. This will lead to a better fundamental understanding of conical microswimmers motion and ideally to the development of a complete theoretical model for the microswimmer motion. A theoretical model could even allow us to study the collective motion of conical microswimmers, a task which is otherwise computationally too demanding. Finally, similarly to part I, the dynamics might become intrinsically $3D$ in certain situations, for example when many bubbles interact and when nucleation occurs on the cone surface. This will require carrying out full $3D$ simulations of this system.

Bibliography

- [1] G. I. Taylor. The formation of emulsions in definable fields of flow. *Proceedings of the Royal Society of London. Series A*, 146(858):501–523, 1934.
- [2] J. M. Rallison and A. Acrivos. A numerical study of the deformation and burst of a viscous drop in an extensional flow. *Journal of Fluid Mechanics*, 89(01):191–200, 1978.
- [3] J. Happel and H. Brenner. *Low Reynolds number hydrodynamics: with special applications to particulate media*, volume 1. Springer Science & Business Media, 2012.
- [4] M. Kojima, E. J. Hinch, and A. Acrivos. The formation and expansion of a toroidal drop moving in a viscous fluid. *Physics of Fluids (1958-1988)*, 27(1):19–32, 1984.
- [5] H. A. Stone and L. G. Leal. The influence of initial deformation on drop breakup in subcritical time-dependent flows at low reynolds numbers. *Journal of Fluid Mechanics*, 206:223–263, 1989.
- [6] C. J. Koh and L. G. Leal. The stability of drop shapes for translation at zero reynolds number through a quiescent fluid. *Physics of Fluids A: Fluid Dynamics (1989-1993)*, 1(8):1309–1313, 1989.
- [7] C. Pozrikidis. The instability of a moving viscous drop. *Journal of Fluid Mechanics*, 210:1–21, 1990.
- [8] H. Leonhard. Experiments on tipstreaming. *Unpublished*, 1996.
- [9] E. Páram and A. Fernández-Nieves. Generation and stability of toroidal droplets in a viscous liquid. *Physical Review Letters*, 102(23):234501, 2009.
- [10] C. J. Koh and L. G. Leal. An experimental investigation on the stability of viscous drops translating through a quiescent fluid. *Physics of Fluids A: Fluid Dynamics (1989-1993)*, 2(12):2103–2109, 1990.
- [11] H. A. Stone, B. J. Bentley, and L. G. Leal. An experimental study of transient effects in the breakup of viscous drops. *Journal of Fluid Mechanics*, 173:131–158, 1986.
- [12] E. Brouzes, M. Medkova, N. Savenelli, D. Marran, M. Twardowski, J. B. Hutchison, J. M. Rothberg, D. R. Link, N. Perrimon, and M. L. Samuels. Droplet microfluidic technology

Bibliography

- for single-cell high-throughput screening. *Proceedings of the National Academy of Sciences*, 106(34):14195–14200, 2009.
- [13] S. Maillot, A. Carvalho, J. P. Vola, C. Boudier, Y. Mély, S. Haacke, and J. Léonard. Out-of-equilibrium biomolecular interactions monitored by picosecond fluorescence in microfluidic droplets. *Lab on a Chip*, 14(10):1767–1774, 2014.
- [14] W. Lee, L. M. Walker, and S. L. Anna. Role of geometry and fluid properties in droplet and thread formation processes in planar flow focusing. *Physics of Fluids*, 21(3):032103, 2009.
- [15] R. Seemann, M. Brinkmann, T. Pfohl, and S. Herminghaus. Droplet based microfluidics. *Reports on Progress in Physics*, 75(1):016601, 2011.
- [16] G. K. Batchelor. *An Introduction to Fluid Dynamics*. Cambridge University Press, 1970.
- [17] G. Mougin and J. Magnaudet. Path instability of a rising bubble. *Physical Review Letters*, 88(1):014502, 2001.
- [18] J. Magnaudet and G. Mougin. Wake instability of a fixed spheroidal bubble. *Journal of Fluid Mechanics*, 572:311–337, 2007.
- [19] J. Tchoufag, J. Magnaudet, and D. Fabre. Linear instability of the path of a freely rising spheroidal bubble. *Journal of Fluid Mechanics*, 751, 2014.
- [20] W. C. Reynolds and M. C. Potter. Finite-amplitude instability of parallel shear flows. *Journal of Fluid Mechanics*, 27(3):465–492, 1967.
- [21] A. Sharma and E. Ruckenstein. Finite-amplitude instability of thin free and wetting films: prediction of lifetimes. *Langmuir*, 2(4):480–494, 1986.
- [22] R. Kessler. Nonlinear transition in three-dimensional convection. *Journal of Fluid Mechanics*, 174:357–379, 1987.
- [23] J. M. Rallison. Note on the time-dependent deformation of a viscous drop which is almost spherical. *Journal of Fluid Mechanics*, 98(03):625–633, 1980.
- [24] L. G. Leal. *Advanced transport phenomena: fluid mechanics and convective transport processes*. Cambridge University Press, 2007.
- [25] L. N. Trefethen, A. Trefethen, S. Reddy, and T. A. Driscoll. Hydrodynamic stability without eigenvalues. *Science*, 261(5121):578–584, 1993.
- [26] P. J. Schmid and D. S. Henningson. *Stability and transition in shear flows*, volume 142. Springer, 2001.
- [27] E. Mellibovsky, A. Meseguer, T. M. Schneider, and B. Eckhardt. Transition in localized pipe flow turbulence. *Physical Review Letters*, 103(5):054502, 2009.

-
- [28] J. D. Skufca, J. A. Yorke, and B. Eckhardt. Edge of chaos in a parallel shear flow. *Physical Review Letters*, 96(17):174101, 2006.
- [29] P. V. R. Snelgrove. The importance of marine sediment biodiversity in ecosystem processes. *Ambio*, pages 578–583, 1997.
- [30] L. Cui, A. Morris, and E. Ghedin. The human mycobiome in health and disease. *Genome Medicine*, 5(7):1, 2013.
- [31] B. J. Nelson, I. K. Kaliakatsos, and J. J. Abbott. Microrobots for minimally invasive medicine. *Annual Review of Biomedical Engineering*, 12(1):55–85, 2010.
- [32] M. Guix, C. C. Mayorga-Martinez, and A. Merkoçi. Nano/micromotors in (bio) chemical science applications. *Chemical Reviews*, 114(12):6285–6322, 2014.
- [33] G. V. Kolmakov, V. V. Yashin, S. P. Levitan, and A. C. Balazs. Designing self-propelled microcapsules for pick-up and delivery of microscopic cargo. *Soft Matter*, 7(7):3168–3176, 2011.
- [34] M. García, J. Orozco, M. Guix, W. Gao, S. Sattayasamitsathit, A. Escarpa, A. Merkoçi, and J. Wang. Micromotor-based lab-on-chip immunoassays. *Nanoscale*, 5(4):1325–1331, 2013.
- [35] J. Burdick, R. Laocharoensuk, P. M. Wheat, J. D. Posner, and J. Wang. Synthetic nanomotors in microchannel networks: Directional microchip motion and controlled manipulation of cargo. *Journal of the American Chemical Society*, 130(26):8164–8165, 2008.
- [36] E. Lauga and T. R. Powers. The hydrodynamics of swimming microorganisms. *Reports on Progress in Physics*, 72(9):096601, 2009.
- [37] E. M. Purcell. Life at low reynolds number. In *Physics and Our World: Reissue of the Proceedings of a Symposium in Honor of Victor F Weisskopf*, pages 47–67. World Scientific, 2014.
- [38] Howard C Berg and Robert A Anderson. Bacteria swim by rotating their flagellar filaments. *Nature*, 245(5425):380, 1973.
- [39] D. Bray. *Cell movements: from molecules to motility*. Garland Science, 2001.
- [40] I. R. Gibbons. Cilia and flagella of eukaryotes. *The Journal of Cell Biology*, 91(3):107–124, 1981.
- [41] S. J. Ebbens and J. R. Howse. In pursuit of propulsion at the nanoscale. *Soft Matter*, 6(4):726–738, 2010.
- [42] A. Walther and A. H. E. Müller. Janus particles. *Soft Matter*, 4(4):663–668, 2008.

Bibliography

- [43] K. M. Manesh, M. Cardona, R. Yuan, M. Clark, D. Kagan, S. Balasubramanian, and J. Wang. Template-assisted fabrication of salt-independent catalytic tubular micro-engines. *ACS Nano*, 4(4):1799–1804, 2010.
- [44] T. R. Kline, W. F. Paxton, T. E. Mallouk, and A. Sen. Catalytic nanomotors: remote-controlled autonomous movement of striped metallic nanorods. *Angewandte Chemie International Edition*, 44(5):744–746, 2005.
- [45] A. A. Solovev, Y. Mei, E. Bermúdez Ureña, G. Huang, and O. G. Schmidt. Catalytic microtubular jet engines self-propelled by accumulated gas bubbles. *Small*, 5(14):1688–1692, 2009.
- [46] W. Gao, S. Sattayasamitsathit, J. Orozco, and J. Wang. Highly efficient catalytic micro-engines: template electrosynthesis of polyaniline/platinum microtubes. *Journal of the American Chemical Society*, 133(31):11862–11864, 2011.
- [47] W. Gao, R. Dong, S. Thamphiwatana, J. Li, W. Gao, L. Zhang, and J. Wang. Artificial micromotors in the mouse’s stomach: A step toward in vivo use of synthetic motors. *ACS Nano*, 9(1):117–123, 2015.
- [48] S. Kim and S. J. Karrila. *Microhydrodynamics: principles and selected applications*. Courier Corporation, 2013.
- [49] C. Pozrikidis. *Boundary integral and singularity methods for linearized viscous flow*. Cambridge University Press, 1992.
- [50] C. Pozrikidis. *A practical guide to boundary element methods with the software library BEMLIB*. CRC Press, 2002.
- [51] H. Zhao and E. S. G. Shaqfeh. The shape stability of a lipid vesicle in a uniaxial extensional flow. *Journal of Fluid Mechanics*, 719:345–361, 2013.
- [52] L. N. Trefethen. *Spectral methods in MATLAB*, volume 10. Siam, 2000.
- [53] H. A. Stone and L. G. Leal. Relaxation and breakup of an initially extended drop in an otherwise quiescent fluid. *Journal of Fluid Mechanics*, 198:399–427, 1989.
- [54] W. Rybczynski. Über die fortschreitende bewegung einer flussigen kugel in einem zahren medium. *Bull. Acad. Sci. Cracovie A*, 1:40–46, 1911.
- [55] V. Cristini, J. Bławdziewicz, and M. Loewenberg. An adaptive mesh algorithm for evolving surfaces: simulations of drop breakup and coalescence. *Journal of Computational Physics*, 168(2):445–463, 2001.
- [56] A. Z. Zinchenko and R. H. Davis. Emulsion flow through a packed bed with multiple drop breakup. *Journal of Fluid Mechanics*, 725:611–663, 2013.

-
- [57] J. B. Freund. Leukocyte margination in a model microvessel. *Physics of Fluids (1994-present)*, 19(2):023301, 2007.
- [58] H. Zhao, A. H. G. Isfahani, L. N. Olson, and J. B. Freund. A spectral boundary integral method for flowing blood cells. *Journal of Computational Physics*, 229:3726–3744, 2010.
- [59] C. Pozrikidis. Expansion of a compressible gas bubble in stokes flow. *Journal of Fluid Mechanics*, 442:171–189, 2001.
- [60] J. Shen, T. Tang, and L. L. Wang. *Spectral methods: algorithms, analysis and applications*, volume 41. Springer Science & Business Media, 2011.
- [61] A. Z. Zinchenko and R. H. Davis. A boundary-integral study of a drop squeezing through interparticle constrictions. *Journal of Fluid Mechanics*, 564:227–266, 2006.
- [62] J. Eggers and S. C. Du Pont. Numerical analysis of tips in viscous flow. *Physical Review E*, 79(6):066311, 2009.
- [63] C. Pozrikidis. The flow of a liquid film along a periodic wall. *Journal of Fluid Mechanics*, 188:275–300, 1988.
- [64] G. K. Youngren and A. Acrivos. On the shape of a gas bubble in a viscous extensional flow. *Journal of Fluid Mechanics*, 76(03):433–442, 1976.
- [65] H. Zhao and E. S. G. Shaqfeh. The dynamics of a vesicle in simple shear flow. *Journal of Fluid Mechanics*, 674:578–604, 2011.
- [66] J. M. Rallison. The deformation of small viscous drops and bubbles in shear flows. *Annual Review of Fluid Mechanics*, 16(1):45–66, 1984.
- [67] J. S. Hadamard. Mouvement permanent lent d’une sphère liquide et visqueuse dans un liquide visqueux. *CR Acad. Sci.*, 152:1735, 1991.
- [68] R. A. Johnson and A. Borhan. Stability of the shape of a surfactant-laden drop translating at low reynolds number. *Physics of Fluids (1994-present)*, 12(4):773–784, 2000.
- [69] H. Wu, H. Haj-Hariri, and A. Borhan. Stability of the shape of a translating viscoelastic drop at low reynolds number. *Physics of Fluids (1994-present)*, 24(11):113101, 2012.
- [70] H. E. Huppert. Flow and instability of a viscous current down a slope. *Nature*, 300(5891):427–429, 1982.
- [71] J. R. de Bruyn. Growth of fingers at a driven three-phase contact line. *Physical Review A*, 46(8):R4500, 1992.
- [72] A. L. Bertozzi and M. P. Brenner. Linear stability and transient growth in driven contact lines. *Physics of Fluids (1994-present)*, 9(3):530–539, 1997.

Bibliography

- [73] S. C. Reddy and D. S. Henningson. Energy growth in viscous channel flows. *Journal of Fluid Mechanics*, 252:209–238, 1993.
- [74] J. S. Baggett, T. A. Driscoll, and L. N. Trefethen. A mostly linear model of transition to turbulence. *Physics of Fluids (1994-present)*, 7(4):833–838, 1995.
- [75] P. J. Schmid. Nonmodal stability theory. *Annual Review of Fluid Mechanics*, 39:129–162, 2007.
- [76] J. M. Davis and S. M. Troian. On a generalized approach to the linear stability of spatially nonuniform thin film flows. *Physics of Fluids (1994-present)*, 15(5):1344–1347, 2003.
- [77] K. Balasubramanian and R. I. Sujith. Thermoacoustic instability in a rijke tube: Non-normality and nonlinearity. *Physics of Fluids (1994-present)*, 20(4):044103, 2008.
- [78] M. P. Juniper. Triggering in the horizontal rijke tube: non-normality, transient growth and bypass transition. *Journal of Fluid Mechanics*, 667:272–308, 2011.
- [79] M. R. Jovanović and S. Kumar. Transient growth without inertia. *Physics of Fluids (1994-present)*, 22(2):023101, 2010.
- [80] L. N. Trefethen and M. Embree. *Spectra and pseudospectra: the behavior of nonnormal matrices and operators*. Princeton University Press, 2005.
- [81] A. Acrivos. The breakup of small drops and bubbles in shear flows. *Annals of the New York Academy of Sciences*, 404(1):1–11, 1983.
- [82] H. A. Stone. Dynamics of drop deformation and breakup in viscous fluids. *Annual Review of Fluid Mechanics*, 26(1):65–102, 1994.
- [83] E. D. Rumscheidt and S. G. Mason. Particle motions in sheared suspensions xii. deformation and burst of fluid drops in shear and hyperbolic flow. *Journal of Colloid Science*, 16(3):238–261, 1961.
- [84] B. J. Bentley and L. G. Leal. An experimental investigation of drop deformation and breakup in steady, two-dimensional linear flows. *Journal of Fluid Mechanics*, 167:241–283, 1986.
- [85] J. M. Rallison. A numerical study of the deformation and burst of a viscous drop in general shear flows. *Journal of Fluid Mechanics*, 109:465–482, 1981.
- [86] D. Barthes-Biesel and A. Acrivos. Deformation and burst of a liquid droplet freely suspended in a linear shear field. *Journal of Fluid Mechanics*, 61(01):1–22, 1973.
- [87] J. Bławdziewicz, V. Cristini, and M. Loewenberg. Critical behavior of drops in linear flows. i. phenomenological theory for drop dynamics near critical stationary states. *Physics of Fluids*, 14(8):2709–2718, 2002.

-
- [88] T. M. Schneider, B. Eckhardt, and J. A. Yorke. Turbulence transition and the edge of chaos in pipe flow. *Physical Review Letters*, 99(3):034502, 2007.
- [89] G. Gallino, L. Zhu, and F. Gallaire. The stability of a rising droplet: an inertialess non-modal growth mechanism. *Journal of Fluid Mechanics*, 786:R2 (11 pages), 1 2016.
- [90] T. Kreilos and T. M. Schneider. Fully localized post-buckling states of cylindrical shells under axial compression. In *Proc. R. Soc. A*, volume 473, page 20170177. The Royal Society, 2017.
- [91] E. Viot, T. Kreilos, T. M. Schneider, and S. M. Rubinstein. Stability landscape of shell buckling. *Physical Review Letters*, 119(22):224101, 2017.
- [92] E. J. Hinch. The evolution of slender inviscid drops in an axisymmetric straining flow. *Journal of Fluid Mechanics*, 101(03):545–553, 1980.
- [93] D. W. Decker and H. B. Keller. Path following near bifurcation. *Communications on Pure and Applied Mathematics*, 34(2):149–175, 1981.
- [94] E. L. Allgower and K. Georg. *Numerical continuation methods: an introduction*, volume 13. Springer Science & Business Media, 2012.
- [95] J. D. Buckmaster and J. E. Flaherty. The bursting of two-dimensional drops in slow viscous flow. *Journal of Fluid Mechanics*, 60(04):625–639, 1973.
- [96] A. Acrivos and T. S. Lo. Deformation and breakup of a single slender drop in an extensional flow. *Journal of Fluid Mechanics*, 86:641–672, 6 1978.
- [97] C. C. T. Pringle and R. R. Kerswell. Using nonlinear transient growth to construct the minimal seed for shear flow turbulence. *Physical Review Letters*, 105(15):154502, 2010.
- [98] S. Cherubini, P. De Palma, J.-Ch. Robinet, and A. Bottaro. The minimal seed of turbulent transition in the boundary layer. *Journal of Fluid Mechanics*, 689:221–253, 2011.
- [99] J. D. Sherwood. Tip streaming from slender drops in a nonlinear extensional flow. *Journal of Fluid Mechanics*, 144:281–295, 1984.
- [100] J. Eggers. Nonlinear dynamics and breakup of free-surface flows. *Reviews of Modern Physics*, 69(3):865, 1997.
- [101] M. Siegel. Cusp formation for time-evolving bubbles in two-dimensional stokes flow. *Journal of Fluid Mechanics*, 412:227–257, 2000.
- [102] P. D. Howell and M. Siegel. The evolution of a slender non-axisymmetric drop in an extensional flow. *Journal of Fluid Mechanics*, 521:155–180, 2004.
- [103] P. Rowghanian, C.D. Meinhart, and O. Campàs. Dynamics of ferrofluid drop deformations under spatially uniform magnetic fields. *Journal of Fluid Mechanics*, 802:245–262, 2016.

Bibliography

- [104] H. A. Stone and L. G. Leal. A note concerning drop deformation and breakup in biaxial extensional flows at low reynolds numbers. *Journal of Colloid and Interface Science*, 133(2):340–347, 1989.
- [105] M. Zabarankin, I. Smagin, O. M. Lavrenteva, and A. Nir. Viscous drop in compressional stokes flow. *Journal of Fluid Mechanics*, 720:169–191, 2013.
- [106] P. T. Brun, M. Nagel, and F. Gallaire. Generic path for droplet relaxation in microfluidic channels. *Physical Review E*, 88(4):043009, 2013.
- [107] I. S. Kang and L. G. Leal. Numerical solution of axisymmetric, unsteady free-boundary problems at finite reynolds number. ii. deformation of a bubble in a biaxial straining flow. *Physics of Fluids A: Fluid Dynamics*, 1(4):644–660, 1989.
- [108] W. Gao and J. Wang. Synthetic micro/nanomotors in drug delivery. *Nanoscale*, 6(18):10486–10494, 2014.
- [109] J. Wang and W. Gao. Nano/microscale motors: biomedical opportunities and challenges. *ACS Nano*, 6(7):5745–5751, 2012.
- [110] B. J. Nelson, I. K. Kaliakatsos, and J. J. Abbott. Microrobots for minimally invasive medicine. *Annual Review of Biomedical Engineering*, 12:55–85, 2010.
- [111] A. A. Solovev, S. Sanchez, M. Pumera, Y. F. Mei, and O.G. Schmidt. Magnetic control of tubular catalytic microbots for the transport, assembly, and delivery of micro-objects. *Advanced Functional Materials*, 20(15):2430–2435, 2010.
- [112] R. Dreyfus, J. Baudry, M. L. Roper, M. Fermigier, H. A. Stone, and J. Bibette. Microscopic artificial swimmers. *Nature*, 437:862–865, 2005.
- [113] A. Ghosh and P. Fischer. Controlled propulsion of artificial magnetic nanostructured propellers. *Nano Lett.*, 9:2243–2245, 2009.
- [114] W. Wang, L.A. Castro, M. Hoyos, and T.E. Mallouk. Autonomous motion of metallic microrods propelled by ultrasound. *ACS Nano*, 6(7):6122–6132, 2012.
- [115] S. J. Ebbens. Active colloids: Progress and challenges towards realising autonomous applications. *Curr. Opin. Colloid Interface Sci*, 21:14–23, 2016.
- [116] W. Duan, W. Wang, S. Das, V. Yadav, T. E. Mallouk, and A. Sen. Synthetic nano- and micro-machines in analytical chemistry: sensing, migration, capture, delivery and separation. *Annual Review of Analytical Chemistry*, 8:311–333, 2015.
- [117] V. Yadav, W. Duan, P. J. Butler, and A. Sen. Anatomy of nanoscale propulsion. *Annual Review of Biophysics*, 44:77–100, 2015.
- [118] L. Xu, F. Mou, H. Gong, M. Luo, and J. Guan. Light-driven micro/nanomotors: from fundamentals to applications. *Chemical Society Reviews*, 46(22):6905–6926, 2017.

- [119] J. Li, I. Rozen, and J. Wang. Rocket science at the nanoscale. *ACS Nano*, 10(6):5619–5634, 2016.
- [120] W. F. Paxton, K. C. Kistler, C. C. Olmeda, A. Sen, S. K. St. Angelo, Y. Cao, T. E. Mallouk, P. E. Lammert, and V. H. Crespi. Catalytic Nanomotors: Autonomous Movement of Striped Nanorods. *J. Am. Chem. Soc.*, 126(41):13424–13431, 2004.
- [121] J. R. Howse, R. A. L. Jones, A. J. Ryan, T. Gough, R. Vafabakhsh, and R. Golestanian. Self-Motile Colloidal Particles: From Directed Propulsion to Random Walk. *Phys. Rev. Lett.*, 99(4):048102, 2007.
- [122] G. Volpe, I. Buttinoni, D. Vogt, H.-J. Kümmerer, and C. Bechinger. Microswimmers in patterned environments. *Soft Matter*, 7:8810–8815, 2011.
- [123] J. L. Moran and J. D. Posner. Phoretic self-propulsion. *Annual Review of Fluid Mechanics*, 49:511–540, 2017.
- [124] J. L. Anderson. Colloid transport by interfacial forces. *Annual Review of Fluid Mechanics*, 21(1):61–99, 1989.
- [125] W. Gao, S. Sattayasamitsathit, and J. Wang. Catalytically propelled micro-/nanomotors: how fast can they move? *The Chemical Record*, 12(1):224–231, 2012.
- [126] F. Mou, Y. Li, C. Chen, W. Li, Y. Yin, H. Ma, and J. Guan. Single-component tio₂ tubular microengines with motion controlled by light-induced bubbles. *Small*, 11(21):2564–2570, 2015.
- [127] F. Zha, T. Wang, M. Luo, and J. Guan. Tubular micro/nanomotors: Propulsion mechanisms, fabrication techniques and applications. *Micromachines*, 9(2):78, 2018.
- [128] M. Manjare, B. Yang, and Y.-P. Zhao. Bubble-propelled microjets: Model and experiment. *The Journal of Physical Chemistry C*, 117(9):4657–4665, 2013.
- [129] V. M. Fomin, M. Hippler, V. Magdanz, L. Soler, S. Sanchez, and O. G. Schmidt. Propulsion mechanism of catalytic microjet engines. *IEEE Transactions on Robotics*, 30(1):40–48, 2014.
- [130] J. Li, G. Huang, M. Ye, M. Li, R. Liu, and Y. Mei. Dynamics of catalytic tubular microjet engines: Dependence on geometry and chemical environment. *Nanoscale*, 3(12):5083–5089, 2011.
- [131] L. Li, J. Wang, T. Li, W. Song, and G. Zhang. Hydrodynamics and propulsion mechanism of self-propelled catalytic micromotors: model and experiment. *Soft matter*, 10(38):7511–7518, 2014.
- [132] P. Lv, H. Le The, J. Eijkel, A. Van den Berg, X. Zhang, and D. Lohse. Growth and detachment of oxygen bubbles induced by gold-catalyzed decomposition of hydrogen peroxide. *The Journal of Physical Chemistry C*, 121(38):20769–20776, 2017.

Bibliography

- [133] C. Pozrikidis. Computation of stokes flow due to the motion or presence of a particle in a tube. *Journal of Engineering Mathematics*, 53(1):1–20, 2005.
- [134] L. Zhu, E. Lauga, and L. Brandt. Low-reynolds number swimming in a capillary tube. *Journal of Fluid Mechanics*, 726:285–311, 2013.
- [135] S. Michelin and E. Lauga. Phoretic self-propulsion at finite pécelet numbers. *Journal of Fluid Mechanics*, 747:572–604, 2014.
- [136] J. Rivero-Rodriguez and B. Scheid. Bubble dynamics in microchannels: inertial and capillary migration forces. *Journal of Fluid Mechanics*, 842:215–247, 2018.
- [137] J. Orozco, B. Jurado-Sánchez, G. Wagner, W. Gao, R. Vazquez-Duhalt, S. Sattayasamitsathit, M. Galarnyk, A. Cortés, D. Saintillan, and J. Wang. Bubble-propelled micromotors for enhanced transport of passive tracers. *Langmuir*, 30(18):5082–5087, 2014.
- [138] J. Li, Z. Liu, G. Huang, Z. An, G. Chen, J. Zhang, M. Li, R. Liu, and Y. Mei. Hierarchical nanoporous microtubes for high-speed catalytic microengines. *NPG Asia Materials*, 6(4):e94, 2014.
- [139] R. Maria-Hormigos, B. Jurado-Sanchez, L. Vazquez, and A. Escarpa. Carbon allotrope nanomaterials based catalytic micromotors. *Chemistry of Materials*, 28(24):8962–8970, 2016.
- [140] J. N. Israelachvili. *Intermolecular and surface forces: revised third edition*. Academic press, 2011.
- [141] G. Gallino, F. Gallaire, E. Lauga, and S. Michelin. Physics of bubble-propelled microrockets. *Advanced Functional Materials*, page 1800686, 2018.
- [142] J. F. Richardson and W. N. Zaki. The sedimentation of a suspension of uniform spheres under conditions of viscous flow. *Chemical Engineering Science*, 3(2):65–73, 1954.
- [143] G. K. Batchelor. Sedimentation in a dilute dispersion of spheres. *Journal of fluid mechanics*, 52(02):245–268, 1972.
- [144] A. Böyum. Isolation of mononuclear cells and granulocytes from human blood. isolation of monuclear cells by one centrifugation, and of granulocytes by combining centrifugation and sedimentation at 1 g. *Scandinavian Journal of Clinical and Laboratory Investigation. Supplementum*, 97:77–89, 1968.
- [145] D. M. Farmer, C. L. McNeil, and B. D. Johnson. Evidence for the importance of bubbles in increasing air–sea gas flux. *Nature*, 361(6413):620, 1993.
- [146] J. C. Bird, R. De Ruiter, L. Courbin, and H. A. Stone. Daughter bubble cascades produced by folding of ruptured thin films. *Nature*, 465(7299):759, 2010.

- [147] G. Barnocky and R. H. Davis. The lubrication force between spherical drops, bubbles and rigid particles in a viscous fluid. *International Journal of Multiphase Flow*, 15(4):627–638, 1989.
- [148] C. Pozrikidis. The deformation of a liquid drop moving normal to a plane wall. *Journal of Fluid Mechanics*, 215:331–363, 1990.
- [149] J. W. Khor, M. Kim, S. S. Schütz, T. M. Schneider, and S. K. Y. Tang. Time-varying droplet configuration determines break-up probability of drops within a concentrated emulsion. *Applied Physics Letters*, 111(12):124102, 2017.
- [150] F. P. Bretherton. The motion of long bubbles in tubes. *Journal of Fluid Mechanics*, 10(2):166–188, 1961.
- [151] E. Reyssat. Drops and bubbles in wedges. *Journal of Fluid Mechanics*, 748:641–662, 2014.

Giacomo Gallino

Curriculum Vitae

✉ giacomo.gallino@epfl.ch



Personal information

Date of birth	August 29, 1988	Nationality	Italian
Place of birth	Genova (GE), Italy	Residence	Lausanne (VD), Switzerland

Research Experiences

- February 2014 - August 2018 **PhD in Mechanical Engineering**, *École Polytechnique Fédérale de Lausanne (EPFL)*, Lausanne, Switzerland.
Four years of academic research in the mathematical modeling of droplet breakup physics. Publications of scientific articles in high profile journals and presentations at international conferences. Projects supervision and teaching at Bachelor and Master level.
- May 2017 - **Research project**, *University of Cambridge*, Cambridge, United Kingdom.
- October 2017 Six-month research project at the Department of Applied Mathematics and Theoretical Physics working on the mathematical modeling of synthetic microswimmers.
- September 2012 - March 2013 **Research Internship**, *École Polytechnique Fédérale de Lausanne (EPFL)*, Lausanne, Switzerland.
Six-month research project at the Laboratory of Fluid Mechanics and Instabilities working on the mathematical modeling of droplets formation in microfluidic channels.

Education

- February 2014 - August 2018 **PhD in Mechanical Engineering**, *Swiss Federal Institute of Technology, Lausanne (EPFL)*, Lausanne, Switzerland.
Thesis title: When droplets deform, break up and propel microswimmers.
- September 2010 - March 2013 **Master of Science Degree in Mechanical Engineering**, *University of Genova*, Genova, Italy.
Master Project title: Local Stability Analysis of a Coaxial Jet at low Reynolds Number.
- September 2007 - March 2010 **Batchelor of Science Degree in Mechanical Engineering**, *University of Genova*, Genova, Italy.
Batchelor Project title: Non linear vibration theory, an introduction: Duffing Equation.

Awards and Scholarships

- November 2016 **SNSF Doc.Mobility Fellowship**. Funding awarded by the Swiss National Science Foundation worth CHF 24k covering living and research costs for a six-month project abroad.
- October 2016 **ZKS Fellowship**. Funding awarded by Zeno Karl Schindler Foundation worth CHF 20k covering living and research costs for a six-month project abroad.

February 2012 **Erasmus Placement Scholarship**. Funding covering living and research costs for a six-month research project abroad.

Language skills

- Italian Mother tongue.
- English Fluent both in writing and speaking.
- French Good level both in writing and speaking. Certificate of B2 level in French from École polytechnique fédérale de Lausanne obtained in January 2016.

Additional schools and trainings

- Complex Motion in Fluids Summer School. Cambridge, United Kingdom, September 24-28 2017.
- Aux Rencontres de Peyresq, Mécanique nonlinéaire: structures et dynamiques. Peyresq, France, June 6-10 2016.
- Complex Motion in Fluids Summer School. Krogerup, Denmark, August 9-15 2015.
- MPI, an introduction to parallel programming. EPFL, Switzerland, April 14-16 2015.
- Flowing Soft Matter: Bridging the Gap between Statistical Physics and Fluid Mechanics. CISM, Udine, Italy June 30 to July 4 2014.
- C++, A Comprehensive Hands-On Introduction. EPFL, Switzerland. June 23-27 2014.

Teaching and Students supervision

- Fluid flow, Bachelor course in Mechanical Engineering at EPFL. Hydrodynamics, Master course in Mechanical Engineering at EPFL. Numerical flow simulations, Master course in Mechanical Engineering at EPFL.
- Tutored one visiting student from Polytechnic University of Catalonia at EPFL. Title of the project: "Relaxation of an ellipsoidal droplet."

Publications

Peer-reviewed journal articles

- G. Gallino, L. Zhu, & F. Gallaire. (2016). The stability of a rising droplet: an inertialess non-modal growth mechanism. *Journal of Fluid Mechanics*, 786, R2.
- G. Gallino, F. Gallaire, E. Lauga & S. Michelin (2018). Physics of bubble-propelled microrockets. *Advanced Functional Materials*, 1800686.
- G. Gallino, T.M. Schneider & F. Gallaire. Edge states control droplet breakup in subcritical extensional flows. *Accepted in Physical Review Fluids*.

Papers in preparation

- G. Gallino, L. Zhu, & F. Gallaire. The hydrodynamics of a microrocket propelled by a deformable bubble.
- G. Gallino, F. Gallaire, E. Lauga & S. Michelin. The motion of a bubble inflating next to a wall.

Conferences and invited talks

The hydrodynamics of a self-propelled conical micromotor and the effect of bubble deformability. Invited talk at LadHyx, Paris, France, January 31 2017.

The hydrodynamics of a self-propelled conical micromotor. 70th Annual Meeting of the APS Division of Fluid Dynamics, Denver, Colorado, USA, November, 19-21, 2017.

Droplet breakup in low Reynolds number flows: a nonlinear mechanism. Invited talk at Unige, Genoa, Italy, October 16 2017.

Edge states control droplet breakup in uniaxial extensional flows. Euromech Symposium 591, Bari, Italy, September, 18-20, 2017.

The hydrodynamics of a self-propelled conical micromotor. 11th European Fluid Mechanics conference, Seville, Spain, September, 12-16, 2016.

The stability of a rising droplet: an inertialess non-modal growth mechanism. 68th Annual Meeting of the APS Division of Fluid Dynamics, Boston, Massachusetts, USA, November, 22-24, 2015.